SCIENCE

JOURNAL OF RESEARCH

OF THE U.S. GEOLOGICAL SURVEY

NOVEMBER–DECEMBER 1977
VOLUME 5, NUMBER 6

UICC LIBRARY
NOV 8 1977
DOCUMENTS

Scientific notes and summaries of investigations in geology, hydrology, and related fields

U.S.
DEPOSITORY

U.S. DEPARTMENT OF THE INTERIOR

UNITED STATES DEPARTMENT OF THE INTERIOR
CECIL D. ANDRUS, Secretary
GEOLOGICAL SURVEY
V. E. McKelvey, Director

For sale by Superintendent of Documents, U.S. Government Printing Office, Washington, DC 20402. Annual subscription rate, $18.90 (plus $4.75 for foreign mailing). Make check or money order payable to Superintendent of Documents. Send all subscription inquiries and address changes to Superintendent of Documents at above address.

Purchase single copy ($3.15) from Branch of Distribution, U.S. Geological Survey, 1200 South Eads Street, Arlington, VA 22202. Make check or money order payable to U.S. Geological Survey.

Library of Congress Catalog-card No. 72-600241.

The Journal of Research is published every 2 months by the U.S. Geological Survey. It contains papers by members of the Geological Survey and their professional colleagues on geologic, hydrologic, topographic, and other scientific and technical subjects.

Correspondence and inquiries concernir Journal (other than subscription inquirie address changes) should be directed to Ar Orellana, Managing Editor, Journal of Re Publications Division, U.S. Geological S 321 National Center, Reston, VA 22092.

Papers for the Journal should be sub through regular Division publication chann

The Secretary of the Interior has determined that the publication of this perio cal is necessary in the transaction of the public business required by law of t Department. Use of funds for printing this periodical has been approved by t Director of the Office of Management and Budget through June 30, 1980.

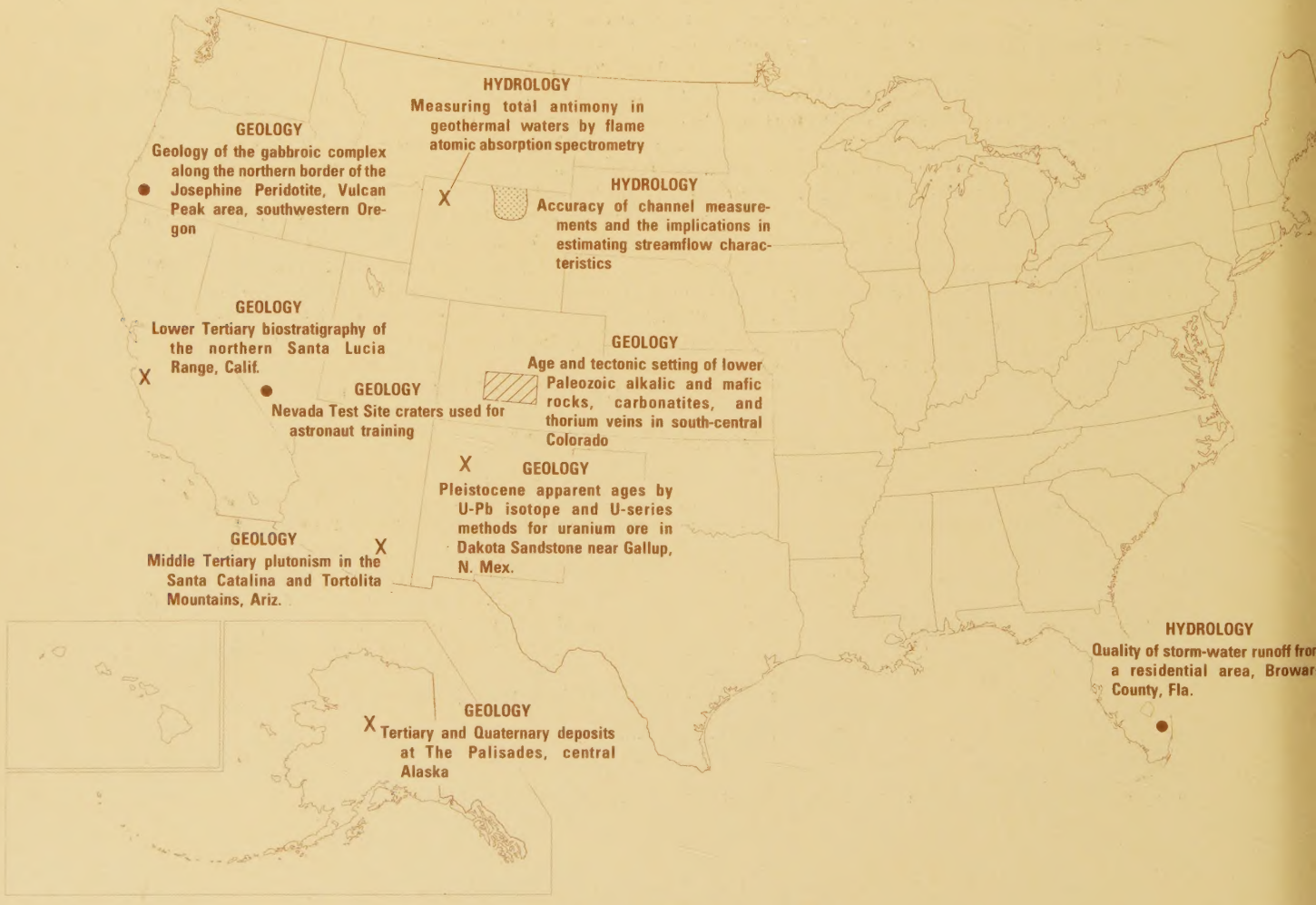
HYDROLOGY
Measuring total antimony in geothermal waters by flame atomic absorption spectrometry
GEOLOGY
Geology of the gabbroic complex along the northern border of the Josephine Peridotite, Vulcan Peak area, southwestern Oregon
HYDROLOGY
Accuracy of channel measurements and the implications in estimating streamflow characteristics
GEOLOGY
Lower Tertiary biostratigraphy of the northern Santa Lucia Range, Calif.
GEOLOGY
Age and tectonic setting of lower Paleozoic alkalic and mafic rocks, carbonatites, and thorium veins in south-central Colorado
GEOLOGY
Nevada Test Site craters used for astronaut training
GEOLOGY
Pleistocene apparent ages by U-Pb isotope and U-series methods for uranium ore in Dakota Sandstone near Gallup, N. Mex.
GEOLOGY
Middle Tertiary plutonism in the Santa Catalina and Tortolita Mountains, Ariz.
HYDROLOGY
Quality of storm-water runoff fro a residential area, Browar County, Fla.
GEOLOGY
Tertiary and Quaternary deposits at The Palisades, central Alaska

GEOGRAPHIC INDEX TO ARTICLES

See "Contents" for articles concerning areas outside the United States and articles without geographic orientation.

JOURNAL OF RESEARCH

of the

U.S. Geological Survey

Vol. 5 No. 6 Nov.–Dec. 1977

CONTENTS

SI units and U.S. customary equivalents II

GEOLOGIC STUDIES

Effect of initial radioactive-daughter disequilibrium on U-Pb isotope apparent ages of young minerals ..... *K. R. Ludwig* 663

Pleistocene apparent ages by U-Pb isotope and U-series methods for uranium ore in Dakota Sandstone near Gallup, N. Mex ..... *K. R. Ludwig, B. J. Szabo, and H. C. Granger* 669

Age and tectonic setting of lower Paleozoic alkalic and mafic rocks, carbonatites, and thorium veins in south-central Colorado ..... *J. C. Olson, R. F. Marvin, R. L. Parker, and H. H. Mehnert* 673

Potassium-argon geochronology of some metamorphic, igneous, and hydrothermal events in Puerto Rico and the Virgin Islands ..... *D. P. Cox, R. F. Marvin, J. W. M'Gonigle, D. H. McIntyre, and C. L. Rogers* 689

Middle Tertiary plutonism in the Santa Catalina and Tortolita Mountains, Ariz ..... *S. C. Creasey, N. G. Banks, R. P. Ashley, and T. G. Theodore* 705

Nevada Test Site craters used for astronaut training ..... *H. J. Moore* 719

Lower Tertiary biostratigraphy of the northern Santa Lucia Range, Calif ..... *R. Z. Poore, W. V. Sliter, and M. H. Link* 735

Tertiary and Quaternary deposits at The Palisades, central Alaska ..... *W. E. Yeend* 747

Petrology of basalt from the East Pacific Rise near 21° north latitude ..... *J. G. Moore, W. R. Normark, G. R. Hess, and C. E. Meyer* 753

Geology of the gabbroic complex along the northern border of the Josephine Peridotite, Vulcan Peak area, southwestern Oregon ..... *R. A. Loney and G. R. Himmelberg* 761

High-resolution gamma-ray spectrometry in uranium exploration ..... *R. M. Moxham and A. B. Tanner* 783

Heat capacities of gibbsite, Al $(OH)_3$, between 13 and 480 K and magnesite, $MgCO_3$, between 13 and 380 K and their standard entropies at 289.15 K, and the heat capacities of Calorimetry Conference benzoic acid between 12 and 316 K ..... *B. S. Hemingway, R. A. Robie, J. R. Fisher, and W. H. Wilson* 797

HYDROLOGIC STUDIES

Measuring total antimony in geothermal waters by flame atomic absorption spectrometry ..... *R. E. Stauffer* 807

Accuracy of channel measurements and the implications in estimating streamflow characteristics ..... *K. L. Wahl* 811

Solution of water-table and anisotropic flow problems by using the strongly implicit procedure ..... *S. P. Larson and P. C. Trescott* 815

Quality of storm-water runoff from a residential area, Broward County, Fla ..... *H. C. Mattraw, Jr., and C. B. Sherwood* 823

ANNUAL INDEX TO VOLUME 5

Subject 835

Author 841

Recent publications of the U.S. Geological Survey ..... Inside of back cover

SI UNITS AND U.S. CUSTOMARY EQUIVALENTS

[SI, International System of Units, a modernized metric system of measurement. All values have been rounded to four significant digits except 0.01 bar, which is the exact equivalent of 1 kPa. Use of hectare (ha) as as alternative name for square hectometer (hm^2) is restricted to measurement of land or water areas. Use of liter (L) as a special name for cubic decimeter (dm^3) is restricted to the measurement of liquids and gases; no prefix other than milli should be used with liter. Metric ton (t) as a name for megagram (Mg) should be restricted to commercial usage, and no prefixes should be used with it. Note that the style of $meter^2$ rather than square meter has been used for convenience in finding units in this table. Where the units are spelled out in text, Survey style is to use square meter]

SI unit		U.S. customary equivalent	
Length			
millimeter (mm)	=	0.039 37	inch (in)
meter (m)	=	3.281	feet (ft)
	=	1.094	yards (yd)
kilometer (km)	=	0.621 4	mile (mi)
	=	0.540 0	mile, nautical (nmi)
Area			
$centimeter^2$ (cm^2)	=	0.155 0	$inch^2$ (in^2)
$meter^2$ (m^2)	=	10.76	$feet^2$ (ft^2)
	=	1.196	$yards^2$ (yd^2)
	=	0.000 247 1	acre
$hectometer^2$ (hm^2)	=	2.471	acres
	=	0.003 861	section (640 acres or 1 mi^2)
$kilometer^2$ (km^2)	=	0.386 1	$mile^2$ (mi^2)
Volume			
$centimeter^3$ (cm^3)	=	0.061 02	$inch^3$ (in^3)
$decimeter^3$ (dm^3)	=	61.02	$inches^3$ (in^3)
	=	2.113	pints (pt)
	=	1.057	quarts (qt)
	=	0.264 2	gallon (gal)
	=	0.035 31	$foot^3$ (ft^3)
$meter^3$ (m^3)	=	35.31	$feet^3$ (ft^3)
	=	1.308	$yards^3$ (yd^3)
	=	264.2	gallons (gal)
	=	6.290	barrels (bbl) (petroleum, 1 bbl=42 gal)
	=	0.000 810 7	acre-foot (acre-ft)
$hectometer^3$ (hm^3)	=	810.7	acre-feet (acre-ft)
$kilometer^3$ (km^3)	=	0.239 9	$mile^3$ (mi^3)
Volume per unit time (includes flow)			
$decimeter^3$ per second (dm^3/s)	=	0.035 31	$foot^3$ per second (ft^3/s)
	=	2.119	$feet^3$ per minute (ft^3/min)
Volume per unit time (includes flow)—Continued			
$decimeter^3$ per second (dm^3/s)	=	15.85	gallons per minute (gal/min)
	=	543.4	barrels per day (bbl/d) (petroleum, 1 bbl=42 gal)
$meter^3$ per second (m^3/s)	=	35.31	$feet^3$ per second (ft^3/s)
	=	15 850	gallons per minute (gal/min)
Mass			
gram (g)	=	0.035 27	ounce avoirdupois (oz avdp)
kilogram (kg)	=	2.205	pounds avoirdupois (lb avdp)
megagram (Mg)	=	1.102	tons, short (2 000 lb)
	=	0.984 2	ton, long (2 240 lb)
Mass per unit volume (includes density)			
kilogram per $meter^3$ (kg/m^3)	=	0.062 43	pound per $foot^3$ (lb/ft^3)
Pressure			
kilopascal (kPa)	=	0.145 0	pound-force per $inch^2$ (lbf/in^2)
	=	0.009 869	atmosphere, standard (atm)
	=	0.01	bar
	=	0.296 1	inch of mercury at 60°F (in Hg)
Temperature			
temp kelvin (K)	=	[temp deg Fahrenheit (°F) +459.67]/1.8	
temp deg Celsius (°C)	=	[temp deg Fahrenheit (°F) −32]/1.8	

The policy of the "Journal of Research of the U.S. Geological Survey" is to use SI metric units of measurement except for the following circumstance:

When a paper describes either field equipment or laboratory apparatus dimensioned or calibrated in U.S. customary units and provides information on the physical features of the components and operational characteristics of the equipment or apparatus, then dual units may be used. For example, if a pressure gage is calibrated and available only in U.S. customary units of measure, then the gage may be described using SI units in the dominant position with the equivalent U.S. customary unit immediately following in parentheses. This also applies to the description of tubing, piping, vessels, and other items of field and laboratory equipment that normally are described in catalogs in U.S. customary dimensions.

S. M. Lang, *Metrics Coordinator,*
U.S. Geological Survey

Any use of trade names and trademarks in this publication is for descriptive purposes only and does not constitute endorsement by the U.S. Geological Survey.

Jour. Research U.S. Geol. Survey
Vol. 5, No. 6, Nov.–Dec. 1977, p. 663–667

EFFECT OF INITIAL RADIOACTIVE-DAUGHTER DISEQUILIBRIUM ON U-Pb ISOTOPE APPARENT AGES OF YOUNG MINERALS

By KENNETH R. LUDWIG, Denver, Colo.

Abstract.—Most calculations of U-Pb isotope apparent ages re made by use of equations that assume initial secular quilibrium of the uranium decay-chains. The possible error calculated Pb/U isotope ratios arising from this assumption especially for ores of sandstone uranium deposits) can be ver 10 percent at 1 million years and exceed analytical error ven at a 30 m.y. apparent age. Use of the more general equaons (adapted from the Bateman equations) is desirable for alculation and interpretation of U-Pb isotope apparent ages f both open and closed systems in the range of 2 to 20 .y. and is essential for apparent ages less than about 2 m.y. or very young sandstone uranium deposits, a significant unertainty in the $^{206}Pb/^{238}U$ systematics may still persist owing the uncertainty in the initial value of $^{234}U/^{235}U$.

The present state of U-Pb isotope analytical techiques permits routine determinations of radiogenic-Pb/U ratios to be made for major uranium minerals lder than ≈ 100 000 years and for accessory igneous inerals with ≳200 ppm U, such as zircon, older nan ≈10 m.y. The common method of calculating U-Pb isotope apparent ages from observed $^{206}Pb/^{238}U$, $^{207}Pb/^{235}U$, and $^{207}Pb/^{206}Pb$ ratios is to use the equaion,

$$\frac{N_d}{N_p} = e^{\lambda p t} - 1 \qquad (1)$$

where N_d and N_p are the present-day abundances f daughter and parent isotopes respectively; λ_p is the ecay constant of the parent isotope, and t is the age f the sample. Although equation 1 requires that any adioactive-daughter isotopes be initially present in mounts inversely proportional to their decay conants (that is, the system is initially and always in ecular equilibrium), any error introduced by deviaons from this requirement is commonly assumed to e insignificant. The fact that the longest lived radioctive daughter in the ^{235}U decay chain, for instance, as a half-life of only 32 500 years, "intuitively" seems justify such an assumption for $^{207}Pb/^{235}U$ ages down at least 1 m.y. However, in the course of interpretng isotopic analyses of uranium ores with U-Pb ages in the range of 0.1–5 m.y., I have observed that use of the simplified equation 1 can introduce errors that are both surprisingly large (13–1.2 percent in the 1–10 m.y. age range) and persistent (beyond analytical error of the $^{207}Pb/^{206}Pb$ ratio even at a 30-m.y. apparent age). The following discussion is intended to show the desirability of using equations that take into account initial radioactive disequilibria of the uranium daughters, and it is focused mainly on the problems of dating very young uranium ores.

DECAY SCHEMES AND INITIAL ISOTOPIC ABUNDANCES

The decay schemes of ^{238}U and ^{235}U, simplified to include only isotopes with half-lives >1 year, are

$$^{238}U \xrightarrow{4.47 \times 10^9\ yr} {}^{234}U \xrightarrow{244{,}000\ yr} {}^{230}Th \xrightarrow{77{,}000\ yr}$$

$$^{226}Ra \xrightarrow{1{,}600\ yr} {}^{210}Pb \xrightarrow{22.3\ yr} {}^{206}Pb \text{ (stable)}$$

and $$^{235}U \xrightarrow{7.04 \times 10^8\ yr} {}^{231}Pa \xrightarrow{32{,}500\ yr}$$

$$^{227}Ac \xrightarrow{21.8\ yr} {}^{207}Pb \text{ (stable)},$$

where the half-lives (Jaffey and others, 1971, and Holden and Walker, 1972) are given to the right of the isotope.

If the various radioactive-daughter isotopes have always been in secular equilibrium (equal number of decays per unit time for all isotopes), then equation 1 accurately describes the $^{206}Pb/^{238}U$ and $^{207}Pb/^{235}U$ values of a closed system. However, the relative amounts of uranium-daughter isotopes in a newly formed mineral will not generally yield secular equilibrium, owing both to variable elemental discrimination by the mineral and to possible radioactive disequilibrium in the environment of crystallization of the mineral (for example, an ore-forming fluid). In particular, most sandstone-host uranium ores of the western United States are highly depleted in thorium and

(common) lead[1] and almost certainly were formed without significant protactinium.[2]

The initial abundances of radium and actinium in sandstone-host uranium ores are poorly known. Perhaps the best indicator would be the distribution of barium, a close chemical analog of radium.[3] The data of Shoemaker and others (1959) suggest that, in the Colorado Plateau, only a few ore bodies are enriched in barium. Harshman (1972) observed that a Wyoming ore body might be only slightly enriched in barium. Thus, on the whole, the available data do not imply that most sandstone-host uranium ore bodies are markedly enriched in barium relative to uranium. The calculations in this report, therefore, assume no initial radium; however, this assumption may introduce significant error for very young deposits ($\lesssim$100 000 yr) that are enriched in barium.

The precise ($^{234}U/^{238}U$),* or activity ratio of $^{234}U/^{238}U$, expected in a newly formed uranium ore mineral is somewhat uncertain. Radiogenic ^{234}U formed in situ differs from the coexisting ^{238}U in oxidation state and type of bonding and is more readily leachable than the ^{238}U (Rosholt and others, 1963). As a consequence, igneous rocks and many old (>1 m.y.) uranium ore bodies exposed to the action of ground water have typically low $(^{234}U/^{238}U)^*$ values (Richardson, 1963; Rosholt and others, 1964a, b; Rosholt and others, 1965). Thus, an ore body formed by precipitation of uranium in ground waters that were actively leaching uranium from igneous rocks might have a high initial $(^{234}U/^{238}U)^*$—perhaps 1.1–1.5. In contrast, an ore body formed by rapid and complete dissolution, transport, and reprecipitation of a much older uranium deposit might have an initial $(^{234}U/^{238}U)^*$ as low as 0.6.[4] For very young (<0.5 m.y.) ore bodies, the most satisfactory method of estimating initial $(^{234}U/^{238}U)^*$ is probably to measure the current $(^{234}U/^{238}U)^*$ and correct for the approximate age of the deposit. This method is possible if $^{207}Pb/^{235}U$ or $^{231}Pa/^{235}U$-$^{230}Th/^{238}U$ ages can be obtained (Ludwig and others, 1977).

The mineral zircon presents different problems. Even though the high-temperature and low oxygen fugacity conditions of magmas probably limit initial $(^{234}U/^{238}U)^*$ values of igneous zircons essentially to unity, prediction of initial ^{230}Th and ^{231}Pa abundances is more difficult than such prediction for most sandstone-host uranium deposits. Mattinson (1973) discussed possible initial ^{230}Th and ^{231}Pa values for zircons and calculated the maximum error in predicted $^{207}Pb/^{206}Pb$ introduced by using equation 1 for a 14-m.y.-old zircon. He concluded that ^{230}Th would be depleted relative to ^{238}U according to the ratio $(Th/U)_{zircon}/(Th/U)_{whole\ rock}$ and that ^{231}Pa would be excluded to a lesser but uncertain extent. His method of estimating initial $^{230}Th/^{238}U$ for zircons assumes that the activity ratio of $^{230}Th/^{238}U=1$ for the magma. However, recent data on $^{230}Th/^{238}U$ activity ratios of volcanic rocks (Allègre and Condomines, 1976) show that this ratio can range at least from 0.8 to 2.1. Thus, both the initial ^{230}Th and ^{231}Pa abundances are uncertain for zircons.

APPARENT-AGE EQUATIONS FOR YOUNG SAMPLES

The general form of the apparent-age equations for a closed system is given by the Bateman equations familiar to radiochemists. For example, see Kirby (1973). For apparent ages >1000 yr, we may consider only daughters with half-lives more than 1 yr, and the resulting equations are

$$\left(\frac{^{207}Pb}{^{235}U}\right) = e^{\lambda_{235}t}\cdot\left(D_1e^{-\lambda_{235}t} + D_2e^{-\lambda_{231}t} + D_3e^{-\lambda_{227}t} + 1\right), \quad (2)$$

$$F_1 = \left(\frac{^{206}Pb}{^{238}U}\right)_{from\ ^{238}U} = e^{\lambda_{238}t}\cdot\left(C_1e^{-\lambda_{238}t} + C_2e^{-\lambda_{234}t} + C_3e^{-\lambda_{230}t} + C_4e^{-\lambda_{226}t} + C_5e^{-\lambda_{210}t} + 1\right), \quad (3)$$

$$F_2 = \left(\frac{^{206}Pb}{^{238}U}\right)_{from\ initial\ ^{234}U} = \frac{\lambda_{238}}{\lambda_{234}}\cdot e^{\lambda_{234}t}\cdot\left(\frac{^{234}U}{^{238}U}\right)_I^*\cdot \left(E_1e^{-\lambda_{234}t} + E_2e^{-\lambda_{230}t} + E_3e^{-\lambda_{226}t} + E_4e^{-\lambda_{210}t} + 1\right), \quad (4)$$

$$\left(\frac{^{206}Pb}{^{238}U}\right)_{total} = F_1 + F_2, \quad (5)$$

where λ_n = decay constant of isotope n; C_i, D_i, and E_i are the Bateman coefficients given by equation 6,

[1] For example, high-grade ores with 10–20 percent U from the Eocene host-rock deposits of Wyoming contain only 1–10 ppm Th and 1–20 ppm common Pb (Ludwig, 1978, and unpub. data, 1977).

[2] Protactinium is very insoluble in aqueous fluids (Elston, 1954), and should be left behind as the uranium is transported in ore-forming fluids.

[3] Because actinium is generally associated with radium in typical sandstone environments (Rosholt, 1958), the discussion is also pertinent to actinium.

[4] Weighted average of the roll-feature analyzed by Rosholt and others (1965).

TABLE 1.—U-Pb *isotope ratios for closed systems of 0.01- to 20-m.y. age*

Initial abundance of Th, Pa, Ra, Ac, and Pb is assumed to be negligible. Half-lives used are ^{238}U—4.4683×10^{9} yr; ^{235}U—7.0381×10^{8} yr (Jaffey and others, 1971); ^{230}Th—77 000 yr; ^{231}Pa—32 500 yr; ^{226}Ra—1600 yr; ^{210}Pb—22.3 yr; ^{227}Ac—21.77 yr (Holden and Walker, 1972); $(^{238}U/^{235}U)$ today was assumed to be 137.88.

The listed $^{206}Pb/^{238}U$ and $^{207}Pb/^{206}Pb$ values were calculated for an initial $^{234}U/^{238}U$ activity ratio of 1.00; K is a correction factor to be used for variations in initial $(^{234}U/^{238}U)^*$. To solve for systems with initial excesses or deficiencies of ^{234}U, use the formula $(^{206}Pb/^{238}U)_a = (^{206}Pb/^{238}U)_1 + K\cdot(\Delta_{234}\%)$, where subscripts a and 1 refer to the values for systems with initial $^{234}U/^{238}U$ ratios of an arbitrary value and one, respectively, and $\Delta_{234}\%$ is the percent excess (negative if deficiency) of initial ^{234}U defined by $\Delta_{234}\% = [(^{234}U/^{238}U)^* - 1]\cdot100$.

Notations such as 4.3460E–8 are equivalent to 4.3460×10^{-8}.

$$C_{i,etc.} = \frac{\prod_{j=1}^{n-1}(\lambda_j)}{\prod_{\substack{j=1\\ j\neq i}}^{n}(\lambda_j-\lambda_i)}; \qquad (6)$$

n = number of isotopes in the decay chain; t = age; and $(^{234}U/^{238}U)_I^*$ is the initial activity ratio of $^{234}U/^{238}U$.

The i and j values for equation 6 are according to the order of the daughter isotope in the ^{238}U or ^{235}U decay chain, and $\lambda_{206} = \lambda_{207} = 0$, so that, for example,

$$C_2 = -\frac{\lambda_{238}\lambda_{230}\lambda_{226}\lambda_{210}}{(\lambda_{234}-\lambda_{238})(\lambda_{234}-\lambda_{230})(\lambda_{234}-\lambda_{226})(\lambda_{234}-\lambda_{210})}$$

These equations assume negligible initial ^{231}Pa, ^{227}Ac, ^{230}Th, ^{226}Ra, ^{210}Pb, ^{206}Pb, and ^{207}Pb but are easily modified to deal with nonzero initial abundances of these isotopes. Because these solutions are tedious to calculate by hand, even with a modern calculator, they are tabulated in table 1. The difference between these values and the solutions to equation 1 are shown in figure 1. Equations 2 and 5 result in a strikingly different $^{207}Pb/^{206}Pb$ age curve compared to the results of equation 1. See figure 2. Using the more general equations, we see that a given $^{207}Pb/^{206}Pb$ value in fact defines two apparent ages and that the $^{207}Pb/^{206}Pb$ ratio is minimum at about 13 m.y. for a system with an initial $(^{234}U/^{238}U)^*$ of one. It is evident that if Pb/U isotope ratios are available, the only serious confusion occurs for samples with apparent ages in the range of about 13±5 m.y. I should also mention that use of the general equations 2 and 5 is important even for evaluating U-Pb isotope apparent ages of open systems. For example, estimation of the integrated daughter loss by use of U-Pb isotope ratios as in Ludwig (1977) would be rigorously meaningful for very young samples only if the concordia curve derived from equations 2 and 5 were used.

TABLE 1.—U-Pb *isotope ratios for closed systems of 0.01- to 20-m.y. age*—Continued

Age (m.y.)	$^{206}Pb/^{238}U$	$^{207}Pb/^{235}U$	$^{207}Pb/^{206}Pb$	K
0.01	4.3460E-8	9.7346E-7	0.162454	4.311E-10
.02	2.0987E-7	3.6515E-6	.126190	2.063E- 9
.03	4.9540E-7	7.7069E-6	.112829	4.824E- 9
.04	8.8989E-7	1.2875E-5	.104932	8.583E- 9
.05	1.3840E-6	1.8942E-5	.099266	1.322E- 8
.06	1.9691E-6	2.5736E-5	.094793	1.863E- 8
.07	2.6373E-6	3.3116E-5	.091071	2.470E- 8
.08	3.3816E-6	4.0971E-5	.087873	3.136E- 8
.09	4.1953E-6	4.9209E-5	.085070	3.852E- 8
.10	5.0726E-6	5.7756E-5	.082579	4.610E- 8
.12	6.9962E-6	7.5554E-5	.078324	6.230E- 8
.14	9.1140E-6	9.4012E-5	.074812	7.951E- 8
.16	1.1394E-5	1.1290E-4	.071865	9.735E- 8
.18	1.3810E-5	1.3207E-4	.069363	1.155E- 7
.20	1.6339E-5	1.5143E-4	.067219	1.338E- 7
.30	3.0126E-5	2.4937E-4	.060034	2.216E- 7
.40	4.4938E-5	3.4782E-4	.056136	2.967E- 7
.50	6.0166E-5	4.4634E-4	.053803	3.569E- 7
.60	7.5565E-5	5.4487E-4	.052297	4.039E- 7
.70	9.1032E-5	6.4342E-4	.051262	4.399E- 7
.80	1.0653E-4	7.4198E-4	.050516	4.674E- 7
.90	1.2204E-4	8.4055E-4	.049954	4.882E- 7
1.0	1.3755E-4	9.3912E-4	.049518	5.040E- 7
1.2	1.6858E-4	1.1363E-3	.048887	5.250E- 7
1.4	1.9961E-4	1.3335E-3	.048453	5.370E- 7
1.6	2.3064E-4	1.5308E-3	.048136	5.438E- 7
1.8	2.6168E-4	1.7281E-3	.047896	5.478E- 7
2.0	2.9272E-4	1.9254E-3	.047707	5.500E- 7
2.2	3.2375E-4	2.1228E-3	.047555	5.513E- 7
2.4	3.5479E-4	2.3202E-3	.047430	5.520E- 7
2.6	3.8583E-4	2.5177E-3	.047327	5.525E- 7
2.8	4.1687E-4	2.7152E-3	.047239	5.527E- 7
3.0	4.4791E-4	2.9127E-3	.047163	5.529E- 7
3.5	5.2552E-4	3.4067E-3	.047016	5.530E- 7
4.0	6.0313E-4	3.9010E-3	.046910	5.531E- 7
4.5	6.8074E-4	4.3954E-3	.046829	5.532E- 7
5.0	7.5837E-4	4.8902E-3	.046767	5.532E- 7
6	9.1363E-4	5.8804E-3	.046680	5.533E- 7
7	1.0689E-3	6.8716E-3	.046624	5.534E- 7
8	1.2242E-3	7.8637E-3	.046586	5.535E- 7
9	1.3796E-3	8.8568E-3	.046562	5.536E- 7
10	1.5349E-3	9.8509E-3	.046546	5.536E- 7
11	1.6903E-3	1.0846E-2	.046537	5.537E- 7
12	1.8457E-3	1.1842E-2	.046533	5.538E- 7
13	2.0012E-3	1.2839E-2	.046532	5.539E- 7
14	2.1566E-3	1.3837E-2	.046534	5.540E- 7
15	2.3121E-3	1.4836E-2	.046538	5.541E- 7
16	2.4676E-3	1.5836E-2	.046545	5.542E- 7
17	2.6232E-3	1.6837E-2	.046553	5.542E- 7
18	2.7787E-3	1.7839E-2	.046562	5.543E- 7
19	2.9343E-3	1.8842E-2	.046572	5.544E- 7
20	3.0899E-3	1.9846E-2	.046583	5.545E- 7

REFERENCES CITED

Allègre, C. J., and Condomines, Michael, 1976, Fine chronology of volcanic process using ^{238}U-^{230}Th systematics: Earth and Planetary Sci. Letters, v. 28, p. 395–406.

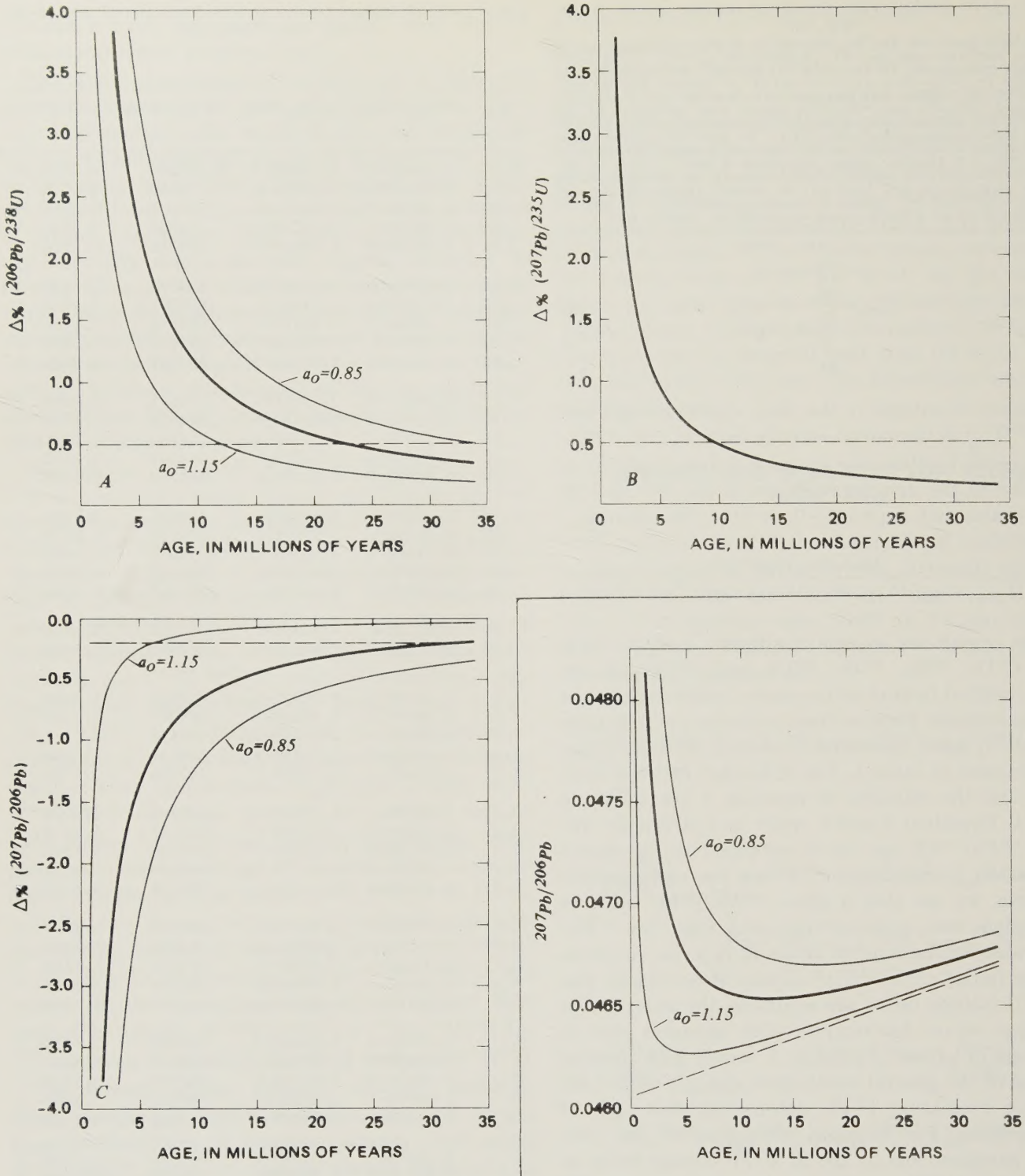

FIGURE 1.—Difference in percent (Δ%) between isotope ratios calculated by assuming secular equilibrium of radioactive uranium daughters and ratios calculated by assuming initial absence of all radioactive daughters but ^{234}U. The bold curve is calculated for an initial $^{234}U/^{238}U$ activity ratio (a_o) of one; light curves, for a_o=0.85 and 1.15. Dashed line shows Δ% values resolvable by careful analytical techniques and with no uncertainty in common-lead correction.

FIGURE 2.—$^{207}Pb/^{206}Pb$ values of radiogenic lead for systems of 0–35 m.y. age with different initial uranium-daughter abundances. Solid curves are calculated for initial absence of all uranium daughters but ^{234}U; bold curve assumes an initial $^{234}U/^{238}U$ activity ratio (a_o) of one; light curves, a_o=0.85 and 1.15. Dashed line is the "conventionally" calculated $^{207}Pb/^{206}Pb$, which assumes initial secular equilibrium of radioactive uranium daughters.

Elston, R. E., 1954, The chemistry of protactinium, *in* Seaborg, G. T., and Katz, J. J., eds., The actinide elements: Natl. nuclear energy ser., Div. IV, v. 14A: New York, McGraw Hill Book Co., p. 117.

Harshman, E. N., 1972, Geology and uranium deposits, Shirley Basin area, Wyoming: U.S. Geol. Survey Prof. Paper 745, 82 p.

Holden, N. E., and Walker, F. W., 1972, Chart of the nuclides [11th ed.]: Atomic Energy Comm., Knolls Atomic Power Lab., Naval Reactors.

Jaffey, A. H., Flynn, K. F., Glendenin, L. E., Bentley, W. C., and Essling, A. M., 1971, Precision measurement of half-lives and specific activities of ^{235}U and ^{238}U: Phys. Rev. C., v. 4, p. 1889–1906.

Kirby, H. W., 1973, Nuclear properties and genetic relationships of the naturally occurring radioactive series: Atomic Energy Comm. Research and Devel. Rept. MLM–2036, p. 25–43.

Ludwig, K. R., 1978, Uranium daughter migration and U-Pb isotope apparent ages of uranium ores, Shirley Basin, Wyoming: Econ. Geology. (In press.)

Ludwig, K. R., Szabo, B. J., and Granger, H. C., 1977, Pleistocene apparent ages by U-Pb isotope and U-series methods for uranium ore in Dakota Sandstone near Gallup, New Mexico: U.S. Geol. Survey Jour. Research, v. 5, no. 6, p. 669–672.

Mattinson, J. M., 1973, Anomalous isotopic composition of lead in young zircons: Carnegie Inst. Washington Yearbook 72, p. 613–616.

Richardson, K. A., 1963, Thorium, uranium and potassium in the Conway Granite, New Hampshire, U.S.A., *in* The natural radiation environment: Chicago Univ. Press, p. 46.

Rosholt, J. N., Jr., 1958, Radioactive disequilibrium studies as an aid in understanding the natural migration of uranium and its decay products, Nations, Survey of raw material resources: Internat. Conf. on Peaceful Uses of Atomic Energy, 2d, Geneva, Proc. v. 2, p. 230–236.

Rosholt, J. N., Shields, W. R., and Garner, E. L., 1963, Isotopic fractionation of uranium in sandstone: Science, v. 137, p. 224–226.

Rosholt, J. N., Garner, E. L., and Shields, W. R., 1964a, Fractionation of uranium isotopes and daughter products in weathered granite and uranium-bearing sandstone, Wind River Basin region, Wyoming, *in* Geological Survey research 1964: U.S. Geol. Survey Prof. Paper 501–B, B84–B87.

Rosholt, J. N., Harshman, E. M., Shields, W. R., and Garner, E. L., 1964b, Isotopic fractionation of uranium related to roll features in sandstone, Shirley Basin, Wyoming: Econ. Geology, v. 59, no. 4, p. 570–585.

Rosholt, J. N., Butler, A. P., Garner, E .L., and Shields, W. R., 1965, Isotope fractionation of uranium in sandstone, Powder River Basin, Wyoming, and Slick Rock district, Colorado: Econ. Geology, v. 60, no. 2, p. 199–213.

Shoemaker, E. M., Miesch, A. T., Newman, W. L., and Riley, L. B., 1959, Elemental composition of sandstone-type deposits, *in* Garrels, R. M., and Larsen, E. S., 3d, eds., Geochemistry and mineralogy of the Colorado Plateau uranium ores: U.S. Geol. Survey Prof. Paper 320, p. 25–54.

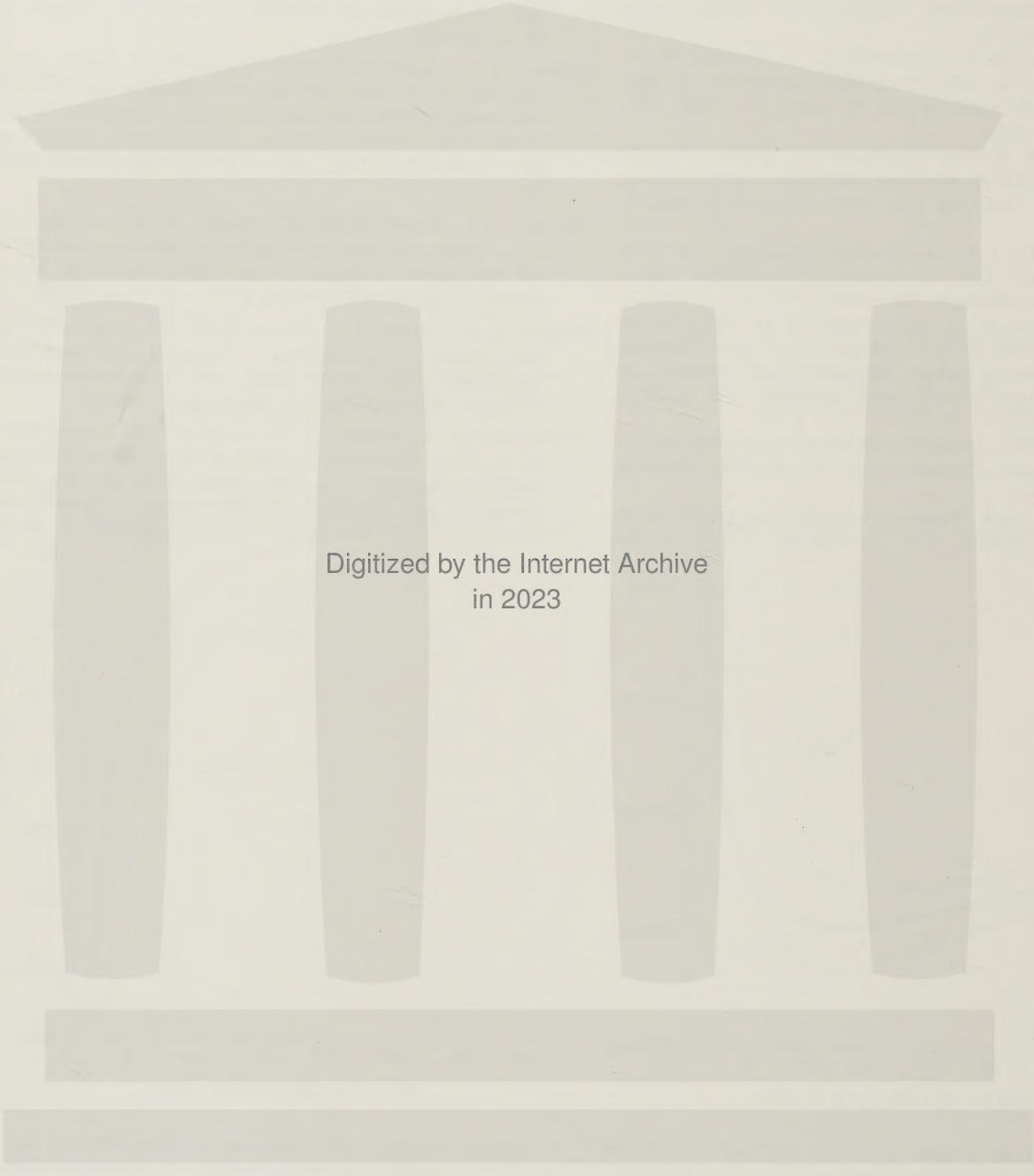

Digitized by the Internet Archive
in 2023

https://archive.org/details/journal-of-research-us-geological-survey_november-december-1977_5_6

Jour. Research U.S. Geol. Survey
Vol. 5, No. 6, Nov.–Dec. 1977, p. 669–672

PLEISTOCENE APPARENT AGES BY U-Pb ISOTOPE AND U-SERIES METHODS FOR URANIUM ORE IN DAKOTA SANDSTONE NEAR GALLUP, NEW MEXICO

By KENNETH R. LUDWIG, BARNEY J. SZABO, and
HARRY C. GRANGER, Denver, Colo.

Abstract.—Radiometric dates of a high-grade uranium ore from the Hogback No. 4 mine in Dakota Sandstone near Gallup, N. Mex., indicate a late Pleistocene age of mineralization. The $^{206}Pb/^{238}U$ and $^{207}Pb/^{235}U$ apparent ages of about 70 000 yr and 100 000 yr, respectively, are discordant, but are in broad agreement with the discordant $^{230}Th/^{238}U$ and $^{231}Pa/^{235}U$ apparent ages of 130 000 yr and 78 000 yr, respectively. Although it is not clear how the analyzed sample relates to the main period of mineralization at this mine, these dates are consistent with previous age limits suggested for Dakota Sandstone uranium-ores.

The Gallup uranium district in new Mexico includes the westernmost extent of the immensely productive Grants mineral belt. This mineral belt contains a substantial portion of the country's uranium reserves, with most of the deposits occurring within sandstone of the Morrison Formation of Late Jurassic age. The overlying Dakota Sandstone of Early(?) and Late Cretaceous age contains many small uranium occurrences, but has not produced significant tonnages of uranium. No isotopic determinations of the age of mineralization for Dakota Sandstone deposits have hitherto been done; however, the very low total Pb/U ratios reported by Hilpert (1969) suggest a time of mineralization no earlier than Tertiary. In contrast, reported U-Pb isotope ages from deposits in the underlying Morrison Formation of Jurassic age are about 80-100 m.y. (Berglof, 1970).

GEOLOGIC SETTING OF THE HOGBACK NO. 4 MINE

The uraninite-pyrite-rich sample discussed in this paper was collected from a low-grade ore pile at the Hogback No. 4 mine near Gallup, N. Mex., in 1965. The mine is in Dakota Sandstone along the crest of a hogback that marks the position of a monocline bounding the east side of a synclinal structure known as the Gallup Sag. The mine was idle at the time of sample collection. Gabelman (1956) described the ore bed as 0.3 to 1 m of black, fissile shale that contained abundant coaly fragments. The shale, and the sporadically mineralized enclosing sandstones, were explored by an opencut. Secondary uranium minerals, iron oxides, jarosite, and gypsum in the ore-bearing shale and adjacent sandstones suggest considerable weathering, leaching, and element migration in near-surface parts of the deposit.

Gabelman (1956) noted that localization of the ore body is not readily explained, as there are no obvious controlling structures or stratigraphic features. In related deposits, however, he observed that ore was apparently controlled by small folds and joint sets of Laramide or later age.

SAMPLE DESCRIPTION

The entire sample was about 30-mm in diameter and consisted of well-cemented, very fine grained, nearly white, quartzose sandstone that contained a gray and black rounded blob of about 10-mm diameter. The gray material was thoroughly cemented by pyrite, and the black material, by uraninite (identified by powder X-ray pattern).

Because most of the ore in the Hogback No. 4 mine was in carbonaceous shale, this sample was somewhat atypical and probably came from a part of the ore body either lying below or armored from strong near-surface oxidation. The relation of the sample to the main period of ore deposition is thus uncertain. The analyzed sample fragments were hand picked from the coarsely crushed sample according to their appearance. (See tables 1 and 2.) The "gray fragments" were steel gray, contained abundant visible pyrite, and proved to be low in uranium (<0.1 percent). The "black fragments" were a deep solid black, contained no visible pyrite, and proved to be quite high in uranium (≈ 20 percent). Some fragments had irregu-

lar coatings of yellow (U VI ?) minerals and were discarded.

ANALYTICAL TECHNIQUES

The fragments selected for analyses were briefly immersed in an ultrasonically agitated bath, first of clean water, then of clean acetone. Two methods of sample attack were used—a complete dissolution with concentrated $HF–HClO_4$ and an HNO_3 leach. The HNO_3-leach attack was done in hope of increasing the radiogenic lead-common lead ratio while still dissolving all ore-related uranium and lead; it consisted of a 3 to 4 hr attack with hot, concentrated HNO_3.

Methods of purification and mass spectrometry for lead and uranium are those described by Ludwig (1978), except that the lead was purified with bromide-form anion-exchange resin for the HNO_3-leach analyses.

The lead-isotope ratios in table 2 are corrected for mass discrimination and are accurate to within about 0.1 percent for $^{206}Pb/^{204}Pb$ and $^{207}Pb/^{204}Pb$. Uncertainties in lead and uranium concentrations are less than 1 percent.

The $^{234}U/^{238}U$ activity ratio and the ^{230}Th and ^{231}Pa concentrations were determined by alpha spectrometry (Szabo and others, 1969). ^{231}Pa was measured by its daughter, ^{227}Th, with the assumption that ^{227}Ac, ^{231}Pa, and ^{227}Th were in secular equilibrium.

RESULTS

^{230}Th and ^{231}Pa apparent ages

The uranium-series dating method[1] makes use of the fact that most low-temperature uranium-enrichment systems (including sandstone-type uranium deposits) have no significant initial thorium or protactinium, so that ^{230}Th (from ^{238}U) and ^{231}Pa (from ^{235}U) must "grow in." For ages of less than about six half-lives of the daughter isotope, the activity ratios of $^{230}Th/^{238}U$ and $^{231}Pa/^{235}U$ are less than one by an analytically resolvable amount, and apparent ages may be calculated from these ratios. For the $^{230}Th/^{238}U$ age, an additional correction must be made for any initial excess or deficiency of ^{234}U, which lies between ^{238}U and ^{230}Th in the ^{238}U-decay chain.

The resulting apparent ages (table 1), though discordant, indicate a late Pleistocene age of uranium mineralization. The pattern of discordance is consistent with finite duration of uranium accumulation, so that the open-system model described by Szabo and Rosholt (1969) is useful. This model attributes all discordance between the ^{230}Th and ^{231}Pa apparent ages to gain of uranium by the system and gives a date of 160 000±30 000 years for the Hogback No. 4 mine sample. The ^{230}Th and ^{231}Pa ages of 130 000 and 78 000 years, respectively, may be considered as minimum ages, whereas the open-system-model age of 160 000 years may be considered a maximum age of mineralization.

The present-day and calculated initial $^{234}U/^{238}U$ values of 0.915 and 0.877, respectively, are pertinent to the origin of the deposit. "Primary" uranium ore bodies, formed by concentration of uranium leached from igneous rocks, should have initial $^{234}U/^{238}U$ values greater than unity, because of the slightly greater leachability of ^{234}U in fresh igneous rocks (Rosholt, Garner, and Shields, 1964). Many "old" (more than a few million years age) uranium ore bodies, however, are distinctly deficient in ^{234}U because of preferential loss of ^{234}U (Rosholt, Harshman, and others, 1964; Rosholt, Butler, and others, 1965; Dooley and others, 1966). If such an ore body were completely destroyed and its uranium mobilized

[1] Used mainly for dating corals, marine shells, cave deposits, and bones (Broecker and others, 1968, Szabi and Rosholt, 1969; Thompson and others, 1974; and Szabo and others, 1969).

TABLE 1.—*U-series data of black fragments*

Sample wt. (mg)	U (percent) (1/)	$^{234}U/^{238}U$ (1/)	$^{230}Th/^{234}U$ (2/)	$^{231}Pa/^{238}U$ (2/)	^{230}Th age (years) (3/)	^{231}Pa age (years) (4/)	Open-system age (years) (5/)
11.1	21.6	0.915±0.009	0.680±0.020	0.81±0.08	130,000 ±8,000	78,000 +26,000 -16,000	160,000±30,000

1/ By isotope dilution/mass-spectrometry.
2/ Measured activity ratios.
3/ Using half-lives of ^{230}Th and ^{234}U of 77,000 and 247,000 years, respectively.
4/ Using a ^{231}Pa half-life of 32,500 years.
5/ Szabo and Rosholt (1969).

(perhaps by a newly active hydrologic system), precipitation and concentration of this uranium could result in an ore body with an initial $^{234}U/^{238}U$ similar to that of the Hogback 4 mine sample. However, we cannot tell whether the "primary" ore body (ore body in the sense of anomalously high uranium concentration, though not necessarily economic) might be located within the underlying, uranium-rich Morrison Formation, or merely in the shale beds in the Hogback 4 mine itself.

U-Pb isotope data

The Pb isotopic composition (table 2) of the black fragments is very nonradiogenic, even though the uranium content is over 20 percent and the lead only about 10 ppm ($^{238}U/^{204}Pb = 2 \times 10^6$). Virtually all the uranium is leachable by HNO_3 (the slightly lower uranium content of the leached material probably indicates sample inhomogeneity rather than the presence of significant insoluble uranium), so that the results for the HNO_3-leached samples are very similar to those of the completely dissolved samples.

Because the lead in the black fragments is so nonradiogenic, the choice of the common lead isotopic composition has a large effect on the calculated U-Pb isotope ratios. The gray fragments proved to be very low in uranium (<0.1 percent U) and provide a useful estimate of the common lead isotopic composition of the black fragments.

Uncertainties which arise from choosing this lead relate to possible initial lead isotopic inhomogeneity in the sample and the possibility that the pyrite may have incorporated radiogenic lead leaked from nearby uranium-rich areas, as described by Ludwig (1978).

The resulting U-Pb isotope apparent ages (table 2) are the youngest heretofore observed. Though discordant, they are generally consistent with the U-series dates. The apparent ages were calculated by use of Bateman solutions as discussed by Ludwig (1977), so that the assumed initial absence of ^{230}Th and ^{231}Pa was taken into account. The $^{206}Pb/^{238}U$ apparent ages were calculated for an initial $^{234}U/^{238}U$ activity ratio of 0.877, as suggested by the U-series data.

The exact degree of U-Pb isotope age discordance is dependent on the choice of initial $^{234}U/^{238}U$ ratio, so that the apparent ages become concordant (at an age of ≈100,000 years) if a value of 0.39 is assumed. Such a low value has not been observed for uranium-rich systems, however, and we conclude that the U-Pb isotope age discordance is real. The observed discordance pattern and the somewhat younger U-Pb isotope apparent ages compared to the $^{231}Pa/^{235}U$ age are consistent with the inferred degrees of Pb and ^{238}U radioactive-daughter leakage described by Ludwig (1978) for Tertiary sandstone uranium ores in Wyoming. If only the uranium gain suggested by the pattern of U-series age discordance had occurred, however, the opposite pattern of $^{207}Pb/^{235}U$ age discordance would result.

Uncertainties in the U-Pb isotope apparent ages arising from the very large common lead correction should not obscure that fact that essentially any possible common lead correction still results in extremely young apparent ages. For example, even if the most isotopically primitive lead available (the feldspar lead of the 1.4- to 1.8-b.y.-old basement rocks of the region) is used for common-lead correction,

TABLE 2.—U-Pb *isotope data*

Sample type	Weight (mg)	U (percent)	Pb (ppm)	^{206}Pb (moles x 10^8)	$\frac{^{206}Pb}{^{204}Pb}$[1]	$\frac{^{207}Pb}{^{204}Pb}$[1]	$\frac{^{208}Pb}{^{204}Pb}$[1]	$\frac{^{206}Pb}{^{238}U}$	Age (years)	$\frac{^{207}Pb}{^{235}U}$	Age[2] (years)	$\frac{^{207}Pb}{^{206}Pb}$	Age[2 3] (years)
Black fragments, complete dissolution	58.8	21.54	10.13	1.395	(22.402) 22.497	(16.304) 16.325	(38.985) 39.014	2.214×10^{-6}	68,000	5.99×10^{-5}	102,000	0.1962	8,000 and 2.80×10^9
Light-gray fragments, complete dissolution	202.0	.0812	24.24	2.997	(19.105) 19.105	(15.629) 15.629	(38.848) 38.843						
Black fragments, HNO_3-Leach	34.2	21.16	7.10	1.004	(23.449) 24.468	(16.530) 16.533	(39.087) 39.091	2.171×10^{-6}	67,200	5.74×10^{-5}	100,000	.1926	9,000 and 2.77×10^9
Light fragments, HNO_3-Leach	113.8	.0658	16.10	1.979	(19.009) 19.009	(15.675) 15.675	(38.941) 38.941						

[1] Observed ratios in parentheses; blank-corrected ratios below.

[2] Calculated using the following half-lives; ^{238}U, 4.468×10^9y; ^{235}U, 7.038×10^8y; ^{234}U, 2.47×10^5y; ^{230}Th, 7.7×10^4y; ^{231}Pa, 3.25×10^4y. The Bateman equations-type solution discussed by Ludwig (1977) was used with initial activity ratios of $^{234}U/^{238}U = 0.877$ (calculated from table 1, using the open-system age), $^{230}Th/^{238}U = 0$, $^{231}Pa/^{235}U = 0$, and $^{226}Ra/^{238}U = 0$.

[3] The age solution for $^{207}Pb/^{206}Pb$ is two-valued if initial absence of ^{230}Th and ^{231}Pa is assumed (Ludwig, 1977b). The higher values, of course, are geologically unreasonable, even for an inherited lead component. These $^{207}Pb/^{206}Pb$ apparent ages, like those of other young uranium-ores, are much more a function of radioactive-daughter leakage (and choice of common-lead correction) than actual age (Ludwig, 1977a). Thus, they should not be compared directly with the Pb/U or U-series apparent ages.

the U-Pb isotope apparent ages of the Hogback 4 mine samples remain less than 150 000 years.

REFERENCES CITED

Berglof, W. R., 1970, Absolute age relationships in selected Colorado Plateau uranium ores: New York, Columbia Univ., Ph. D. thesis, 149 p.

Broecker, W. S., Thurber, D. L., Goddard, John, Ku, Leh-Lung, Mathews, R. K., and Mesolella, K. J., 1968, Milankovitch hypothesis supported by precise dating of coral reefs and deep-sea sediments: Science, v. 159, p. 297–300.

Dooley, J. R., Jr., Granger, H. C., and Rosholt, J. N., 1966 Uranium-234 fractionation in the sandstone-type uranium deposits of the Ambrosia Lake district, New Mexico: Econ. Geology, v. 61, no. 8, p. 1362–1382.

Gabelman, J. W., 1956, Uranium deposits in paludal black shales, Dakota sandstone, San Juan Basin, New Mexico, *in* Page, L. R., Stocking, H. E., and Smith, H. B., compilers, Contributions to the geology of uranium and thorium, by the United States Geological Survey and Atomic Energy Commission for the United Nations International Conference on Peaceful Uses of Atomic Energy, Geneva, Switzerland, 1955: U.S. Geol. Survey Prof. Paper 300, p. 303–319.

Hilpert, L. S., 1969, Uranium resources of northwestern New Mexico: U.S. Geol. Survey Prof. Paper 603, 166 p.

Ludwig, K. R., 1978, Uranium daughter migration and U-Pb isotope apparent ages of uranium ores, Shirley Basin, Wyoming: Econ. Geology. (In press.)

——— 1977, Effect of initial radioactive-daughter disequilibrium on U-Pb isotope apparent ages of young minerals: U.S. Geol. Survey Jour. Res., v. 5, no. 6, p. 663–667.

Rosholt, J. N., Butler, A. P., Garner, E. L., and Shields, W. R., 1965, Isotopic fractionation of uranium in sandstone, Powder River Basin, Wyoming, and Slick Rock district, Colorado: Econ. Geology, v. 60, no. 2, p. 199–213.

Rosholt, J. N., Garner, E. L., and Shields, W. R., 1964, Fractionation of uranium isotopes and daughter products in weathered granite and uranium-bearing sandstone, Wind River Basin region, Wyoming, *in* Geological Survey research 1964: U.S. Geol. Survey Prof. Paper 501–B, p. B84–B87.

Rosholt, J. N., Harshman, E. N., Shields, W. R., and Garner, E. L., 1964, Isotopic fractionation of uranium related to roll features in sandstone, Shirley Basin, Wyoming: Econ. Geology, v. 59, no. 4, p. 570–585.

Szabo, B. J., Malde, H. E., and Irwin-Williams, C. I., 1969, Dilemma posed by uranium-series dates on archeologically significant bones from Valsequillo, Puebla, Mexico: Earth and Planetary Sci. Letters, v. 6, p. 237–244.

Szabo, B. J., and Rosholt, J. N., 1969, Uranium-series dating of Pleistocene molluscan shells from southern California—an open system model: Jour. Geophys, Research, v. 74, no. 12, p. 3253–3260.

Thompson, P., Schwarcz, H. P., and Ford, D. C., 1973, Continental Pleistocene climatic variations from speleothem age and isotopic data: Science, v. 184, p. 893–895.

Jour. Research U.S. Geol. Survey
Vol. 5, No. 6, Nov.–Dec. 1977, p. 673–687

AGE AND TECTONIC SETTING OF LOWER PALEOZOIC ALKALIC AND MAFIC ROCKS, CARBONATITES, AND THORIUM VEINS IN SOUTH-CENTRAL COLORADO

By JERRY C. OLSON, RICHARD F. MARVIN, RAYMOND L. PARKER, and HARALD H. MEHNERT, Denver, Colo.

Abstract.—Alkalic igneous rocks were emplaced into heterogeneous terrane of Precambrian X and Precambrian Y rocks about 570 m.y. ago (Cambrian or upper Precambrian) in the Powderhorn area in Gunnison County and about 520 m.y. ago (Cambrian) in the McClure Mountain, Gem Park, and Democrat Creek areas in the northern Wet Mountains, Fremont and Custer Counties. The radiometric ages are based upon studies by K–Ar, Rb–Sr, and fission-track methods. Associated with these alkalic rock complexes are numerous thorium-bearing veins and red syenite dikes; some, if not all, in the northern Wet Mountains were formed about 495 m.y. ago. Diabase, gabbro, and other mafic dikes appear to be slightly younger than the thorium veins in the Powderhorn area and both older and younger in the Wet Mountains region. In the Powderhorn district, an older group of syenites also intruded Precambrian rocks as plugs or small stocks about 1350–1400 m.y. ago. The various dike rocks and the thorium veins were formed in extensive, deep fractures, indicating a condition of tension or shear in this part of the crust during Cambrian or very late Precambrian to Ordovician time. The localized alkalic magmatism may reflect melting spots in the mantle. In the two principal areas, 135 km apart, the episodes of alkalic magmatism differ in age by about 50 m.y., the younger toward the east. The age relations might be explained by migration of the sites of localized melting or volatile enrichment in the mantle or westward movement of the continent above a single site.

Alkalic igneous complexes have been known for about a century in the Powderhorn district, Colorado (fig. 1), and more recently were discovered in the McClure Mountain, Gem Park, and Democrat Creek areas in the Wet Mountains region, Colorado. Thorium-bearing veins, discovered about 1949–1950 during the "uranium boom" in the Powderhorn and Wet Mountains districts, are evidently related to the alkalic complexes. Geologic mapping in the two regions has disclosed swarms of dikes including gabbro, diabase, and lamprophyre thought to be related tectonically to the alkalic magmatism.

Isotopic ages of selected alkalic and the other dike rocks have been determined to elucidate their mutual relationships and their bearing on the tectonic history of the region during Cambrian and Ordovician time.

PREVIOUS WORK

The field relations and petrography of alkalic rocks of the Powderhorn area are known through the work of Larsen (1942), Olson and Wallace (1956), Temple and Grogan (1965), Nash (1972), Hedlund and Olson (1961, 1975), and Olson (1975). The alkalic rocks and thorium-bearing veins in the Wet Mountains region have been described by Singewald and others (1955), Christman and others (1959), Parker and Hildebrand (1963), Shawe and Parker (1967), Brock and Singewald (1968), and Parker and Sharp (1970).

Previously the age of zircon from two samples of syenite (probably fenite) collected by E. S. Larsen, Jr., from the complex of alkalic rocks at Iron Hill,

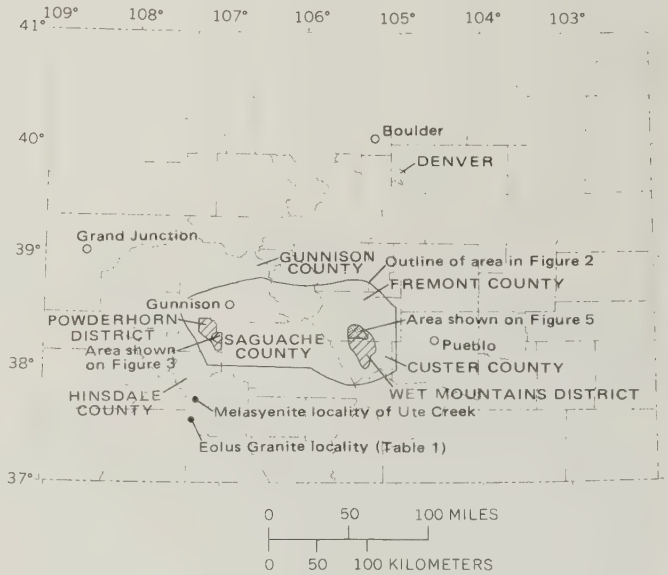

FIGURE 1.—Index map of Colorado showing location of Powderhorn and Wet Mountains districts.

Powderhorn area, was determined by lead-alpha methods to be 525 and 583 m.y. (Jaffe and others, 1959, p. 127). In the Wet Mountains area, fresh and metamict zircon from six samples of the quartz syenite in Democrat Creek, collected by Q. D. Singewald, gave lead-alpha ages of 580, 601, 590, 644, 605, and 655 m.y. (Jaffe and others, 1959, p. 127–128). The Rb–Sr whole-rock isochrons for the carbonatite-alkalic rock complexes of Iron Hill and McClure Mountain were presented by Fenton and Faure (1970, 1971) and discussed by Olson and Marvin (1971).

Paleomagnetic studies by Larson and Mutschler (1971, p. 1662–1663) of some of the igneous rocks in the Powderhorn, Wet Mountains, and Black Canyon of the Gunnison River areas have indicated a Cambrian-Ordovician paleopole close to the late Paleozoic pole position.

The present investigation was undertaken to determine the ages of the various alkalic rocks and to relate them to the geologic history of south-central Colorado. We wish to acknowledge the collaboration in field mapping by D. C. Hedlund, the contribution of rubidium-strontium analyses by Z. E. Peterman and C. E. Hedge, fission-track ages by C. W. Naeser, and mineral separation work by G. T. Cebula. M. R. Brock kindly consented to the inclusion of unpublished analytical data and radiometric ages for samples from the Democrat Creek pluton.

REGIONAL GEOCHRONOLOGY

Geochronologic studies of Precambrian rocks in Colorado have demonstrated the existence of three major magmatic events. Synkinematic to slightly postkinematic intrusive rocks, ranging mostly from quartz diorite and granodiorite to quartz monzonite, formed about 1700–1800 m.y. ago (Precambrian X) during the regional metamorphism of mafic to felsic volcanic rocks and associated sedimentary rocks (Peterman and others, 1968; Hedge and others, 1968). These intrusive rocks are commonly correlated with the regional magnatism that formed the Boulder Creek Granodiorite in the Colorado Front Range at about 1700 m.y. (Peterman and others, 1968; Stern and others, 1971).

The second major event occurred about 1400–1450 m.y. ago (Precambrian Y) and is typified by the Silver Plume igneous event in the Front Range. Igneous rocks of this major event commonly vary from quartz monzonite to granite and pegmatite; they are locally discordant to the older sequence of metamorphic and igneous rocks and generally show less foliation.

The third event occurred about 1000 m.y. ago (Precambrian Y) with the emplacement of the Pikes Peak Granite.

Into this heterogeneous Precambrian terrane, ultramafic, mafic, and alkalic magmas were intruded. The resultant intrusive rocks cut a variety of Precambrian country rocks, with discordant contacts, and appear to have been emplaced without regard to the composition or origin of the enclosing country rocks (fig. 2).

In the Powderhorn area, the host rock of the alkalic complex at Iron Hill is the Precambrian X Powderhorn Granite. Although it has not been dated radiometrically, structural and petrographic features suggest that the Powderhorn Granite may be Precambrian X or Boulder Creek age. Several small melasyenite plutons occur in the Powderhorn district and are petrologically similar to the melasyenite stock on Ute Creek (fig. 1), 68 km south-southwest of Powderhorn (Barker and others, 1970). Biotite from the Ute Creek melasyenite stock gave K-Ar ages of 1380 and 1410 m.y., slightly younger than the nearby Eolus Granite which was dated as 1460 m.y. by Rb-Sr and U-Pb methods (Bickford and others, 1969; Silver and Barker, 1968). Additional K-Ar ages on the Eolus Granite (sample Bsj–93, table 1), are presented here as 1390 m.y. (biotite) and 1460 m.y. (hornblende). The K-Ar ages given by biotite from three of the small melasyenite stocks and a biotite-calcite syenite dike in the Powderhorn area range from 1390–1330 m.y. (table 1).

In the northern Wet Mountains, the host rocks of the alkalic intrusions are Precambrian X granite gneiss, amphibolite, and other metamorphic rocks that predate the 1700-m.y. granites.

DETERMINATION OF RADIOMETRIC AGES

Results of K-Ar isotopic analyses are given in tables 1 and 4, Rb-Sr analyses in tables 2 and 5, and fission-track ages and analytical data in table 3. Sample localities are shown in figures 3 and 5. Most of the analytical work was done in the Denver laboratories of the U.S. Geological Survey. For K-Ar ages, argon was determined using standard isotope-dilution procedures and potassium was determined by flame photometry using lithium as an internal standard (Dalrymple and Lanphere, 1969). For minerals having less than 1 percent K_2O, potassium content was determined by isotope-dilution procedures in most cases. The analytical error quoted for each K-Ar age was evaluated in the manner described by Cox and Dalrymple (1967).

Analytical techniques used in determining Rb-Sr ages have been described by Peterman and others (1967). Where sufficient data were generated, Rb-Sr whole-rock or mineral-whole-rock isochrons were constructed (figs. 4, 6, 7).

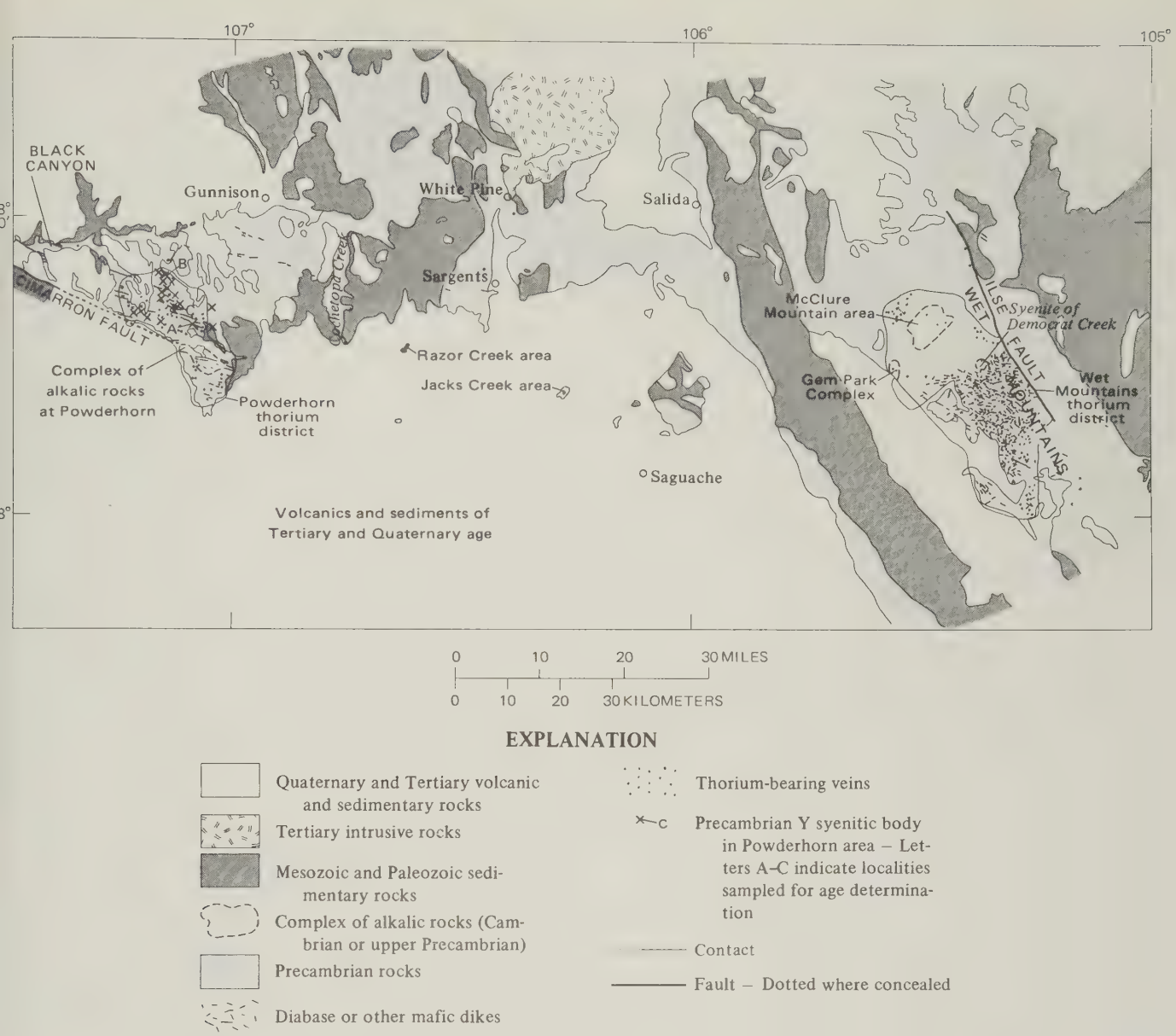

FIGURE 2.—Generalized geologic map showing locations of alkalic rocks, thorium deposits, mafic dikes, and other features, south-central Colorado.

The analytical techniques and equations used in determining fission-track ages have been described by Naeser (1967).

GEOLOGIC RELATIONS OF THE ALKALIC ROCKS

Powderhorn district

Alkalic rocks of two general ages are known in the Powderhorn district, Gunnison County (table 1). An older group of syenite plugs or small stocks was intruded into preexisting Precambrian rocks about 1350–1400 m.y. ago; a younger group—the complex at Iron Hill—of pyroxenite, carbonatite, and other alkalic rocks was emplaced about 570 m.y. ago.

Older group of syenitic rocks

Rocks of the older alkalic group are predominantly syenitic in composition and range from mafic to felsic types. These occur in about 20 small stocks or plugs and numerous smaller dikes in the Powderhorn district; the largest of these plugs is about 0.6 × 1.3 km. The individual plugs generally consist of several textural and compositional rock types. Coarse-grained augite-biotite melasyenite is a common rock type. It consists of 50 percent or more mafic minerals, chiefly biotite and augite but locally hornblende, together with microcline and small amounts of apatite, sphene, magnetite, and other accessories. Samples P7406, C9803,

TABLE 1.—*K-Ar ages and analytical data for samples from the Powderhorn district, Gunnison County and from Hinsdale County, Colorado*

[Decay constants: K^{40} $\lambda_\beta = 4.72 \times 10^{-10}$/yr.; $\lambda_\varepsilon = 0.584 \times 10^{-10}$/yr. Abundance: $K^{40} = 1.22 \times 10^{-4}$g/gK
Analysts (except as[3]footnoted): R. F. Marvin, H. H. Mehnert, Violet Merritt]

Sample No.	Analyzed mineral	K_2O (percent)	Radiogenic argon		Age	Location		Rock type; local geographic feature
			10^{-10} mol/g	Percent	(m.y.±2σ)	Lat N	Long W	
			Alkalic complex at Iron Hill					
J365N	Biotite--------	[2]9.25 9.27	90.46	96	567±10	38°14'35"	107°01'43"	Pyroxenite; ESE of Iron Hill.
IH-1-2	---do----------	[2]9.33 9.30	91.13	97	568±9	38°15'16"	107°01'22"	Pegmatitic biotite-diopside dike in pyroxenite; east of Iron Hill.
IH-3-3	---do----------	[2]9.57 9.55	94.59	99	574±9	38°15'34"	107°01'26"	Pegmatitic biotite-diopside dike in pyroxenite; ENE of Iron Hill.
P-9-901	Aegirine-------	[3].069 .066	.8901	91	731±23	38°15'13"	107°00'42"	Ijolite; southeast of Iron Hill.
IH-4	Biotite--------	[2]9.23 9.20	85.46	98	543±8	38°15'30"	107°01'	Nepheline syenite; ENE of Iron Hill.
J256	Muscovite------	[2]10.15 10.14	97.86	97	561±10	38°14'36"	107°04'02"	Carbonatite; south of Iron Hill and east side of Cebolla Creek.
IH-18	Biotite--------	9.22 9.27	91.29	96	573±14	38°14'32"	107°04'00"	Do.
IH-2-2d	Vermiculite(?)-	[2]2.53 2.53	25.03	98	574±9	38°15'	107°01'	Carbonatite dike; east of Iron Hill.
IH-23-2a	---do----------	[2]4.55 4.57	43.20	97	553±9	38°14'30"	107°03'16"	Carbonatite dike; south of Iron Hill.
IH-21	Plagioclase----	[2].747 .763	10.45	95	762±15	38°16'07"	107°03'22"	Diabase dike; northeast of Iron Hill.
			Road Beaver Creek					
IH-11	Phlogopite-----	[2]10.32 10.33	100.98	93	568±9	38°13'50"	107°02'	Mafic dike cutting felsic stock; Road Beaver Creek.
			Minor alkalic stocks in northwest area of Powderhorn district					
P7406	Biotite--------	9.21 9.16	278.4	98	1,390±40	38°19'18"	107°05'33"	Augite-biotite-hornblende syenite stock (loc. A, fig. 1).
C9803	---do----------	9.33 9.32	278.4	99	1,380±40	38°23'45"	107°08'26"	Mafic syenite facies of small stock (loc. B, fig. 1).
2G3200	---do----------	9.36 9.26	281.5	99.6	1,390±40	38°21'33"	107°07'39"	Biotite syenite (loc. C, fig. 1).
G3730N	---do----------	9.33 9.32	267.0	99	1,330±36	38°20'43"	107°08'20"	Biotite-calcite syenite dike (1.8 km SW of loc. C, fig. 1).
			San Cristobal quadrangle, Hinsdale County					
Bsj-93[1]	Biotite--------	7.42 7.46	225.1	99	1,390±60	37°32'	107°26'	Eolus Granite.
	Hornblende-----	1.22 1.21	39.52	99	1,460±70	37°32'	107°26'	Do.

[1]Collected by Fred Barker; R. E. Zartman and Wayne Mountjoy, analysts, Denver.
[2]Lois Schlocker, analyst, Menlo Park.
[3]Potassium determined by isotope dilution, W. T. Henderson, analyst, Denver.

and 2G3200 (table 1) are typical of this facies of the syenitic rock; biotite from these samples gave minimum K-Ar ages ranging from 1380–1390 m.y.

Another common rock type is fine- to medium-grained augite-biotite syenite, mostly porphyritic with phenocrysts of augite and biotite. A third type that is present in many of the small stocks is leucosyenite, which locally has enough quartz to be quartz syenite or even granite. The leucosyenite is both fine and coarse grained. Most of the rock in the syenite plugs can be grouped into the three main types listed above, but local variants are common.

Some syenite plugs of the older group are practically monolithologic, composed of quartz leucosyenite, augite-biotite syenite porphyry, or poikilitic biotite-microcline syenite. As these rock types are found in the composite intrusives, it is possible that the monolithologic bodies would appear composite at a different level of erosion. More commonly, however, several of the varieties of syenite are present in one intrusive

body. The coarse-grained augite-biotite melasyenite, represented by the first three samples in table 1, typically occurs near the margins of these composite bodies, with lighter colored, progressively younger syenites toward the center. Leucosyenite, quartz syenite, or granite commonly occur in the middle of a plug and in places cut the earlier-formed marginal zones or the surrounding country rocks. Similar lithologic relations have been observed in the same kinds of small stocks in the Mountain Pass district, California (Olson and others, 1954).

Sample G3730N, which has a minimum age of 1330 m.y. (table 1), is from a calcite-biotite-microcline (minette) dike. About 35 dikes and lenticular bodies of lamprophyre (chiefly minette) have been mapped in the Powderhorn district. These dikes are as much as 50 m thick, but mostly 1–15 m thick, and as long as 500 m.

Owing to the analytical uncertainties of the K-Ar ages, the age differences between the minette dike and the syenite stocks (1380–1390 m.y.) may be quite small (table 1). However, the ages suggest that the narrow dikes represent younger intrusions, possibly late differentiates related to the stocklike bodies. In the Black Canyon of the Gunnison River, Hansen and Peterman (1968, p. C86) found two ages of lamprophyre dikes, an older group of deformed dikes cut by the Curecanti Quartz Monzonite (1420 m.y.) and a younger group not obviously deformed or metamorphosed.

Hornblende melasyenite, occurring in an inlier of the Precambrian granite in the Jacks Creek area (fig. 2) in sec. 20, T. 46 N., R. 6 E., resembles the older pre-1420 m.y. group in appearance, but it has not been dated isotopically. It forms a northeast-trending thick dike about 120–150 m wide and at least 700 m long and covered by Tertiary volcanics at each end.

Complex around Iron Hill

Rocks of the younger alkalic group are in or very near the complex of alkalic rocks which occupies 30 km² around Iron Hill at Powderhorn (fig. 3). Rocks of this complex comprise, in order of decreasing age, pyroxenite, uncompahgrite (melilite rock with small amounts of pyroxene and magnetite), ijolite (pyroxene-nepheline rock), diverse hybrid pyroxenite-syenite rocks, magnetite-ilmenite-perovskite bodies, nepheline syenite, and carbonatite. Locally at the borders of the complex is rock of syenite composition that is interpreted to be fenite, metasomatically altered granite. Nepheline syenite and carbonatite are found both in the pyroxenite body and in granite or metamorphic rocks outside the outer pyroxenite contact, mostly within 1 km of the contact. Discordant contacts show a relative age sequence for most of these rocks, but evidence can be found of both carbonatite and nepheline syenite being younger than the other, suggesting some overlap between these two rocks.

The radiometric ages do not establish an order of intrusion. The pyroxenite, the oldest member of the complex, has a K-Ar age of 570 m.y. as opposed to the K-Ar age of 565 m.y. for the carbonatite, the youngest member of the complex. The K-Ar ages indicate that the various intrusives of the complex probably formed in a relatively short time during the very late Precambrian Z and Early Cambrian. However, the K-Ar ages of the early members of the complex may reflect thermal effects of later intrusives. Thus the heat from the carbonatite magma may have caused the loss of radiogenic argon from the pyroxenite, thus resetting the K-Ar isotopic system in those rocks. Similarly, the K-Ar age (543 m.y.) for the nepheline syenite seems too young but may indicate the thermal effect of a cross-cutting late-phase diabase dike. (See fig. 3.)

Unfortunately, most of the rocks in the complex are not suitable for Rb-Sr age determination. However, Rb-Sr systematics for four micas and an accompanying whole rock (table 2) produced an isochron indicating an age of 579±10 m.y. for the emplacement of the pyroxenite and syenite (fig. 4). These results refute the age assignment of 1487 m.y. for the complex at Iron Hill by Fenton and Faure (1971).

The micas analyzed from samples IH–2–2d and IH–23–2a (table 1) have a shiny yellowish to tannish color, resembling vermiculites in appearance. Their potassium content is one-half to one-fourth of the potassium content of ordinary biotite, indicating that potassium has been leached from the crystal structure. Similarly, the Rb and Sr values shown in table 2 for these micas probably reflect the effects of leaching, presumably by ground waters. The Rb and Sr isotopic data indicate spurious radiometric ages for the micas of between 300 and 400 m.y. on a Rb^{87}/Sr^{86} to Sr^{87}/Sr^{86} plot. However, the K-Ar ages appear reliable, this being a case where leaching has not been sufficient to negate a reliable K-Ar age determination (Kulp and Engels, 1963).

Additional complications to the age study arose with the determination of a K-Ar age for aegirine from ijolite. The 731-m.y. age obtained (table 1) is spurious and it is probably the result of excess radiogenic argon incorporated in the mineral crystal during its growth. Radiogenic argon may be present in the other analyzed minerals, but it probably constitutes only a very minor amount of the total radiogenic-argon content. Because

FIGURE 3.—Generalized geologic map of the complex of alkalic rocks of Iron Hill, showing sample localities.

TABLE 2.—*Rb–Sr analytical data for samples from the complex at Iron Hill, Gunnison County, Colorado*

[Decay constant: Rb^{87} $\lambda_\beta = 1.39 \times 10^{-11}$/yr.; Abundance: $Rb^{87} = 0.283$ gm/gm Rb.
Analysts: C. E. Hedge, W. T. Henderson, and Kiyoto Futa]

Sample No.	Analyzed material	Rb (ppm)	Sr (ppm)	Rb^{87}/Sr^{86}	Sr^{87}/Sr^{86}	Location		Rock type; local geographic feature
						Lat N	Long W	
J365N	Biotite--------	318	230	4.021	0.7359	38°14'35"	107°01'43"	Pyroxenite, ESE of Iron Hill.
IH-1-2	---do----------	332	124	7.807	.7677	38°15'16"	107°01'22"	Pegmatitic biotite-diopside dike in pyroxenite; east of Iron Hill.
IH-11	Phlogopite-----	688	42.2	49.06	1.0971	38°13'50"	107°02'	Biotite-calcite melasyenite dike cutting felsic stock; Road Beaver Creek.
IH-4	Whole-rock-----	74	1432	.1497	.7052	38°15'30"	107°01'	Nepheline syenite; ENE of Iron Hill.
	Biotite--------	825	71.4	34.36	.9880	38°15'30"	107°01'	
IH-2-2d	Vermiculite(?)-	114	138	2.400	.7160	38°15'	107°01'	Carbonatite dike; east of Iron Hill
IH-23-2a	---do----------	183	334	1.586	.7130	38°14'30"	107°03'16"	Carbonatite dike; south of Iron Hill.

EXPLANATION FOR FIGURE 3

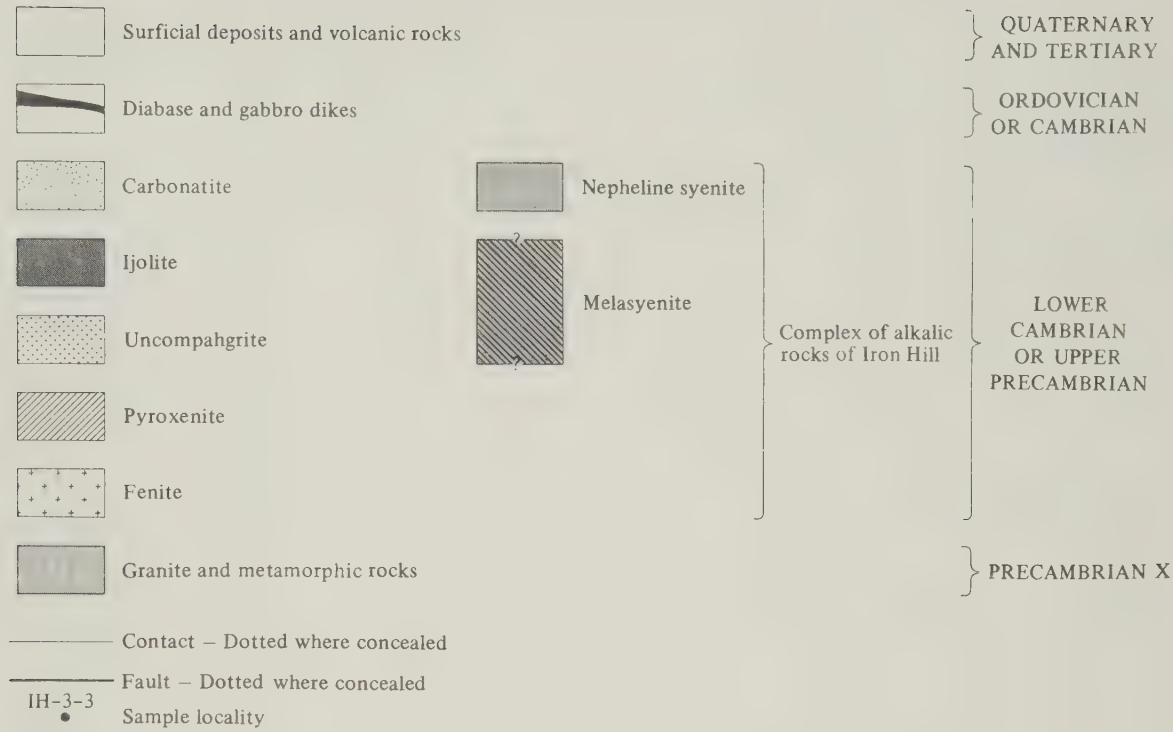

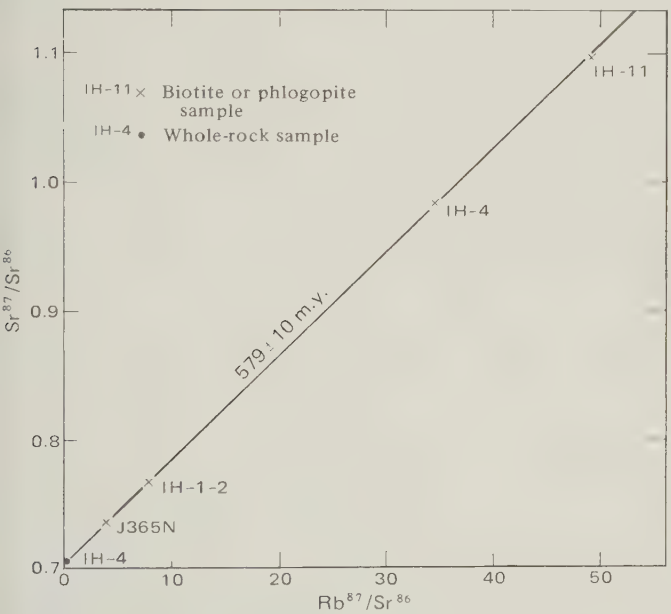

FIGURE 4.—Mineral-whole-rock isochron for selected samples from complex of Iron Hill of late Precambrian Z or Early Cambrian age, Gunnison County, Colorado. Initial Sr^{87}/Sr^{86} ratio for the samples is 0.7046.

aegirine contains only a small amount of potassium, the argon incorporated during growth constitutes a significant amount of the measurable radiogenic argon present. Similar spurious ages have been reported by several investigators— Damon and Kulp (1958), Hart and Dodd (1962), and especially Shafiqullah and others (1970), who studied the carbonatite complex at Oka, Quebec.

The fission-track age of 550 m.y. for the ijolite seems reasonable and agrees well with the proposed 579- to 565-m.y. age span of the complex. The fission-track age of 55 m.y. (table 3), given by apatite from the ijolite, probably indicates an annealing temperature coinciding with the approximate time of uplift and cooling of the rocks (below 100°C) of this area.

Wet Mountains

Three alkalic intrusive complexes in the northern Wet Mountains are the McClure Mountain Complex, the Gem Park Complex, and the syenite complex at the head of Democrat Creek (fig. 5). The complexes are clustered inside a 130-km² area a few kilometers north of Westcliffe, Colo., and are considered to be genetically related.

The McClure Mountain Complex occupies an area of about 46 km². It is composed of an older series of mafic and ultramafic rocks, largely stratiform, and younger but related syenitic rocks. The stratiform rocks, described in detail by Shawe and Parker (1967), consist of olivine gabbro, anorthosite, pyroxenite, and dunite of several textural and intergradational varieties. The syenitic rocks, which collectively form the largest part of the complex, consist of coarsely crystalline biotite-hornblende syenite, nepheline syenite, and mafic nepheline-bearing rocks. The nepheline-

bearing rocks are extremely variable in texture and grain size and grade in composition from felsic to mafic. A rough concentric zoning of the complex is evident, especially at the northeast end, with the older mafic-ultramafic rocks at the periphery and the younger nepheline-bearing rocks toward the center.

The Gem Park Complex (Parker and Sharp, 1970), a few kilometers southwest of the McClure Mountain Complex, underlies an area of about 5 km². The complex is almost entirely pyroxenite and gabbro of a wide variety of textures that closely resemble some of the mafic-ultramafic rocks in the northeastern part of the McClure Mountain Complex. The Gem Park rocks are altered in places and complexly intruded by numerous carbonatite dikes that contain niobium and rare-earth minerals. In places the pyroxenite contains copper-nickel-iron sulfide minerals.

The syenite complex at Democrat Creek (Christman and others, 1959), about 10 km southeast of the McClure Mountain Complex, underlies an area of 9 km². It consists chiefly of composite intrusives of quartz syenite and explosion breccias. Small peripheral bodies of syenite occur both east and west of the main body, and a lensoid mass of gabbro, the genetic relationship of which has not been established with certainty, lies at the south side of the complex.

Red syenite dikes are common in the Wet Mountains region and are particularly abundant in the vicinity of the alkalic complexes. These dikes intrude both the alkalic rocks and the host gneisses and associated rocks, but their abundance in proximity to the alkalic complexes suggests a genetic relation. Some of the dikes are anomalously radioactive due to thorium, suggesting also a genetic relation with the thorium veins of the region.

Heinrich and Dahlem (1966) discovered about 150 lamprophyre dikes in a "halo area" north and northwest of the McClure Mountain Complex. These dikes are commonly associated with carbonatite and are mafic to ultramafic and alkalic in composition. Lamprophyre dikes, classed as spessartite, cut gabbro of the Gem Park Complex (Parker and Sharp, 1970).

Radiometric ages and analytical data for samples from the complexes at McClure Mountain, Gem Park, and Democrat Creek are given in tables 3 through 5 and figures 6 and 7.

For the biotite-hornblende syenite and nepheline-bearing rocks of the McClure Mountain Complex, the age results are summarized as follows: 520 m.y. (averaged hornblende K-Ar ages), 521 m.y. (8-point mineral–whole-rock Rb-Sr isochron); 508 m.y. (averaged biotite K-Ar ages), and 506 m.y. (sphene fission-track age).

For the fenite in the Gem Park Complex, a K-Ar age of 551 m.y. was obtained. For the syenite in the complex at Democrat Creek, the averaged K-Ar ages are 512 m.y. (biotite) and 534 m.y. (hornblende).

Red syenite dikes (commonly thorium bearing) in the northern Wet Mountains have an age of 495 m.y. (4-point whole-rock Rb-Sr isochron).

The above ages indicate that most of the alkalic plutons were emplaced during the Middle Cambrian (the hornblende K-Ar age and Rb-Sr isochron age are minimum ages) followed by red syenite dikes and accompanying thorium mineralization during Early Ordovician. Igneous activity may have occurred during the Late Cambrian, but this has not been established by radiometric ages.

TABLE 3.—*Fission-track ages for apatite and sphene from the complex at Iron Hill, Gunnison County, and the McClure Mountain Complex, Custer County, Colorado*

[Constant: $\lambda_F = 6.85 \times 10^{-17}$/yr. Analyst: C. W. Naeser]

Sample No.	Analyzed mineral	Density			Age (m.y.±2σ)	Location		Rock types; local geographic features
		Fossil track (t/cm^2)	Induced track (t/cm^2)	Neutron flux (ϕ/cm^2)		Lat N	Long W	
				Complex at Iron Hill				
P8649	Apatite--	2.83×10^5 (708 tracks counted)	15.31×10^5 (1701 tracks counted)	4.90×10^{15}	55±12	38°15'17"	107°00'53"	Ijolite (nepheline-pyroxene); southeast of Iron Hill.
	Sphene--	2.87×10^6 (2151 tracks counted)	1.34×10^6 (511 tracks counted)	4.45×10^{15}	550±54	38°15'17"	107°00'53"	Do.
				McClure Mountain Complex				
WM-62-143	Apatite--	1.24×10^6 (2580 tracks counted)	0.278×10^6 (580 tracks counted)	1.10×10^{15}	293±62	38°22'	105°29'	Hornblende-biotite syenite; near Indian Spring.
	Sphene--	8.26×10^6 (2256 tracks counted)	5.22×10^6 (713 tracks counted)	5.42×10^{15}	506±43	38°22'	105°29'	Do.

TABLE 4.—*K-Ar ages and analytical data for samples from the northern Wet Mountains, Fremont and Custer Counties, Colorado*

[Decay constants: K^{40} $\lambda_\beta = 4.72 \times 10^{-10}$/yr.; $\lambda_\varepsilon = 0.584 \times 10^{-10}$/yr. Abundance $K^{40} = 1.22 \times 10^{-4}$ g/g K. Leaders (--) indicate no data. Analysts (except as footnoted): R. F. Marvin, H. H. Mehnert, Violet Merritt]

Sample No.	Analyzed material	K_2O (percent)	Radiogenic argon 10^{-10} mol/g	Radiogenic argon Percent	Age (m.y.±2σ)	Location Lat N	Location Long W	Rock type; local geographic feature
			McClure Mountain Complex					
WM-62-140	Biotite-------	9.11 9.20	79.13	98	510±13	38°20'	105°26'	Hornblende-biotite syenite; near McClure Spring, southeastern part of Complex.
	Hornblende----	1.73 1.76	15.44	98	523±14	38°20'	105°26'	Do.
WM-62-143	Biotite-------	9.24 9.22	78.96	98	506±13	38°22'	105°29'	Hornblende-biotite syenite; near Indian Spring.
	Hornblende----	[1]1.849 1.865	16.26	98	516±11	38°22'	105°29'	Do.
WM-62-114	---do---------	[1]1.874 1.879	16.18	98	509±11	38°18'	105°29'	Hornblende syenite; Elkhorn Mountain.
WM-62-115	Biotite-------	8.48 8.44	72.65	96	507±17	38°18'	105°29'	Mafic nepheline-bearing rock; Elkhorn Mountain
	Hornblende----	1.70 1.65	15.19	97	532±15	38°18'	105°29'	Do.
WM-66-116c	Biotite-------	8.90 8.83	76.51	98	510±13	38°20'	105°29'	Mafic nepheline-bearing rock; Copper Gulch Divide.
	Pyroxene------	[1].088 .089	.8090	84	536±17	38°20'	105°29'	Do.
	Nepheline-----	5.57 5.51	44.54	98	479±12	38°20'	105°29'	Do.
			Gem Park Complex					
WM-63-723	Riebeckite---- (Crocidolite)-	0.32 .31	3.072	95	551±30	38°16'	105°32'30"	Fenite; Vermiculite mine, central part of Complex.
WM-63-707	Vermiculite---	.10 .11	.5457	11	323±46	38°16'02"	105°32'40"	Altered fenite; Vermiculite mine, Fremont County.
WM-67-728	---do---------	.33 .34	2.442	61	439±22	38°16'02"	105°32'40"	Do.
WM-67-1029a	---do---------	[2].0410 .0413	.1398	7	217±7	38°15'35"	105°33'10"	Altered mafic rock; Niles mine, southwestern part of Complex, Custer County.
			Complex at Democrat Creek					
52-B-53	Biotite-------	[3]8.42	[4]71.8	--	[5]504±25	38°15'(?)	105°21'(?)	Quartz syenite stock; upper Grape Creek.
63-B-20	---do---------	8.60 8.55	75.64	98	519±13	38°15'30"	105°22'	Biotite-rich facies of quartz syenite stock; upper Grape Creek.
	Hornblende----	1.37 1.38	12.62	97	534±16	38°15'30"	105°22'	Do.
63-B-23	Whole-rock----	[3]3.90	[4]32.0	96	[5]485±24	38°14'26"	105°22'03"	Syenite dike; Dead Mule Gulch.
63-B-24	---do---------	2.08	[4]20.2	96	[5]560±28	38°16'46"	105°20'12"	Aphanitic red syenite dike; east of Democrat Creek syenite stock.
63-B-24b	---do---------	[3]5.10	[4]36.3	97	[5]427±22	38°16'	105°20'	Aphanitic red syenite dike.

[1]Potassium determined by isotope dilution, W. T. Henderson, analyst, Denver.
[2]Lois Schlocker, analyst, Menlo Park.
[3]Paul Elmore, analyst, Washington, D. C.
[4]H. H. Thomas and R. F. Marvin, analysts, Washington, D. C.
[5]Age published by Brock and Singewald (1968). Age for sample 52-B-53 has been recalculated and age for sample 63-B-24 was mistakenly published as 585 m.y.

Although the field relations in the McClure Mountain Complex indicate that the biotite-hornblende syenite preceded the emplacement of the nepheline-bearing syenite, K-Ar ages cannot resolve the age difference, which is probably less than 1 million yr. The difference between the K-Ar ages of coexisting minerals, such as biotite and hornblende, may, in part, reflect the gradual cooling of the igneous bodies. Thus, hornblende crystals became closed systems, capable of quantitatively retaining argon, at a higher temperature than biotite crystals. Similarly, the 479-m.y. K-Ar nepheline age (sample WM–66–116c, table 4) may indicate that this nepheline became a closed system at an even lower temperature than biotite.

These bodies were formed at sufficient depth that the normal geothermal gradient kept their temperature above 100°C for many millions of years. Fission tracks in apatite are annealed at temperatures above 100°C (Naeser, 1967). The 293±62-m.y. fission-track age given by an apatite concentrate (sample WM–62–143, table 3) therefore indicates that about 300 m.y. ago the rock temperature cooled below 100°C, probably as

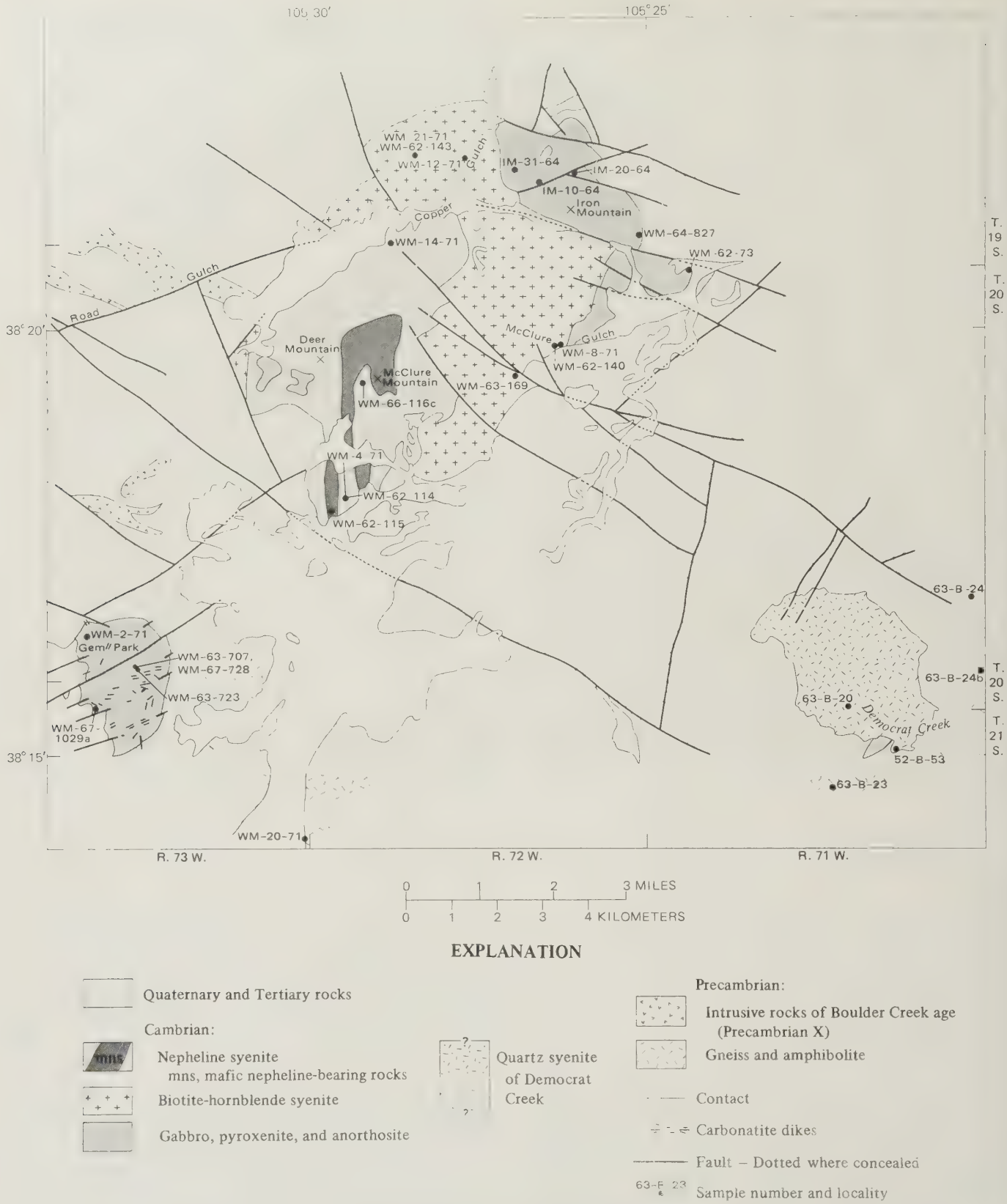

EXPLANATION

Quaternary and Tertiary rocks

Cambrian:

mns — Nepheline syenite
mns, mafic nepheline-bearing rocks

Biotite-hornblende syenite

Gabbro, pyroxenite, and anorthosite

Quartz syenite of Democrat Creek

Precambrian:

Intrusive rocks of Boulder Creek age (Precambrian X)

Gneiss and amphibolite

Contact

Carbonatite dikes

Fault – Dotted where concealed

63-B-23 Sample number and locality

FIGURE 5.—Generalized geologic map of the alkalic rocks of the Wet Mountains region, showing sample localities.

TABLE 5.—*Rb-Sr analytical data for samples from the northern Wet Mountains, Fremont and Custer Counties, Colorado*

[Constants: Rb^{87} $\lambda_\beta = 1.39 \times 10^{-11}$/yr.; $Rb^{87} = 0.283$ gm/gm Rb; leaders (---) indicate no data. Analysts (except as footnoted): Z. E. Peterman, C. E. Hedge, W. T. Henderson, and R. A. Hildreth]

Sample No.	Analyzed material	Rb (ppm)	Sr (ppm)	Rb^{87}/Sr^{86}	Sr^{87}/Sr^{86}	Location Lat N	Location Long W	Rock type; local geographic feature
				Mafic rocks at Iron Mountain				
WM-62-73[1]	Whole-rock--	<5	970	<0.015	0.7048	38°20'38"	105°24'22"	Pyroxene-rich anorthosite; mouth of Black Gulch.
IM-10-64[1]	---do-------	<5	280	<.052	.7041	38°21'34"	105°26'34"	Olivine-rich gabbro; west of Iron Mountain.
IM-20-64[1]	---do-------	<5	840	<.017	.7039	38°21'46"	105°26'01"	Olivine-rich anorthosite; northwest of Iron Mountain.
WM-64-827[1]	---do-------	[2]0	[2]692	-----	-----	38°21'15"	105°25'33"	Gabbro; Black Gulch.
IM-31-64[1 3]	---do-------	[2]6.0	[2]1661	-----	-----	38°21'52"	105°26'56"	Anorthosite; northwest of Iron Mountain.
				McClure Mountain Complex				
WM-8-71[4]	Whole-rock--	92.6	475	0.604	0.7082	38°19'52"	105°26'07"	Biotite-hornblende syenite; McClure Gulch.
	Biotite-----	476	35.8	39.82	1.0002			
WM-12-71	Whole rock--	108	551	.607	.7080	38°21'59"	105°27'39"	Biotite-hornblende syenite; upper Copper Gulch.
	Biotite-----	545	13.9	123.3	1.5964			
WM-21-71[5]	Whole-rock--	87.3	566	.563	.7073	38°22'05"	105°28'29"	Biotite-hornblende syenite; near Indian Springs.
	Biotite-----	515	24.7	63.06	1.1659			
WM-4-71	Whole-rock--	171	2248	.235	.7048	38°19'26"	105°29'14"	Nepheline syenite; Copper Gulch Divide.
	Biotite-----	498	98.1	17.11	.8209			
				Red syenite dikes in or adjacent to the McClure Mountain and Gem Park Complexes				
WM-2-71	Whole-rock--	57.5	202	0.825	0.7087	38°16'21"	105°33'26"	Aphanitic red syenite dike; Gem Park.
WM-14-71	---do-------	152	37.2	11.91	.7830	38°20'57"	105°28'43"	Aphanitic red syenite dike; upper Copper Gulch.
WM-20-71	---do-------	115	35.2	9.46	.7735	38°14'05"	105°30'02"	Aphanitic red syenite dike; Copper Gulch Road.
WM-63-169	---do-------	136	[6]54.7	7.23	.7573	38°19'	105°27'	Aphanitic red syenite dike; 3 km east of McClure Mountain.

[1]Chemical analyses, norms, modes, and spectrographic analyses are given by Shawe and Parker (1967, table 3, p. A23).
[2]Values determined by X-ray fluorescence, W. P. Doering, analyst, Denver.
[3]Rb/Sr is 0.0036.
[4]Collected from same sample site as sample WM-62-140, table 4.
[5]Collected from same sample site as sample WM-62-143, table 4.
[6]Radiogenic Sr^{87} = 6.4 percent.

a result of regional uplift and erosion.

The Rb-Sr whole-rock isochron age determined by Fenton and Faure (1971) of 517±14 m.y. is in good agreement with our findings. Their other isochron of 704 m.y. is apparently spurious.

Samples of the mafic rocks from Iron Mountain, in the McClure Mountain Complex (fig. 5), were collected for Rb-Sr dating, but the samples proved unsuitable for age work. The analytical data for these samples are presented in table 5. Although a radiometric age was not determined, these rocks are probably close in age to other rocks of the McClure Mountain Complex because they are structurally cohesive and show chemical affinities with those alkalic rocks.

The Gem Park fenitized rocks that were collected were unsuited for age work. The 551-m.y. K-Ar age given by riebeckite (table 4) might suggest an older age for this complex, but the large analytical uncertainty associated with the riebeckite age permits agreement with the 520-m.y. age for the McClure Mountain Complex. In an attempt to strengthen the evidence for coeval emplacement of the McClure Mountain and Gem Park Complexes, three vermiculites from the Gem Park Complex were also dated by the K-Ar method. The K-Ar ages (table 4) are spurious and demonstrate that vermiculites, as a rule, unsuitable for age determinations. It is important to note the very low potassium content of these vermiculites in

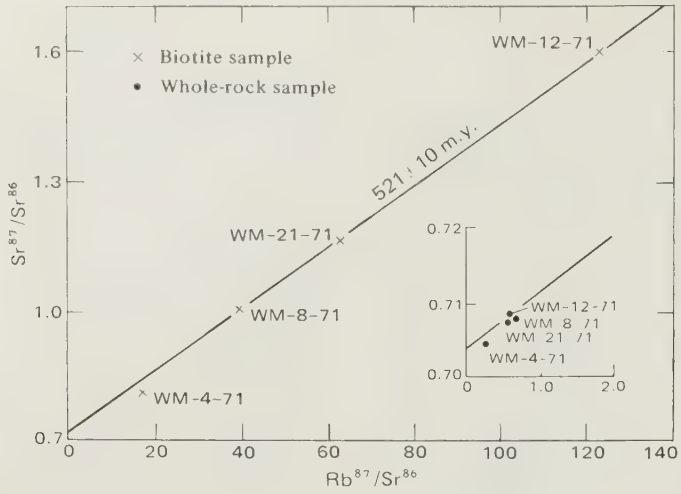

FIGURE 6.—Mineral–whole-rock isochron for Middle Cambrian rocks in McClure Mountain Complex, northern Wet Mountains, Fremont County, Colorado. Initial Sr^{87}/Sr^{86} ratio for these rocks is 0.7036.

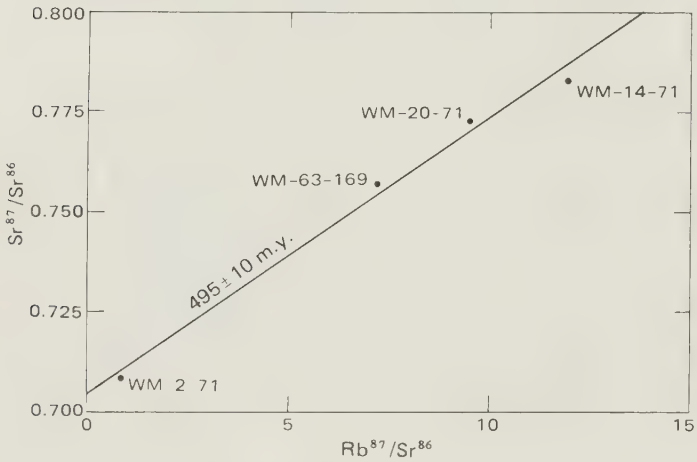

FIGURE 7.—Whole-rock isochron of red syenite dikes of Ordovician age in northern Wet Mountains, Fremont and Custer Counties, Colorado. Initial Sr^{87}/Sr^{86} ratio for these dikes is 0.7048.

comparison to the "leached" micas that gave apparently reliable K-Ar ages for the complex at Iron Hill, Gunnison County.

The K-Ar ages for the Democrat Creek syenite stock indicate that it is part of the 520 m.y. igneous event. Thus, the associated phaneritic red syenite dikes should be approximately the same age. Sample 63–B–23 (table 4) gave a whole-rock K-Ar age of 458±24 m.y., which is appreciably younger than 520 m.y. In general, however, for rocks in this age range, whole-rock K-Ar ages tend to be younger—10–50 percent younger—than the mineral crystallization age.

Widespread red porphyritic to aphanitic syenite dikes, either thorium-bearing or associated with thorium veins, have been dated at 495 m.y. with a 4-point Rb-Sr whole-rock isochron (fig. 7). This age seems reasonable from field relations; but, because the analyzed samples were not as fresh as desired and xenocrysts and (or) xenoliths from the host rock may be present but not detectable, the validity of the age is somewhat uncertain. The K-Ar whole-rock ages for similar samples are 560 and 427 m.y. (table 4); these ages are not in agreement with the geochronology deduced from the above radiometric ages and thus are quite probably incorrect.

RELATION TO THORIUM VEINS

Several hundred thorium-bearing veins occur in both the Powderhorn and Wet Mountains districts. These veins typically are tabular bodies about 0.1–2 m thick. Some can be traced for 1000 m or more, many for only 20–100 m, emplaced in fracture zones in the Precambrian rocks. A few thorium-bearing zones in the Wet Mountains are as much as 15 m wide and can be traced as far as 1500 m (Christman and others, 1959, p. 519). The veins consist chiefly of quartz, carbonate minerals, potassic feldspar, barite, and iron oxides. Many veins are characterized by the presence of a fetid gas, noticeable when the rock is broken. Heinrich and Anderson (1965, p. 1916) described similar gases in the fenite and carbonatite northwest of the McClure Mountain area as consisting of C_5 and C_6 hydrocarbons and fluorine in the form of F_2, HF, and F_2O. A few tenths percent thorium is present, chiefly as thorite, and rare-earth elements are present in variable amounts, generally about as abundant as thorium.

Most thorium veins dip steeply to vertical and are clustered in groups within which they tend to be roughly parallel to one another. In the northwest part of the Powderhorn district the veins strike mostly northwest, but those in the eastern part strike predominantly east to N. 60° E. In the Wet Mountains area a northwest strike, usually about N. 60° W., is typical.

A few thorium-bearing veins are also sparsely distributed in Saguache and Gunnison Counties between the Powderhorn and Wet Mountains districts (fig. 2), for example on Cochetopa and Razor Creeks, in the Jacks Creek area, near Sargents, and a deposit 2.5 km south of White Pine. The vein near Jacks Creek contains uranium as well as thorium. A relation of these veins to the alkalic magmatism and thorium veins of Powderhorn and the Wet Mountains region is possible but uncertain.

In the Powderhorn district, thorium concentrations are known to be associated with the 579–565-m.y. alkalic rocks because thorium is abundant in some carbonatite, trachyte dikes, and magnetite-ilmenite-perovskite bodies; some veins cut across and are within the alkalic rocks. Some thorium veins may also be

related to the older (Precambrian Y) group of syenitic rocks, but this has not been proved. The older syenitic intrusives occur in the same 400-km² area as the principal thorite veins, although in detail the thorite veins are not noticeably concentrated near individual Precambrian Y syenite bodies. Locally, however, some minette is replaced by potassic feldspar, and such feldspathized rocks are commonly abnormally radioactive because of thorium, showing that some thorium mineralization postdates the minette dikes. Similarly, thin feldspathic fracture fillings, 20–50 mm thick, in the shonkinites or other older syenitic rocks are locally radioactive with scintillation counter readings up to three times the background values.

It seems probable that at least the great majority of, if not all, the thorium veins are associated with the Cambrian or Early Ordovician alkalic intrusions. The veins occur most commonly in fractures and shear zones, and they are found 30 km or more from the alkalic rock complexes. It seems clear that the vein-forming fluids were able to migrate great distances. The thorium-bearing veins may therefore delineate a system of fractures in the Earth's crust that existed about the time of the alkalic magmatism.

DIABASE AND OTHER MAFIC DIKES

About 40 diabase dikes occur in the 400-km² Powderhorn district and are as much as 100 m thick and 7 km long. Most trend N. 60° W. to east-west and dip steeply; one has an exceptional N. 30° E. trend in the Carpenter Ridge quadrangle. Similar numbers and sizes of diabase dikes occur northwestward along this trend in the Black Canyon of the Gunnison River region, where they form a zone or set as much as 4 km across extending more than 50 km northwest of the edge of the area of figure 1. One of the dikes in the Black Canyon of the Gunnison River has been dated as about 510±60 m.y. (Cambrian or Ordovician) in age by the Rb-Sr method on whole rock and potassium-feldspar (Hansen and Peterman, 1968, p. C87). Two such dikes cut across the alkalic complex of Iron Hill with a N. 78° W. strike and steep dip, demonstrating that they are younger than the alkalic rocks and compatible in age with the 510-m.y. dike. A plagioclase concentrate from one of these diabase dikes in the complex of Iron Hill (fig. 1) gave an age of 762±15 m.y. (table 1), clearly a spurious age and the result of excess radiogenic argon, as was the case for the aegirine age (sample P–9–901, table 1). Diabase dikes also have been found cutting the thorium-bearing veins.

The diabase dikes of the Powderhorn region are generally tholeiitic. The rocks comprising the northern part of the complex of Iron Hill (fig. 3), and the adjacent fenitized granite, are cut by similar dikes called quartz gabbro by Larsen (1942, p. 28–29) that contain 4 percent quartz and are hypersthene normative. In addition, one of the discordant diabase (gabbro) dikes trending N. 78°W. contains nepheline and olivine, is nepheline normative, and was called nepheline gabbro by Larsen (1942, p. 28–29). The nepheline gabbro is nearer the interior of the complex and is virtually all within the pyroxenite and nepheline syenite; its alkalic composition may indicate some mixing of the tholeiitic and alkalic magma types, or contamination of one by the other, in this one local area.

Mafic dikes are abundant in the Mount Tyndall quadrangle, in the same region as the alkalic complexes in the Wet Mountains. They have been classed as gabbro; lamprophyre; porphyritic olivine basalt, augite basalt, and peridotite; and diabase and nonporphyritic basalt (Brock and Singewald, 1968). The gabbro is considered Cambrian(?) and the other dikes as Cambrian(?) and (or) Tertiary. Most of these dikes trend westward to northwestward in the Mount Tyndall quadrangle.

Other mafic dikes including diabase are irregularly distributed elsewhere in the region. Our observations and review of geologic maps indicate that diabase and gabbro dikes are most abundant in the Powderhorn-Black Canyon of the Gunnison River and the northern Wet Mountains areas, occur sparsely in the intervening area, and are rare to absent in most areas flanking this west-northwest-trending belt.

REGIONAL PALEOTECTONICS

Several significant, related features of this region of alkaline magmatism thus may contribute to the interpretation of regional tectonic history: (1) deep fractures, probably formed in conjunction with arching or doming of the region, persisted for a long time and influenced the emplacement of igneous rocks, veins, and dikes, (2) igneous rocks of a relatively limited interval of geologic time are widely varied in composition and include both alkalic and tholeiitic types, (3) CO_2 and other volatiles were relatively abundant and played an important role in the carbonatite-alkalic rock petrogenesis, and (4) the two principal centers of alkalic intrusion differ in age by about 50 m.y. and are about 135 km apart, the younger toward the east.

The diabase and other mafic dikes were evidently emplaced in an extensive system of fractures that probably extended to a great depth. Geologic relations in the Powderhorn district show diabase dikes to be younger than the alkalic rock complex of Iron Hill and probably the same age as the Cambrian or Ordovician (Hansen and Peterman, 1968, p. C87) diabase dikes in the Black Canyon of the Gunnison River. In the Wet Mountains region, mafic dikes are both older and younger than syenites (Christman and others,

1959, p. 510). As the thorium-bearing veins, which are associated with the alkalic rocks, also formed in extensive deep fracture zones, it is likely that the Precambrian crustal material was being subjected to tensional and shear stresses over a long time period including the emplacement of these several rock types. It is of interest to note that several northwest-trending faults such as the Cimarron fault, on which there was 1000 m or more of displacement in Laramide time, are roughly parallel to this zone and thus probably had an early Paleozoic or late Precambrian ancestry. Though the Ilse fault, trending N. 30° W., near the east edge of the Wet Mountains region, shows evidence of Laramide movement, it also antedated the intrusion of the Cambrian dikes and influenced their emplacement (Singewald, 1966, p. C24).

The area discussed in this report trends along an extension of the 38th-parallel lineament, which Heyl (1972) traced from Virginia as far west as eastern Kansas and, with more tenuous evidence, to the Wet Mountains in Colorado. Structural movements and igneous events occurred irregularly along the lineament from Cambrian through at least Eocene time; some of the faulting probably originated in Precambrian time. Evidence of nearly horizontal fault movement has been found along the lineament in the Eastern States, and Heyl (1972, p. 892) postulated a right-lateral displacement of many miles in the Precambrian basement.

Alkalic rocks have generally been emplaced in the more stable parts of continental plates and commonly are associated with tensional features over upward bulges or swelling in the crust (LeBas, 1971; Bailey, 1964). Compressional arching was suggested by Bailey (1964) to explain these features, but the characteristic association with tensional features suggests the prevalence of vertical-acting forces. Some possible explanations of forces responsible for arching and crustal extension include localized melting and upward movement of mantle material at melting spots (hot spots) due to mantle plumes, localized melting due to concentrations of volatiles (degassing) in the mantle, or phase changes in the mantle to less dense mineral assemblages.

Origin of the alkalic rocks from magma derived from the mantle, with little contamination by preexisting crustal material, is compatible with the initial Sr^{87}/Sr^{86} ratios of 0.7036–0.7059 obtained thus far for the alkalic rocks in the Powderhorn and Wet Mountains regions (tables 2 and 5; figs. 4, 6, 7; Fenton and Faure, 1971; Powell and others, 1966). Comparable Sr isotope ratios have been noted for alkalic rocks and carbonatites in many other areas. The important role of CO_2 and other volatiles in the petrogenesis is shown by their abundance in the carbonatites and other rocks in the Powderhorn and Wet Mountains regions and in similar rocks elsewhere in the world. The alkalic magmatism of Powderhorn and the Wet Mountains is inferred to have had its source in mantle that was locally enriched in volatiles beneath this portion of the crust. The presence in the Powderhorn area of two distinct magma types of nearly the same age, tholeiitic (diabase and gabbro) and alkalic (carbonatite, nepheline syenite, and others), may indicate source magmas from different levels in the mantle. A deeper, localized source for the alkalic complex of Iron Hill may have been followed by a shallower mantle source for magma of the tholeiitic diabase dikes.

The two principal centers of alkalic intrusion are about 135 km apart and differ in age by about 50 m.y., the younger toward the east. The age relations might be explained by migration of sites of localized melting or volatile enrichment in the mantle or westward movement of the continent above a single site. The process appears episodic, culminating in the Powderhorn and then in the McClure Mountain-Gem Park areas but with lesser effects in the area between them. It is possible that other such complexes may be present, but buried by younger rocks, eastward or westward along this belt.

REFERENCES CITED

Bailey, D. K., 1964, Crustal warping—A possible tectonic control of alkaline magmatism: Jour. Geophys. Research, v. 69, p. 1103–1111.

Barker, Fred, Peterman, Z. E., and Marvin, R. F., 1970, Precambrian melasyenite of Ute Creek, San Juan Mountains, Colorado—Chemistry, petrology, and strontium isotopes: U.S. Geol. Survey Bull. 1311–C, p. C1–C15.

Bickford, M. E., Wetherill, G. W., Barker, Fred, and Lee-Hu, Chin-Nan, 1969, Precambrian Rb-Sr chronology in the Needle Mountains, southwestern Colorado: Jour. Geophys. Research, v. 74, p. 1660–1676.

Brock, M. R., and Singewald, Q. D., 1968, Geologic map of the Mount Tyndall quadrangle, Custer County, Colorado: U.S. Geol. Survey Geol. Quad. Map GQ–596, 2 sheets.

Christman, R. A., Brock, M. R., Pearson, R. C., and Singewald, Q. D., 1959, Geology and thorium deposits of the Wet Mountains, Colorado—A progress report: U.S. Geol. Survey Bull. 1072–H, p. H491–H535.

Cox, Allan, and Dalrymple, G. B., 1967, Statistical analysis of geomagnetic reversal data and the precision of potassium-argon dating: Jour. Geophys. Research, v. 72, p. 2603–2614.

Dalrymple, G. B., and Lanphere, M. A., 1969, Potassium-argon dating—Principles, techniques, and applications to geochronology: San Francisco, Calif., W. H. Freeman and Co., 258 p.

Damon, P. E., and Kulp, J. L., 1958, Excess helium and argon in beryl and other minerals: Am. Mineralogist, v. 43, p. 433–459.

Fenton, M. D., and Faure, Gunter, 1970, Rb-Sr whole-rock age determinations of the Iron Hill and McClure Mountain carbonatite-alkalic complexes, Colorado: The Mtn. Geologist, v. 7, no. 4, p. 269–275.

——— 1971, The age of the Iron Hill Complex of Colorado: Reply: The Mtn. Geologist, v. 8, no. 4, p. 223.

Hansen, W. R., and Peterman, Z. E., 1968, Basement-rock geochronology of the Black Canyon of the Gunnison, Colorado: U.S. Geol. Survey Prof. Paper 600–C, p. C80–C90.

Hart, S. R., and Dodd, R. T., Jr., 1962, Excess radiogenic argon in pyroxenes: Jour. Geophys. Research, v. 67, p. 2998–2999.

Hedge, C. E., Peterman, Z. E., Case, J. E., and Obradovich, J. D., 1968, Precambrian geochronology of the northwestern Uncompahgre Plateau, Utah and Colorado: U.S. Geol. Survey Prof. Paper 600–C, p. C91–C96.

Hedlund, D. C., and Olson, J. C., 1961, Four environments of thorium-, niobium-, and rare-earth-bearing minerals in the Powderhorn district of southwestern Colorado, Art. 121: U.S. Geol. Survey Prof. Paper 424–B, p. B283–286.

——— 1975, Geologic map of the Powderhorn quadrangle, Gunnison and Saguache Counties, Colorado: U.S. Geol. Survey Map GQ–1178.

Heinrich, E. W., and Anderson, R. J., 1965, Carbonatites and alkalic rocks of the Arkansas River area, Fremont County, Colorado—pt. 2, Fetid gas from carbonatite and related rocks: Am. Mineralogist, v. 50, nos. 11 and 12, p. 1914–1920.

Heinrich, E. W., and Dahlem, D. H., 1966, Carbonatites and alkalic rocks of the Arkansas River Area, Fremont County, Colorado, *in* International Mineralogical Association, Gen. Mtg., 4th, New Delhi, Dec. 15 and 22, 1964, Papers and Proc.: Mineralog. Soc India, I. M. A. Vol., p. 37–42.

Heyl, A. V., 1972, The 38th parallel lineament and its relationship to ore deposits: Econ. Geology, v. 67, no. 7, p. 879–894.

Jaffe, H. W., Gottfried, David, Waring, C. L., and Worthing, H. W., 1959, Lead-alpha age determinations of accessory minerals of igneous rocks (1953–1957): U.S. Geol. Survey Bull. 1097–B, p. B65–B148.

Kulp, J. L., and Engels, Joan, 1963, Discordances in K-Ar and Rb-Sr isotopic ages, *in* Radioactive dating: Internat. Atomic Energy Agency, Vienna, p. 219–239.

Larsen, E. S., Jr., 1942, Alkalic rocks of Iron Hill, Gunnison County, Colorado: U.S. Geol. Survey Prof. Paper 197–A, 64 p.

Larson, E. E., and Mutschler, F. E., 1971, Anomalous paleomagnetic pole from isotopically dated Cambro-Ordovician intrusives in Colorado: Geol. Soc. America Bull., v. 82, no. 6, p. 1657–1666.

LeBas, M. J., 1971, Per-alkaline volcanism, crustal swelling, and rifting: Nature Phys. Sci., v. 230, no. 12, p. 85–87.

Naeser, C. W., 1967, The use of apatite and sphene for fission track age determinations: Geol. Soc. America Bull., v. 78, p. 1523–1526.

Nash, W. P., 1972, Mineralogy and petrology of the Iron Hill Carbonatite Complex, Colorado: Geol. Soc. America Bull., v. 83, no. 5, p. 1361–1382.

Olson, J. C., 1974, Geologic map of the Rudolph Hill quadrangle, Gunnison, Hinsdale, and Saguache Counties, Colorado: U.S. Geol. Survey Map GQ–1177 [1975].

Olson, J. C., and Marvin, R. F., 1971, Rb-Sr whole-rock age determinations of the Iron Hill and McClure Mountain carbonatite-alkalic complexes, Colorado: Discussion: The Mtn. Geologist, v. 8, no. 4, p. 221.

Olson, J. C., and Wallace, S. R., 1956, Thorium and rare-earth minerals in the Powderhorn district, Gunnison County, Colorado: U.S. Geol. Survey Bull. 1027–0, p. 0693–0723.

Olson, J. C., Shawe, D. R., Pray, L. C., and Sharp, W. N., 1954, Rare-earth mineral deposits of the Mountain Pass district, San Bernardino County, California: U.S. Geol. Survey Prof. Paper 261, 75 p.

Parker, R. L., and Hildebrand, F. A., 1963, Preliminary report on alkalic intrusive rocks in the northern Wet Mountains, Colorado, *in* Geological Survey research 1962: U.S. Geol. Survey Prof. Paper 450–E, p. E8–E10.

Parker, R. L., and Sharp, W. N., 1970, Mafic-ultramafic igneous rocks and associated carbonatites of the Gem Park Complex, Custer and Fremont Counties, Colorado: U.S. Geol. Survey Prof. Paper 649, 24 p.

Peterman, Z. E., Doe, B. R., and Bartel, A., 1967, Data on the rock GSP–1 (granodiorite) and the isotope-dilution method of analysis for Rb and Sr, *in* Geological Survey research 1967, Chap. B: U.S. Geol. Survey Prof. Paper 575–B, p. B181–B186.

Peterman, Z. E., Hedge, C. E., and Braddock, W. A., 1968, Age of Precambrian events in the northeastern Front Range, Colorado: Jour. Geophys. Research, v. 73, p. 2277–2296.

Powell, J. L., Hurley, P. M., and Fairbairn, H. W., 1966, The strontium isotopic composition and origin of carbonatites, *in* Tuttle, O. F., and Gittins, John, eds., Carbonatites: New York, John Wiley & Sons, Inc., p. 365–378.

Shafiqullah, M., Tupper, W. M., and Cole, T. J. S., 1970, K-Ar age of the carbonatite complex, Oka, Quebec, *in* Alkaline rocks, the Monteregian Hills—Symposium, Montreal, 1969, Proc.: Canadian Mineralogist, v. 10, p. 3, p. 541–552.

Shawe, D. R., and Parker, R. L., 1967, Mafic-ultramafic layered intrusion at Iron Mountain, Fremont County, Colorado: U.S. Geol. Survey Bull. 1251–A, p. A1–A29.

Silver, L. T., and Barker, Fred, 1968, Geochronology of Precambrian rocks of the Needle Mountains, southwestern Colorado—pt. 1, U-Pb zircon results [abs.]: Geol. Soc. America Spec. Paper 115, p. 204–205.

Singewald, Q. D., 1966, Description and relocation of part of the Ilse fault zone, Wet Mountains, Colorado, *in* Geological Survey research 1966: U.S. Geol. Survey Prof. Paper 550–C, p. C20–C24.

Singewald, Q. D., and others, 1955, Geologic and radiometric maps of the McKinley Mountain area, Wet Mountains, Colorado: U.S. Geol. Survey Mineral Inv. Field Studies Map MF–37, 4 sheets.

Stern, T. W., Phair, G., and Newell, M. F., 1971, Boulder Creek Batholith Colorado, pt. II, Isotopic age of emplacement and morphology of zircon: Geol. Soc. America Bull., v. 82, p. 1615–1633.

Temple, A. K., and Grogan, R. M., 1965, Carbonatite and related alkalic rocks at Powderhorn, Colorado: Econ. Geology, v. 60, p. 672–692.

Jour. Research U.S. Geol. Survey
Vol. 5, No. 6, Nov.–Dec. 1977, p. 689–703

POTASSIUM-ARGON GEOCHRONOLOGY OF SOME METAMORPHIC, IGNEOUS, AND HYDROTHERMAL EVENTS IN PUERTO RICO AND THE VIRGIN ISLANDS

By DENNIS P. COX,[1] RICHARD F. MARVIN,[2] JOHN W. M'GONIGLE,[1]
DAVID H. McINTYRE,[2] and CLEAVES L. ROGERS,[2]
Reston, Va.,[1] Denver, Colo.[2]

Abstract.—Potassium-argon ages of hornblende, biotite, and whole rocks in Puerto Rico include the following: 126 m.y. for amphibolites in the southwest part of the island; 109 m.y. for the oldest known quartz diorite plutons; 88 to 65 m.y. for emplacement of various quartz diorite and granodiorite batholiths and stocks; 38 to 46 m.y. for intrusions of quartz diorite porphyry stocks and their hydrothermal alteration and mineralization. These intrusions are the youngest known igneous rocks in Puerto Rico.

In addition, a 35-m.y. age was determined for hornblende and biotite from the Virgin Gorda batholith.

Although widespread hydrothermal alteration as old as 75 m.y. is known in Puerto Rico, all important copper deposits are related to the 38- to 46-m.y. old intrusions.

A discontinuous program of rock sampling and isotopic analysis was begun in 1970 in Puerto Rico; part of the sampling was done in conjunction with mineral-resource studies, part in conjunction with quadrangle mapping, and part in an attempt to gain a broader understanding of the history of the area. (The British Virgin Islands sample was collected by one of the authors while on vacation.) In general, the analytical work confirms ages determined on the basis of stratigraphic and paleontologic studies of workers over the past twenty years. Six important contributions are present in the new data however:

1. A K-Ar age of 126 m.y. (Valanginian) for amphibole from metamorphic rocks of the so-called "Bermeja Complex" is older than previous K-Ar determinations for the unit but is anomalously younger than the age indicated by radiolaria for a nearby, probably younger, chert unit (upper Tithonian to upper Valanginian-Hauterivian) (Mattson and Pessagno, 1974).
2. K-Ar determinations suggest that major diorite and quartz diorite plutons were emplaced by Aptian time (100–109 m.y.), earlier than previously supposed.
3. The major quartz diorite-granodiorite batholiths were emplaced from Coniacian (88 m.y.) to the end of the Cretaceous Period (65 m.y.). At least two phases are recognized for the San Lorenzo batholith: in the Campanian (73 m.y. and Maestrichtian (66 m.y.).
4. Areally extensive, structurally controlled hydrothermal alteration zones, without economic base-metal mineralization, were formed at about the same time as the early phase of the San Lorenzo batholith (75 m.y.).
5. All known economic copper mineralization is contemporaneous with and spatially related to quartz diorite and quartz diorite porphyry of late Eocene age (40 m.y.), representing the last igneous activity in Puerto Rico.
6. Hornblende and biotite from the Virgin Islands batholith at Virgin Gorda gave an early Oligocene age (35 m.y.), indicating the possibility that the youngest volcanic strata in the British Virgin Islands are somewhat younger than previously believed.

GEOLOGY AND GEOCHRONOLOGY

The island of Puerto Rico (figs. 1 and 2) can be considered as comprising three major tectonic blocks separated by two fault zones of large left-lateral and possibly important vertical displacement (Briggs and Akers, 1965; Glover, 1971; Cox and Briggs, 1973). All three blocks are composed mainly of volcanic and sedimentary rocks of Cretaceous and lower Tertiary age. A profound angular unconformity separates these rocks from overlying middle and upper Tertiary coastal plain deposits. The southwestern block is distinguished by areally extensive masses of serpentine and minor amphibolite. The central block contains granitic batholiths of Cretaceous age and many stocks

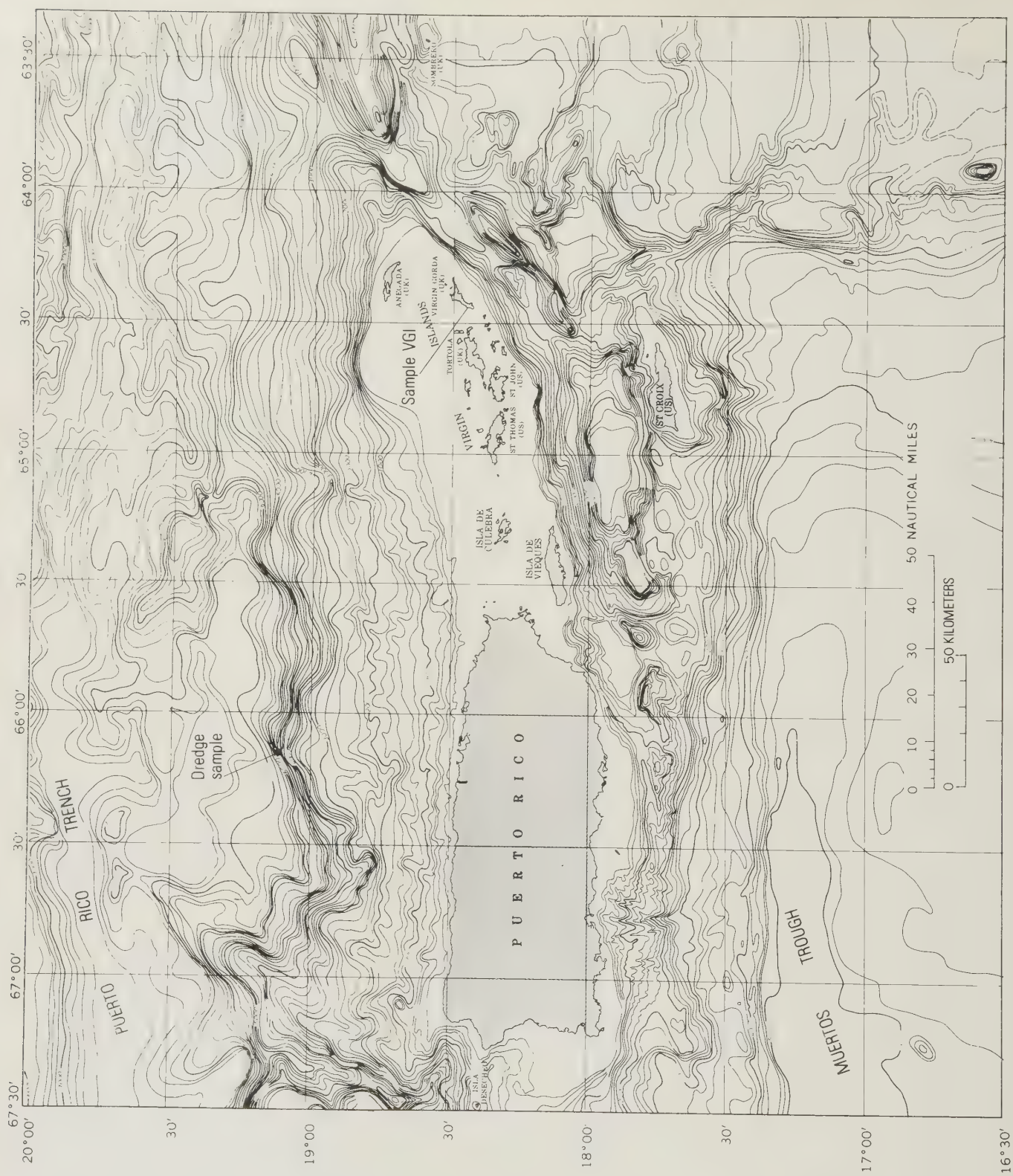

FIGURE 1.—Map showing bathymetry around Puerto Rico and the Virgin Islands, modified from Garrison, Martin, and others (1972). Dredge sample location from Perfit (written commun., 1975).

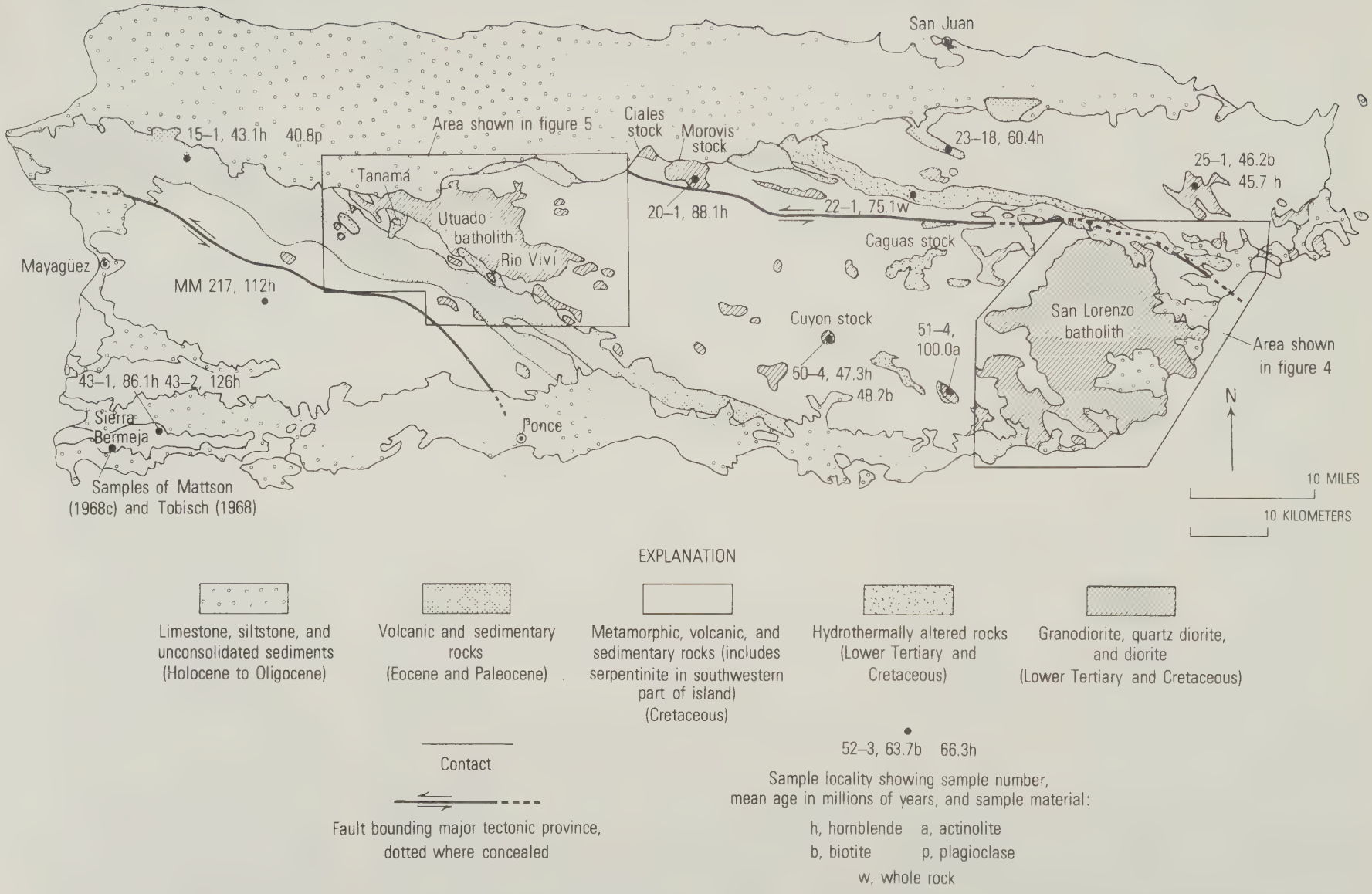

FIGURE 2.—Generalized geologic map of Puerto Rico.

and volcanic rocks of Eocene age. The northeastern block lacks Cretaceous batholiths but contains widespread Eocene volcanic and intrusive rocks. Stratigraphic correlation of Cretaceous rocks from one block to another has not been possible indicating that wrench movement on the intervening faults has been large relative to the size of the island.

The Virgin Islands east of Puerto Rico (fig. 1) contain volcanic rocks that may be coeval with volcanic units in eastern Puerto Rico, as well as extensive lower Tertiary volcanic and sedimentary units. The lower Tertiary rocks locally are intruded by the Virgin Islands batholith.

In the following pages, isotopic ages determined in this and earlier studies will be discussed. K-Ar ages shown in table 1 and figure 3 were determined in the laboratories of the U.S. Geological Survey in Denver, Colo. The analytical techniques used are essentially those described by Dalrymple and Lanphere (1969).

METAMORPHIC ROCKS

Evidence concerning a significant part of the early history of Puerto Rico must be gleaned from occurrences of amphibolite and serpentinite that are restricted to an area of less than 100 km² in the southwestern part of the island. Within the Sierra Bermeja, the amphibolite-serpentinite terrane is overlain by a sequence of chert and minor amounts of volcanic rock. Radiolaria from the chert suggest a Late Jurassic to Early Cretaceous age (early Tithonian to late Valanginian-Hauterivian; Mattson and Pessagno, 1974). These rocks are overlain unconformably by a widespread sequence of marine volcanic and sedimentary rocks that has been inferred to be as old as Cenomanian (Slodowski, 1956; Mattson, 1960), or Albian (Mattson, 1973). Elsewhere in southwestern Puerto Rico, this predominantly Upper Cretaceous sequence commonly rests with erosional unconformity upon serpentinite.

Attempts to establish the age of the amphibolite by the K-Ar age method have not yielded results wholly in agreement with the age suggested by paleontology and stratigraphy. Mattson (1964) reported an age of 110 m.y. (Aptian-Albian) on hornblende from a sample collected near the west end of the Sierra Bermeja (fig. 2). Hornblende from a sample collected by Tobisch from the same area (fig. 2) yielded ages of 86.3 and 84.9 m.y. (Senonian; Tobisch, 1968, table 2). Tobisch (1968, p. 569–570) considered all these ages to be too young and attributed the disturbance to later heating.

During the present investigation, samples were collected near the east end of the Sierra Bermeja (fig. 2). In this area, the amphibolite locally is cut by some small porphyry intrusions, although none are found immediately adjacent to the sample locality Both the amphibolite and the porphyry were sampled. A hornblende concentrate from the amphibolite yielded a K-Ar age of 126 m.y.; hornblende from the porphyry gave an age of 86.1 m.y. Sample locations and analytical data for the K-Ar age determinations are presented in table 1.

A concentrate of brown amphibole from cobble-sized amphibolite blocks enclosed in serpentinite in a breccia pipe 4 km southeast of Maricao (fig. 2, sample MM–217; McIntyre, 1975) gave a K-Ar age of 112±15 m.y. (table 1).

The 126 m.y. age for the amphibolite (Early Cretaceous, Valanginian) is in better agreement with the known geologic relations than those previously available. However, as noted earlier, the amphibolite may have been affected an unknown amount by the porphyry intrusions or other as yet unknown heating events and therefore provides only a younger limit to the age of the amphibolite-facies metamorphism. The Jurassic age implied by the data of Mattson and Pessagno (1974) appears more reasonable. The age of the porphyry (86.1 m.y., Coniacian) is quite close to the K-Ar ages for the amphibolite samples collected by Tobisch (86.3 and 84.9 m.y.). It appears likely, therefore, that Tobisch's samples were strongly affected by the thermal event that accompanied emplacement of the porphyry intrusions.

In the Dominican Republic, hornblendes from amphibolite have yielded K-Ar ages of 127 m.y. (Bowin, 1975, p. 533) and 122 m.y. (Kesler and others, written commun., 1976).

CRETACEOUS VOLCANIC AND SEDIMENTARY ROCKS

The Cretaceous section in central Puerto Rico has been summarized by Briggs (Cox and Briggs, 1973).

> The oldest rocks described . . . are chiefly massive volcanic breccias that contain occasional limestone lenses near the top . . . Overlying the breccia section are lower Cretaceous (Albian) to Upper Cretaceous (Santonian?) thin-bedded tuffaceous sandstone and siltstone intercalated with basalt and andesite volcanic breccia . . . Resting with partial unconformity on this moderately well-bedded section are sequences containing marine and nonmarine tuffaceous conglomerate limestone, marine and subaerial tuff, and subaerial volcanic breccias of late Cretaceous (Santonian? to Maestrichtian) age.

No volcanic or sedimentary rocks of this age were analyzed in this study.

TABLE 1.—*Potassium-argon ages, analytical data, and locations for Puerto Rico and Virgin Island samples*

[Analysts: R. F. Marvin and H. H. Mehnert, argon; Violet Merritt, potassium by flame photometry; W. T. Henderson, potassium by isotope dilution. Decay constants: $K^{40}\lambda\varepsilon = 0.585 \times 10^{-10}$/yr; $\lambda\beta = 4.72 \times 10^{-10}$/yr. Atomic abundance: $K^{40}/K = 1.19 \times 10^{-4}$.]

Field No. Analyzed mineral[1]	K_2O (percent)	Radiogenic Ar^{40} 10^{-10}mole/g	Radiogenic Ar^{40} Percent	Apparent age (m.y.) $\pm 2\sigma$	Quadrangle lat long	Rock type and comments
15-1 hornblende	0.326[2] .326	0.2100	62	43.1±0.9	Central La Plata 18°20'13"N 67°02'49"W	Andesite porphyry which occurs as residual boulders in the Río Culebrines Formation.
plagioclase (andesine)	.248[2] .248	.1506	56	40.8±0.8		
17-140 quartz-sericite	1.54 1.59 1.59 1.68	1.037	86	43.4±1.3	Bayaney 18°15'20"N 66°47'33"W (drill hole collar location)	Gangue from hydrothermally altered porphyry at Tanamá in a core from 811 foot interval, Drill Hole No. T116 (inclined at 45°).
17-141 quartz-sericite	.75 .76 .73 .73	.4581	79	41.5±1.9	do.	Gangue from hydrothermally altered porphyry at Tanamá in a core from 419 foot interval, Drill Hole No. T116 (inclined at 45°).
18-5 hornblende	.399[2] .394	.4075	64	68.4±2.1	Utuado 18°16'47"N 66°39'25"W	Quartz monzonite from the Utuado batholith; collected below dam face at Lago Caonillas.
20-1 hornblende	.559[2] .561	.7455	84	88.1±1.8	Ciales 18°18'08"N 66°24'39"W	Quartz monzonite from the Morovis stock.
22-1 quartz-sericite	3.28 3.25	3.690	95	75.1±1.8	Naranjito 18°17'23"N 66°08'27"W	Hydrothermally altered Santa Olaya Lava.
23-18 hornblende	.643[2] .648	.5843	83	60.4±1.2	Aquas Buenas 18°20'30"N 66°05'44"W	Guaracanal Andesite.
25-1 biotite	8.32 8.37	5.760	87	46.2±1.1	El Yunque 18°17'35"N 65"47'40"W	Quartz diorite from Río Blanco stock.
hornblende	.39 .39	.2660	57	45.7±2.2		
MM-217-C-1 hornblende-garnet	.14 .15	.2475	35	112 ± 15	Maricao 18°10'N 66°57'15"W	Amphibolite enclosed by serpentinite. Hornblende concentrate contains about 15 percent hydrogrossular garnet.
31-1 hornblende (-60+100 mesh)	.18 .18	.1122	46	41.8±5.6	Monte Guilarte 18°14'23"N 66°51'26"W	Hornblende porphyry from the Torrecilla stock.
hornblende (100+150 mesh)	.186[2] .187	.1232	36	44.3±4.0		
32-5 hornblende	.279[2] .276	.1710	56	41.3±1.9	Adjuntas 18°11'30"N 66°40'43"W	Quartz diorite from stream bed of Río Viví.
32-12 hornblende	.399[2] .394	.2240	59	37.9±1.5	Adjuntas 18°14'06"N 66°43'19"W	Quartz diorite from stream bed of Río Grande de Arecibo.
32-129 biotite	5.16 5.16	3.708	84	48.1±1.2	Adjuntas 18°12'37"N 66°40'41"W	Altered and fractured diorite collected in stream bed of Río Viví. Biotite age was lowered by thermal effects of Eocene intrusive.
hornblende	.753[2] .743	.7323	85	65.2±1.3		
33-16 hornblende	.389[2] .372	.4174 .4345	78 76	73.2±1.5	Jayuya 18°10'00"N 66°36'22"W	Quartz diorite.

TABLE 1.—*Potassium-argon ages, analytical data, and locations for Puerto Rico and Virgin Island samples*—Continued

Field No. Analyzed mineral[1/]	K_2O (percent)	Radiogenic Ar^{40} 10^{-10}mole/g	Radiogenic Ar^{40} Percent	Apparent age (m.y.) $\pm 2\sigma$	Quadrangle lat long	Rock type and comments
33-17					Jayuya	Quartz diorite
hornblende	.512[2/]	.5165	81	67.2±1.4	18°12'13"N	
	.511				66°37'25"W	
33-24					Jayuya	Quartz diorite porphyry, hydrothermally altered, from outlier of the Utuado batholith.
biotite	6.02	6.403	86	70.7±1.7		
	6.03					
hornblende	.45	.4614	70	69.0±3.3		
	.44					
33-25					Jayuya	Quartz diorite
hornblende	.360[2/]	.3632	69	66.5±1.3	18°11'39"N	
	.367				66°31'25"W	
38-4					Juncos	Quartz monzonite from the San Lorenzo batholith.
biotite	4.94	5.401	89	72.7±2.0	18°09'08"N	
	4.94				65°58'50"W	
hornblende	.652[2/]	.7257	82	73.5±1.5		
	.661					
38-5					Juncos	Quartz monzonite from the San Lorenzo batholith. Chlorite-biotite age appears to be too young.
chlorite-biotite	1.27	1.172	78	61.8±1.5	18°12'23"N	
	1.26				65°52'41"W	
hornblende	.54	.5731	83	70.6±3.2		
	.54					
39-1					Humaco	Granodiorite from the San Lorenzo batholith. Biotite age probably lowered by thermal effects of a younger intrusive.
biotite	8.36	8.214	87	65.7±1.6	18°07'33"N	
	8.29				65°51'48"W	
hornblende	.972[2/]	1.093	87	74.3±1.5		
	.983					
43-1					San German	Diorite porphyry, so-called "Bermeja Complex" in Sierra Bermeja.
hornblende	.648[2/]	.8403	82	86.1±2.1	18°00'11"N	
	.644				67°05'18"W	
43-2					San German	Amphibolite, so-called "Bermeja Complex" in Sierra Bermeja.
hornblende	.301[2/]	.5803	74	126 ± 3	18°00'05"N	
	.302				67°05'19"W	
50-4					Cayey	Quartz diorite from the Cuyon stock.
biotite-chlorite	2.43	1.752	87	48.2±1.3	18°06'37"N	
	2.43				66°14'45"W	
hornblende	.243[2/]	.1714	50	47.3±1.0		
	.243					
51-4					Patillas	Diorite
actinolite(?)	.06	.0911	31	100 ± 16	18°02'50"N	
	.06				66°05'57"W	
52-1					Yabucoa	Quartz diorite
hornblende	.25	.4136	76	109 ± 9	18°03'05"N	
	.25				65°59'20"W	
53-1A					Punta Guayanés	Diorite from the San Lorenzo batholith.
hornblende	.266[2/]	.3107	70	77.8±1.6	18°02'33"N	
	.264				65°51'19"W	
53-1B					Punta Guayanés	Diorite from the San Lorenzo batholith.
hornblende	.352[2/]	.4154	60	78.4±1.6	18°02'28"N	
	.352				65°51'14"W	
53-2					Punta Guayanés	Quartz monzonite from the San Lorenzo batholith.
biotite	8.58	8.461	78	65.7±1.6	18°05'54"N	
	8.59				65°50'22"W	
hornblende	.57	.5670	81	66.3±2.9		
	.57					
V-G-1						Quartz diorite from the Virgin Islands batholith.
biotite	8.90	4.816	78	36.3±0.9	18°26'15"N	
	8.92				64°26'10"W	
hornblende	.48	.2447	65	34.2±1.6		
	.48					

[1/] Mineral separations were done by G. T. Cebula and J. W. Groen except for sample MM-217-C-1 which D. H. McIntyre separated.

[2/] Potassium determined by isotope dilution.

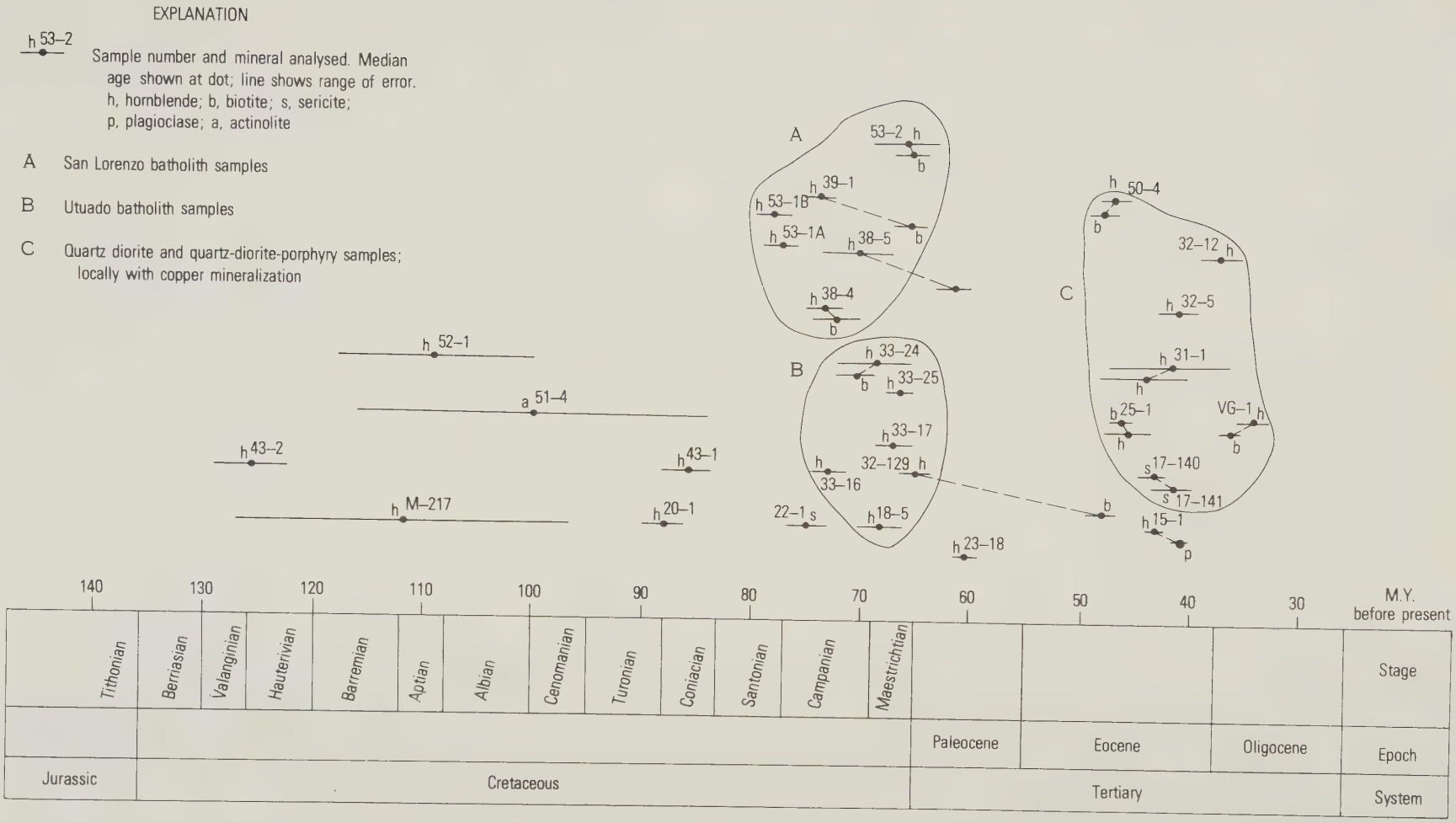

FIGURE 3.—Diagram showing potassium-argon age ranges for Puerto Rican and Virgin Island samples. Time scale from Van Eysinga (1975).

CRETACEOUS PLUTONS AND HYDROTHERMALLY ALTERED ROCKS

The oldest intrusive rocks in Puerto Rico, as determined by isotopic methods, are diorite and quartz diorite plutons in the southeast part of the central tectonic block (fig. 2). These intrude volcanic rocks dated stratigraphically as pre-Albian (Glover, 1971). Hornblende and actinolite from two of these plutons give ages of 100 and 109 m.y., respectively (samples 51–4, 52–1; table 1 and fig. 2). Analytical errors are high because of the low potassium content of the amphiboles. These ages are similar to that of a dike (108 m.y.) cutting volcanic rocks of the so-called "Water Island Formation" in northern Virgin Islands (Donnelly 1966, p. 130).

Northwest-striking hydrothermal alteration zones are spatially related to these older plutons in southeast Puerto Rico, but no important mineral resources have been located to date.

Two batholiths are in the central tectonic block: the San Lorenzo in the east, and Utuado in the west-central part. Between these batholiths are the Caguas, Morovis, and Ciales plutons. These plutons are chiefly medium- to coarse-grained quartz diorite and granodiorite.

The oldest of these plutons for which an age has been determined is the Morovis stock. Hornblende from granodiorite in this pluton gave an 88.1 m.y. age (early Coniacian) (sample 20–1). Berryhill (1965) quoted a lead-alpha age of 70±20 m.y. for the Ciales stock a few kilometers to the east.

The San Lorenzo batholith includes three principal units which have at this time been only partly mapped (fig. 4): (1) Diorite and gabbro which form several small bodies (xenoliths) generally within or close to the border zone of the batholith; the 78 m.y. date provided by sample 53–1 is minimal for this unit, as exposures show that it was engulfed and intruded, and so presumably reheated, by younger units, (2) a predominant granodiorite-quartz diorite unit which forms about 75 percent of the batholith and has an average age of 73.1 m.y. (sample 38–4), and (3) a unit which forms a large outcrop area near Punta Guayanés, ranges from quartz monzonite near the center of the batholith to quartz diorite near the border, and has an average age of about 66 m.y. (sample 53–2). This unit can be distinguished from the older unit in the field by its light color, a general predominance of biotite over hornblende, and the common presence of quartz in rounded grains or phenocrysts.

Two of the six dated samples from the San Lorenzo batholith have discordant ages suggesting that the biotite in these rocks has been affected by later thermal events.

Sample 39–1 was probably affected by the 66-m.y. quartz monzonite-quartz diorite unit to the east. Sample 38–5 is lithologically similar to the predominant type of granodiorite exposed in the northeastern part of the San Lorenzo batholith. The hornblende age (70.6 m.y.) of the sample agrees with other ages for this unit, but the chlorite-biotite age (61.8 m.y.) is discordant; it may have been thermally reset by a later intrusive phase of the batholith. A younger intrusive body is exposed 2 km directly east of the sample site, and may extend to within 1 km, beneath a Quaternary alluvial cover. This intrusion, mapped after the collection of sample 38–5, is a quartz monzonite, which, although much lower in mafic minerals, is otherwise similar in appearance to the granodiorite at Punta Guayanés and is correlated with it. The dated part of the Punta Guaynés granodiorite is 12 km to the southeast (sample 53–2). Other late intrusive phases of the San Lorenzo batholith may be west of the 38–5-sample site; batholithic rocks in that area have not been subdivided.

The Utuado batholith (Weaver, 1958 and Chen, 1969) in east-central Puerto Rico (figs. 3, 5) is of interest because porphyry copper deposits are found along its southwestern border. The copper deposits are of a distinctly younger age, however, (Barabas, 1971) and the batholith may have provided only the structural control for their emplacement.

The K-Ar ages of samples from the Utuado batholith and its eastern outliers (table 1, fig. 5) suggest that emplacement may have begun in the Campanian and continued into the Paleocene. Isotopic ages do not give a definitive picture as the younger ages may have been reduced, by an unknown amount, by thermal effects of subsequent peripheral Eocene intrusive rocks.

Rocks of the oldest age, 73.2 m.y., (sample 33–16, table 1, fig. 2) were collected from the elongate outlier trending southeast through the southern part of the Jayuya quadrangle. These rocks are more dioritic than the other phases of the batholith and may represent a distinct intrusive phase.

Locally, mineralizing solutions may have accompanied this early phase of intrusion. In a small road-cut exposure of the extreme eastern outlier of the batholith at Quebrada de la Mina (near sample locality 33–25), chalcopyrite and molybdenite are found in numerous thin veinlets cutting quartz porphyry. Biotite and hornblende from this porphyry (sample 33–24) gave ages of 70.7 and 69.0 m.y., respectively.

The major intrusion probably took place during the Maestrichtian as indicated by ages that range from

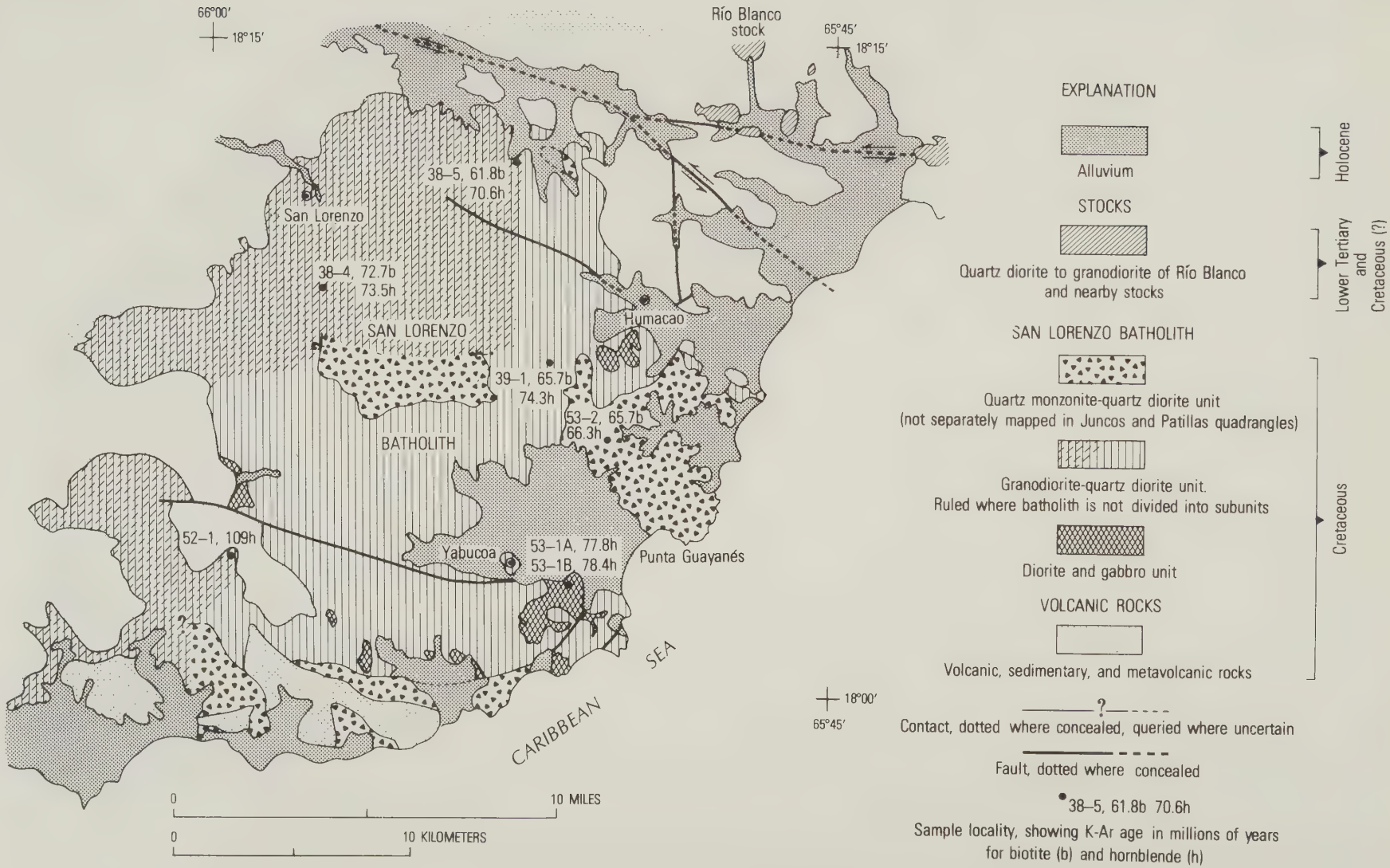

FIGURE 4.—Generalized geologic map of the San Lorenzo batholith.

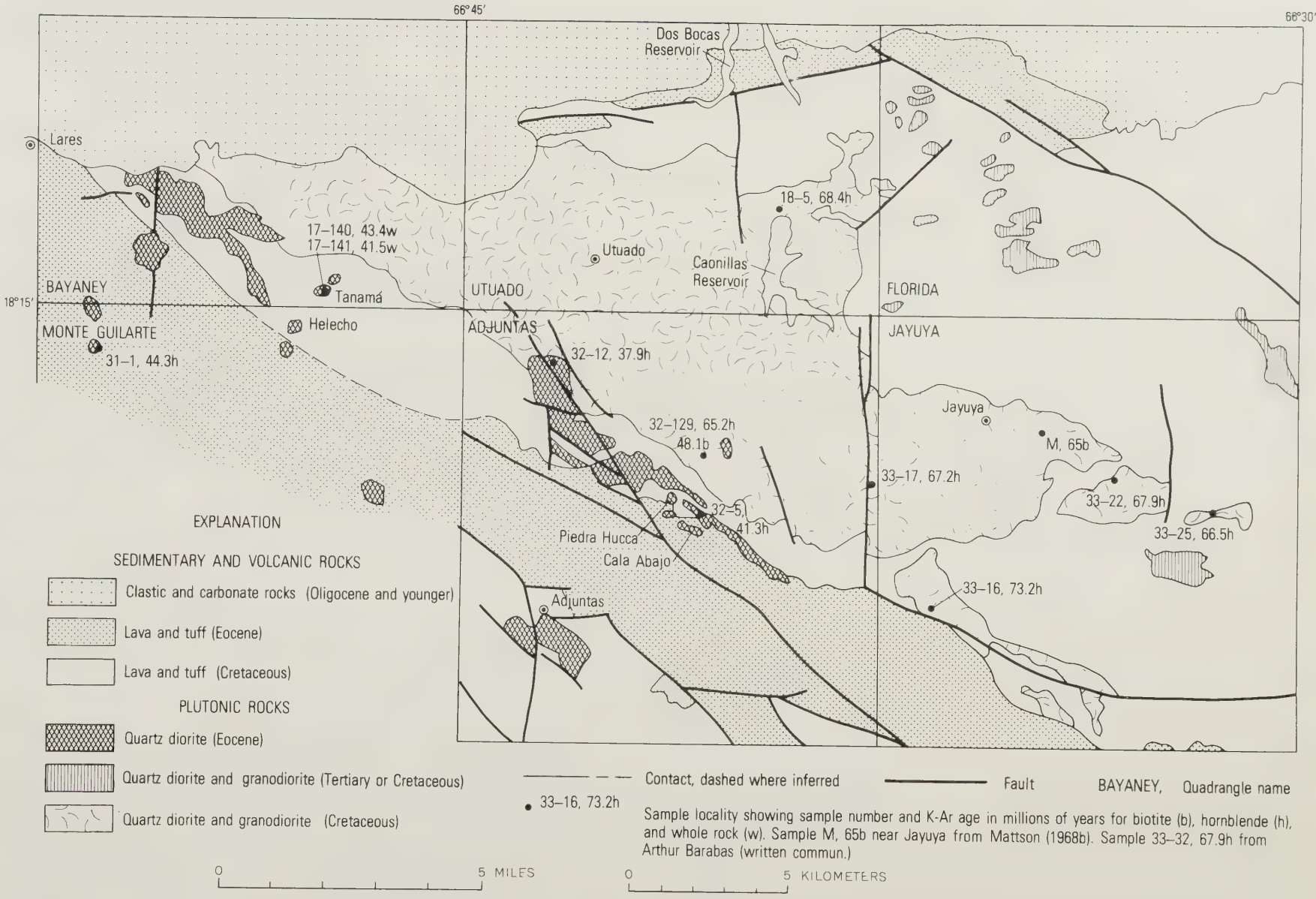

FIGURE 5.—Generalized geologic map of the Utuado batholith and vicinity.

65.2 to 68.4 m.y. (samples 32–129, 33–17, 33–25, and 18–5; table 1). These ages supplement a K-Ar biotite age of 65±3 m.y. (Mattson, 1968b) obtained for a sample collected from the east side of the main batholith (fig. 5). Barabas (1971) gives 62 m.y., Paleocene, as the average age of several samples taken from the batholith. One sample (32–129) of quartz diorite in the border zone of the batholith yielded discordant K-Ar ages; biotite gave an age of 48.1 m.y., distinctly younger than the 65.2 m.y. given by the coexisting hornblende. This discordance can be explained by thermal effects from a nearby Eocene intrusion.

Mattson mapped two facies of the Utuado batholith in the Utuado and Jayuya quadrangles: a main quartz monzonite-granodiorite facies and a quartz diorite-granodiorite facies along the southern border and in the eastern end. No conclusive difference in age between rocks of these facies was determined in the present study. Two small porphyry bodies originally mapped as part of the quartz diorite-granodiorite facies near the Río Arecibo and Río Viví gave Eocene ages (sample 32–12; table 1; A. H. Barabas, written commun.) (fig. 5).

In general, copper mineralization is very weakly developed in Cretaceous plutonic rocks, although extensive hydrothermal activity (Hildebrand, 1961) may be temporally related to them. Figure 3 shows several areas of hydrothermal alteration in east-central Puerto Rico. These areas, described by Pease (1960), include propylitic, argillic, and sericitic alteration. Sample 22–1, a quartz sericite rock derived from alteration of an Upper Cretaceous lava in the largest of these alteration zones, yielded an age of 75.1 m.y. (table 1, fig. 3). The similarity of this age to that of the San Lorenzo batholith suggests a genetic relationship. A Late Cretaceous age is assumed for the large east-trending alteration zones in eastern Puerto Rico. Copper mineralization is not known to be associated with this alteration.

LOWER TERTIARY VOLCANIC AND SEDIMENTARY ROCKS

Lower Tertiary rocks are in a northwest-trending belt extending from east of Ponce, northwestward along the south side of the Utuado batholith to Punta Jiquera north of Mayagüez. Small areas of lower Tertiary rocks are to the north of the Utuado batholith, as well as in the southwest tectonic block, and in the northeast tectonic block, south and southwest of San Juan.

In western Puerto Rico, McIntyre, Aaron, and Tobisch (1970) have described Eocene dacite to rhyodacite, lapilli tuff, crystal and vitric tuff, volcanic sandstone, and mudstone. These are overlain by lower middle Eocene basalt and keratophyre. Chert, siliceous and calcareous mudstone overlain by tuff breccia, tuff, volcanic sandstone, and mudstone make up the overlying Río Culebrinas Formation of middle Eocene age. Hornblende from sample 15–1 (table 1; figs. 2, 3) establishes a minimum age of 43.1 m.y. for a tuff breccia in the Río Culebrinas Formation. Coexisting plagioclase gave a younger age, 40.8 m.y.

Along the south side of the Utuado batholith, lower Tertiary rocks are localized in a complex graben that trends northwest as described by Mattson (1967). In this area, middle Eocene lapilli tuff and volcanic sandstone overlie Maestrichtian and older basaltic and andesitic pyroclastic rocks. These are overlain by thin- to medium-bedded laminated mudstone and by up to 1400 m of dacitic pyroclastic and flow rocks of the Anon Formation. A sample from the Anon, analyzed by Arthur Barabas at Yale University, gave an age of 44.3 m.y., confirming the middle- to late-Eocene stratigraphic age of the unit (Barabas, written commun., 1972). Eocene rocks are chloritized, epidotized, pyritized, and silicified in the vicinity of the mineralized stocks at Río Viví.

On the north side of the Utuado batholith, lower Tertiary rocks include up to 3000 m of fine-grained bedded tuffs and volcanic sandstone of late Paleocene to middle Eocene age (Nelson and Monroe, 1966) overlain by about 1700 m of Eocene massive volcanic breccia (Nelson, 1967).

South of San Juan, in a small area of lower Tertiary rocks, the Paleocene dacitic Guaracanal Andesite is overlain by thin-bedded tuff and laminated siltstone of late Paleocene or Eocene age (Pease, 1968a, 1968b). Sample 23–18, a hornblende-rich volcanic breccia from the Guaracanal Andesite gave a hornblende age of 60.4 m.y., which agrees with the stratigraphic age.

Mattson (1967) and McIntyre, Aaron, and Tobisch (1970) have noted a major unconformity between Maestrichtian and Tertiary deposits in the belt of lower Tertiary rocks west of the approximate longitude of Ponce. Paleocene and lower Eocene rocks are missing in this area, and possibly 5000 m of Upper Cretaceous rocks were removed by erosion prior to the deposition in the middle Eocene (Mattson, 1967, p. B33).

EOCENE INTRUSIVE AND HYDROTHERMALLY ALTERED ROCKS

Stocks of quartz diorite and quartz diorite porphyry, partly intrusive into the Anon Formation of Eocene age, were mapped as Eocene by Mattson

(1968a) in the Río Viví area, and similar rocks, 15 km to the northeast were assigned a Tertiary age by Nelson and Tobisch (1968). Numerous small stocks are found along the north side of the northwest-trending belt of Eocene volcanic rocks.

Because these stocks are close to and, in part, intrude rocks of the Utuado batholith, radiometric dating has been very useful in distinguishing them from the older intrusive rocks. Figure 5 shows the approximate distribution of upper Eocene intrusive rocks along the south flank of the Utuado batholith. The isotopic ages obtained in this study for these intrusive rocks range from 44.3 to 37.9 m.y. (samples 31–1, 32–5, 32–12; table 1), substantiating the age assigned by Mattson (1968a) and Nelson and Tobisch (1968) but also indicating that one or more of these intrusive rocks may be early Oligocene in age. Barabas (1971) obtained an averaged age of 38 m.y. for several samples from this group of intrusive rocks.

In addition, some of the small stocks in east-central Puerto Rico now broadly classified as Cretaceous or Tertiary may be Eocene. Only one such intrusive rock, the Cuyon stock (Berryhill and Glover, 1960), was, however, sampled in the present study. Concentrates of hornblende and partly chloritized biotite from this intrusive rock yielded ages of 47.3 and 48.2 m.y., respectively (sample 50–4; table 1).

Eocene intrusive rocks range from equigranular, medium-grained hornblende-quartz diorite and diorite to hornblende-quartz diorite porphyry with a saccharoidal quartz-plagioclase groundmass, and to andesitic and dacitic porphyry with fine to glassy groundmass. The quartz diorite porphyry is spatially and genetically related to the porphyry copper deposits at Tanamá and Río Viví (Cox, Larsen, and Tripp, 1973) and to weak copper mineralization at Cuyon (Bergey, 1966). All three rock types are found as unmineralized intrusions cutting across the copper orebodies at Tanamá and Río Viví areas.

Gangue minerals associated with the copper mineralization were dated. Quartz sericite concentrates from the Tanamá orebody yielded an average age of 42.4 m.y. (late Eocene) (samples 17–140, 17–141; table 1).

Except for one complicating factor, there seems to be clear evidence for assigning an Eocene age to the porphyry copper deposits in west-central Puerto Rico. The complication arises from the fact that all of the K-Ar ages for plutons closely associated with the copper deposits were determined on very fresh specimens that show no copper mineralization. As some of these rocks intrude the mineralized zones and are unaltered, their ages are thus minimum ages for the mineralization. No ages on obvious premineralization intrusive rocks are available because of widespread propylitic alteration and attendant chloritization of hornblende and biotite in these rocks. As these apparently postore intrusive rocks are fairly widespread in the ore zones, the hydrothermal mineral ages could represent thermally reduced ages, and the true age of mineralization may be older, perhaps equivalent to that of the Utuado batholith. If this were the actual situation, some ages intermediate between the Eocene and an older mineralization event would be expected. The consistently young ages of hydrothermal minerals determined in this study and by Barabas (written commun., 1973), and the absence of any anomalously intermediate older ages (fig. 3) strongly indicate that the mineralization is Eocene. The several phases of intrusion, hydrothermal alteration, and mineralization probably occurred during a relatively short time span; the order of occurrence can not be resolved conclusively by our K-Ar ages.

Eocene plutonic rocks are found in the northeastern tectonic block of the island. Biotite and hornblende from quartz diorite of the Río Blanco stock on El Yunque have ages of 46.2 and 45.7 m.y. respectively (sample 25–1, table 1). This confirms Seiders' Eocene age for the stock on the basis of the observation that it intruded branches and dikes along fault zones which in turn displaced lower Tertiary rocks (Seiders, 1971). Contact metamorphic chalcopyrite-pyrrhotite deposits are noted in limestones near the southeast contact of this stock (Domenech, 1899, Cox and Briggs, 1973), and chalcopyrite molybdenite mineralization at La Muda (Pease, 1966, p. 109–110; Cox, Larsen, and Tripp, 1973) is closely related to intrusive porphyries of probable Eocene age.

MIDDLE AND UPPER TERTIARY ROCKS

The north and south coastal plains of Puerto Rico are underlain mainly by carbonate rocks of Oligocene to Pliocene age. These rocks are greatly disrupted by normal faults along the south coast but show mainly a gentle northerly dip on the north coast where they are only very locally faulted. In the Utuado area, the basal unit is the San Sebastian Formation of middle Oligocene age. It consists of boulder conglomerate passing upward into clay, siltstone, sandstone, and local lignite beds. Erosional outliers of conglomerate are found within 1 km of the Tanama deposit. The southwest contact of the Utuado batholith and the belt of Eocene stocks and copper deposits disappear to the northeast beneath middle and upper Tertiary strata.

VIRGIN ISLANDS BATHOLITH

Hornblende and biotite from a granodiorite sample of the Virgin Islands batholith from southern Virgin Gorda, British Virgin Islands (BVI), yielded Oligocene ages of 34.2 and 36.3 m.y., respectively (sample V–G–1, table 1, fig. 3). This pluton had previously been thought to be Eocene because the youngest volcanic unit (Necker Formation) in the BVI was thought to be Eocene from stratigraphic evidence (Helsley, 1960, p. 116). An Oligocene age for the batholith may be interpreted in several ways: (1) the Necker Formation may be in part Oligocene in age; (2) the Virgin Island batholith is a composite batholith which has a considerable age range for its different phases—ranging from Eocene to Oligocene (our age determination was made on a late phase); and (3) the age determined is a cooling age representing a time of uplift rather than the time of emplacement. More ages are needed to resolve this problem but both explanation 1 and 2 seem viable.

Plutons of late Eocene or early Oligocene age intrude lower Tertiary rocks in St. Martin (Solomiac, 1974, p. 101). This suggests that the eastern Virgin Islands are more similar in igneous activity to the Limestone Carribees than to Puerto Rico.

Rocks of the Virgin Islands batholith are cut by quartz-chalcopyrite-molybdenite veins at Copper Mine Point, Virgin Gorda (Martin-Kaye, 1959, p. 106–110). Plutons of Oligocene age in St. Martin are hydrothermally altered and are being examined as potential porphyry copper deposits (Solomiac, 1974, p. 100).

SUMMARY AND CONCLUSIONS

Amphibolite in the Sierra Bermeja records a regional metamorphism by the end of earliest Cretaceous time. The amphibolite underlies cherts reported to contain Jurassic fossils. This suggests that the amphibolite is older than indicated by K-Ar measurements. Further, the amphibolitic rocks of the Sierra Bermeja are intruded by or tectonically mixed with serpentine of uncertain age and overlain by volcanic and sedimentary rocks as old as Cenomanian or perhaps Albian. The tectonic significance of the metamorphism as well as the geometry of plate motions in this early period are unknown.

The presence of these old rocks on the south side of the main batholiths in Puerto Rico suggests that the trench which marked the zone of subduction during the Late Cretaceous was south of the island. Supporting this suggestion is the fact that the Lesser Antilles and several other island arcs have a belt of older rocks between the magmatic arc and the trench. The Cretaceous trench may have coincided with the modern Muertos Trough which shows evidence of underthrusting of the Caribbean Plate (Garrison, Cooper, and others, 1972). The modern Puerto Rico trench may not have come into existence until much later, during the late Tertiary (Monroe, 1968).

The possibility that the Puerto Rico trench was the site of subduction of the Americas Plate from the north seems to be ruled out by Perfit's determination of a Cretaceous age for thermally metamorphosed rocks on the south wall of the trench. Perfit (written commun., 1975) reported ages of 66 m.y. for muscovite and 63 m.y. for whole rock from dredge samples. These rocks were described by Perfit and others (1974) as mica schists, marbles, and tremolite-actinolite schists containing garnet. This suite of rocks is not likely to have been formed in the low heat flow environment that should have existed near the trench if the trench had marked the site of the downgoing slab of Americas Plate during Cretaceous time.

Volcanism, beginning at some time before the Albian and lasting until the late Eocene, some 60 to 85 m.y. duration, produced a pile of volcanic and sedimentary rocks 10 000 to 15 000 m thick. This volcanism is believed to be related to underthrusting of oceanic crust which resulted from a northeastward movement of the Caribbean Plate. This movement appears not to have been continuous, however, but to have been interspersed with northwest-striking left-lateral strike-slip displacement of large magnitude affecting rocks as old as Cenomanian (Glover, 1971, p. 90) and as young as Eocene (McIntyre, 1975).

Plutonic activity in the volcanic pile began in Aptian time and reached a culmination in the Maestrichtian, with the intrusion of large batholiths. Regional thermal metamorphism that produced the rocks described by Perfit may have taken place at deeper levels in the crust at this time. No metamorphic rocks of this type or age are exposed on the island, but the large batholiths may have been generated in and ascended from this broad thermal metamorphic zone. The metamorphic rocks were exposed by large tectonic movements in the trench during Tertiary time.

Following this main pulse, uplift and erosion of part of the region occurred and continued for most of the Paleocene Epoch in west-central Puerto Rico. In the middle Eocene, volcanism was renewed along what may have been a fault-controlled trough at least 100 km long and 10 km wide. Sporadic transcurrent faulting continued to the end of this phase of volcanism. This volcanism lasted no more than 10 m.y. and only about 5000 m of lava and tuff were deposited.

The lavas of this sequence tend to be dacitic to basaltic in contrast to the andesites and basalts of the Upper Cretaceous.

Near the end of this volcanic episode, in late Eocene time, small stocks of quartz diorite were emplaced along the Eocene trough and elsewhere in east-central and northeast Puerto Rico, while major transcurrent faulting between the tectonic blocks was taking place. Copper mineralization and hydrothermal alteration accompanied the earlier phases of this intrusive event. Plutonic activity of large magnitude continued until late Oligocene time with the formation of the Virgin Islands batholith and smaller plutons in the Limestone Caribees.

In Puerto Rico, uplift and erosion began in the Oligocene followed by submergence and clastic and carbonate deposition during the middle and late Tertiary. Monroe (1968) has related the Oligocene uplift to the first appearance of the Puerto Rico trench. Malfait and Dinkleman (1972) propose that the major transform fault passing through the Cayman trough broke through to the present Puerto Rican trench. The Caribbean Plate changed its motion from northeastward to eastward, and subduction in the Greater Antilles ceased.

It may be significant that all known economic concentrations of copper were formed in the late Eocene during the last stage of igneous activity and just prior to the end of subduction activity. A similar relation may exist in Panama where three porphyry copper deposits (Río Pito, Petaquilla, and Cerro Colorado) are arranged with progressively younger ages toward the end of the middle Americas trench (Clark, oral commun., 1975). Van Andel and others (1971) describe the progressive closing of this trench from southeast to northwest. Copper mineralization may have coincided with the end of subduction activity at various stages in this trench-closing process. When the chronology of igneous, hydrothermal, and tectonic processes in island arcs is better understood, this type of transitional tectonic environment may prove to have general significance in the formation of ore deposits.

REFERENCES CITED

Barabas, A. H., 1971, K-Ar dating of igneous events and porphyry copper mineralization in west central Puerto Rico [abs.]: Econ. Geology, v. 66, no. 6, p. 977.

Bergey, W. R., 1966, Geochemical prospecting for copper in Puerto Rico: Third Annual Caribbean Geol. Conf., Jamaica Geol. Survey Pub. 95, p. 113–119.

Berryhill, H. L., Jr., 1965, Geology of the Ciales quadrangle, Puerto Rico: U.S. Geol. Survey Bull. 1184, 116 p.

Berryhill, H. L., Jr., and Glover, Lynn, III, 1960, Geology of the Cayey quadrangle, Puerto Rico: U.S. Geol. Survey Misc. Geol. Inv. Map I–319.

Bowin, C. O., 1975, Geology of Hispaniola, *in* Nairn, A. E. M., and Stelli, F. G., Ocean Basins and Margins, v. 3, Gulf of Mexico and Caribbean: New York, Plenum Press, p. 501–552.

Briggs, R. P., and Akers, J. P., 1965, Hydrogeologic map of Puerto Rico and adjacent islands: U.S. Geol. Survey Hydrologic Inv. Atlas HA–197.

Chen, Ju-Chin, 1969, Petrological and chemical studies of Utuado Pluton, Puerto Rico: Acta Geol. Taiwanica, no. 13, p. 21–41.

Cox, D. P., and Briggs, R. P., 1973, Metallogenic map of Puerto Rico: U.S. Geol. Survey Misc. Geol. Inv. Map I–721.

Cox, D. P., Larsen, R. R., and Tripp, R. B., 1973, Hydrothermal alteration in Puerto Rican porphyry copper deposits: Econ. Geol., v. 68, no. 8, p. 1329–1334.

Dalrymple, G. B., and Lanphere, M. A., 1969, Potassium-argon dating—principles, techniques, and applications to geochronology: San Francisco, Calif., W. H. Freeman & Co., 258 p.

Domenech, M. V., 1899, Porto Rico, her mineral resources—their value and extent and the reasons why they are not more developed: Mines and Minerals, v. 19, p. 529–532.

Donnelly, T. W., 1966, Geology of St. Thomas and St. John, U.S. Virgin Islands: Geol. Soc. America Mem. 98, p. 85–176.

Garrison, L. E., Cooper, A. K., Hijmans, Martin, Marlow, M. S., Patrick, R. A., Trumbull, J. V. A. Martin, R. G., Himmel, R. L., Hill, Trevor, 1972, USGS–IDOE leg 3: Geotimes, v. 17, no. 3, p. 14–15.

Garrison, L. E., Martin, R. G., Jr., and Berryhill, H. L., Jr., 1972, Preliminary tectonic map of the eastern Greater Antilles region: U.S. Geol. Survey Misc. Geol. Inv. Map I–732.

Glover, Lynn, III, 1971, Geology of the Coamo area, Puerto Rico, and its relation to the volcanic arc-trench association: U.S. Geol Survey Prof. Paper 636, 102 p.

Helsley, C. E., 1960, Geology of the British Virgin Islands: Princeton Univ., Ph. D. thesis.

Hildebrand, F. A., 1961, Hydrothermally altered rocks in eastern Puerto Rico: U.S. Geol. Survey Prof. Paper 424 B, p. B219–B221.

Malfait, B. T., and Dinkelman, M. G., 1972, Circum-Caribbean tectonic and igneous activity and the evolution of the Caribbean plate: Geol. Soc. America Bull., v. 83, no. 2, p. 251–271.

Martin-Kaye, P. H. A., 1959, Reports on the geology of the Leeward and British Virgin Islands: Voice Publishing Co., St. Lucia, p. 95–117.

Mattson, P. H., 1960, Geology of the Mayaguez area, Puerto Rico: Geol. Soc. America Bull., v. 71, p. 319–362.

——— 1964, Petrography and structure of serpentinite from Mayaguez, Puerto Rico, *in* Burk, C. A., ed., A study of serpentinite: Nat. Acad. Sci.—Natl. Research Council, Pub. 1188, p. 7–24.

——— 1967, Cretaceous and lower Tertiary stratigraphy in west-central Puerto Rico: U.S. Geol. Survey Bull. 1254–B, p. B1–B35.

——— 1968a, Geologic map of the Adjuntas quadrangle, Puerto Rico: U.S. Geol. Survey Misc. Geol. Inv. Map I–519.

——— 1968b, Geologic map of the Jayuya quadrangle, Puerto Rico: U.S. Geol. Survey Misc. Geol. Inv. Map I–520.

——— 1973, Middle Cretaceous nappe structures in Puerto Rican ophiolites and their relation to the tectonic history of the Greater Antilles: Geol. Soc. America Bull., v. 84, no. 1, p. 21–37.

Mattson, P. H., and Pessagno, E. A., Jr., 1974, Tectonic significance of Late Jurassic-Early Cretaceous radiolarian chert from Puerto Rican ophiolite [abs.]: Geol. Soc. America Abs. with Programs, v. 6, no. 7, p. 859.

McIntyre, D. H., 1975, Geologic map of the Maricao quadrangle, western Puerto Rico: U.S. Geol. Survey Misc. Geol. Inv. Map I–918.

McIntyre, D. H., Aaron, J. M., and Tobisch, O. T., 1970, Cretaceous and lower Tertiary stratigraphy in northwestern Puerto Rico: U.S. Geol. Survey Bull. 1294–D, 16 p.

Monroe, W. H., 1968, The age of the Puerto Rico trench: Geol. Soc. America Bull., v. 79, no. 4, p. 487–493.

Nelson, A. E., 1967, Geologic map of the Utuado quadrangle, Puerto Rico: U.S. Geol. Survey Misc. Geol. Inv. Map I–480.

Nelson, A. E., Monroe, W. H., 1966, Geology of the Florida quadrangle, Puerto Rico: U.S. Geol. Survey Bull. 1221–C, p. C1–C22.

Nelson, A. E., and Tobisch, O. T., 1968, Geologic map of the Bayaney quadrangle, Puerto Rico: U.S. Geol. Survey Misc. Geol. Inv. Map I–525.

Pease, M. H., Jr., 1960, Structural control of hydrothermal alteration in some volcanic rocks in Puerto Rico: U.S. Geol. Survey Prof. Paper 400–B, p. B360–B363.

——— 1966, Some characteristics of copper mineralization in Puerto Rico, *in* Caribbean Geol. Conf. 3d, Kingston, Jamaica, 1962, Trans. Jamaica Geol. Survey Pub. 95, p. 107–112.

——— 1968a, Cretaceous and lower Tertiary stratigraphy of the Naranjito and Aguas Buenas quadrangles and adjacent areas, Puerto Rico: U.S. Geol. Survey Bull. 1253, 57 p.

——— 1968b, Geologic map of the Aguas Buenas quadrangle, Puerto Rico: U.S. Geol. Survey Misc. Inv. Map I–479.

Perfit, Michael, Heezen, B. C., and Rawson, Michael, 1974, Metamorphic rocks from the Puerto Rico Trench [abs.]: Geol. Soc. America Abs. with Programs, v. 6, no. 7, p. 907.

Seiders, V. M., 1971, Geologic map of the El Yungue quadrangle, Puerto Rico: U.S. Geol. Survey Misc. Geol. Inv. Map I–658.

Slodowsky, T. R., 1956, Geology of the Yauco area, Puerto Rico: Princeton Univ., Ph. D. thesis, 130 p.

Solomiac, H., 1974, La geologie et la metalogenie de L'Ile de Saint-Martin (zone Francais) *in* Guidebook to Excursions in the French Antilles: Caribbean Geol. Conf., 7th, Pointe a Pitre FWI, p. 95–108.

Tobisch, O. T., 1968, Gneissic amphibolite at Las Palmas, Puerto Rico, and its significance in the early history of the Greater Antilles island arc: Geol. Soc. America Bull., v. 79, no. 5, p. 557–574.

Weaver, J. D., 1958, The Utuado Pluton, Puerto Rico: Geol. Soc. America Bull., v. 69, no. 9, p. 1125–1141.

Van Andel, T. H., Heath, G. R., Malfait, B. T., Heinrichs, D. F., and Ewing, J. T., 1971, Tectonics of the Panama Basin, eastern equatorial Pacific: Geol. Soc. America Bull., v. 28, p. 1489–1508.

Van Eysinga, F. W. B., compiler, 1975, Geological time table [3d ed.]: Amsterdam, ElSevier Publishing Co., 1 sheet.

Jour. Research U.S. Geol. Survey
Vol. 5, No. 6, Nov.–Dec. 1977, p. 705–717

MIDDLE TERTIARY PLUTONISM IN THE SANTA CATALINA AND TORTOLITA MOUNTAINS, ARIZONA

By S. C. CREASEY, NORMAN G. BANKS, R. P. ASHLEY,
and TED G. THEODORE, Menlo Park, Calif.

Abstract.—Recent reconnaissance geologic mapping in the Santa Catalina and Tortolita Mountains of southeastern Arizona, supplemented by new and published potassium-argon and fission-track ages, suggests that a large composite batholith of middle Tertiary (about 25 million years) age crops out extensively in both mountains. More than two-thirds of the batholith and contiguous wallrocks is gneissic, the gneissosity comprising strong cataclasis and mylonitization, penetrative planar and linear structures, and crystallization of muscovite and biotite in the foliation planes. New radiometric ages indicate that the deformation followed the crystallization of the batholith so closely that the K-Ar dating method cannot distinguish a difference, whereas previously published ages from the gneisses indicate a short time between the two events.

The authors recently mapped the geology of the Santa Catalina Mountains and a small part of the Tortolita Mountains in reconnaissance (Creasey and Theodore, 1975; Banks, 1976) and made 26 new radiometric age determinations to help interpret the plutonic and structural history of the region. A synopsis of the geology of the Santa Catalina Mountains, which includes some heretofore unpublished geology of the northern flank of the mountains, is shown on figure 1.

The Santa Catalina Mountains were mapped twice by the U.S. Geological Survey previous to our work. The first map was made by C. F. Tolman, Jr., at a scale of 1:125,000 in 1911–12. He also prepared a report in 1914, but neither was published. In 1930, B. N. Moore of the U.S. Geological Survey was assigned to update the report for publication. In 1938, he submitted a report, but before it was approved for publication, he left the Geological Survey, and this work, too, was never published. However, a summary of Moore's report, prepared by B. S. Butler and R. M. Hernon, and a black-and-white version of the map were released in open file (Moore and others, 1949). In addition, many maps from theses by students at the University of Arizona cover separate parts of the Santa Catalina Mountains. Except for a middle Tertiary rather than a Late Cretaceous or early Tertiary age for emplacement of the batholith and development of the gneiss, our interpretations do not differ substantially from those of B. N. Moore. Damon and Bikerman (1964) and Damon (1968) also recognized middle Tertiary magmatism in the Santa Catalina, Rincon, and Tortolita Mountains.

New K-Ar and fission-track ages are listed in table 1, and to permit comparison, previously published K-Ar and Rb-Sr ages of rocks in the Santa Catalina Mountains are listed in tables 2 and 3. These data are summarized by the bar graphs of figures 3 and 4. Chemical and spectrographic analyses, modes, and norms of our dated rocks and two additional undated samples are listed at the end of the report (table 4). The locations of all samples, except for dated samples reported in the literature without location information, are indicated on figure 2. The analytical data supporting the radiometric ages are given in tables 5 and 6.

GENERAL GEOLOGY

The Santa Catalina Mountains are one of the structurally and lithologically complex ranges of the Basin and Range province in southeastern Arizona (fig. 1). At the northern end of the Santa Catalina, the Mogul fault is the dominant structure. North of the Mogul fault, only the Oracle Granite of Peterson (1938), locally cut by dikes and quartz veins, crops out, whereas south of the fault and along the northeastern flank, the range consists of Precambrian, Paleozoic, and Mesozoic sedimentary rocks, all intruded by quartz diorite, quartz monzonite, and granodiorite porphyry.

The central core of the Santa Catalina Mountains consists of a large composite batholith of middle Tertiary age. Apparently the batholith extends to the northwest into the Tortolita Mountains, where it has been partly mapped in reconnaissance by the authors, and to the southeast into the Rincon Mountains (fig. 2, inset). The batholith comprises at least two intru-

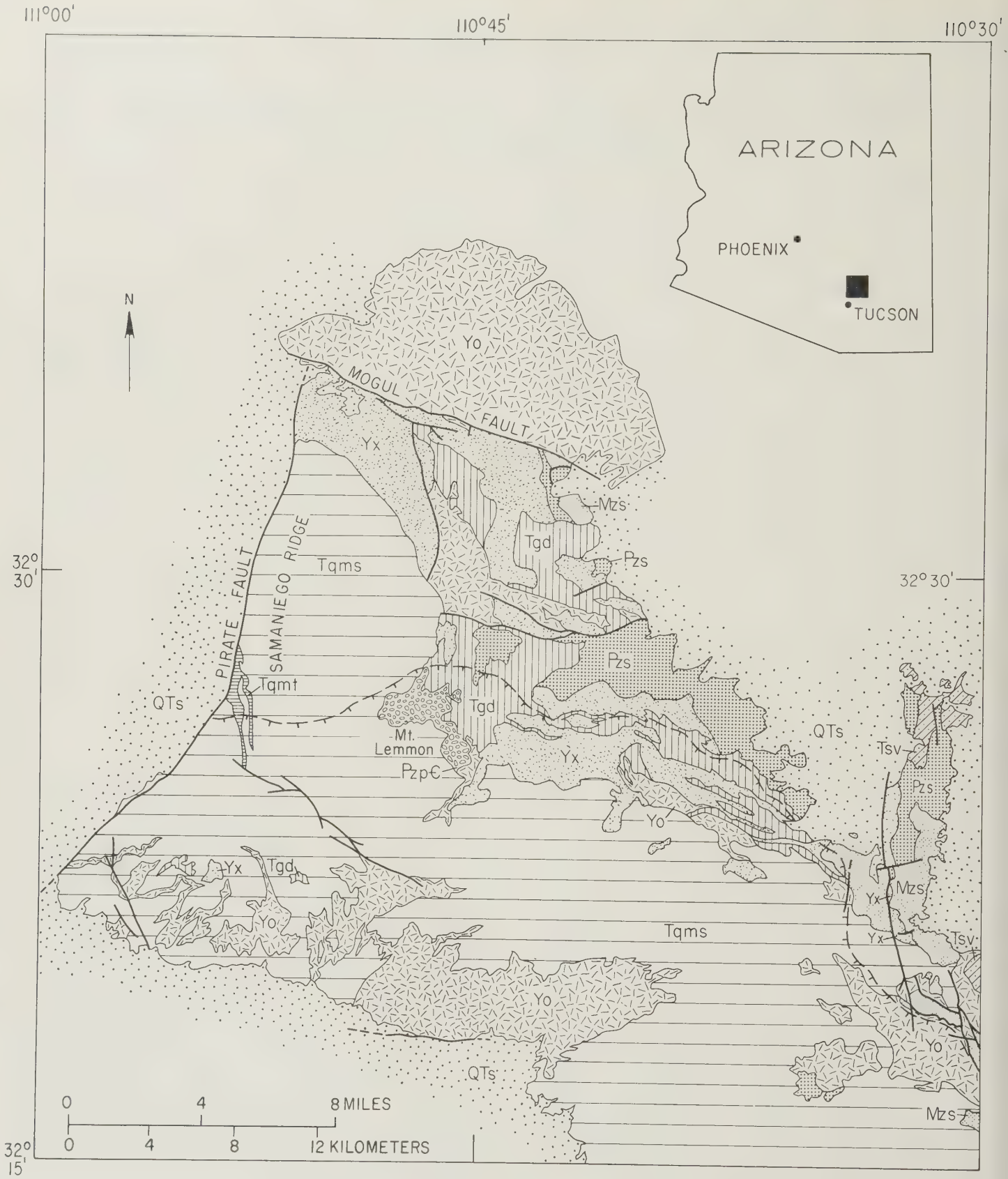

FIGURE 1.—Geologic sketch map of the Santa Catalina Mountains.

Quaternary and Tertiary sedimentary rocks: sand, gravel, conglomerate, sandstone, and lake deposits

Tertiary sedimentary and volcanic rocks: redbeds, shale, sandstone, conglomerate, minor volcanic rocks near east edge of map

Tertiary quartz monzonite of the Tortolita Mountains: fine- to medium-grained equigranular dikes. Probably correlative with similar rocks in the Tortolita Mountains

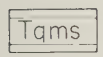

Tertiary quartz monzonite of Samaniego Ridge and gneissic quartz monzonite of Samaniego Ridge; includes porphyritic and equigranular phases and large areas with abundant xenoliths of the Precambrian Y Oracle Granite of Peterson (1938)

Tertiary quartz diorite (Leatherwood Quartz Diorite of DuBois, 1959), granodiorite, and granodiorite porphyry; gneissic in southern half of map area

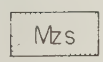

Mesozoic sedimentary rocks: limestone, sandstone, shale, and conglomerate

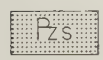

Paleozoic sedimentary and metasedimentary rocks: includes (descending) Naco Limestone, Escabrosa Limestone, Martin Formation, Abrigo Formation, Bolsa Quartzite

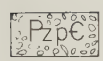

Mixed Paleozoic rocks and Precambrian Y Apache Group near Mt. Lemmon

Apache Group (Precambrian Y) and Pinal Schist (Precambrian X)

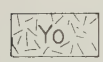

Oracle Granite of Peterson (1938) (Precambrian Y); gneissic in southern half of map area

Fault, dashed where approximately located

Contact

Approximate location of gradational contact between foliated and nonfoliated rocks. Foliated rocks on the side with the barbs

sive phases hereafter referred to as the quartz monzonite of Samaniego Ridge and the quartz monzonite of the Tortolita Mountains (table 4). Except for two dikes of the quartz monzonite of the Tortolita Mountains, just east of the Pirate fault, only the quartz monzonite of Samaniego Ridge crops out in the Santa Catalina Mountains. The main mass of the quartz monzonite of the Tortolita Mountains lies to the west of the area in figure 1.

The southwestern flank of the Santa Catalina consists of a mixture of quartz monzonite of Samaniego Ridge and roof pendants principally of Oracle Granite. Roof pendants and xenoliths of the metamorphosed Pinal Schist, Apache Group, Paleozoic and Mesozoic sedimentary rocks, and quartz diorite (Leatherwood Quartz Diorite of Du Bois, 1959) occur locally throughout the outcrop area of the quartz monzonite; they are particularly common near Mount Lemmon, which is the highest peak in the Santa Catalina Mountains. In general, the quartz monzonite in the central part of the mountains intruded along the contact between the Oracle Granite and the overlying Apache Group, but local crosscutting relations are common.

Emplacement of the batholith was nearly coeval with the development of extensive penetrative planar and linear structures that characterize the gneisses forming the southwestern forerange of the Santa Catalina Mountains and extending both northwestward into the Tortolita Mountains and southeastward into the Rincon Mountains. The contact between gneissic and nongneissic parts of the batholith is gradational. The approximate location of the contact is shown on figure 1.

The fabric of the batholith east of the Pirate fault and north of the gneissic front near Cargadero Canyon is typically igneous. The rock is massive except for joints and sparse aplite dikes. Textures are porphyritic with a medium-grained hypidiomorphic groundmass, and locally, near the northeastern margin of the batholith, equigranular hypidiomorphic granular. In this part of the batholith, penetrative deformation and rock alteration are absent, suggesting no subsolidus reheating. These features indicate that the quartz monzonite has undergone no significant changes since crystallization. Because the minerals dated have not changed since crystallization, our radiometric ages from this area (table 1, fig. 2) are interpreted to be the age of crystallization and to reflect the cooling history of the batholith.

In contrast, the rocks forming the gneissic parts of the batholith show strong cataclasis and mylonitization, and, in the foliation planes, secondary muscovite and some secondary biotite abound; primary biotite may also have been rotated into the movement planes, and garnet is a common rock-forming mineral. The rock is metamorphic, the deformation is penetrative,

TABLE 1.—*New fission-track and* K-Ar *ages of the quartz monzonite of Samaniego Ridge and the quartz monzonite of the Tortolita Mountains, from the Santa Catalina and Tortolita Mountains*

[Analysts: S. C. Creasey, K-Ar; R. A. Ashley, fission track]

Loc., fig. 2	Sample	Mineral dated	Method	Apparent age	Rock type	Location	Comments
II	GGN-S1	Biotite	K-Ar	22.7±0.7	Quartz monzonite of Samaniego Ridge	32°22' N. 110°43' W.	Gneissic
		Muscovite	K-Ar	24.1±0.7			
		Apatite	F.T.	18.7±2.7			
IV	ML-61	Biotite	K-Ar	24.0±0.7	Quartz monzonite of Samaniego Ridge	32°27.5' N. 110°52' W.	Massive, porphyritic with medium-grained hypidiomorphic granular groundmass
		Hornblende	K-Ar	22.3±0.7			
		Apatite	F.T.	20.2±2.1			
		Zircon	F.T.	26.3±3.4			
		Sphene	F.T.	27.5±3.1			
IV	ML-60	Biotite	K-Ar	23.5±0.7	Mafic inclusion	32°27.5' N. 110°53' W.	Original rock formation is uncertain
		Hornblende	K-Ar	36.1±1.0			
		Apatite	F.T.	20.7±2.5			
		Sphene	F.T.	27.9±3.7			
VII	BR-21	Biotite	K-Ar	23.1±0.7	Quartz monzonite of Samaniego Ridge	31°31.5' N. 110°50' W.	Massive, porphyritic with medium-grained hypidiomorphic granular groundmass
		Hornblende	K-Ar	23.4±1.2			
		Apatite	F.T.	22.8±2.8			
		Zircon	F.T.	28.1±3.3			
		Sphene	F.T.	29.1±3.0			
VIII	BR-16	Biotite	K-Ar	23.2±0.7	Quartz monzonite of Samaniego Ridge	32°31.5' N. 110°48' W.	Massive, medium-grained hypidiomorphic granular
		Apatite	F.T.	19.8±2.1			
		Zircon	F.T.	25.1±2.5			
		Sphene	F.T.	27.2±3.1			
---	RC3-1	Biotite	K-Ar	20.6±0.6	Quartz monzonite of Samaniego Ridge	32°29.5' N. 111°04' W.	Ages probably reset by gneissic dikes of quartz monzonite of Tortolita Mountains Location not on figure 2. Sample from Tortolita Mountains
		Hornblende	K-Ar	21.1±0.6			
---	RC-25	Biotite	K-Ar	22.1±0.7	Quartz monzonite of Tortolita Mountains	32°28' N. 111°02' W.	Sample from Tortolita Mountains Location not on figure 2
		Apatite	F.T.	18.0±2.4			
VI	ML-105	Apatite	F.T.	16.5±2.1	Quartz monzonite of Tortolita Mountains	32°27.5" N. 110°58' W.	Massive, slight foliation, fine-grained hypidiomorphic granular

and the rock types are gneisses and schists.

The distribution of the gneissic and nongneissic parts of the batholith is locally erratic. Although most of the batholith shown on figure 1 is gneissic, patches of relatively massive quartz monzonite occur within the gneissic area, particularly in the southeastern area of the figure. Some of the deformation extends as much as 3 km beyond the northern limits of the batholith. The sedimentary rocks adjacent to the batholith along the northern flank of the mountains have been so intensely sheared and recrystallized that the original formations generally cannot be distinguished from one another. Here, too, the contact between sheared and unsheared sedimentary rocks is gradational. In the nongneissic terrane, comparatively few aplite and pegmatite dikes occur. In the gneissic terrane, however, both the intrusive and country rocks contain locally abundant pegmatite dikes, some of which are foliated, but others are massive.

RADIOMETRIC AGES

The K-Ar and fission-track ages (tables 1 and 2) of unaltered and undeformed minerals from the quartz monzonite of Samaniego Ridge indicate an apparent

FIGURE 2.—Locations of samples listed in tables 1 through 3. Stipple pattern indicates the outcrop area of the quartz monzonite of Samaniego Ridge. Heavy solid lines indicate faults, which are dashed where approximately located.

TABLE 2.—*Previously published* K-Ar *ages of the quartz monzonite of Samaniego Ridge, Oracle Granite, and gneissic rocks, Santa Catalina and Tortolita Mountains*

Locality, fig. 2	Sample	Mineral dated	Apparent age (m.y.)	Rock type	Location	Reference
III	PED-16-59	Biotite	25.0±3	Quartz monzonite of Samaniego Ridge	Approximately 32°26.5' N. 110°52.2' W.	Damon and others (1963)
III	PED-17-59	Biotite	24.0±3	Quartz monzonite of Tortolita Mountains[1]	Approximately 32°26.5' N. 110°52.2' W.	Damon and others (1963)
II	PED-4A-58	Biotite	24.8±1.0	Gneissic rock	32°22.1' N. 110°43' W.	Damon and others (1963) Mauger and others (1968)
II	PED-4A-58	Muscovite	29.5±0.9	Gneissic rock	32°22.1' N. 110°43' W.	Mauger and others (1968) Damon and others (1963)
II		Muscovite	32 ±3	Gneissic rock	32°22.1' N. 110°43' W.	Catanzaro and Kulp (1964)
I	PED-18-62L	Muscovite	25.4±1	Gneissic rock	32°20.3' N. 110°41.4' W.	Livingston and others (1967) Mauger and others (1968)
I	PED-18-62L	Biotite	25.1±1.0	Gneissic rock	32°20.3' N. 110°41.4' W.	Livingston and others (1967) Mauger and others (1968)
I	PED-18-62L	Orthoclase	26.8±0.8	Gneissic rock	32°20.3' N. 110°41.4' W.	Livingston and others (1967) Mauger and others (1968)
I	PED-18-62L	Plagioclase	[2]29.3±1.0	Gneissic rock	32°20.3' N. 110°41.4' W.	Livingston and others (1967) Mauger and others (1968)
I	PED-18-62D	Biotite	27.5±0.9	Gneissic rock	32°20.3' N. 110°41.4' W.	Mauger and others (1968)
Uncertain	PED-4-58	Muscovite	25.9±1.1	Gneissic rock	Sabino Canyon	Damon and others (1963) Mauger and others (1968)
I	PED-56-66	Muscovite	31.2±0.9	Gneissic rock	32°20.6' N. 110°55.4' W.	Mauger and others (1968)
Uncertain	RM-1-66	Muscovite	31.2±0.9		Unknown	Mauger and others (1968)
IX	PED-27-57	Biotite	38.5±3	Quartz monzonite of Samaniego Ridge	South of Mogul fault	Damon and others (1963)
Uncertain		Whole rock	20.5±3	Trachyte dike	Ventana Canyon	Shakel (1974)
XII	PED-1-58	Biotite	49.2±3	Oracle Granite	Approximately 32°35' N. 110°50' W.	Damon and others (1963)
XIII	PED-3-58	Pegmatite Muscovite	1420 ±40	Oracle Granite	Near Oracle, Arizona	Damon and others (1963)
XI	PED-2-58	Biotite	1420 ±40	Oracle Granite	Approximately 32°33' N. 110°43' W.	Damon and others (1963)
	PED-20-62	Biotite	27.3±0.9	Gneissic rock	32°28.8' N. 111°05' W.	Mauger and others (1968)

[1]Described as a fine-grained granite. Probably the quartz monzonite of the Tortolita Mountains but could be a younger aplite.

[2]Livingston and others (1967) and Mauger, Damon, and Livingston (1968) believe that this figure does not indicate the age of the rock.

middle Tertiary age of crystallization of the batholith; they also give some information on the cooling history. The age of deformation is more ambiguous. It is based on one biotite-muscovite mineral pair derived from deformed quartz monzonite; their ages suggest that deformation followed crystallization of the quartz monzonite so closely that no age difference is discernible between gneissic and nongneissic phases (table 1). However, the published K-Ar ages, which were obtained from 10 samples of either biotite or muscovite from three localities in foliated rock (table 2), are discernibly older than the age of crystallization; this age difference is discussed later.

The K-Ar isotopic ages from biotite and hornblende, samples ML–61 and BR–21, and from biotite, samples ML–60 and BR–16, are concordant; the range, including the ranges of analytical uncertainty for all the individual ages, is from 21.6 to 24.7 million years, the mean is 23.3 m.y., and the middle point of the range is 23.2 m.y. Biotite from sample PED–16–59 (table 2) is nearly the same (25.0±3 m.y.), considering the larger stated analytical error.

Concordant ages of two biotite-hornblende mineral pairs and the concordance between the two pairs, which are from different localities (samples ML–61 and BR–21), provide strong evidence for the age of crystallization. Biotite and hornblende have different argon retention properties, and it is highly unlikely that their ages would agree if the rock had been reheated subsequent to crystallization, unless the heating was so severe that all radiogenic argon was dispelled from both minerals. Such reheating, however, would leave other manifestations of alteration, which are not present.

Hornblende from sample ML–60 (table 1), a mafic inclusion in the quartz monzonite of Samaniego Ridge, has a K-Ar age of 36.1±1 m.y. Biotite from the same sample has a K-Ar age of 23.5±0.7 m.y. Because the biotite age agrees with several other K-Ar ages, including mineral pairs, we suggest that it has been completely equilibrated to the age of the quartz monzonite host. We do not know whether the older age of the hornblende is due to excess argon from a local, abnormally high partial pressure of argon in the quartz monzonite or whether it is due to partial retention of the radiogenic argon that was generated in the rock before intrusion of the batholith and before the thermal metamorphism of the inclusion by the quartz monzonite magma.

The quartz monzonite of the Tortolita Mountains is the equigranular younger phase of the composite batholith. It intrudes the porphyritic quartz monzonite of Samaniego Ridge in the Tortolita Mountains, and crosscutting relationships of possibly equivalent dikes also occur in Cargadero Canyon in the Santa Catalina Mountains. Two K-Ar biotite ages of the quartz monzonite of the Tortolita Mountains, as given by sample RC–25 (table 1) and perhaps by sample PED–17–59 (table 2), are 22.1±0.7 and 24.0±3 m.y., respectively. The ranges in age of the two samples overlap in part, and, until more ages are determined, our best estimate of the age of the quartz monzonite is between 21 and 25 m.y. Rock sample RC3–1, which is gneissic porphyritic quartz monzonite of Samaniego Ridge, was collected within 1 m of dikes of the equigranular younger phase of the batholith (quartz monzonite of the Tortolita Mountains). A biotite-hornblende mineral pair (sample RC3–1, table 1) from this rock sample gives K-Ar ages of 20.6±0.6 and 21.1±0.6 m.y., respectively. We believe (1) that these ages were reset by the heat of the dikes and, therefore, reflect the age of the quartz monzonite of the Tortolita Mountains and (2) that the quartz monzonite of the Tortolita Mountains, although a part of the composite batholith, is perceptibly younger than the quartz monzonite of Samaniego Ridge, as demonstrated by K-Ar dates. The fission-track ages on apatite (samples RC–25 and ML–105, table 1), which are discussed later, support this contention.

The new K-Ar ages of metamorphic biotite and muscovite (sample GGN–S1, table 1) from the gneissic quartz monzonite of Samaniego Ridge are 22.7±0.7 and 24.1±0.7 m.y., respectively. Their average age (23.4 m.y.) and range (22.0–24.8 m.y.) are nearly the same as the average age and range for igneous biotite and hornblende from the massive quartz monzonite. These ages, however, differ from the previously published ages of metamorphic biotites and muscovites, which range from 23.8 to 35 m.y., including analytical error ranges for lowest and highest ages; their average age is 27.6 m.y. (gneissic rocks of table 2). We have no adequate explanation for the difference between our ages and the previously published ages. A possible explanation might be related to the proximity of some of the earlier sampled gneisses to outcrops of Oracle Granite (loc. I, fig. 2). This, however, could not explain the age differences of the samples collected at locality II. Within the previously published ages of micas from gneissic rocks, the average age of the four biotites is 26.1 m.y. and of the five muscovites is 28.8 m.y. We also have no data to explain this difference, but Mauger, Damon, and Livingston (1968, p. 586) believe that the older age of the muscovite is due to excess inherited argon trapped in large grains. Among the dated muscovite samples, the coarser the grain size, the older the apparent age.

The fission-track ages (table 1) are internally consistent and suggest that the batholith cooled slowly over a relatively long period of time. From annealing studies (Fleischer and others, 1965; Naeser and Faul, 1969; Calk and Naeser, 1973; Naeser, 1976), which indicate the temperatures at which the minerals begin to accumulate tracks, apatite should indicate the youngest age and zircon and sphene, progressively older ones. For the massive quartz monzonite of Samaniego Ridge, the average age and the range, including analytical error, for apatite are 20.9 and 17.7–25.6 m.y. for zircon 26.5 and 22.6–31.4 m.y., and for sphene 27.9 and 24.1–32.1 m.y. (table 1, and fig. 2). As an approximation, the cooling history of the samples should reflect that of the batholith, and, on this basis, these ages suggest that the batholith had cooled to about 500°C approximately 28 m.y. ago and had reached about 100°C about 21 m.y. ago. This suggested cooling history is similar to that determined by Damon (1968) on the bases of argon loss, grain size, and diffusion rates of micas. By relating older ages of large muscovite grains to younger ages of smaller biotite, he estimated that cooling started at 400°C at 28 m.y. and reached 100°C at 23 m.y. The average age of 26.5 m.y. for zircons suggests that zircon began to accumulate tracks at a somewhat lower temperature than sphene. The biotite and hornblende K-Ar ages, however, indicate more rapid cooling. If there is a protracted cooling history, hornblende should begin to retain radiogenic argon before biotite. To judge the cooling history from the fission-track ages, the hornblende should yield ages slightly older than biotite. Actually the biotite and hornblende indicate the same ages, which implies that the temperature of the cooling batholith dropped through the argon retention temperatures of hornblende and biotite so rapidly that the K-Ar method cannot detect any difference between their ages. The data from the two techniques, taken together, suggest that the cooling and crystallization history is more complex than is indicated by either method alone. We have no data, on the other hand, that allow us to delineate the complexities.

The apatite fission-track age for the gneissic quartz monzonite of Samaniego Ridge is 18.7±2.7 m.y., which is slightly younger than the average for the massive phase. For the quartz monzonite of the Tortolita Mountains, the average of two apatite ages is 17.3 m.y., and the range, including analytical error, is 14.4–20.4 m.y. This average age is 3.6 m.y. younger than the 20.9 m.y. average age for apatites from the massive porphyritic Samaniego Ridge. This younger average age is supported by the three K-Ar ages for samples RC3–1 and RC–25, which average 21.3 m.y., 2 m.y. younger than the average for massive Samaniego

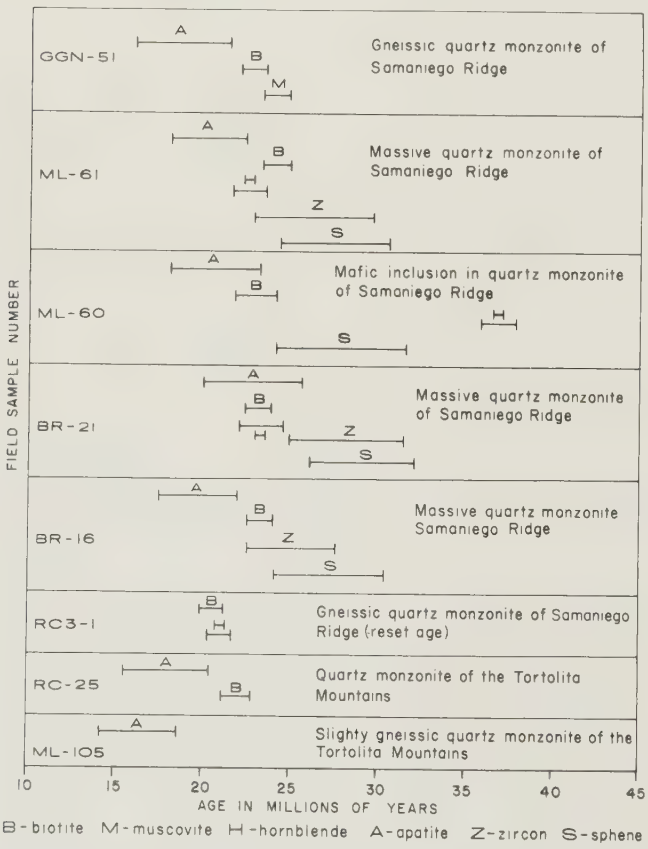
FIELD SAMPLE NUMBER
GGN-51
Gneissic quartz monzonite of Samaniego Ridge
ML-61
Massive quartz monzonite of Samaniego Ridge
ML-60
Mafic inclusion in quartz monzonite of Samaniego Ridge
BR-21
Massive quartz monzonite of Samaniego Ridge
BR-16
Massive quartz monzonite Samaniego Ridge
RC3-1
Gneissic quartz monzonite of Samaniego Ridge (reset age)
RC-25
Quartz monzonite of the Tortolita Mountains
ML-105
Slighty gneissic quartz monzonite of the Tortolita Mountains
10 15 20 25 30 35 40 45
AGE IN MILLIONS OF YEARS
B-biotite M-muscovite H-hornblende A-apatite Z-zircon S-sphene

FIGURE 3.—Bar graphs of new fission-track and K-Ar ages of the quartz monzonite of Samaniego Ridge and the quartz monzonite of the Tortolita Mountains, Santa Catalina and Tortolita Mountains.

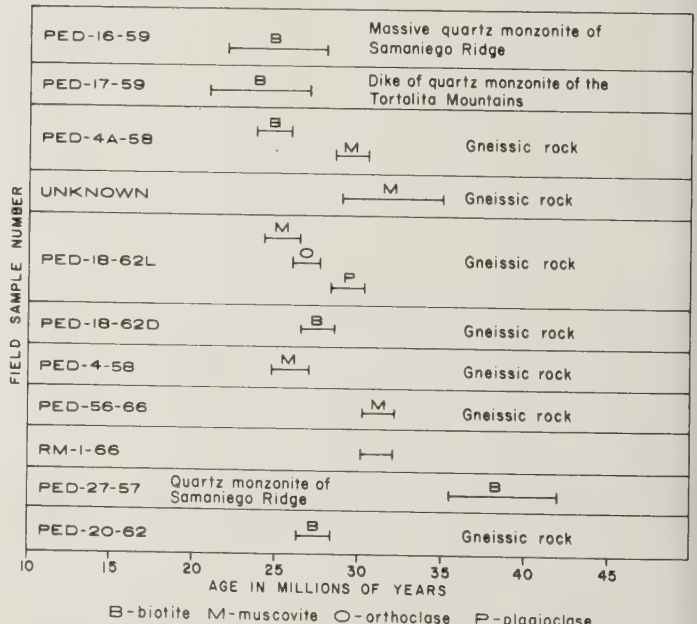

FIGURE 4.—Bar graphs of published K-Ar ages of the quartz monzonite of Samaniego Ridge and gneissic rocks, Santa Catalina and Tortolita Mountains.

TABLE 3.—*Previously published* Rb-Sr *ages of the quartz monzonite of Samaniego Ridge, Oracle Granite, and gneissic rocks, Santa Catalina Mountains*

Locality, fig. 2	Sample	Mineral dated	Apparent age m.y.	Rock type	Locality	Reference
V	---	Biotite	30. ±30	Quartz monzonite of Samaniego Ridge	500 ft from Pirate fault east of Cañada Del Oro	Giletti and Damon (1961); Damon and Giletti (1961)
II	---	Biotite muscovite mix	150. ±90	Gneissic rock	32°22.1' N. 110°43' W.	Giletti and Damon (1961); Damon and Giletti (1961)
II	PED-4A-58	Biotite	23.9±14	Gneissic rock	32°22.1' N. 110°43' W.	Livingston and others (1967)
II	PED-4A-58	Muscovite	37.6± 1.0	Gneissic rock	32°22.1' N. 110°43' W.	Livingston and others (1967)
		Whole rock	90	Quartz monzonite of Samaniego Ridge[1]	---	Shakel, Livingston, and Pushkar (1972)
X	---	Biotite	1,450	Oracle Granite	32°33.5' N. 110°44' N.	Giletti and Damon (1961); Damon and Giletti (1961)

[1]Called "Catalina granite" by Shakel, Livingston, and Pushkar (1972).

Ridge, and by field relations that show the Tortolita phase intrudes the Samaniego Ridge.

Notwithstanding the differences in ages from different dating methods and the differences of our ages from those previously published, examination of figures 3 and 4 shows that a magmatic and deformational event occurred about 25 m.y. ago. Our data suggest that the time interval between plutonism and intense deformation was too short for the K-Ar dating method to distinguish, whereas the previously published K-Ar ages suggest the deformation may have preceded plutonism by about 4 m.y. based on the average age of muscovite and biotite from gneissic rocks. In either case, plutonism and intense deformation were close together.

Additional permissive support for the short time between intrusion and deformation of the composite batholith is supplied by the lithology and age of the Mineta Formation of Chew (1962), which lies along the northeastern flank of the Rincon Mountains and contains no gneissic clasts (Clay, 1970). Chew (1952) recovered teeth and fragments of a young rhinoceros jaw from the Mineta, and J. F. Lance dated the fossils as probable late Oligocene to early Miocene. Clay (1970) also recognized an andesite which intruded the Mineta Formation; the K-Ar age of the andesite is 26.3±2.4 m.y. These data indicate that gneissic fragments from the composite batholith only occur in nearby sedimentary rocks that are younger than 24–26 m.y.; this relation supports both the previously published and our radiometric ages of deformation.

We have not determined Rb-Sr ages, but published Rb-Sr ages apparently are not internally consistent even for samples from the same locality (table 3). These data are not sufficient to be interpreted properly, and other published Rb-Sr data for the Santa Catalina Mountains are equally difficult to interpret (Shakel, 1974), suggesting that an in-depth Rb-Sr study coupled with careful geologic control of sampling might be prudent before attempting explanation of discrepancies in the existing Rb-Sr data and differences between Rb-Sr data and K-Ar and fission-track data.

EPILOG

Special mention of some of the ideas of B. N. Moore and C. F. Tolman, Jr., and their colleagues is merited because of their extensive and careful work. The short summary report (Moore and others, 1949) mentions the quartz monzonite of Samaniego Ridge (Santa Catalina granitic complex) only briefly, and it scarcely mentions the deformation responsible for the gneisses. It does indicate, however, that the pluton was of batholithic size; therefore, although this concept was available in 1949, it subsequently seems to have had little acceptance.

TABLE 4.—*Chemical, spectrographic, normative, and modal analyses of rocks from the Santa Catalina and Tortolita Mountains*

[Rapid-rock analyses: Analyst, Hezekiah Smith; analytical method as described under "single solution" by Shapiro (1975). Analysis of Cl by R. Moore and B. McCall; spectrophotometric analytical method. Quantitative spectrographic analyses: Analyst, Chris Heropoulos. The results are reported to have significant figures and have an overall accuracy near the limit of detection where only one digit is intended. N, not detected at value shown; tr, trace; ---, not present; N.d., not determined]

	Massive quartz monzonite of Samaniego Ridge			Gneissic quartz monzonite of Samaniego Ridge	Quartz monzonite of Tortolita Mountains	Gneissic Oracle Granite
Lab. No.	M124370WD	M124371WD	M124372WD	M124757WD	M124374WD	M124373WD
Field No.	BR-16	BR-21	ML-61	GGN-S1	ML-105	ML-62R
Rapid-rock analyses						
SiO_2	73.2	68.6	67.0	74.1	73.2	70.0
Al_2O_3	13.6	15.3	15.5	15.1	14.4	15.4
Fe_2O_3	.89	1.3	2.0	.33	.72	1.6
FeO	.64	1.3	1.9	.52	.52	.92
MgO	.50	.90	1.7	.08	.24	.52
CaO	1.1	2.2	3.0	1.3	1.1	1.9
Na_2O	3.6	3.8	4.2	4.3	3.5	3.4
K_2O	4.6	4.6	3.8	3.9	5.0	4.8
H_2O+	.32	.79	.72	.49	.42	.74
H_2O-	.22	.19	.08	.05	.17	.26
TiO_2	.20	.38	.62	.01	.10	.34
P_2O_3	.11	.19	.28	.04	.07	.20
MnO	.03	.05	.09	.02	.02	.04
CO_2	.02	.01	.02	.02	.02	.01
Cl	.01	.01	.005	.01	.003	.005
F	.03	.01	.06	<.01	<.01	<.01
Sum	99+	100-	101-	100+	99+	100+
Quantitative spectrographic analyses [Plate EM-1224; results given in parts per million except results for Ti are given in percent]						
Ti	0.15	0.27	0.37	0.05	0.11	0.30
Mn	370	470	800	260	250	330
Ba	330	1100	640	1500	1100	2400
Be	7	5	6	N1	2	N1
Co	N2	8	11	N2	N2	8
Cr	N2	8	12	N2	N2	N2
Cu	13	9	9	11	5	65
Ni	1.6	8	14	N1	1.5	2
Sc	N1.5	7	8	N1.5	N1.5	7
Sr	170	350	380	220	180	650
V	23	44	72	N3	16	39
Y	10	19	26	N10	10	26
Zr	48	36	110	31	82	50
Ga	18	18	21	12	16	17
Yb	1	1	2	N1	1	1

The following excerpts from B. N. Moore and others (unpub. data, 1938) clearly reveal that our concepts on the extent and origin of the batholith and on the relation of deformation to the batholith differ little from theirs. Their Late Cretaceous or early Tertiary age for the pluton was based on field relations with which we concur, and our middle Tertiary designation is based on radiometric ages obtained only recently.

[For convenience the granites in the Tortollita (sic) Mountains, Mt. Lemmon, Youtcy Ranch, and Happy Valley are described separately in this report but they are considered parts

TABLE 4.—*Chemical, spectrographic, normative, and modal analyses of rocks from the Santa Catalina and Tortolita Mountains*—Continued

	Massive quartz monzonite of Samaniego Ridge			Gneissic quartz monzonite of Samaniego Ridge	Quartz monzonite of Tortolita Mountains	Gneissic Oracle Granite
Lab. No.	M124370WD	M124371WD	M124372WD	M124757WD	M124374WD	M124373WD
Field No.	BR-16	BR-21	ML-61	GGN-S1	ML-105	ML-62R
Norms						
quartz	32.2	23.2	19.5	31.0	31.4	27.6
corundum	1.0	.6	---	1.6	1.5	1.7
orthoclase	27.5	27.3	22.3	23.0	29.8	28.4
albite	30.8	32.3	35.2	36.3	29.8	28.8
anorthite	4.7	9.7	12.1	6.0	4.9	8.1
wollastonite	---	---	.3	---	---	---
enstatite	1.3	2.3	4.2	.2	.6	1.3
ferrosilite	.2	.8	1.0	.7	.2	---
forsterite	---	---	---	---	---	---
fayalite	---	---	---	---	---	---
magnetite	1.3	1.9	2.9	.5	1.1	2.1
ilmenite	.4	.7	1.2	tr	.2	.6
apatite	.3	.5	.7	.1	.2	.5
Modes						
quartz	33.0	16.3	30.4	33.2	39.2	N.d.
K-feldspar and perthite	38.3	30.5	24.1	22.8	31.2	N.d.
plagioclase	24.4	41.0	37.7	35.8	26.4	N.d.
biotite	2.9	9.1	6.1	3.8	3.2	N.d.
hornblende	---	1.4	.3	---	---	N.d.
magnetite	.9	1.0	.5	.2	tr	N.d.
sphene	.3	.3	.6	tr	---	N.d.
apatite	.2	.4	.3	tr	---	N.d.
zircon	tr	tr	tr	tr	tr	N.d.
muscovite	---	---	---	4.2	---	N.d.
garnet	---	---	---	tr	---	N.d.
Sum	100	100	100	100	100	N.d.
An-content of plagioclase	An_{20}?	An_{20}	An_{20}	An_{20}	An_{20}	An_{20}?

of the Catalina batholith and on the map the symbol of the Catalina granite is applied to all these localities.

It may be suggested that the post-Cretaceous igneous rocks were intruded during a period of stresses which reached their peak in the intrusion of the granites of the Catalina batholith. Whether this zone can be traced east and west from this region and whether other regions of Tertiary thrusting show evidence of earlier deformation remains to be shown.

These intrusions are of great interest in the history of this region because they differ from those to the north and to the south. The alignment of the bodies and the presence of strong pressure effects in the formation of the gneisses suggest intrusion along a zone of deformation. The great amounts of solutions probably resulted from the effects of pressure in squeezing out solutions from partly consolidated magmas.

Tables 5 and 6 follow "References Cited."

REFERENCES CITED

Banks, N. G., 1976, Reconnaissance geologic map of the Mount Lemmon quadrangle, Arizona: U.S. Geol. Survey Misc. Field Studies Map MF-747.

Calk, L. C., and Naeser, C. W., 1973, The thermal effect of a basalt intrusion on fission tracks in quartz monzonite: Jour. Geology, v. 81, p. 189–198.

Catanzaro, E. J., and Kulp, J. L., 1964, Discordant zircons from the Little Belt (Montana), Beartooth (Montana), and Santa Catalina (Arizona) Mountains: Geochim. et. Cosmochim. Acta, v. 28, p. 87–124.

Chew, R. T., 3d, 1952, Geology of the Mineta Ridge area, Pima and Cochise Counties, Arizona: Tucson, Arizona Univ., M.S. thesis, 53 p.

——— 1962, The Mineta Formation, a middle Tertiary unit in southeastern Arizona, *in* Cenozoic geology of Arizona—A symposium: Arizona Geol. Soc. Digest, v. 5, p. 35–43.

Clay, D. W., 1970, Stratigraphy and petrology of the Mineta Formation in Pima and eastern Cochise Counties, Arizona: Tucson, Arizona Univ., Ph. D. thesis, 187 p.

Creasey, S. C., and Theodore, T. G., 1975, Preliminary reconnaissance geologic map of the Bellota Ranch quadrangle, Pima County, Arizona: U.S. Geol. Survey Open-File Rept. 75–295.

Damon, P. E., 1968, Application of the potassium-argon method to the dating of igneous and metamorphic rock within the Basin Ranges of the southwest, *in* Southern Arizona Guidebook 3—Geol. Soc. America Cordilleran Sec.—64th Ann. Mtg., Tucson 1968: Arizona Geol. Soc., p. 7–20.

Damon, P. E., and Bikerman, Michael, 1964, Potassium-argon dating of post-Laramide plutonic and volcanic rocks within the Basin and Range province of southeastern Arizona and adjacent areas: Arizona Geol. Soc. Digest, v. 7, p. 63–68.

Damon, P. E., Erickson, R. C., and Livingston, D. E., 1963, K-Ar dating of Basin and Range uplift Catalina Mountains, Arizona: Natl. Acad. Sci.—Natl. Research Council Pub. 1075, p. 113–121.

Damon, P. E., and Giletti, B. J., 1961. The age of the basement rocks of the Colorado Plateau and adjacent areas, *in* Geochronology of rock systems: New York Acad. Sci. Annals, v. 91, art. 2, p. 443–453.

Du Bois, R. L., 1959, Geology of the Santa Catalina Mountains, *in* Arizona Geol. Soc. Guidebook 2, April 1959: Arizona Geol. Soc. Digest, 2d. Ann., p. 106–116.

Fleischer, R. L., Price, P. B., and Walker, R. M., 1965, Effects of temperature, pressure, and ionization on the formation and stability of fission tracks in minerals and glasses: Jour. Geophys. Research, v. 70, p. 1497–1502.

Giletti, B. J., and Damon, P. E., 1961, Rubidium-strontium ages of some basement rocks from Arizona and northwestern Mexico: Geol. Soc. America Bull., v. 72, no. 4, p. 639–643.

Livingston, D. E., Damon, P. E., Mauger, R. L., Bennett, Richmond, and Laughlin, A. W., 1967, Argon 40 in cogenetic feldspar-mica mineral assemblages: Jour. Geophys. Research, v. 72, no. 4, p. 1361–1375.

Mauger, R. L., Damon, P. E., and Livingston, D. E., 1968, Cenozoic argon ages from metamorphic rocks from the Basin and Range province: Am. Jour. Sci., v. 266, no. 7, p. 579–589.

Moore, B. N., Tolman, C. F., Jr., Butler, B. S., and Hernon, R. M., 1949, Geology of the Tucson quadrangle, Arizona: U.S. Geol. Survey open-file rept., 20 p.

Naeser, C. W., 1976, Fission track dating: U.S. Geol. Survey Open-File Rept. 76–190.

Naeser, C. W., and Faul, H. O., 1969, Fission-track annealing in apatite and sphene: Jour. Geophys. Research, v. 74, no. 2, p. 705–710.

Peterson, N. P., 1938, Geology and ore deposits of the Mammoth mining camp area, Pinal County, Arizona: Arizona Bur. Mines Bull. 144, Geol. ser. 11, 63 p.

Shakel, D. W., 1974, The geology of layered gneisses in part of the Santa Catalina forerange, Pima County, Arizona: Tucson, Arizona Univ., M.S. thesis, 233 p.

Shakel, D. W., Livingston, D. E., and Pushkar, P. D., 1972, Geochronology of crystalline rocks in the Santa Catalina Mountains, near Tucson, Arizona: Geol. Soc. America Abs. with Programs, v. 4, no. 6, p. 408.

Shapiro, Leonard, 1975, Rapid analyses of silicate, carbonate, and phosphate rocks [revised ed.]: U.S. Geol. Survey Bull. 1401, 76 p.

TABLE 5.—*Analytical data for fission-track ages for the Santa Catalina and Tortolita Mountains*

[Methods for fission-track age determinations are similar to those currently employed by Naeser (1976); $\lambda_F = 6.85 \times 10^{-17}$ yr^{-1}. Number of tracks counted is given in parentheses. The figures for estimated analytical uncertainty are based on numbers of tracks counted for ρs, ρi, and ϕ determinations]

Sample	Mineral	$\rho s \times 10^6$ (tracks/cm^2)	$\rho i \times 10^6$ (tracks/cm^2)	$\phi \times 10^{15}$ (neutrons/cm^2)	Age ± 2σ (x10^6 years)
ML-61	Apatite	0.323 (1220)	3.50 (1487)	3.59	20.2±2.1
ML-61	Zircon	3.29 (625)	14.9 (1330)	1.83	26.3±3.4
ML-61	Sphene	1.15 (1014)	4.74 (2087)	1.85	27.5±3.1
BR-21	Apatite	.204 (773)	1.97 (835)	3.59	22.8±2.8
BR-21	Zircon	5.18 (797)	18.1 (1396)	1.61	28.1±3.3
BR-21	Sphene	2.79 (1308)	9.54 (2238)	1.63	29.1±3.0
ML-60	Apatite	.201 (761)	2.13 (905)	3.59	20.7±2.5
ML-60	Sphene	.918 (551)	3.76 (1129)	1.87	27.9±3.7
BR-16	Apatite	.305 (1152)	3.38 (1434)	3.59	19.8±2.1
BR-16	Zircon	4.98 (1436)	19.7 (2841)	1.62	25.1±1.5
BR-16	Sphene	1.39 (912)	5.15 (1691)	1.65	27.2±3.1
GGN-S1	Apatite	.0393 (297)	.462 (1749)	3.59	18.7±2.7
RC-25	Apatite	.113 (429)	1.23 (2066)	3.19	18.0±2.4
ML-105	Apatite	.163 (617)	2.17 (921)	3.59	16.5±2.1

TABLE 6.—*Analytical data for* K-Ar *ages for the Santa Catalina and Tortolita Mountains*

[$\lambda_\varepsilon = 0.585\times10^{-10}$/yr. $\lambda_\beta = 4.72\times10^{-10}$/yr. $K^{40}/K_{total} = 1.19\times10^{-4}$ mole/mole]

Sample	Mineral	Percent	K_2O	$*Ar^{40}$moles/g	$*Ar^{40}/\Sigma Ar^{40}$	Age, 10^6 yr
GGN-S1	Biotite	8.79	8.78	2.96482×10^{-10}	62.2%	22.7±0.7
GGN-S1	Muscovite	9.78	9.75	3.50169×10^{-10}	74.6	24.1±0.7
ML-61	Biotite	8.59	8.62	3.07432×10^{-11}	78.6	24.0±0.7
ML-61	Hornblende	.927	.924	3.07276×10^{-10}	38.6	22.3±0.7
ML-60	Biotite	9.10	9.10	3.18397×10^{-10}	78.4	23.5±0.7
ML-60	Hornblende	1.042	1.040	5.70900×10^{-11}	53.0	36.8±1.0
BR-21	Biotite	7.28	7.32	2.50623×10^{-10}	63.8	23.1±0.7
BR-21	Hornblende	.598	.598	2.07901×10^{-11}	20.4	23.4±1.2
BR-16	Biotite	9.10	9.10	3.13143×10^{-10}	67.3	23.2±0.2
RC3-1	Biotite	8.64	8.63	2.64175×10^{-10}	52.5	20.6±0.6
RC3-1	Hornblende	.933	.934	2.92466×10^{-11}	49.9	21.1±0.6
RC-25	Biotite	8.33	8.40	2.74315×10^{-10}	69.1	22.1±0.7

$*Ar^{40}$ = radiogenic argon

Jour. Research U.S. Geol. Survey
Vol. 5, No. 6, Nov.–Dec. 1977, p. 719–733

NEVADA TEST SITE CRATERS USED FOR ASTRONAUT TRAINING

By H. J. MOORE, Menlo Park, Calif.

Abstract.—Craters produced by chemical and nuclear explosives at the Nevada Test Site were used to train astronauts before their lunar missions. The craters have characteristics suitable for reconnaissance-type field investigations. The Schooner test produced a crater about 300 m across and excavated more than 72 m of stratigraphic section deposited in a fairly regular fashion so that systematic observations yield systematic results. Other features common on the Moon, such as secondary craters and glass-coated rocks, are present at Schooner crater. Smaller explosive tests on Buckboard Mesa excavated rocks from three horizontal alteration zones within basalt flows so that the original sequence of the zones could be determined. One crater illustrated the characteristics of craters formed across vertical boundaries between rock units. Although the exercises at the Nevada Test Site were only a small part of the training of the astronauts, voice transcripts of Apollo missions 14, 16, and 17 show that the exercises contributed to astronaut performance on the Moon.

This paper describes the salient field characteristics of selected craters produced by chemical and nuclear explosives at the Nevada Test Site (fig. 1) that were used to train Apollo astronauts for their lunar missions. Earlier field trips to the Nevada Test Site to study craters were initiated and conducted by E. M. Shoemaker of the U.S. Geological Survey in February 1965. Subsequently, two major field exercises were conducted, one at Schooner crater on Pahute Mesa and the other on Buckboard Mesa. Other craters, such as Sedan at the northern end of Yucca Flat, were used to a limited extent and are not discussed here.

Astronauts for Apollo 14 participated in an exercise at Schooner crater and briefly visited Sedan crater in November 1970. Astronauts for Apollo 16 visited Schooner crater in November 1970 with D. J. Roddy of the U.S. Geological Survey and participated in an exercise there in October 1971; inclement weather prohibited an exercise on Buckboard Mesa. Astronauts for Apollo 17 participated in exercises at Schooner crater and on Buckboard Mesa in August 1972.

Acknowledgments.—Many individuals contributed to the geologic aspects of the exercises described here; particularly noteworthy contributors were Michael C. McEwen (Johnson Spacecraft Center) and Kenneth A. Sargent, Paul P. Orkild, and George E. Ulrich (U.S. Geological Survey). R. W. Henny of the U.S. Air Force Weapons Laboratory, Kirtland Air Force Base, N. Mex., kindly reviewed this manuscript. His own more complete study will be published at a later date. This work was performed under National Aeronautics and Space Administration contract W13,130. The Nevada Operations Office of the U.S. Atomic Energy Commission provided invaluable support for the training exercises.

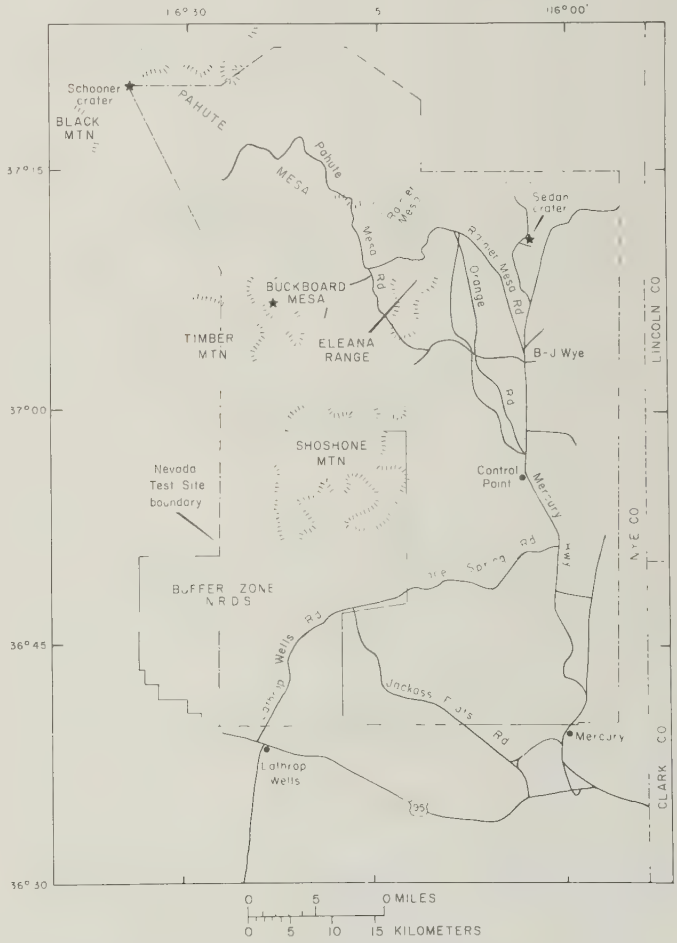

FIGURE 1.—Map of Nevada Test Site showing locations of Schooner crater, Buckboard Mesa, and Sedan crater.

SCHOONER CRATER

Schooner crater was produced by a 31±4-gigagram nuclear device detonated at a depth of 108.2 m (Henny, 1970). It is located on the northeastern flank of the Black Mountain caldera, and most of the ejecta from Schooner crater are ash-flow tuffs that issued from the caldera (Christiansen and Noble, 1968; Noble and Christiansen, 1968; Orkild and others, 1969; Ekren and others, 1971). The crater measures about 300 m from rim crest to rim crest, and the floor is about 75 m below the rim. Schooner crater has eight characteristics that made it an excellent site for astronaut training.

1. The large size of Schooner crater allows a better appreciation of the problems of observing and sampling large craters on the Moon.
2. More than 72 m of the stratigraphic section is excavated and deposited in a fairly regular fashion so that systematic observations yield systematic results.
3. Inverted stratigraphy is vividly displayed in the upper crater walls so that most samples collected can be related to their original stratigraphic sequence. Part of the normal stratigraphic sequence can be determined from lower crater walls.
4. Glass-coated rocks, fragments of shocked tuff, glass, and complex aggregates are present in the ejecta —common features in lunar craters.
5. Secondary impact craters produced by impacts of ejected blocks on soil are common beyond the zone of thick continuous ejecta—similar to those craters produced by ejecta from South Ray crater at the Apollo 16 landing site on the Moon.
6. Faults, open fractures, and slumped units are present.
7. The geologic setting of Schooner crater and geology of the crater itself permit clearly defined and achievable goals for a field reconnaissance.
8. Schooner is a good analog for Cone crater on the Moon because they are nearly the same size. Sampling and photography of Cone crater and its ejecta were prime objectives of the Apollo 14 landed lunar mission (Swann and others, 1971).

Stratigraphy

Stratigraphic units exposed in the ejecta from Schooner crater are vividly colored and markedly different in mechanical and lithologic properties so that identification of them and correlation of collected samples with the units exposed within the crater are relatively straightforward. A generalized stratigraphic section and lithologic units are shown in figure 2.

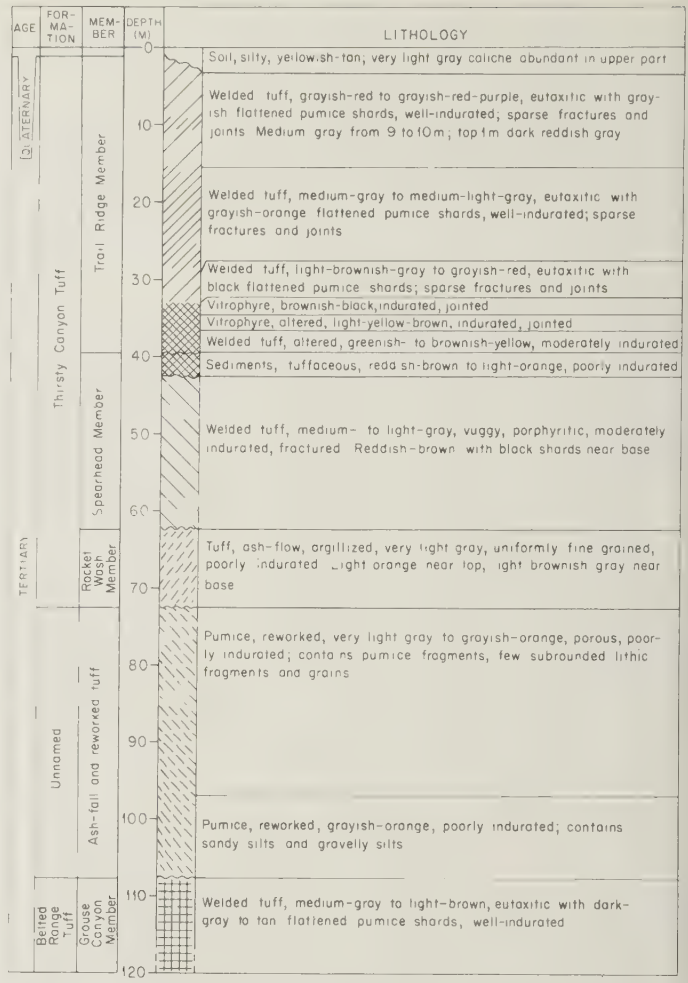
AGE
FORMATION
MEMBER
DEPTH (M)
LITHOLOGY
Soil, silty, yellowish-tan, very light gray caliche abundant in upper part
Welded tuff, grayish-red to grayish-red-purple, eutaxitic with grayish flattened pumice shards, well-indurated; sparse fractures and joints Medium gray from 9 to 10 m; top 1 m dark reddish gray
Welded tuff, medium-gray to medium-light-gray, eutaxitic with grayish-orange flattened pumice shards, well-indurated; sparse fractures and joints
Welded tuff, light-brownish-gray to grayish-red, eutaxitic with black flattened pumice shards; sparse fractures and joints
Vitrophyre, brownish-black, indurated, jointed
Vitrophyre, altered, light-yellow-brown, indurated, jointed
Welded tuff, altered, greenish- to brownish-yellow, moderately indurated
Sediments, tuffaceous, reddish-brown to light-orange, poorly indurated
Welded tuff, medium- to light-gray, vuggy, porphyritic, moderately indurated, fractured Reddish-brown with black shards near base
Tuff, ash-flow, argillized, very light gray, uniformly fine grained, poorly indurated Light orange near top, light brownish gray near base
Pumice, reworked, very light gray to grayish-orange, porous, poorly indurated; contains pumice fragments, few subrounded lithic fragments and grains
Pumice, reworked, grayish-orange, poorly indurated; contains sandy silts and gravelly silts
Welded tuff, medium-gray to light-brown, eutaxitic with dark-gray to tan flattened pumice shards, well-indurated
QUATERNARY
TERTIARY
Thirsty Canyon Tuff
Trail Ridge Member
Spearhead Member
Rocket Wash Member
Unnamed
Ash-fall and reworked tuff
Belted Range Tuff
Grouse Canyon Member
0
10
20
30
40
50
60
70
80
90
100
110
120

FIGURE 2.—Generalized stratigraphic section and lithologic units at Schooner crater (from Sargent, 1969, see footnote 1).

The uppermost unit in the section is a yellowish-tan soil with abundant caliche in its upper part. The soil is as thick as 3.3 m, but locally it is absent. Beneath the soil, densely welded ash-flow tuffs and vitrophyre of the Trail Ridge Member of the Thirsty Canyon Tuff (Noble and others, 1964; K. A. Sargent, written commun.,[1] 1969) extend to depths of 39 m. The Trail Ridge Member has four zones within it: (1) an upper grayish-red to grayish-red-purple zone about 14 m thick that has a thin dark-reddish-gray zone at the top and a thin medium-gray zone in the middle, (2) a central medium-gray to medium-light-gray zone about 13.5 m thick, (3) a lower light-brownish-gray to grayish-red zone about 3.8 m thick, and (4) a basal zone, about 6 m thick, of banded brownish-black vitrophyre locally altered to light yellow brown and greenish- to brownish-yellow altered tuff. This basal zone of the Trail Ridge Member and the underlying 3.3 m of red-

[1] "Summary geologic report on the U 20e emplacement hole, Pahute Mesa, Nevada Test Site." Report to the Atomic Energy Commission; available at the Nevada Test Site, Mercury, Nev.

dish-brown to light-orange tuffaceous sediments of the uppermost Spearhead Member form conspicuous brightly colored marker beds. Flow banding, flattened pumice fragments, relatively low porosity, and rare occurrence of joints and fractures are striking features of the upper three zones of the Trail Ridge Member.

The Spearhead Member of the Thirsty Canyon Tuff extends from a depth of 39 to 62 m. About 3.3 m of poorly indurated reddish-brown to light-orange tuffaceous sedimentary rock is included in its uppermost part (K. A. Sargent, oral commun., 1975). The major part of the member, 20 m thick, is a medium- to light-gray moderately welded ash-flow tuff that grades into a reddish-brown tuff at its base. Unlike the Trail Ridge, the Spearhead is vuggy, fractured, and only moderately indurated.

The Rocket Wash Member of the Thirsty Canyon Tuff is composed of 10 m of very light gray argillized ash-flow tuff. The unit is porous, poorly indurated, and easily disaggregated with finger pressure; it has the lowest cohesion of all the members of the Thirsty Canyon Tuff.

Unnamed beds of very light gray to grayish-orange reworked pumic extend from 72.5 m to 97 m. This reworked pumice is porous and easily disaggregated by finger pressure like the Rocket Wash. Ash-fall and reworked tuff from 97 to 107.5 m and welded ash-flow tuffs of the Grouse Canyon Member of the Belted Range Tuff below 107.5 m were not clearly excavated as such but as shock-metamorphosed fragments and glass.

Ejecta distribution

Ejecta from Schooner crater are found over 2 km away (Henny, 1971). Thick continuous ejecta deposits extend from the rim outward in lobes to distances of 530 m from the crater center (fig. 3). Beyond the lobes of continuous ejecta, scattered angular blocks and fragments of ash-flow tuff are strewn across the surface, and secondary craters produced by the impact of debris abound. The frequency of blocks and secondary craters decreases outward.

Studies of other explosive craters (Roddy, written commun., 1970; Roddy, 1969, 1973) show that stratigraphic units are distributed in a fairly systematic manner in the ejecta. This is also true for Schooner crater (fig. 3). Along traverses proceeding radially outward from the crater rim, materials from progressively shallower layers are exposed, and blocks found at the sinuous edges of the continuous ejecta are chiefly from the upper layers (0–33 m). Most of the surface of the thick continuous ejecta is mantled with fallout of fine debris, fragments, and complex porous fragments of glass and shocked tuff, so that exposures are fairly well confined to the crater rim, the flanks near the rim, and near the edges of the thick continuous ejecta (figs. 3 and 4). Spotty occurrences of stratigraphic units originally 37 m or more below the surface are found on topographic highs of the rim crest. Ejected ash-flow tuffs of the Spearhead Member are particularly thick on the west-northwestern rim and flank, but they also occur on local highs elsewhere on the rim. Ejected tuff from the Rocket Wash Member and probably from the reworked tuff below 72.5 m are found on the topographic highs of the southern rim and the southern flank. Brownish-black and light-yellow-brown vitrophyre and the greenish- to brownish-yellow altered tuff from the Trail Ridge Member are well exposed on the topographic highs and flanks along the eastern side of the crater. Lower to middle parts of the dense, blocky, welded ash-flow tuff of the Trail Ridge are exposed in topographic saddles of the rim and valleys of the immediate crater flanks.

In the zone of thick continuous ejecta, isolated exposures are surrounded by fine debris, small fragments, and shocked reworked pumice and tuff. Exposures are typically found on local radial ridges and on hilltops (fig. 3). They are commonly blocky ash-flow tuff of the Trail Ridge Member and its basal units, although lower stratigraphic horizons are present.

Blocks of ash-flow tuffs of the Trail Ridge Member lie along the edges of the thick continuous ejecta. The basal units of the Trail Ridge Member are generally near the centers of the exposures in lobes and outliers. Two outliers of thick continuous ejecta occur to the southwest of the crater. One exposes the lower limits of the Trail Ridge, excluding the basal 9 m, but the other outlier has the basal vitrophyre near its center.

Outside of the lobes of thick continuous ejecta, the scattered blocks are chiefly from the upper part of the Trail Ridge Member, although basal vitrophyres and greenish- to yellowish-brown altered tuffs are present. Relative frequencies of large blocks from zones within the Trail Ridge change with radial distance. Near the rim saddle on the south-southwestern side of the crater, blocks are chiefly light brownish gray to grayish red (from depths of 28 to 33 m); but, outward along a radial, the fraction of medium-gray to medium-light-gray blocks, originally from depths of 16 to 28 m, increases, and, at 216 m from the crater center, medium-gray to medium-light-gray blocks are dominant. Along a north-south radial where scattered blocks occur, medium-gray to medium-light-gray blocks originally from depths of 16 to 28 m are dominant at 480 m from the crater center, then grayish-red to grayish-red-purple blocks from higher in the section become domi-

FIGURE 3.—Geologic sketch map of Schooner crater and its ejecta. Topographic base prepared by American Aerial Surveys, Inc., at 1:1200 scale.

nant, then at 900 m there are equal numbers of medium-gray and grayish-purple blocks. These sequences correspond to those in the stratigraphic section.

The appearance of the ejecta is profoundly affected by the original mechanical properties of the ejected unit. Coherent blocks from the upper dense, indurated, and sparsely fractured and jointed Trail Ridge Member are huge (fig. 4). Blocks 1 m across and greater are abundant near the crater, and some are more than 6 m across. Coherent blocks of this size from the vuggy, fractured Spearhead Member are practically nonexistent, and exposures of the Member are commonly powdery. Other ejecta units originally below the Spearhead are also powdered and not blocky. The ap-

EXPLANATION

Ejecta

te — Trail Ridge Member of Thirsty Canyon Tuff

me — Marker beds of basal Trail Ridge and upper Spearhead Members of Thirsty Canyon Tuff

se — Spearhead Member of Thirsty Canyon Tuff

re — Rocket Wash Member of Thirsty Canyon Tuff and reworked pumice

fo — Fallout

Units in crater

c — Caliche-rich ejecta, uplifted original ground surface, and uplifted caliche-rich soil

s — Uplifted soil

tr — Uplifted or slumped Trail Ridge Member

mb — Slumped marker beds

sp — Slumped Spearhead Member

rp — Slumped Rocket Wash Member and reworked pumice

ta — Talus

fl — Fine-grained fill of crater floor

Contact, approximately located

Edges of road and trench

Workings

pearance of the ejecta is partly related to their distance from the explosion. The dense glasses, aggregates of shocked and glassy tuffs, and some powdered materials were close to the explosion and substantially altered by the shock wave, but this does not account for the contrast in sizes of ejected blocks between the Trail Ridge and Spearhead Members. This difference in block size is the result of the initial character of the rocks.

Inverted stratigraphy

Like natural impact craters (Shoemaker, 1960) and experimental craters (Moore, 1971), the original stratigraphic sequence is preserved, but inverted, in the ejecta of Schooner crater. This inversion is best preserved near the crater rim, but vestiges are present throughout the thick continuous ejecta. At the west-northwestern rim some 62–65 m of section is represented. Here, small amounts of the Rocket Wash Member beneath a veneer of fallout occur at the rim crest (fig. 5). These are underlain successively by attenuated layers of ash-flow tuff of the Spearhead Member, discontinuous layers of the brightly colored marker beds, massive blocks of tuff from the upper part of the Trail Ridge Member, and caliche-coated blocks and fragments that were near the original surface. Although not present along the western wall, ejected soil is relatively thick on the eastern wall. The units of the inverted ejecta sequence on the east-northeastern rim include the basal units of the Trail Ridge Member. Under the basal unit, the remainder of the Trail Ridge is exposed in the wall. Lower in the upper wall, ejected caliche and soil is present. On the south rim unusual thicknesses of ejected very light gray tuff of the Rocket Wash Member and probably reworked pumice overlie ejected rocks of the Spearhead Member, which in turn overlie the Trail Ridge Member.

Inspection of the trench from the crater rim along a radial to the south (fig. 3) shows that the ejected units tend to mix with one another and become jumbled, but inverted sequences are locally preserved. Blocky ejecta exposed through the surface debris on the thick continuous ejecta show that the inverted stratigraphic sequence is locally preserved at great distances from the crater. Northeast of the rim, hills are capped by greenish, yellowish, and brownish-black blocks and debris of the basal part of the Trail Ridge Member, but exposures topographically lower are from originally higher parts of the Trail Ridge (fig. 3). Similar exposures occur elsewhere, such as at the outlier of the thick continuous ejecta southwest of the crater and on nearby lobes (fig. 3). Because the ejecta units tend to be mixed with one another and because demonstrably inverted stratigraphic sequences are scarce beyond the near-rim crater flanks, exposures on the upper crater walls and crater rim afford the best opportunity to determine the original stratigraphic sequence from the ejecta.

FIGURE 4.—Ejecta on northwestern flank of Schooner crater: Spearhead Member (se), marker beds near base of Trail Ridge Member (me), blocks of tuff and vitrophyre from the Trail Ridge (te), caliche near original ground surface (c), and fallout of fine debris and complex aggregates (fo). Note large blocks from Trail Ridge Member in foreground rim-crest saddle.

Beyond the edge of the continuous ejecta, evidence for inverted stratigraphy of primary ejecta is rare to nonexistent; instead a mixture of blocks and soil excavated from the substrate, secondary impact craters, and scattered blocks is present. At progressively greater distances, separation of blocks and secondary craters are found in large expanses of undisturbed soil and weathered rocks of the Trail Ridge Member. To the west, where bare rock is exposed, impacting blocks produced shallow secondary craters in some places and none at all in other places. Isolated secondary craters (fig. 6) excavated soil, where present, and their ejecta are inverted in down-trajectory and lateral directions.

Crater walls

Inspection and observation of the walls of Schooner crater enable the original stratigraphic sequence to be determined and rocks seen in the ejecta to be correlated with their corresponding stratigraphic horizons. Best exposures of the soil and caliche horizon occur on the eastern wall (fig. 7). The brightly colored marker beds in the upper part of the Spearhead Member and the basal part of the Trail Ridge Member, locally overlain by medium- to light-gray tuffs of the Spearhead Member, commonly form the high points of the rim crest. Beneath these, medium-gray to grayish-red-purple tuff of the Trail Ridge forms blocky slopes, and the originally uppermost but now inverted weathered part of the Trail Ridge is dark reddish gray. Ejected soil and caliche underlie the ejected weathered tuff of the Trail Ridge Member. A mirror-image sequence of upwarped but not inverted layers of caliche and soil, dark-reddish-brown weathered tuff of the Trail Ridge Member, and steep cliffs of Trail Ridge tuff rise above talus slopes of blocky tuff. The upwarped original ground surface is the plane of mirror symmetry. Soil is thin to absent on the western wall of the crater, but the original ground surface, which separates upturned layers from overturned layers of ejecta, is marked by a very light gray caliche horizon.

Crater walls beneath the upturned caliche and soil have three units: steep cliffs of Trail Ridge Member tuff, talus slopes composed chiefly of large blocks of tuff of the Trail Ridge Member, and large uplifted and then slumped tuff and reworked pumice from original depths of 42 m to more than 75 m (fig. 7). In the slumped units, the original sequences are preserved so that the Spearhead Member overlies the Rocket Wash Member, which in turn overlies the reworked pumice. Scattered blocks of basal rocks from the Trail Ridge are present in the slumped materials, although difficult to see from the rim.

The floor of the crater is filled with fine-grained materials to a flat level surface.

Concentric fractures and partly slumped blocks created by seismic waves from the Handley explosion some 5.5 km to the east-southeast are present on the rim (Shackelford, 1971).

A

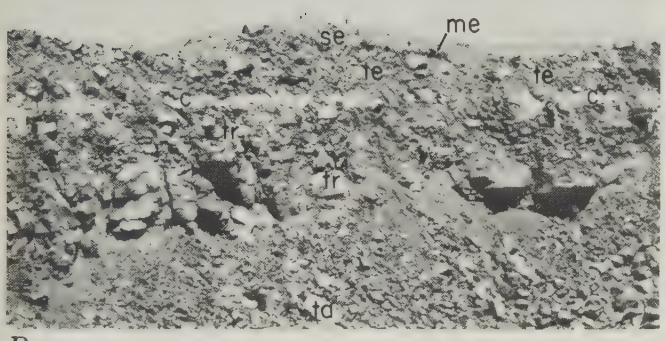

B

FIGURE 5.—Inverted stratigraphy of ejected Thirsty Canyon Tuff at Schooner crater. *A*, West-northwestern rim; Rocket Wash Member (re), Spearhead Member (se), marker beds near base of Trail Ridge Member (me), and Trail Ridge Member (te); approximate location of original ground surface indicated by very light gray caliche (c); uplifted Trail Ridge Member (tr in lower right) forms cliffs; Apollo 17 Commander E. A. Cernan stands at left. *B*, Northern rim; Spearhead Member (se), marker beds (me) near base of Trail Ridge Member (te), original ground surface indicated by very light gray caliche (c); uplifted Trail Ridge Member (tr) forms cliffs below caliche; talus (ta) is composed of blocks from Trail Ridge Member; note that ejecta units exposed on rim from greatest depths (se and me) occur on local high points, and those from intermediate depths (te) occur in rim-crest saddles; Apollo 16 astronauts J. W. Young and C. M. Duke, Jr., and observers on skyline.

FIGURE 6.—Secondary crater and its ejecta of caliche-rich soil. A block of rock from the Trail Ridge Member produced the secondary crater and rests in the crater. Note caliche that was excavated from below surface on down-trajectory side of crater (to right of block). Block is 1.6 m long.

Lithologies

A wide variety of lithologies, both original and imposed by shock metamorphism, are present in the ejecta. Silty soil having low cohesion, locally cemented with very light gray caliche as well as weathered rock, could be sampled directly or in the ejecta of secondary craters well beyond the thick continuous ejecta. The field characteristics of these units contrast sharply with the large unweathered dense ejected blocks of welded tuff from the Trail Ridge Member. These unweathered ejected blocks contain large flattened gray to very dark gray alined pumice fragments set in an aphanitic banded groundmass. Also set in the matrix are alined feldspar crystals and rhyolite fragments; vugs and vesicles are alined and flattened. The black vitrophyre contains abundant lithic fragments and feldspar crystals. The light-yellow-brown altered vitrophyre contains lithic fragments, alined feldspar crystals, and elongate alined and flattened vesicles. The greenish- to brownish-yellow tuff at the base of the Trail Ridge contains abundant lithic fragments, and the aphanitic matrix is banded. Poorly welded tuffs from the Spearhead Member do not exhibit the marked parallel fabric of the Trail Ridge, rather the feldspar crystals in the aphanitic matrix show little parallelism, and vugs and vesicles are irregular to equidimensional.

Degrees of shock metamorphism range from rocks that were completely melted to those which, although partly melted, retain their original textures. Glass coatings are common on block surfaces (fig. 8*A*, *B*)

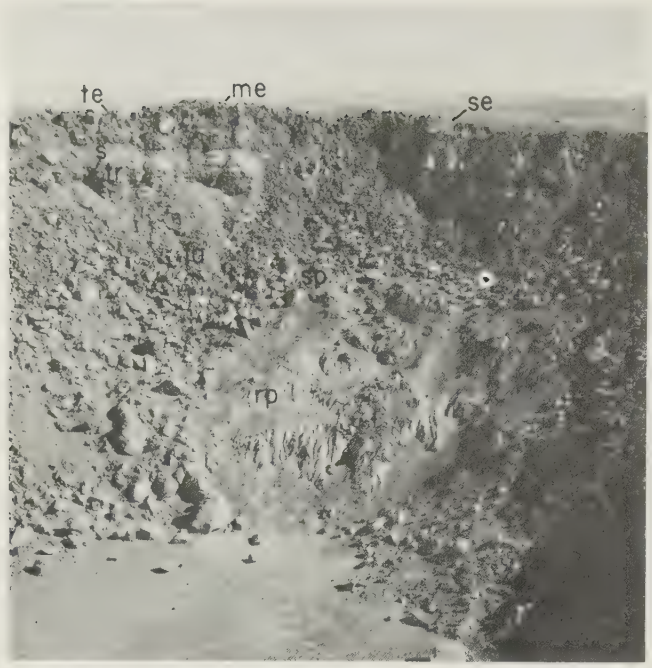

FIGURE 7.—Eastern wall of Schooner crater showing uplifted then slumped beds of reworked pumice (rp) and Spearhead Member of the Thirsty Canyon Tuff (sp). Rocket Wash Member is also present in slumped units. Thickest exposures of uplifted soil and caliche (s) occur above cliffs of uplifted Trail Ridge Member (tr). Ejecta units overlie units and include Trail Ridge Member (te) basal marker beds of the Trail Ridge Member (me) and Spearhead Member (se). Talus (ta) is composed chiefly of blocks from the Trail Ridge Member.

and pieces of glass are strewn about the area. Intensely shocked reworked pumice occurs in the cores of complex dirty-gray aggregates (fig. 8*C*). Although rounded to subrounded fragments in the reworked pumice can be identified, inspection of the fragments shows that they are vesicular and have small glass fibers extending into the vesicles—a feature not found in unshocked specimens. Most of the recognizable shocked samples come from depths near 90–107 m. Some are demonstrably from about 100 m. The gradation from intensely shocked but recognizable samples through barely recognizable and highly vesiculated samples to pure glass can be seen at Schooner crater.

Summary

In summarizing I will describe briefly the planned stops along the traverse used by the Apollo 16 and 17 crews (fig. 9). The broad hypothetical goals of the exercise mission were to establish the origin of the Black Mountain caldera, to establish the sequence of the rock layers using geology, and to collect samples suitable for chemical analyses and for determinations of the various rock layers associated with the Black Mountain caldera as well as the exposure age of Schooner crater. Traverse station 1, where the Lunar Module mockup was located, provides a splendid view of the surrounding region. Prominent landmarks such as Black Mountain and the blocky rim of Schooner crater are visible. The surface, transected by gullies, slopes gently eastward. Generally, outcrops and rocks of the Trail Ridge Member are weathered and covered with desert varnish. A few rocks of the Trail Ridge Member ejected from Schooner crater, some of which have glass coatings, are present. In the gully wall to the north of station 2, gently eastward dipping tuffs of the Trail Ridge Member are exposed in steep cliffs. These exposures include the basal vitrophyres underlain by tuffs of the Spearhead Member on moderate slopes. In alluvium in the valley west of station 2 large blocks and secondary craters disrupt the otherwise smooth, undulating terrain. As one proceeds from station 2 to station 3, surfaces of bare tuff of the Trail Ridge Member become covered with progressively greater thicknesses of soil, and the frequency of blocks, chiefly from the upper part of the Trail Ridge Member, and the number of secondary craters increase. Near station 3, the uppermost soil can be sampled in place between widely separated blocks and secondary craters. Secondary craters expose soil and caliche from below the surface. The traverse from station 3 to station 4 follows a road constructed after formation of the crater because blocks surrounding the thick continuous ejecta here are so large and so many that the terrain is too rough for vehicles. Along the road, the relative frequency of different colored blocks can be noted and correlated with distance from the crater until the trench and debris piles are reached. At station 4 on the thick continuous ejecta, disaggregated material from below a depth of 63 m can be sampled along with tuff from central horizons of the Trail Ridge Member, shocked tuff, glass, and complex aggregates. At station 5 and near the rim, samples from the Trail Ridge Member, marker beds, Spearhead and Rocket Wash Members, and fallout can be collected. Descriptions of rocks in the lower crater walls and inverted stratigraphy of the upper crater walls can then be correlated with the samples.

BUCKBOARD MESA

Buckboard Mesa is capped chiefly by basalt flows and lies within the moat of the Timber Mountain caldera, an annular depression surrounding Timber Mountain (Byers and others, 1966; Carr and Quinlivan, 1966; Hinrichs and others, 1967; Byers and Cummings, 1967; Byers and others, 1968). Several experi-

A

B

C

FIGURE 8.—Glass and shocked pumice produced by shock metamorphism. Geology pick is 30.5 cm long. *A*, Glass (g) on block of welded tuff of the Trail Ridge Member (te). *B*, Glass coatings (g) on medium-gray ash-flow tuff from the Trail Ridge Member (te) of the Thirsty Canyon Tuff; note large white flattened pumice fragments (p). *C*, Complex aggregate of shocked reworked pumice and glass surrounded by fallout of fine debris.

ments using chemical and nuclear explosives produced craters and mounds in the basalt (Nugent and Banks, 1966; Lutton and Girucky, 1966; Spruill and Paul, 1965; and R. B. Johnson, written commun., 1962). Eight features of the Buckboard Mesa site made it an excellent site for an astronaut training exercise:

1. Craters ranging in size from 15 cm to 80 m are present on the mesa.
2. The smallest craters formed chiefly by spalling from solid rock.
3. One crater, 42 m across, exposed a nearly vertical contact between massive to vesicular dark-gray basalt and reddish cinders and clinkers.
4. A sequence of zones of alteration in the basalt flows could be established by systematic observations of ejecta from craters as a function of crater size as well as from ejecta of the larger individual craters.
5. Recognition of subtle differences in rock colorations and properties are required to establish the alteration zones.
6. The exercise traverse was long (7.5 km) like the lunar traverses.
7. Some of the ejecta from the craters were crushed and sheared by the shock waves.
8. The geologic setting of Buckboard Mesa and the geology of the craters permitted well-defined and achievable goals for a field reconnaissance.

General geology and lithologies

The principal events at the Buckboard Mesa site, from oldest to youngest, are (1) the extrusion of basalt into the moat of the Timber Mountain caldera, (2) the formation of dikes, (3) the deposition of reddish cinders, scoria, and clinkers to form the Scrugham Peak cone, (4) the formation of soil, and (5) the formation of experimental craters and mounds. Ejecta from most of the craters are blocks from massive vesicular basalt flows, but ejecta from the crater that crosses a vertical contact contains reddish cinders, scoria, clinkers, agglomerates, and breccias as well.

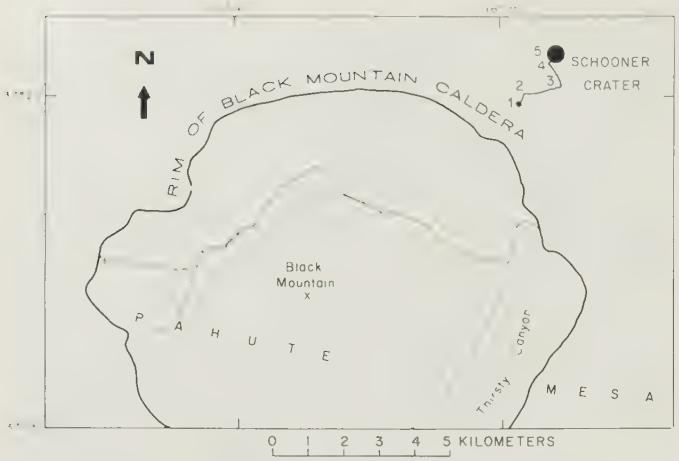

FIGURE 9.—Map showing location of Black Mountain, approximate rim of Black Mountain caldera, Schooner crater, and traverse for astronaut training exercise. Numbers 1–5 are stations along traverse where stops were planned to collect samples and to examine contacts and units inferred from studies of aerial photographs.

Although there are no recognized stratigraphic units or relations to be unraveled in the field, the horizontal alteration zones within a single flow, their sequence, and approximate depths can be determined using crater geology. Drill cores from the uppermost 3–4 m of the basalt flows are dark gray and vesicular, and fractures are commonly covered with caliche. From about 3–4 m to 7–8 m, basalts are colored reddish gray by the iddingsite alteration-mineral group. Below 7–8 m, the basalts are unaltered and medium gray. Small craters (about 10 m across) in the flows excavate dark-gray basalt from the upper zone exclusively, whereas the larger craters in the flows excavate basalt from all three alteration zones.

Important parts of the exercise were the careful observations required to distinguish the subtle differences between the rocks from the three alteration zones in the basalt and to decipher the ejecta distribution of the crater formed partly in basalt and partly in cinders and clinkers.

The traverse

The traverse proceeds from a point on a ridge north of Little Dan crater in a general southeastward direction to the tip of Buckboard Mesa (fig. 10).

Lunar Module.—The Lunar Module mockup station was ideally located for descriptions of the surrounding terrain. Timber Mountain, 8 km to the southwest (fig. 1), rises some 600 m above the Lunar Module station. On Buckboard Mesa, 1.2 km to the north, Scrugham Peak rises 165 m above the station. Distant views to the north, east, and south include the elevated terrain

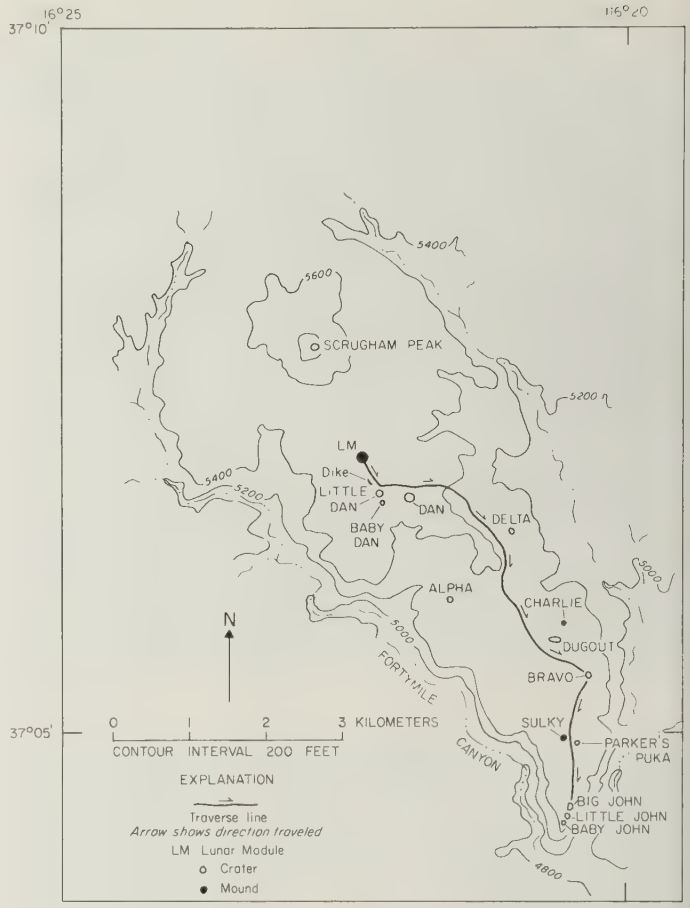

FIGURE 10.—Traverse map of astronaut training exercise on Buckboard Mesa.

of Pahute Mesa, Rainier Mesa, the Eleana Range, and Shoshone Mountain.

Dike.—An exposed dike south of the Lunar Module mockup offers an opportunity to describe and observe structure, rock fabric, rock texture, weathering, and impact craters on rock surfaces, as well as the surrounding surface. The dike protrudes about 3 m above the local surface and can be traced 27 m in a north-northwestward direction. Rock units within the dike form slabs dipping about 60° E. and locally 15° W. near the center of the dike; also, the dike is jointed. Weathering has produced a dusky-brown patina on exposed surfaces. A thin tan oxidized zone is immediately beneath the patina. Unweathered rock is a moderate-grayish-brown fine-grained basalt that contains olivine phenocrysts and feldspar laths. Several small impact craters nearly 30 cm across are present (fig. 11). These craters, produced by the impact of ejecta from the local crater, are typical of craters in hard dense rock that have centers of sheared and crushed rock surrounded by spall surfaces, radial fractures, and concentric fractures (Moore and others, 1963).

FIGURE 11.—Small craters on surface of dike. (1) Dark-gray surfaces are weathered basalt of dike, (2) light-gray surfaces are fresh basalt exposed by spalling, and (3) centers of small craters contain very light gray crushed and sheared basalt. Geology pick is 30.5 cm long.

Surfaces around the dike include a variety of rocks and soils. Weathered reddish cinders and weathered massive gray basalts occur along with unweathered rocks, so that locally derived rocks can be distinguished from exotic ones by weathering alone.

Little Dan (shot 12[2]) crater.—This crater, about 42 m across, is partly in gray vesicular basalt and partly in reddish cinders, clinkers, agglomerates, and breccias (fig. 12). Large blocks and fragments of dark-gray vesicular basalt occur as ejecta and talus in the southern sector. Reddish cinders and clinkers, with a few massive basalt blocks that have oxidized edges and contacts with agglomerates, occur as ejecta and talus in the northwestern sector. Reddish cinders and clinkers and zones of mixed cinders and massive basalts occur as ejecta and talus in the northeastern sector. Thus, this crater is a good example of one produced in rock units having very steeply dipping contacts. Locally, where a caliche layer is present along with vertical changes in lithology, inverted stratigraphy and original ground surfaces can be identified.

A variety of rock types has been ejected. The northwestern sector of ejecta has reddish cinders, scoria, clinkers, agglomerates with vesicular fragments, breccias of massive dark-gray basalt, and mixtures of breccias and agglomerates. At the southwestern edge of this sector, there is a gradational contact within the ejecta between the reddish cinders and clinkers and the massive to vesicular dark-gray basalts. Here, contacts

[2] Numbers in parentheses are crater numbers used by Vortman and MacDougall (1962).

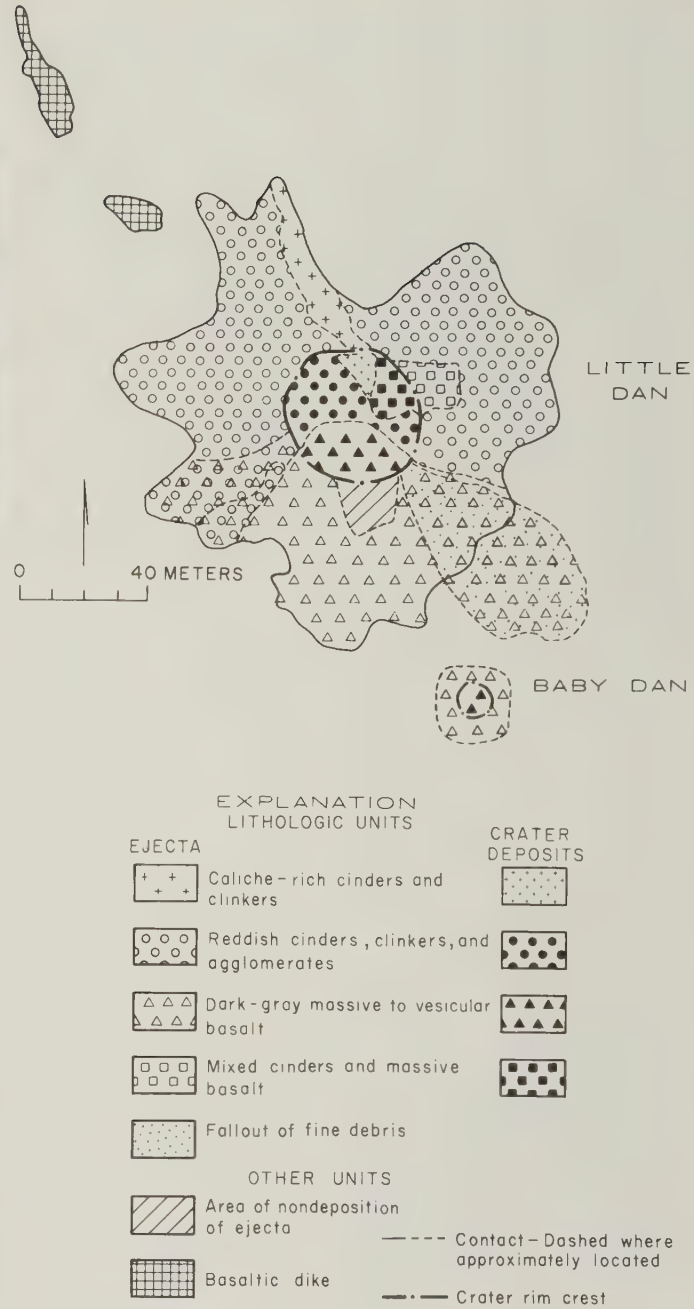

FIGURE 12.—Geologic sketch map of Little Dan and Baby Dan craters.

between the two units are preserved within single blocks. The exclusive presence of the massive to vesicular basalts in the southern sector of ejecta is suggested not only by the blocky ejecta from Little Dan but also by Baby Dan crater (shot 10) immediately south of Little Dan, which exposed and ejected only the massive basalt. The northeastern sector of ejecta contains rocks similar to those in the northwestern sector, but the proportion of massive basalt fragments is greater.

The traverse proceeds to the east past Dan crater and then southeast to Bravo crater. Along the traverse, craters and mounds such as Delta (excavated crater), Charlie (mound), and Dugout (elongate crater) can be seen to the east.

Bravo crater.—Bravo crater, 41 m across, provides the first evidence for the three alteration zones in the flow basalts and their sequence (fig. 13). At four crater radii from the center on the northwestern side of the crater, 70–100 percent of the scattered blocks and fragments of ejecta is dark-gray vesicular basalt with caliche-coated surfaces; as much as 30 percent of the blocks and fragments is reddish-gray massive to vesicular basalt. Blocks and fragments completely cover the surface two and one-half crater radii from the center, and here there are equal numbers of dark-gray and reddish-gray rocks. Nearly all the blocks and fragments on the rim and flanks are massive to vesicular reddish-gray basalts. Locally, elsewhere on the rim and near flanks, medium-gray basalt constitutes as much as 20 percent of the fragments. Many fragments are crushed and sheared. This distribution of ejecta is typical of ejecta from craters in basalts with horizontal zones, from top to bottom, of dark-gray vesicular basalt, reddish-gray basalt, and medium-gray basalt.

Inspection of the western crater wall shows that the dark-gray basalt overlies the reddish-gray basalt. Here, the original ground surfact can be identified, and exposures of tilted dark-gray basalt are found overlain by ejected reddish-gray basalt. Also, on the western rim, a small amount of ejected medium-gray basalt overlies the reddish-gray basalt in an inverted sequence.

The medium-gray basalts originally near the detonated charge are crushed and sheared. Striations on some of these ejecta are well developed; one shatter cone was found (fig. 14).

Parker's Puka (shot 8).—Parker's Puka is a small irregularly shaped crater about 12 m across. Surface rocks around it are dark-gray basalts with desert varnish. Ejecta from Parker's Puka are exclusively blocks and fragments of dark-gray vesicular basalt with some caliche and caliche-coated blocks and fragments, demonstrating that the uppermost altered zone consists of this rock. Steep planar walls and linear edges show that joints and fractures controlled the shape of the crater. Exposures in the walls are dark-gray vesicular basalts.

Sulky, a mound produced by an experiment, is just west of Parker's Puka and affords an opportunity for descriptions of an unusual landform.

Big John (shot 13) crater.—Ejecta distribution from Big John crater, 35 m across, is decidedly asymmetrical (fig. 15), but the indicated stratigraphy is the same as at Bravo crater: Alteration zones of basalt are, from

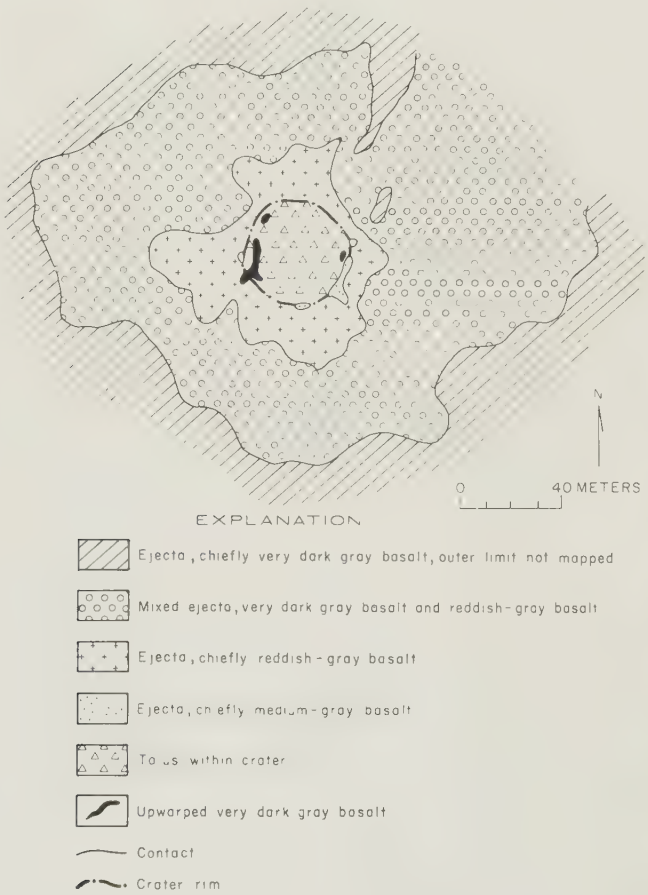

FIGURE 13.—Geologic sketch map of Bravo crater.

FIGURE 14.—Shatter cone in ejecta on western rim of Bravo crater. Geology pick is 30.5 cm long.

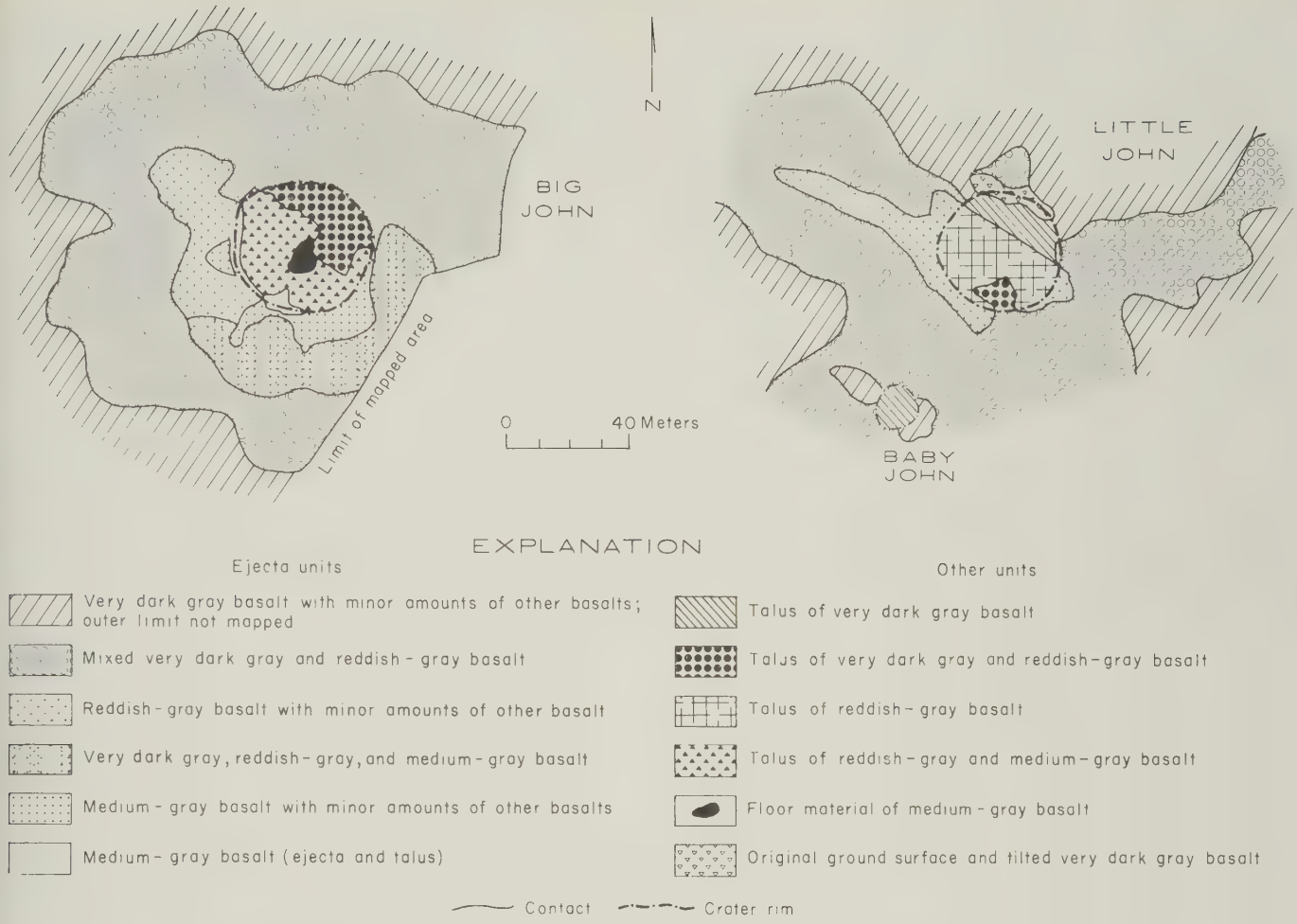
N
BIG JOHN
LITTLE JOHN
BABY JOHN
Limit of mapped area
0 40 Meters
EXPLANATION
Ejecta units
Very dark gray basalt with minor amounts of other basalts; outer limit not mapped
Mixed very dark gray and reddish-gray basalt
Reddish-gray basalt with minor amounts of other basalt
Very dark gray, reddish-gray, and medium-gray basalt
Medium-gray basalt with minor amounts of other basalts
Medium-gray basalt (ejecta and talus)
Other units
Talus of very dark gray basalt
Talus of very dark gray and reddish-gray basalt
Talus of reddish-gray basalt
Talus of reddish-gray and medium-gray basalt
Floor material of medium-gray basalt
Original ground surface and tilted very dark gray basalt
Contact
Crater rim

FIGURE 15.—Geologic sketch map of Big John, Little John, and Baby John craters.

top to bottom, dark-gray vesicular basalt, reddish-gray massive to vesicular basalt, and medium-gray basalt. Except where altered by bulldozing, the relative amounts of dark-gray vesicular basalt blocks and fragments at the surface decrease as the crater rim is approached, but the decrease is more pronounced on the southern and western crater flanks. Reddish-gray basalt blocks and fragments are concentrated on the western rim and flanks and on the southern flanks, whereas medium-gray basalts are almost exclusively confined to the southern rim. A patch of ejected medium-gray basalt, superposed on ejected reddish-gray basalt, is exposed on the highest part of the western rim crest.

Little John (shot 11) crater.—Little John crater, 33 m across, also has an asymmetrical distribution of ejecta (fig. 15). In contrast with Big John crater, the amount of medium-gray basalt is small, indicating that the medium-gray basalt comes from deeper horizons. Again, relative amounts of very dark gray basalt tend to decrease as the crater rim is approached except on the northern rim and flank. Part of the northern rim and its flank have only scattered ejecta of dark-gray vesicular basalt resting on the tilted ground surface of the same material. Upper crater walls below the northern rim expose the dark-gray vesicular basalt. Ejected reddish-gray basalt is concentrated on the eastern and western rim and in a fracture-related ray of small fragments that extends westward.

Baby John (shot 4) crater.—Baby John crater (fig. 15), 10 m across, has dark-gray vesicular basalts in its ejecta and its steep walls also contain dark-gray vesicular basalts with caliche-covered joint surfaces.

In summary, the observer is able to establish the sequence of zones of alteration in the basalt flows by careful observation of the subtle differences in the ejecta and rocks in walls of crater as a function of their size, the distribution of ejecta around single craters, and local occurrences of inverted stratigraphy. Little Dan crater provides an opportunity to see the effect of steeply dipping contacts on the distribution of ejecta.

CONCLUSION

The exercises at Schooner crater and Buckboard Mesa represent a very small part of the training of astronauts for their lunar missions. However, they illustrate well the type of geologic training given to these very able students. Voice transcripts of the astronauts, while on the Moon, show that the training became a part of their thinking. Astronaut Edgar Mitchell definitely had the training exercise at Schooner crater in mind as he approached Cone crater at the Apollo 14 site (Bailey and Ulrich, 1975a, p. 93), and, although the walls of Cone crater were never observed and described because of mission time constraints, he sincerely desired to do so (Bailey and Ulrich, 1975a, p. 96). Astronaut J. W. Young correctly applied the principles learned at the secondary craters of Schooner crater, as well as those illustrated by missile impact craters (Moore, 1971), in recognizing a secondary crater produced by ejecta from South Ray crater at Apollo 16 station 4 and in collecting samples from it (Bailey and Ulrich, 197b, p. 119). Description of the wall of North Ray crater did not yield immediate evidence of distinctly different layered units although astronauts Young and C. M. Duke, Jr., looked carefully for such evidence and photographed the crater wall permitting subsequent searches for such evidence (Bailey and Ulrich, 1975b, p. 220–223). Astronaut H. H. Schmitt referred to Little Dan crater on Buckboard Mesa while describing a 600-m lunar crater in the Haemus Mountains west of Sulpicius Gallus (Apollo Spacecraft Program Office, 1972):

"* * * looks similar to—Yes, it's about a 600-meter crater. And it looks very much like—in its geologic pattern to the—that crater out in the Nevada Test Site on Buckboard Mesa that had an explosion along a contact between two very contrasting rock types. In this case, however, the line does not go completely across the crater, and that's why we feel it may be a dike or a vein which fortuitously has been hit by that impact." There are many other descriptions by Schmitt from orbit that clearly reflect all the training he received from countless individuals. The Nevada Test Site crater exercises illustrate, when combined with lunar results, the value of astronaut training.

REFERENCES CITED

Apollo Spacecraft Program Office, 1972, Apollo 17 technical air-to-ground voice transcription: Manned Spacecraft Center, Houston, Tex., MSC–07629, Tape 154/2, Apollo elapsed time 09 13 04 43.

Bailey, N. G., and Ulrich, G. E., 1975a, Apollo 14 voice transcript pertaining to the geology at the landing site: U.S. Dept. Commerce, Natl. Inf. Service, PB–242 056, 147 p.

——— 1975b, Apollo 16 voice transcript pertaining to the geology of the landing site: U.S. Dept. Commerce, Natl. Tech. Inf. Service, PB–243 870, 323 p.

Byers, F. M., Jr., and Cummings, David, 1967, Geologic map of the Scrugham Peak quadrangle, Nye County, Nev.: U.S. Geol. Survey Geol. Quad. Map GQ–695, scale 1:24 000.

Byers, F. M., Jr., Orkild, P. P., Carr, W. J., and Quinlivan, W. D., 1968, Timber Mountain Tuff, southern Nevada, and its relation to cauldron subsidence, *in* Eckel, E. B., ed., Nevada Test Site: Geol. Soc. America Mem. 110, p. 87–97.

Byers, F. M., Jr., Rogers, C. L., Carr, W. J., and Luft, S. J., 1966, Geologic map of the Buckboard Mesa quadrangle, Nye County, Nev.: U.S. Geol. Survey Geol. Quad. Map GQ–552, scale 1:24 000.

Carr, W. J., and Quinlivan, W. D., 1966, Geologic map of the Timber Mountain quadrangle, Nye County, Nev.: U.S. Geol. Survey Geol. Quad. Map GQ–503, scale 1:24 000.

Christiansen, R. L., and Noble, D. C., 1968, Geologic map of the Trail Ridge quadrangle, Nye County, Nev.: U.S. Geol. Survey Geol. Quad. Map GQ–774, scale 1:24 000.

Ekren, E. B., Anderson, R. E., Rogers, C. L., and Noble, D. C., 1971, Geology of Northern Nellis Air Force Base Bombing and Gunnery Range, Nye County, Nevada: U.S. Geol. Survey Prof. Paper 651, 91 p.

Henny, R. W., 1970, Schooner ejecta studies, *in* Proceedings of the symposium on engineering with nuclear explosives: Am. Nuclear Soc. and U.S. Atomic Energy Comm., Las Vegas, Nev., Jan. 14–16, 1970, v. 2, p. 1746–1770.

Hinrichs, E. N., Krushensky, R. D., and Luft, S. J., 1967, Geologic map of the Ammonia Tanks quadrangle, Nye County, Nev.: U.S. Geol. Survey Geol. Quad. Map GQ–638, scale 1:24 000.

Lutton, R. J., and Girucky, F. E., 1966, Geologic and engineering properties investigations—Project Sulky: U.S. Army Corps of Engineers, Vicksburg, Miss., Plowshare Final Report PNE–720, 136 p.

Moore, H. J., 1971, Craters produced by missile impacts: Jour. Geophys. Research, v. 76, p. 5750–5755.

Moore, H. J., Gault, D. E., and Lugn, R. V., 1963, Experimental impact craters in basalt: Am. Inst. Mining Metall. Eng. Trans., v. 226, p. 258–262.

Noble, D. C., Anderson, R. E., Ekren, E. B., and O'Connor, J. T., 1964, Thirsty Canyon Tuff of Nye and Esmeralda Counties, Nevada, *in* Geological Survey research 1963: U.S. Geol. Survey Prof. Paper 475–D, p. D24–D27.

Noble, D. C., and Christiansen, R. L., 1968, Geologic map of the southwest quarter of the Black Mountain quadrangle, Nye County, Nev.: U.S. Geol. Survey Misc. Geol. Inv. Map I–562, scale 1:24 000.

Nugent, R. C., and Banks, D. C., 1966, Engineering-geologic investigation, Project Danny Boy: U.S. Army Engineer Nuclear Cratering Group, Plowshare Final Report PNE–5005, 98 p.

Orkild, P. P., Sargent, K. A., and Snyder, R. P., 1969, Geologic map of Pahute Mesa, Nevada Test Site and vicinity, Nye County, Nev., U.S. Geol. Survey Misc. Geol. Inv. Map I–567, scale 1:48 000.

Roddy, D. J., 1969, Project LN–303 geologic survey activities, *in* Dudash, M. J., ed., Operation prairie flat, preliminary report: Defense Atomic Support Agency 2228–I, v. 1, p. 317–333.

——— 1973, Project LN–303 geologic studies of the Middle Gust and Mixed Company craters: Mixed Company/Mid-

dle Gust Results Mtg., Mar. 3–15, 1973, Proc., v. 2, Defense Nuclear Agency, DNA 3151, pt. 2, p. 79–123.

Shackelford, T. J., 1971, Crater stability under the influence of large seismic motions: U.S. Army Engineer Nuclear Cratering Group, PNE–5013, 32 p.

Shoemaker, E. M., 1960, Penetration mechanics of high velocity meteorites, illustrated by Meteor Crater, Arizona: Internat. Geol. Cong., 12th Sess., Norden 1960, Rept., pt. 18, p. 418–434.

Spruill, J. L., and Paul, R. A., 1965, Crater measurements, Project Pre-Schooner: U.S. Army Engineer Nuclear Crater Group, Plowshare Fial Rept., UNE–502F, 134 p.

Swann, G. A., Bailey, N. G., Batson, R. M., Eggleton, R. E., Hait, M. H., Holt, H. E., Larson, K. B., McEwen, M. C., Mitchell, E. D., Schaber, G. G., Schafer, J. P., Shepard, A. B., Sutton, R. L., Trask, N. J., Ulrich, G. E. Wilshire, H. G., and Wolfe, E. W., 1971, Preliminary geologic investigations of the Apollo 14 landing site: Apollo 14 Prelim. Sci. Rept., pt. 3, Natl. Aeronautics Space Admin. Spec. Pub. NASA SP–272, p. 39–85.

Vortman, L. J., and MacDougall, H. R., 1962, Project Buckboard, 20-ton and 1/2-ton high explosive crater experiments in basalt rock, final report, August 20: Sandia Corp., SC–4675 (RR), 308 p.

Jour. Research U.S. Geol. Survey
Vol. 5, No. 6, Nov.–Dec. 1977, p. 735–745

LOWER TERTIARY BIOSTRATIGRAPHY OF THE NORTHERN SANTA LUCIA RANGE, CALIFORNIA

By R. Z. POORE, W. V. SLITER; and M. H. Link,
Menlo Park, Calif.; and Wilmington, Calif.

Abstract.—Lower Tertiary strata in the northern Santa Lucia Range of California are correlated by means of planktonic and benthonic foraminifers. Benthonic foraminiferal assemblages from eight stratigraphic sections range in age from Ynezian to possible basal Refugian. The Paleocene mudstone contains a Ynezian benthonic foraminiferal assemblage. The Ulatisian benthonic assemblage of the Lucia Mudstone and the Penutian to Ulatisian benthonic assemblages of the Eocene sandstone and mudstone unit are associated with planktonic foraminifers referable to Zones P 7–P 8 and P 9. The Church Creek Formation is characterized by a Narizian to possibly Refugian benthonic assemblage. Two questionable associations of early Eocene planktonic foraminifers with Narizian benthonic foraminifers occur near Arroyo Seco Creek. No age-diagnostic foraminifers were found in The Rocks Sandstone. Data from previous studies, along with our data, suggest a Ulatisian to Narizian age for this unit. Paleoenvironments interpreted from foraminiferal assemblages suggest a general shoaling from lower bathyal or deeper water depths in the middle Paleocene and early Eocene to bathyal water depths during the middle Eocene. In addition, the Ulatisian water depths deepen across the Santa Lucia Range from east to west.

Approximately 7620 m of predominantly marine clastic sedimentary rocks, ranging in age from Cretaceous to Quaternary, is exposed in the northwest-trending northern Santa Lucia Range of central California. Forty samples from the lower Tertiary part of this sequence were examined for microfossils to complement ongoing sedimentologic and stratigraphic studies. In addition, these data provided the opportunity to correlate several benthonic foraminiferal teilzones with the planktonic foraminiferal zonation of Berggren (1972). This paper presents those data that have proved useful for interpreting the geologic history of this area (Nilsen and Link, 1975; Link, 1975, unpub. data).

GENERAL STRATIGRAPHY

The pre-middle Miocene rocks of the northern Santa Lucia Range are divisible into two presumably continuous sequences that in most areas are bounded by unconformities and whose basal beds rest locally upon a pre-Tertiary granitic and metamorphic crystalline basement complex. The older, unnamed Late Cretaceous and Paleocene sequence is as much as 3050 m thick and rests unconformably on basement rocks along the western flank of the northern Santa Lucia Range (fig. 1).

The Eocene to lower Miocene sequence is as much as 1525 m thick (fig. 2) and rests unconformably upon either basement rocks or the Cretaceous and Paleocene sequence. It includes the Junipero Sandstone of Thorup (1941), the Lucia Mudstone of Dickinson (1965), The Rocks Sandstone of Thorup (1941), the Berry Formation, the Church Creek Formation, and the Vaqueros Formation (fig. 2).

Paleocene and Eocene rocks, exposed along the San Antonio River (fig. 1), are strikingly similar in lithologic appearance and, in many places, are undifferentiated in map compilation (Dibblee, 1971). The unnamed Paleocene formation of Compton (1957) and Eocene formations here consist of massive mudstone and thick- to thin-bedded medium- to coarse-grained sandstone. The Eocene rocks are best exposed in Reliz Canyon and the Church Creek area (fig. 1), where they rest unconformably upon pre-Cenozoic basement rock (Thorup, 1941, 1943; Dickinson, 1956, 1959, 1965; Durham, 1963, 1974). Along the San Antonio River, the Eocene rocks rest conformably(?) upon Paleocene strata, forming, perhaps, one of the few well-exposed Paleocene and Eocene sequences to be found in the northern Santa Lucia Range.

Dickinson (1956, 1959, 1965), Dibblee (1971), and Durham (1974) prepared geologic maps of this area. Pertinent faunal studies of the Paleocene and Eocene rocks in the northern Santa Lucia Range include those of Reiche (1937), Thorup (1941, 1943), Compton (1957), Wardle (1957), Dickinson (1956, 1959), Mallory (1959), Masters (1962), Waters (1963), and Durham (1963, 1974). Additional data are summarized by Graham (1976).

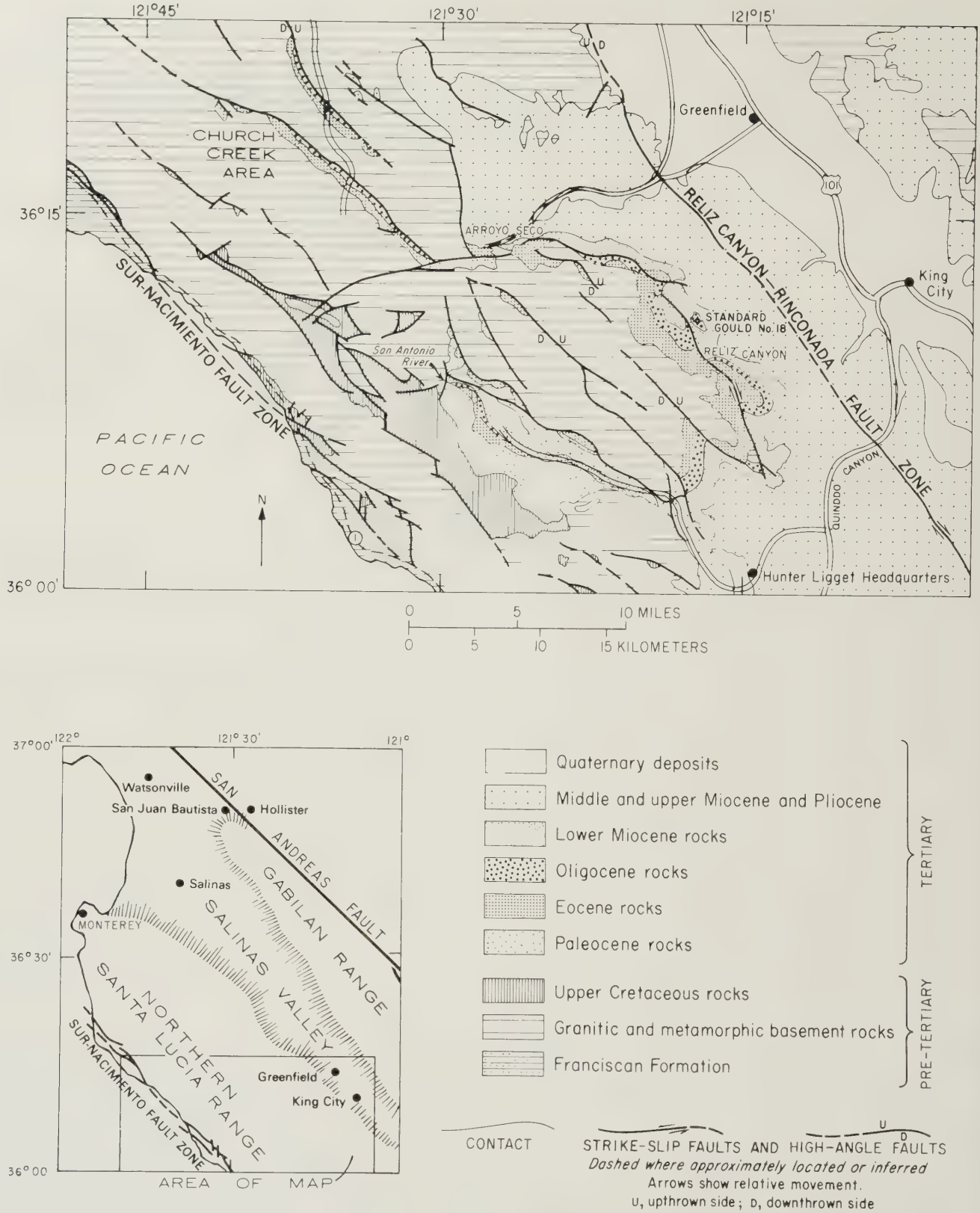

FIGURE 1.—Simplified geologic map of part of the northern Santa Lucia Range, Calif. Modified from Jennings and Strand (1958), Dibblee (1971), Durham (1974), and Nilsen and Link (1975).

SERIES	FORMATION	LITHOLOGY	THICKNESS FEET (METERS)	DESCRIPTION
Miocene / Oligocene	Vaqueros Formation		800–2,000 (244–610)	Thick-bedded to massive, white to gray arkosic sandstone with minor conglomerate and mudstone interbeds; highly crossbedded and contains abundant mollusks.
	Conformable contact			
Eocene	Church Creek Formation		0–1,500 (0–457)	Thin- to thick-bedded olive-gray to light-brown white- to brown-weathering sequence of mudstone and arkosic sandstones; contains minor conglomerate interbeds and abundant foraminifers.
	Berry Formation		0–1,500 (0–457)	Thick-bedded to massive white to yellow sequence of arkosic sandstone and conglomerate. Minor yellow to reddish-purple mudstone interbeds in upper part.
	Unconformity?			
	The Rocks Sandstone of Thorup (1941)		400–2,000 (122–610)	Thick-bedded to massive, gray, resistant arkosic sandstone with minor sandy mudstone interbeds and conglomerate intervals; forms prominent hogbacks and flatirons; contains large dolomitic concretions and mudstone clasts that commonly weather out.
	Lucia Mudstone of Dickinson (1965)		0–500 (0–152)	Thin-bedded greenish-gray silty mudstone; contains a few thin sandstone interbeds; locally is crossbedded and contains abundant foraminifers.
	Junipero Sandstone of Thorup (1941)		0–500 (0–152)	Thick-bedded white to gray pebbly arkosic sandstone with basal conglomerate intervals; locally is crossbedded and contains orbitoidal foraminifers.
	Unconformity			
Paleocene	Unnamed formation (Compton, 1957)		0–5,000 (0–1,524)	Thin- to thick-bedded dark-gray to white sequence of siltstone, mudstone, and arkosic sandstone with minor conglomerate interbeds; locally contains abundant foraminifers.
	Unconformity			
Upper Cretaceous	Unnamed formation	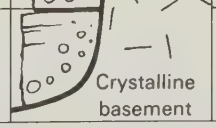	0–5,000 (0–1,524)	Thin- to thick-bedded dark-gray to white sequence of sandstone, conglomerate, mudstone, and siltstone.
	Unconformity			

FIGURE 2.—Composite stratigraphic section of Mesozoic and Cenozoic rocks of the northern Santa Lucia Range, Calif.

MICROFOSSIL DATA

Locations of sections and samples yielding foraminifers are shown on figures 3 through 5. All samples were collected by Link from massive mudstone or mudstone interbeds within sandstone sequences. In general, foraminifers recovered from these samples (table 1) are poorly preserved and commonly deformed. Benthonic foraminifers were found more frequently than planktonic foraminifers, but neither group occurs abundantly.

TABLE 1.—*Occurrence of foraminifers, northern Santa Lucia Range*

[x = present, 0 = cf., ? = questionable identification. See figures 3-5 for location of sections.]

Section	H	G	F	E				D			C	B			A	
Sample No.	Mf2364	Mf2368	Mf2382	Mf2337	Mf2342	Mf2336	Mf2335	Mf2343	Mf2339	Mf2338	Mf2346	Mf2351	Mf2347	Mf2345	Mf2344	Mf2373	Mf2374
Planktonic foraminifers:																	
Clavigerinella sp.	-	-	-	-	-	-	-	-	?	-	-	-	-	-	-	?	
Globorotaloides turgida (Finlay)	x	-	-	-	-	-	-	0	-	x	?	-	-	-	-	-	x
G. sp.	-	-	-	-	-	-	-	-	-	-	-	x	-	-	-	-	-
Morozovella aequa (Cushman and Renz)	-	-	-	-	-	-	-	-	-	-	-	-	-	-	-	-	x
M. aragonensis aragonensis (Nuttall)	0	-	-	-	-	-	-	x	x	0	x	x	x	-	-	x	x
M. aragonensis caucasica (Glaessner)	-	-	-	-	-	-	-	-	x	-	x	-	-	-	-	-	x
M. brodermanni (Cushman and Bermudez)	-	-	-	-	-	-	-	-	0	-	-	-	-	-	-	-	-
M. convexa (Subbotina)	x	-	-	-	-	-	-	-	x	x	-	0	-	-	-	-	x
M. subbotinae (Morozova)	x	-	-	-	-	-	-	-	-	-	x	-	-	-	-	0	x
M. spp.	x	-	-	-	-	-	-	x	-	x	x	-	x	-	-	x	x
Planorotalites pseudochapmani (Gohrbandt)	-	-	-	-	-	-	-	-	-	-	-	-	-	-	-	-	0
Pseudohastigerina spp.	-	-	-	-	-	-	-	-	-	-	-	-	-	-	-	x	x
Subbotina linaperta (Finlay)	-	-	-	-	-	-	-	x	-	-	-	-	-	-	-	-	-
S. patagonica (Todd and Kniker)	-	-	-	-	-	-	-	x	-	-	-	-	0	-	-	-	0
S. pseudoeocaena (Subbotina)	x	-	-	-	-	-	-	x	x	x	x	x	x	-	-	x	x
"S." senni (Beckmann)	-	-	-	-	-	-	-	-	x	x	-	-	-	-	-	-	-
S. spp.	x	-	-	-	-	-	-	x	x	x	x	x	x	-	-	x	x
Truncorotaloides bullbrooki (Bolli)	-	-	-	-	-	-	-	x	0	x	-	-	-	-	-	-	x
T. nitidus (Martin)	-	-	-	-	-	-	-	-	-	0	-	x	-	-	-	-	0
T. pentacameratus (Subbotina)	-	-	-	-	-	-	-	-	-	-	x	0	-	-	-	x	0
T. primitivus (Finlay)	x	-	-	-	-	-	-	0	x	-	x	-	x	-	-	x	x
T. quetrus (Bolli)	-	-	-	-	-	-	-	-	-	-	-	-	-	-	-	-	?
T. soldadoensis angulosus (Bolli)	x	-	-	-	-	-	-	-	-	x	x	-	-	-	-	x	x
T. soldadoensis soldadoensis (Brönnimann)	x	-	-	-	-	-	-	-	-	-	-	x	-	-	-	x	x
T. spp.	-	-	-	-	-	-	-	-	x	x	-	x	x	-	-	x	-
Selected benthonic foraminifers:																	
Ammodiscus incertus d'Orbigny	-	-	-	x	-	-	-	-	-	-	x	x	-	-	-	-	-
Ammodiscoides turbinatus Cushman	-	-	-	-	-	x	-	-	-	-	-	-	-	-	-	-	-
Anomalina dorri aragonensis Nuttall	x	-	-	-	-	-	-	-	x	-	-	-	-	-	-	x	x
A. garzaensis Cushman and Siegfus	-	-	-	-	-	-	-	-	-	x	-	-	-	-	-	-	x
A. umbonata Cushman	-	-	-	-	-	-	-	-	-	-	x	-	x	-	-	-	x
Bathysiphon eocenicus Cushman and Hanna	-	-	-	-	-	-	-	-	-	-	-	x	-	-	-	-	-
Bulimina debilis Martin	0	-	-	-	-	-	-	-	-	-	x	-	-	-	-	x	-
B. macilenta Cushman and Parker	x	-	-	-	-	-	-	-	-	-	x	-	-	-	-	x	-
B. microcostata Cushman and Parker	-	-	-	-	-	-	-	-	-	-	-	-	-	-	-	-	0
Cibicides blanpiedi Toulmin	-	-	-	-	-	-	-	-	-	-	x	-	-	-	-	-	-
C. martinezensis Cushman and Barksdale	-	-	-	-	-	-	-	-	x	-	-	-	-	-	-	-	-
C. pachyderma (Rzehak)	x	-	-	-	-	-	-	-	-	-	-	-	-	-	-	-	-
C. spiropunctatus Galloway and Morrey	-	-	-	-	-	-	-	-	-	-	x	-	-	-	-	-	-
Coryphostoma spiralis (Cushman)	-	-	-	-	-	-	-	-	-	-	-	-	-	-	-	x	-
Cribrostomoides cretaceus Cushman and Goudkoff	-	-	-	x	-	x	x	-	-	-	-	-	-	-	-	-	-
Cyclammina pacifica Beck	-	-	-	-	-	-	-	-	-	-	-	-	x	x	-	-	-
C. samanica (Berry)	-	-	0	-	-	-	-	-	-	-	-	-	-	-	x	-	-
C. sp.	-	-	-	-	-	-	-	-	-	-	-	-	-	-	-	x	-
Dentalina approximata Reuss	-	-	-	-	-	-	-	-	-	-	-	-	-	-	-	-	x
Dorothia cubana (Cushman and Bermudez)	x	-	-	-	-	-	-	-	-	-	-	-	-	-	-	-	-
D. principiensis Cushman and Bermudez	-	-	-	-	-	-	-	-	-	-	-	-	-	-	-	-	-
D. sp.	-	-	-	-	-	-	-	-	-	-	-	-	-	-	-	-	-
Eggerella subconica Parr	-	-	-	-	-	x	-	-	-	-	-	x	-	-	-	-	-
Gaudryina jacksonensis coalingensis Cushman and Hanna	-	-	-	-	-	-	-	-	-	-	x	-	-	-	-	-	-

TABLE 1.—*Occurrence of foraminifers, northern Santa Lucia Range*—Continued

Section	H	G	F	E				D			C	B			A	
Sample No.	Mf2364	Mf2368	Mf2382	Mf2337	Mf2342	Mf2336	Mf2335	Mf2343	Mf2339	Mf2338	Mf2346	Mf2351	Mf2347	Mf2345	Mf2344	Mf2373	Mf2374
Selected benthonic foraminifers--Con.:																	
Globulina laerima Reuss	-	-	0	-	-	-	-	-	-	-	-	-	-	-	-	-	-
Gyroidina florealis White	-	-	-	-	-	-	-	-	-	-	-	-	-	-	-	x	x
G. orbicularis planata Cushman	-	-	-	-	-	-	-	-	-	-	-	x	x	-	-	-	-
Haplophragmoides coalingensis Cushman and Hanna	-	-	-	-	-	-	-	-	-	-	-	0	-	-	-	-	-
H. sp.	-	-	-	-	-	-	-	x	-	-	-	-	-	x	-	-	-
Hyperammina elongata Brady	-	-	-	x	x	x	-	-	x	-	x	-	x	-	-	x	-
Karriella mediaaguaensis Mallory	-	-	-	-	-	-	-	x	-	-	-	-	-	-	-	-	-
Lenticulina altolimbata (Guembel)	-	-	-	-	-	-	-	-	-	-	x	-	-	-	-	x	-
L. convergens Bornemann	x	-	-	-	-	-	-	-	-	-	-	-	-	-	-	-	-
L. inornata (d'Orbigny)	-	-	-	x	-	-	-	-	-	-	-	-	-	-	-	-	-
L. pseudocultrata Cole	-	-	-	-	-	-	-	-	-	-	-	-	-	-	-	x	x
Lituotuba lituiformis (Brady)	-	-	-	-	-	-	-	-	-	-	-	-	-	-	-	-	x
Martinottiella eocenica Cushman and Bermudez	-	-	-	-	-	-	-	-	-	-	-	-	-	-	-	x	-
M. petrosa (Cushman and Bermudez)	-	-	-	0	-	-	-	-	-	-	-	-	-	-	-	-	-
Nodosaria ewaldi Reuss	-	-	-	x	-	-	-	-	-	-	-	x	-	-	-	-	-
N. latejugata Guembel	-	-	-	-	-	-	-	-	-	-	-	-	-	-	-	x	x
Oridorsalis umbonatus (Reuss)	-	-	-	-	-	-	-	-	-	x	-	-	-	-	-	-	-
Osangularia cultur midwayana (Cushman and Todd)	-	-	-	-	-	-	-	-	-	x	-	-	-	-	-	x	x
Pelosina complanata Franke	-	-	-	x	-	x	-	-	-	-	-	-	-	-	-	-	-
Plectofrondicularia kerni Cook	-	-	-	-	-	-	-	-	-	-	-	-	-	-	-	x	x
Pseudonodosaria ovata (Cushman and Applin)	-	-	-	-	-	-	-	-	-	-	-	-	-	x	-	-	x
Pullenia quinqueloba angustata Cushman and Todd	x	-	-	-	-	-	-	-	-	-	-	-	-	-	-	-	-
Rheophax sp.	-	-	-	-	-	-	x	-	-	-	-	-	-	-	-	-	-
Rhabdammina eocenica Cushman and Hanna	x	x	-	x	x	x	x	x	x	x	x	-	x	-	-	-	x
Siliciosigmoilina californica Cushman and Church	-	-	-	x	x	x	x	-	-	-	-	-	-	-	-	-	-
Spiroplectammina directa (Cushman and Siegfus)	-	-	-	-	-	-	-	-	-	x	-	-	-	-	-	-	-
S. gryzbowskii Frizzel	-	-	-	x	-	x	-	-	-	-	-	-	-	-	-	-	-
S. richardi Martin	-	-	-	-	-	-	-	-	-	-	-	-	-	-	-	x	-
Stilostomella cocoaensis (Cushman)	-	-	-	-	-	-	-	-	-	-	x	-	-	-	-	-	x
Textularia lajollaensis Lalicker	x	-	-	-	-	-	-	-	-	-	-	-	-	-	-	-	-
T. sp.	-	-	-	x	-	-	-	-	-	-	-	-	-	-	-	-	-
Tritaxia californica (Mallory)	-	-	-	-	-	-	-	-	-	-	-	-	-	-	-	x	-
Tritaxilina colei Cushman Siegfus	x	-	-	-	-	-	-	-	-	-	-	-	-	-	-	-	x
Trochammina globigeriniformis (Parker and Jones)	-	-	-	-	-	-	x	-	-	-	-	-	-	-	-	-	-
Vaginulinopsis asperuliformis (Nuttall)	-	-	-	-	-	-	-	-	-	-	-	-	-	-	-	x	x
V. mexicana nudicostata Cushman and Hanna	-	-	-	-	-	-	-	-	-	-	-	-	-	-	-	x	x
Vulvulina curta Cushman and Siegfus	-	-	-	-	-	-	-	-	-	-	-	-	-	-	-	-	x

Planktonic foraminifers

Planktonic foraminifers were detected in samples from sections A, B, C, D, and H. The presence of *Morozovella aragonensis aragonensis* or *Globorotaloides turgida* in all the samples indicates a biostratigraphic position no lower than Zone P 7 of Berggren (1972). And, although some of the species recorded range into the middle Eocene, for example, *Subbotina patagonica* and *"S." senni*, no species known to be restricted to the middle Eocene could be reliably identified. For this reason, our preferred interpretation is to assign samples Mf2346, Mf2347, Mf2351, Mf2364, and Mf2373 to Zones P 7–P 8 of Berggren (1972).

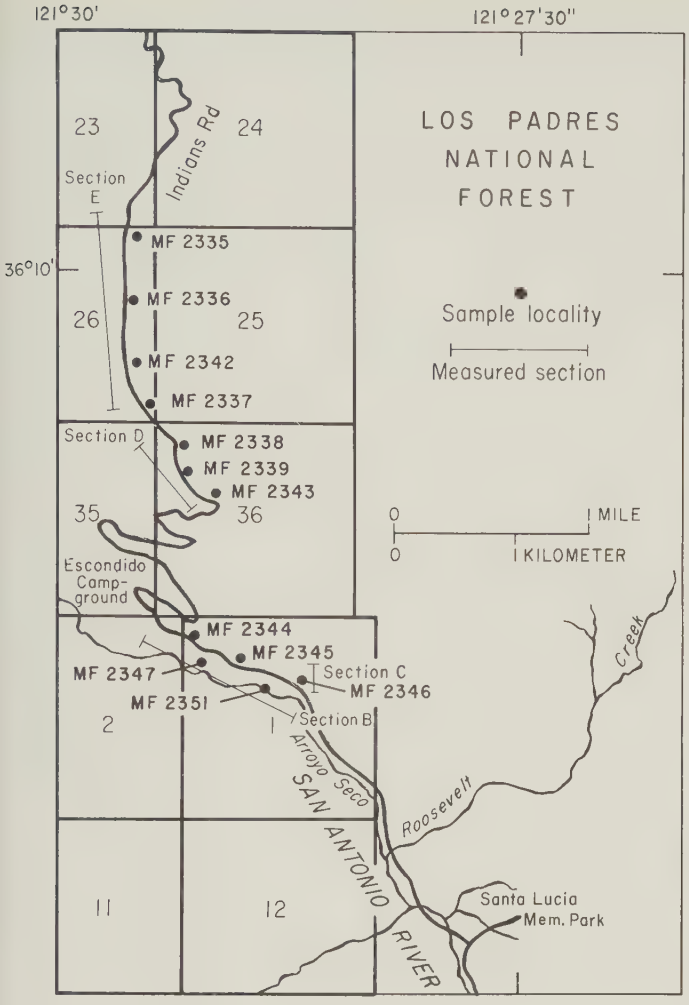

FIGURE 3.—Locations of sections and samples yielding foraminifers, The Indians and Tassajara Hot Spring areas. Base from U.S. Geological Survey, Junipero Serra 15-minute quadrangle.

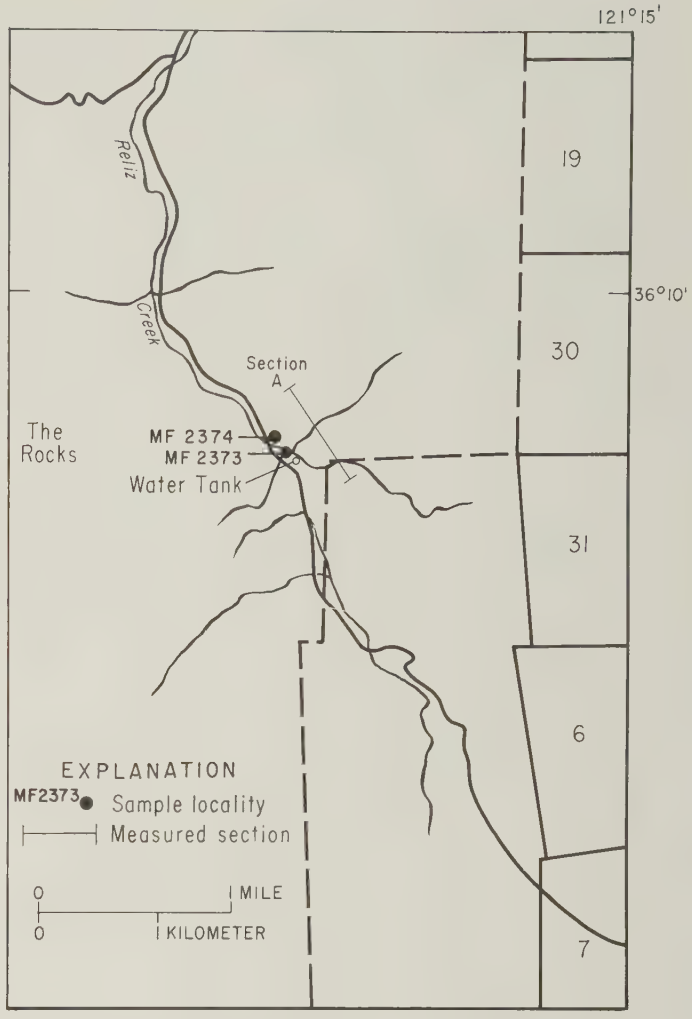

FIGURE 4.—Location of section and samples yielding foraminifers, Reliz Creek. Base from U.S. Geological Survey, Junipero Serra 15-minute quadrangle.

Samples Mf2338, Mf2339, Mf2343, and Mf2374 with *Truncorotaloides bullbrooki* [=*Acarinina densa* (Cushman) sensu Berggren (1968, 1972)] are referred to Zone P 9. Following the calibrations of Berggren (1972), the Zone P 9–P 10 boundary approximates the early-middle Eocene boundary. The planktonic foraminiferal assemblages in our samples are considered to be, therefore, of early Eocene age.

Our interpretation of the planktonic assemblages is supported, in part, by Bukry and others (1977). They reported a nannofossil assemblage referable to the *Tribrachiatus orthostylus* Zone of Bukry (1973) occurring 10 m below the top of the Lucia Mudstone near our section H (see fig. 5). The *Tribrachiatus orthostylus* Zone of Bukry (~Zones NP 11–NP 12 of Martini, 1971) correlates with foraminiferal Zones P 6b to lower part of P 8 (see Berggren, 1972, fig. 5). The foraminiferal and nannofossil data from the Lucia Mudstone in this area are thus in agreement. To the east at section A, our data suggest a slightly younger age for the upper Lucia Mudstone in that the Zone P 8–P 9 boundary occurs in the uppermost Lucia Mudstone. Nannofossils from the Lucia Mudstone in the upper Reliz Creek (Sullivan, 1965) are referable to the *Discoaster lodoensis* Zone of Bukry (1973) (see Poore, 1976). This zone is approximately equivalent to Zone NP 13 of Martini (1971). Berggren (1972) correlated nannofossil Zone NP 13 with the upper part of Zone P 8. Our data suggest that Zone NP 13 extends into the lower part of foraminiferal Zone P 9. The critical point, however, is that the foraminiferal and nannofossil data from the Lucia Mudstone in this area are in basic agreement.

The microfossils with which we are dealing are poorly preserved and, in many cases, are from isolated

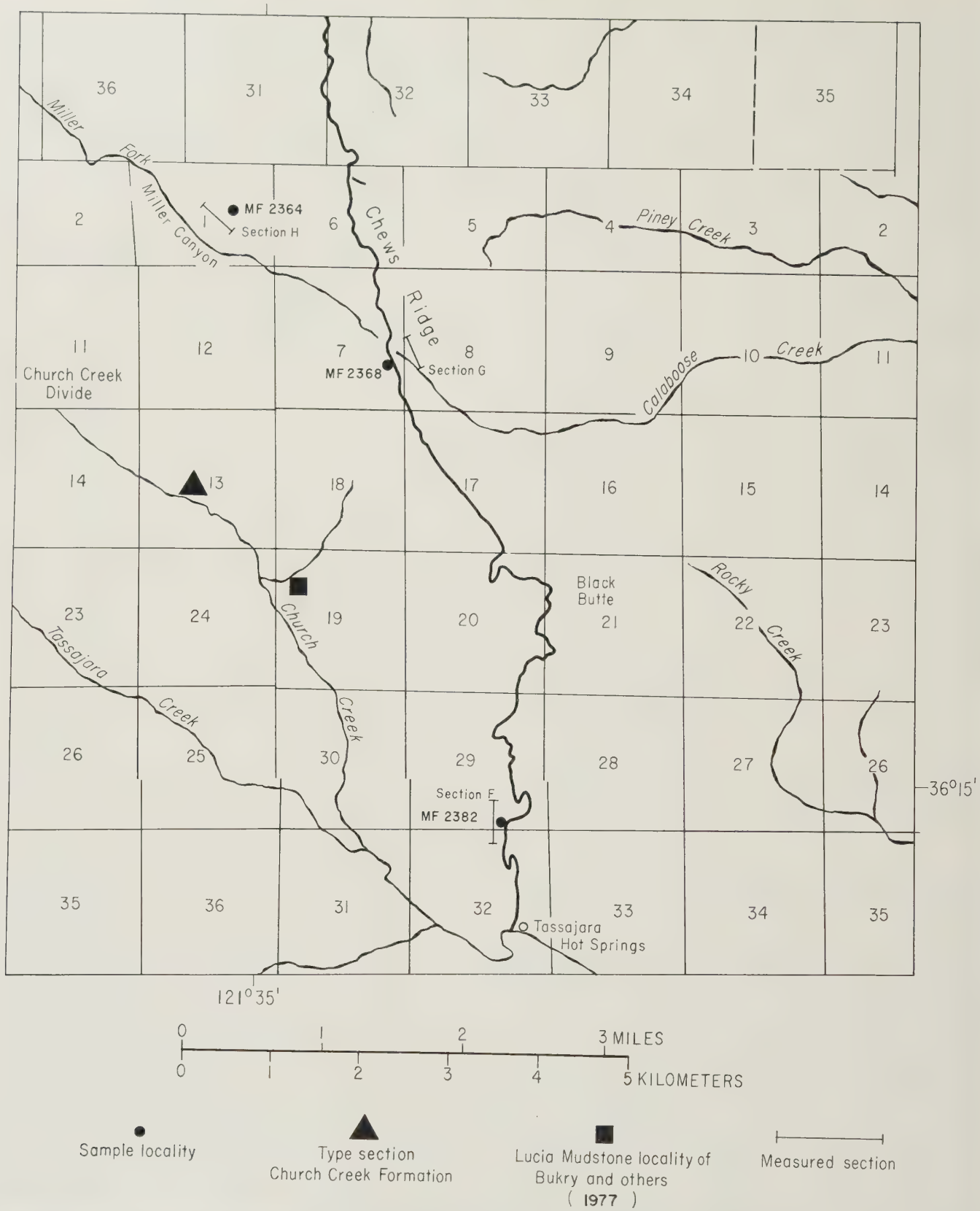

FIGURE 5.—Locations of sections and samples yielding foraminifers, Church Creek area. Base from U.S. Geological Survey, Jamesburg and Lucia 15-minute quadrangles.

samples. We cannot entirely exclude the possibility that some of these assemblages represent basal middle Eocene levels.

Benthonic foraminifers

Benthonic foraminifers recovered from the eight sections examined in this study (fig. 6) range in age from Paleocene to middle Eocene.

Paleocene assemblages containing *Ammodiscoides turbinatus*, *Cribrostomoides cretaceus*, *Silicosigmoilina californica*, and *Spiroplectammina gryzbowskii* among others were found in the Paleocene mudstone unit of section E. These foraminifers are referable to the Ynezian Stage on the basis of known ranges of these species in California.

Early Eocene foraminifers representing the Penutian and Ulatisian Stages were found in sections A, C, D, F, and H. Sample Mf2346 from the Eocene sandstone and mudstone unit of section C is assigned a Penutian age on the basis of the cooccurrence of *Anomalina umbonata*, *Bulimina debilis*, *Cibicides blanpiedi*, and *C. spiropunctatus*. A similar or possibly slightly younger age is suggested for sample Mf2339 from the Eocene sandstone and mudstone unit of section D by the presence of *Anomalina dorri aragonensis* and *Cibicides martinezensis*. Sample Mf2338 from the same unit of section D, however, is assigned a definite Ulatisian age on the basis of the cooccurrence of *Anomalina garzaensis*, *Oridorsalis umbonatus*, *Osangularia cultur midwayana*, and *Spiroplectammina directa*.

In section A, the Lucia Mudstone contains a relatively diverse late Ulatisian assemblage that includes *Anomalina garzaensis*, *Bulimina debilis*, *Gaudryina jacksonensis coalingensis*, *Nodosaria latejugata*, *Osangularia cultur midwayana*, *Stilostomella cocoaensis*, and *Vaginulinopsis mexicana nudicostata*. A similar assemblage was found in the Lucia Mudstone of section H. Diagnostic species in sample Mf2364 include *Anomalina dorri aragonensis*, *Cibicides pachyderma*, *Pullenia quinqueloba angustata*, and *Tritaxilina colei*.

Sample Mf2382 from the Eocene unit of section F is likewise referred to the Ulatisian Stage on the basis of the presence of *Cyclammina* cf. *C. samanica*. Little more can be said concerning the correlation of this section with sections A and H owing to the paucity of foraminifers.

The youngest bethonic foraminifers of middle Eocene age were recovered from section B. Samples Mf2351 and Mf 2347 from the Church Creek Formation contain a Narizian assemblage that includes *Anomalina umbonata*, *Eggerella subconica*, *Gyroidina orbicularis planata*, and *Haplophragmoides* cf. *H. coalingensis*. The appearance of *Cyclammina pacifica* in the upper two samples, Mf2344 and Mf2345, suggests a Narizian to possibly basal Refugian age.

PALEOBATHYMETRY

Benthonic assemblages from the eight sections are indicative of bathyal water depths greater than 1000 m with access to open marine conditions. The presence of planktonic foraminifers in many samples corroborates the open-marine conditions interpreted from the benthonic assemblages. The following paleobathymetric interpretations are based on modern foraminiferal distributions as utilized by Sliter and Baker (1972).

Lower bathyal water depths of 2000 m or more are indicated for the Paleocene mudstone of section E by the presence of *Ammodiscus*, *Cribrostomoides*, *Dorothia*, *Martinottiella*, *Pelosina*, *Silicosigmoilina*, *Rhabdammina*, and *Hyperammina*. Slightly shallower lower bathyal water depths ranging from 1500 to 2500 m are suggested for the early Eocene sediments of the Lucia Mudstone and the Eocene sandstone and mudstone unit of sections C, D, F, and H. Assemblages from these sections contain species of *Anomalina*, *Osangularia*, *Hyperammina*, *Bulimina*, *Stilostomella*, *Ammodiscus*, *Cyclammina*, *Pullenia*, and *Karreriella* and several nodosariid species.

Conversely, assemblages from the Lucia Mudstone of section A indicating middle to lower bathyal paleoenvironments ranging from 1000 to 2000 m include *Gaudryina*, *Bulimina*, *Hyperammina*, *Osangularia*, *Coryphostoma*, *Gyroidina*, *Lituotuba*, *Stilostomella*, and a diverse group of nodosariids characterized by *Dentalina*, *Lenticulina*, *Nodosaria*, *Pseudonodosaria*, *Plectofrondicularia*, and *Vaginulinopsis*.

Middle Eocene samples from the Church Creek Formation of section B are most suggestive of middle bathyal water depths (500–1500 m). The assemblages contain *Anomalina*, *Cyclammina*, *Gyroidina*, *Haplophragmoides*, and *Pseudonodosaria*.

Two trends are apparent from these paleobathymetric data. The first is an apparent upward shoaling from lower bathyal or possibly abyssal water depths in the Paleocene to middle bathyal water depths in the middle Eocene. The second is a westward deepening of the early Eocene bathymetric gradient evidenced by the depth interpretations from coeval assemblages in the Lucia Mudstone of section A to deeper water assemblages in sections B and H.

CORRELATIONS

Correlation of sections A through H is shown in figure 6. Ynezian deep-water assemblages of section E

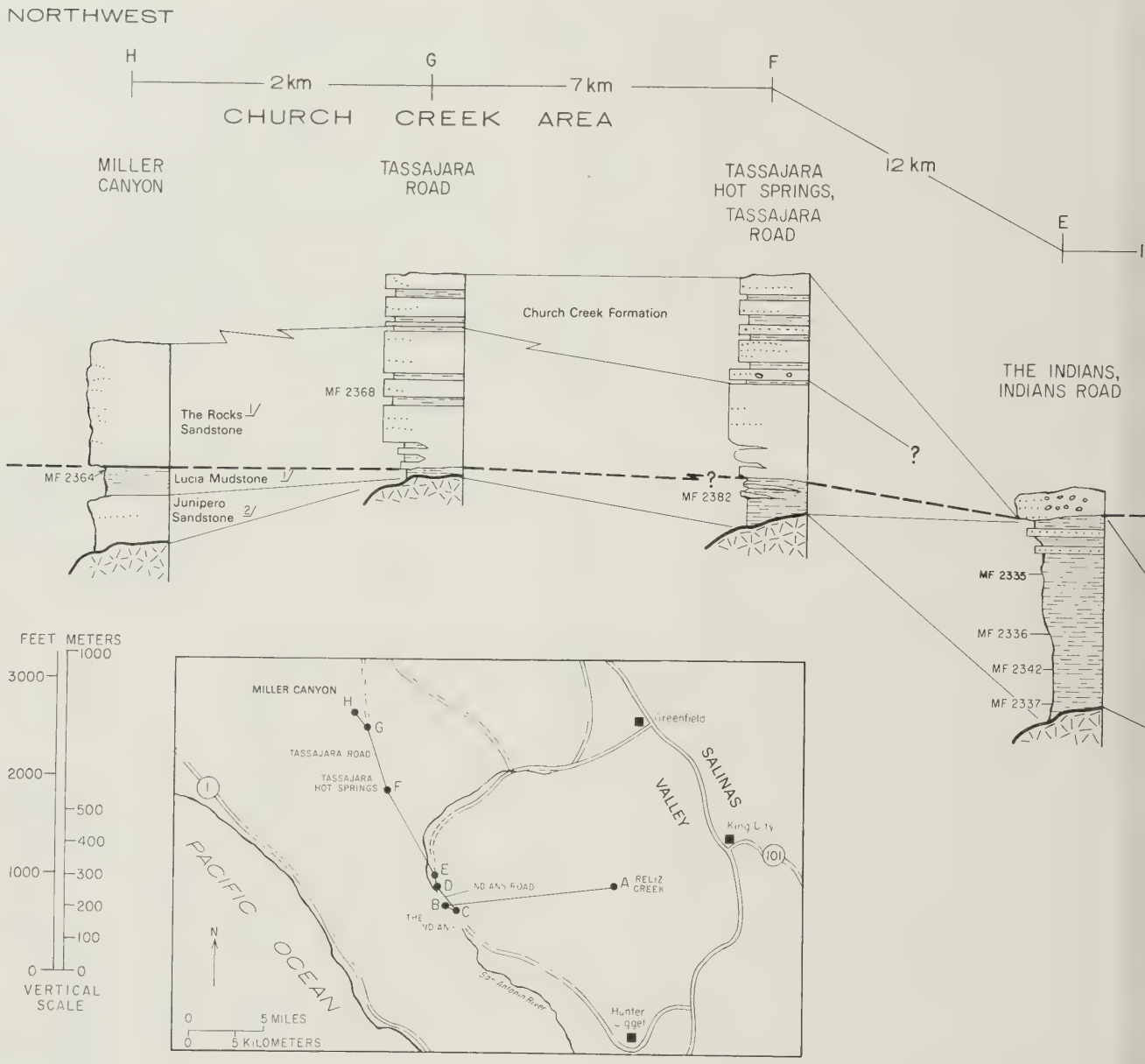

FIGURE 6.—Generalized cross section from Miller Canyon to Reliz Creek, northern Santa Lucia Range. See figure 2 for co
sections not drawn to scale. Heavy dashed line, estimated positio

are succeeded by the Penutian to Ulatisian assemblages from the Eocene sandstone and mudstone of sections C and D. Ulatisian assemblages from the Lucia Mudstone of section A are apparently coeval to similar assemblages in sections F and H. The Rocks Sandstone and Church Creek(?) Formation of section B contain the youngest foraminiferal assemblage, Narizian and Ulatisian benthonic assemblages (see table 2). agree with previous age interpretations (see Nilsen and Link, 1975).

The single sample from The Rocks Sandstone, sample Mf2368 of section G, unfortunately contains only nondiagnostic, rare, and poorly preserved foraminifers. Ulatisian benthonic foraminifers are known from shale layers within The Rocks Sandstone in the Church Creek area (see Kleinpell and others, 1967). On the basis of this information and data from the adjacent Lucia Mudstone and Church Creek(?) Formation, the age of The Rocks Sandstone is considered as Ulatisian to Narizian.

The approximate position of the Zone P 9–P 10 boundary, which approximates the early Eocene-middle Eocene boundary of international usage, is shown on figure 6 by a heavy dashed line drawn above con-

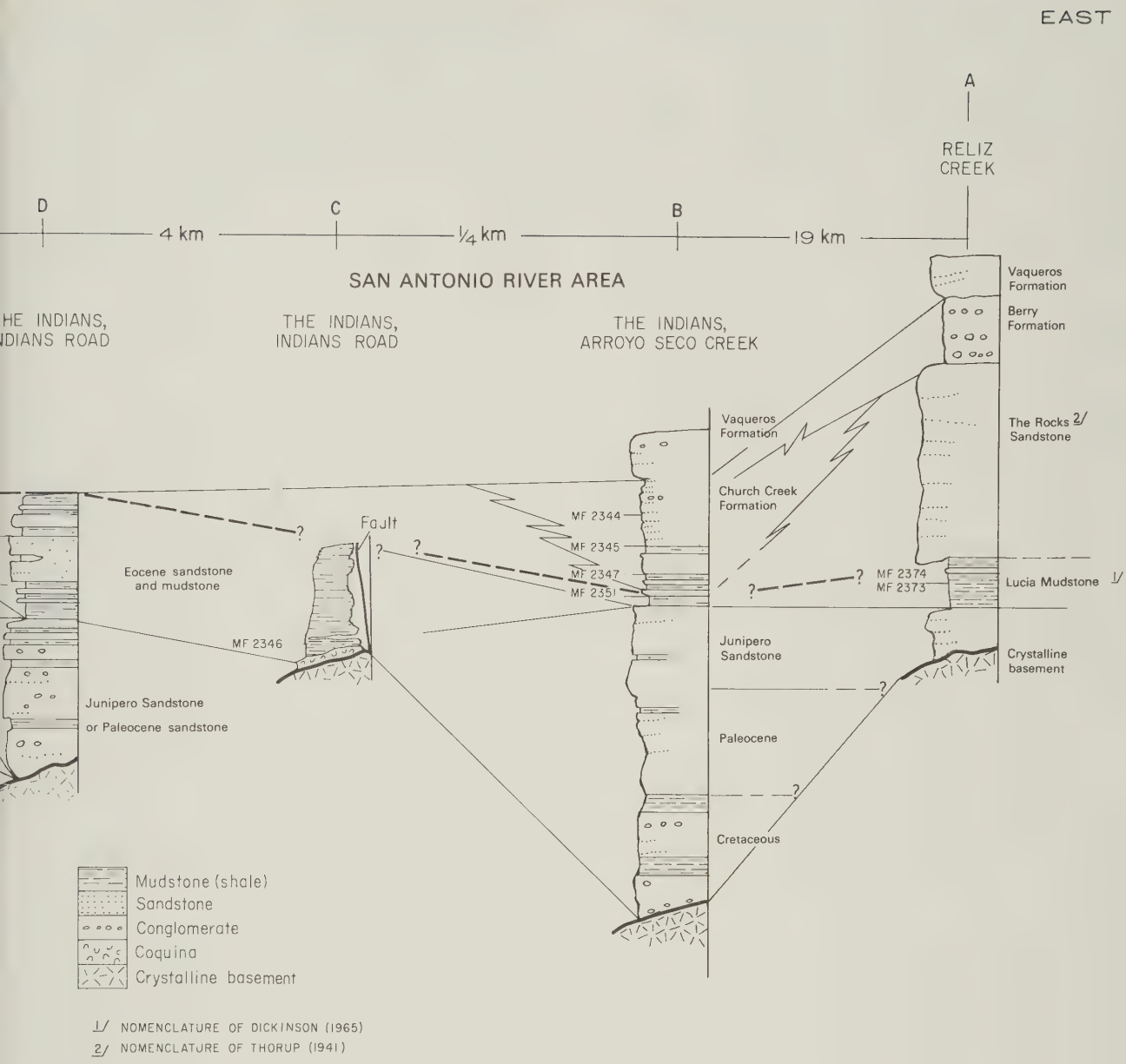

phic column. See figures 3 through 5 for locations of sections and foraminifer samples. Horizontal distance between cene-middle Eocene boundary as determined by planktonic foraminifers.

trol points considered to be of early Eocene age on the basis of planktonic foraminifers. With the exception of samples from section B, planktonic foraminiferal assemblages are found in association with Penutian and Ulatisian benthonic assemblages (see table 2). The association of Penutian and Ulatisian benthonic foraminifers with early Eocene planktonic microfossils is in accord with other recent studies (for example, Bukry and others, 1977; Schmidt, 1975; Steineck and Gibson, 1971; and Poore, 1976). In section B, however, planktonic foraminiferal assemblages that we interpret as early Eocene are associated with Narizian benthonic assemblages. At the present time, data from the Santa Lucia Mountains are not sufficient to determine if this association is correct.

The Rocks Sandstone, where recognizable, conformably overlies units considered to be of early Eocene age (fig. 6) and could be, therefore, as old as early Eocene. An upper limit for the age of The Rocks Sandstone in terms of planktonic microfossils can be estimated from the work of Brabb and others (1971), who report nannofossils of the youngest Eocene *Discoaster barbadiensis* Zone from the type Church Creek Formation (adjacent to our sections G and H, see

TABLE 2.—*Provincial benthonic foraminiferal stage, planktonic foraminiferal zone, and age assignments of foraminiferal assemblages, northern Santa Lucia Range, Calif.*

[See figures 3, 4, and 5 for location of sections and microfossil samples. P zones after Berggren (1972).]

Section	Microfossil sample No.	Benthonic foraminiferal stage	Planktonic foraminiferal zone	Age
A	Mf2374	Ulatisian	P 9	Early Eocene
	Mf2373	Ulatisian	P 7 - P 8	Early Eocene
B	Mf2344	Narizian, possibly Refugian	---	Middle Eocene
	Mf2345	Narizian, possibly Refugian	---	Middle Eocene
	Mf2347	Narizian	P 7 - P 8	Early Eocene
	Mf2351	Narizian	P 7 - P 8	Early Eocene
C	Mf2346	Penutian	P 7 - P 8	Early Eocene
D	Mf2338	Ulatisian	P 9	Early Eocene
	Mf2339	Penutian-Ulatisian	P 9	Early Eocene
	Mf2343	(nondiagnostic)	P 9	Early Eocene
E	Mf2335	Ynezian	---	Paleocene
	Mf2336	Ynezian	---	Paleocene
	Mf2342	Ynezian	---	Paleocene
	Mf2337	Ynezian	---	Paleocene
F	Mf2382	Ulatisian	---	Early Eocene
G	Mf2368	(nondiagnostic)	---	---
H	Mf2364	Ulatisian	P 7 - P 8	Early Eocene

fig. 5). Assuming time-equivalence of the Church Creek Formation in this area, it is apparent that The Rocks Sandstone could be as young as late Eocene provided The Rocks Sandstone and Church Creek Formation represent a continuous sequence.

REFERENCES CITED

Berggren, W. A., 1968, Phylogenetic and taxonomic problems of some Tertiary planktonic foraminiferal lineages: Tulane Studies in Geology, v. 6, no. 1, p. 1–22.

——— 1972, A Cenozoic time-scale—some implications for regional geology and paleobiogeography: Lethaia, v. 5, p. 195–215.

Brabb, E. E., Bukry, David, and Pierce, R. L., 1971, Eocene (Refugian) nannoplankton in the Church Creek Formation near Monterey, central California: U.S. Geol. Survey Prof. Paper 750–C, p. C44–C47.

Bukry, David, 1973, Low-latitude coccolith biostratigraphic zonation: Deep Sea Drilling Proj. Initial Repts., v. 15, p. 685–703.

Bukry, David, Brabb, E. E., and Vedder, J. G., 1977, Correlation of Tertiary nannoplankton assemblages from the Coast and Peninsular Ranges of California: Latin American Geol. Cong., 2d, Caracas, Venezuela, 1973. (In press.)

Compton, R. R., 1957, New Paleocene formation in the central Coast Ranges, California [abs.]: Geol. Soc. America Bull., v. 68, no. 12, pt. 2, p. 1820–1821.

Dibblee, T. W., Jr., 1971, Geologic maps of four 15-minute quadrangles (1:62 500) in the northern Santa Lucia Range (King City, Soledad, Jamesburg, and Junipero Serra quadrangles): U.S. Geol. Survey open-file maps.

Dickinson, W. R., 1956, Tertiary stratigraphy and structure west of the Arroyo Seco, Monterey County, California: Stanford, Calif., Stanford Univ. M.S. thesis, 160 p.

——— 1959, Structural relationships of Church Creek and Creek faults. Santa Lucia Range, California [abs.]: Geol. Soc. America Bull., v. 70, no. 12, pt. 2, p. 1715.

——— 1965, Tertiary stratigraphy of the Church Creek area, Monterey County, California: California Div. Mines and Geology Spec. Rept. 86, p. 25–44.

Durham, D. L., 1963, Geology of the Reliz Canyon, Thompson Canyon, and San Lucas quadrangles, Monterey County, California: U.S. Geol. Survey Bull. 1141–Q, 41 p.

——— 1974, Geology of the southern Salinas Valley area, California: U.S. Geol. Survey Prof. Paper 819, 111 p.

Graham, S. A., 1976, Tertiary stratigraphy and depositional environments near Indians Ranch, Monterey County, California, *in* Fritsche, A. E., ed., and others, The Neogene symposium: Soc. Econ. Paleontologists and Mineralogists, Pacific Sec., Ann. Mtg., San Francisco, Calif., April 1976, p. 125–136.

Jennings, C. W., and Strand, R. G., 1958, Geologic map of California, Olaf P. Jenkins edition, Santa Cruz sheet: California Div. Mines, scale 1:250 000.

Kleinpell, R. M., Weaver, D. W., and Doerner, D. P., 1967, Glimpses of the Paleogene depositional record west, north, northeast, and east of the Gabilan Mesa, *in* Guidebook, Gabilan Range and adjacent San Andreas fault: Am. Assoc. Petroleum Geologists and Soc. Econ. Paleontologists and Mineralogists, Pacific Sec., p. 38–44.

Link, M. H., 1975, Stratigraphy and sedimentology of The Rocks Sandstone, Santa Lucia Range, California: Geol. Soc. America Abs. with Programs, v. 7, no. 3, p. 341–342.

Mallory, V. S., 1959, Lower Tertiary biostratigraphy of the California Coast Ranges: Tulsa, Okla., Am. Assoc. Petroleum Geologists, 416 p.

Martini, E., 1971, Standard Tertiary and Quaternary calcareous nannoplankton zonation: Internat. Conf. Planktonic Microfossils, 2d, Rome, Proc., p. 739–785.

Masters, B. A., 1962, Eocene Foraminifera from the Church Creek area, Santa Lucia Mountains, Monterey County, California: Berkeley, California Univ., M.A. thesis, 91 p.

Nilsen, T. H., and Link, M. H., 1975, Stratigraphy, sedimentology, and offset along the San Andreas fault of Eocene to lower Miocene strata of the northern Santa Lucia Range and the San Emigdio Mountains, Coast Ranges, central California, *in* Weaver, D. W., ed., and others, Paleogene symposium and selected technical papers: Am. Assoc. Petroleum Geologists–Soc. Econ. Paleontologists and Mineralogists–Soc. Explor. Geophysicists, Pacific Secs., Ann. Mtg., Long Beach, Calif., April 1975, p. 367–400.

Poore, R. Z., 1976, Microfossil correlation of California lower Tertiary sections, a comparison: U.S. Geol. Survey Prof. Paper 743–F, 8 p.

Reiche, Parry, 1937, Geology of the Lucia quadrangle, California: California Univ. Pubs., Dept. Geol. Sci., Bull., v. 24, p. 115–168.

Schmidt, R. R., 1975, Upper Paleocene-middle Eocene planktonic biostratigraphy from the Great Valley of California and adjacent areas, and correlation to the west coast microfaunal stages, *in* Weaver, D. W., ed., and others, Paleogene symposium and selected technical papers: Am. Assoc. Petroleum Geologists–Soc. Econ. Paleontologists and Mineralogists–Soc. Explor. Geophysicists, Pacific Secs., Ann. Mtg., Long Beach, Calif., 1975, p. 439–455.

Sliter, W. V., and Baker, R. A., 1972, Cretaceous bathymetric distribution of benthic foraminifers: Jour. Foraminiferal Research, v. 2, no. 4, p. 167–183.

Steineck, P. L., and Gibson, J. M., 1971, Age and correlation of the Eocene Ulatisian and Narizian Stages, California: Geol. Soc. America Bull., v. 82, p. 477–480.

Sullivan, F. R., 1965, Lower Tertiary nannoplankton from the California Coast Ranges—Pt. 2, Eocene: California Univ. Pubs., Dept. Geol. Sci., Bull., v. 53, p. 1–75.

Thorup, R. R., 1941, Vaqueros Foramation (Tertiary) at its type locality, Junipero Serra quadrangle, Monterey County, California [abs.]: Geol. Soc. America Bull., v. 52, no. 12, pt. 2, p. 1957–1958.

——— 1943, Type locality of the Vaqueros Formation: California Div. Mines Bull. 118, p. 463–466.

Wardle, W. C., 1957, Eocene foraminifera from the Lucia Shale: Berkeley, California Univ., M.A. thesis, 88 p.

Waters, J. N., 1963, Oligocene foraminifera from Church Creek, Santa Lucia Mountains, California: Berkeley, California Univ., M.A. thesis, 102 p.

Jour. Research U.S. Geol. Survey
Vol. 5, No. 6, Nov.–Dec. 1977, p. 747–752

TERTIARY AND QUATERNARY DEPOSITS AT THE PALISADES, CENTRAL ALASKA

By WARREN E. YEEND, Menlo Park, Calif.

Abstract.—The Palisades of the Yukon River, located near the geographic center of Alaska, has long been an attraction to people traveling along the river. Numerous scientific field parties have viewed or visited the locality and published short accounts of their observations. The river bluffs are as much as 90 meters high and are composed of Tertiary lignite-rich sedimentary rocks and frozen Quaternary sand, silt, and gravel. Resampling and analysis of pollen show that the Tertiary rocks are Miocene rather than Miocene and Pliocene as previously thought. The Miocene flora, possessing a number of conifer and hardwood-tree types, was more varied than the present vegetation and indicates a warmer and wetter climate than at present. The area is frequently referred to as the boneyard because of the common occurrence of large bones of Pleistocene mammals within the frozen silts.

Approximately 56 kilometers down the Yukon River from the village of Tanana, Alaska, are high silt bluffs forming the south bank of the river. Known as The Palisades (Orth, 1967), the bluffs extend for 11 km along the river, are as much as 90 meters high, and stand as vertical to slightly overhanging walls where composed of frozen silt. Also referred to as the boneyard because of the occasional large animal bones found in the frozen silt, the area has been visited by many who have traveled on the river. In addition to frozen silt, sand, and gravel, the bluffs also contain gently dipping, Tertiary clastic sediments with lignite beds.

During my visit to The Palisades in the summer of 1974, I measured several sections, collected samples for pollen analysis, and found part of a bison skull on the narrow beach near the west end of the bluffs. This paper reviews and summarizes the scattered published accounts dealing with The Palisades and presents the results of my study.

PREVIOUS WORK

H. T. Allen seems to have been responsible for the naming of The Palisades (Orth, 1967). Allen's (1887) report described the exploration, landforms, and general geology of the areas adjacent to the Copper, Tanana, and Koyukuk Rivers. No mention of The Palisades was made in the text of the report, but the name appeared on the map of the Koyukuk River. Allen probably named it either on July 11, 1885, during his trip down the Yukon River from Noklúket (Tanana) to Nuláto, or on the return trip in late July 1885.

In 1889, I. C. Russell of the U.S. Geological Survey accompanied a U.S. Coast and Geodetic Survey party on a trip up the Yukon River for the purpose of establishing the boundary between Alaska and the Northwest Territory. Russell probably viewed The Palisades from the deck of the steamboat *Yukon* and obtained most of his information about the area from the captain, Charles Peterson. Russell (1890) stated that the area is shown on the U.S. Coast and Geodetic Survey map of Alaska and adjoining territory and gave a general description of the locality, mentioning that the fine-grained deposits are of lacustrine origin. He said that mammoth remains were reported to have come from the locality and referred to the frozen deposits as bone beds.

J. E. Spurr was the first to include any detailed geology of the area and devoted about 2½ pages to a discussion with a sketch of the section. He named the light-colored sandstone and conglomerate at the base of the cliffs the "Palisades Conglomerate." From the unit, he collected "finely preserved cones" that subsequently were tentatively identified by F. H. Knowlton as *Pinus macclurii* of late Miocene or Pliocene age. Spurr recognized that a fault had juxtaposed the Palisades Conglomerate against younger, unconsolidated deposits that he termed the "Yukon Silts." Writing of the Yukon Silts, he stated, "about 6 feet below the surface, part of the skeleton of a mammoth was found, and tusks and other bones of this and other mammals are so commonly found here that, as has been said, the locality is known among the miners as the 'Boneyard,' although it is put down on the maps as The Palisades." A tooth was identified by F. A. Lucas, of the National Museum, as belonging to the species *Elephas primigenius*. Lignite beds within the silt were described as

having burned, and beds that were still hot and smoking contained baked, fused, and brilliantly colored adjacent rocks.

Brooks (1902, p. 557) quoted the following statement, about a coal deposit, received in a personal letter from H. N. Wood, assistant engineer, Revenue Cutter Service: " 'about 60 miles below Tanana, just above the bluff known as The Palisades, is a vein claimed to be 20 feet thick. A prospecting tunnel has been dug, but no coal has been taken out for the use of steamers that I am aware of.' "

In the summer of 1903, A. J. Collier spent 3 months studying the geology and coal resources along 1900 km of the Yukon River. Collier (1903) reported that the silt at The Palisades was unique in that it contained lignite. Because a tunnel driven through one of the lignite beds (6 m thick) had collapsed by 1902, the bed could not be examined underground. The lignite was reported to be of inferior quality, scarcely changed from wood or peat.

As part of the first Smithsonian expedition to Alaska, A. C. Maddren visited The Palisades in 1904 but found only a few scattered bone fragments. His report (1905) included a general description of the locality.

As a continuation of Maddren's study, G. W. Gilmore was detailed in 1907 to continue the work under the sponsorship of the Smithsonian. He devoted 4½ pages of text to The Palisades and included two photographs and two sketches (Gilmore, 1908). Gilmore found numerous mammoth and several bison bones (*Bison crassicornis*(?)). The small streams dissecting the bluffs were followed inland for "considerable distances," and although their banks in many places presented clean-cut exposures of silt, no fossil remains were found. The skull of an *Ovibos* sp. nov. was found on a narrow shelf near the underlying Palisades Conglomerate. Gilmore devoted a major part of his discussion on The Palisades to a description of the wasting of the frozen banks into the Yukon River.

In a paper on the unconsolidated sediments of the lower Yukon Valley, Eardley (1938a) presented a detailed discussion of The Palisades section. Included in the report are a sketch map showing a prominent east-west-trending fault, a geologic cross section, a columnar composite section showing more than 360 m of measured section, and two photographs of the area. The lignite-bearing section, approximately 180 m thick, is believed to be part of the "coal-bearing formation" of the Healy region (Capps, 1919, p. 44–51). The Palisades Conglomerate of Spurr, which Eardley (1938a, fig. 6) places above the lignite-rich beds, is tentatively correlated by Eardley with the Nenana Gravel of Capps (1919, p. 58). Overlying the Palisades Conglomerate of Spurr (1898) is a series of gravel, sand, and loam layers more than 120 m thick. A mammoth tusk dug out of a gravel lens in this part of the section allowed Eardley to state that this upper part of the section is "definitely Pleistocene." From an analysis of the sedimentary structures in the fine-grained silt and its contained, air-breathing snails, Eardley concluded that the silt was deposited on a valley plain by aggrading streams and was not of lacustrine origin, as Russell (1890) had concluded earlier.

In another article, Eardley (1938b) devoted only a short discussion to bank slumping at The Palisades; however, the three photographs of The Palisades he used as illustrations are some of the best published.

Hrdlička (1943, p. 178) mentioned the boneyard only briefly in his accounts of experiences in Alaska from 1926 to 1931. He described the area as "terrifying frozen mud bluffs, smell of a huge cow stable about the place, blackish dirty ice in uppermost twenty to thirty feet of the gloomy exposures." He landed at the base of the exposures but did not see any fossils.

Cass (1959) showed a narrow band of Tertiary(?) rocks at The Palisades on a reconnaissance geologic map compiled from previous published accounts and photogeology. His information on The Palisades was taken from Eardley (1938a).

MacNeil, Wolfe, Miller, and Hopkins (1961) published the most recent work dealing with the age of the Tertiary rocks at The Palisades. On the basis of fossil flora, including a cone of *Pinus banksiana* and pollen, collected by D. M. Hopkins of the U.S. Geological Survey, the rocks were dated as Miocene and Pliocene.

THIS STUDY

I spent parts of August 1, 3, and 4, 1974 at The Palisades. The study area is near the geographic center of the State. Good exposures with beach access were those at sample localities 1, 3, 4, and 5 (fig. 1); however, had the river been much higher, these exposures would have been accessible only from a boat. The river banks between sample localities 3 and 4 (4.8 km) are vertical or nearly vertical and extend into the river with no exposed beach. These cliffs are made up of frozen silt that gives off an objectionable odor of putrefaction. I walked the beach between sample localities 1 and 3 (6.4 km) but, because of extensive slumping and slope wash, found no good exposure.

General geology

The Tertiary rocks are exposed only north of the east-west-trending fault that cuts the unconsolidated

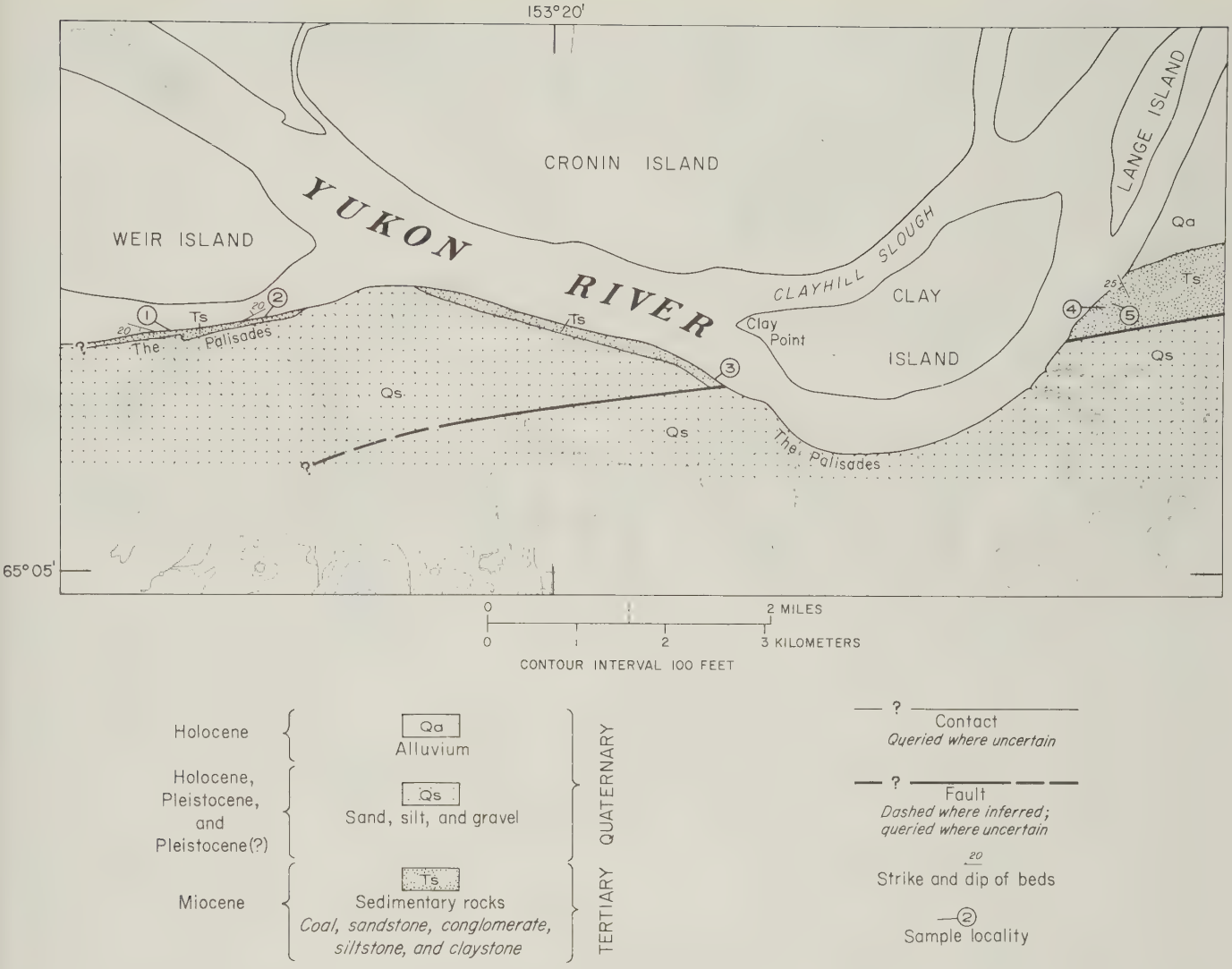

FIGURE 1.—Simplified geology and sample localities of The Palisades. Base from U.S. Geological Survey Melozitna A–1 quadrangle, 1:63 360.

Quaternary sediments (fig. 1). All of the overlying sediments shown in the measured sections (fig. 2) are lumped together as silt, sand, and gravel (fig. 1).

An east-west fault, most likely an extension of the Kaltag fault system (Patton, 1973), cuts rocks as young as Pleistocene and juxtaposes Tertiary and Pleistocene rocks.

Sample area 1 (fig. 2) near the west edge of the map area exposes a thin Tertiary section that dips 20° S. The contact with the flat, overlying, unconsolidated Pleistocene(?) gravel is covered. Approximately 30 m of silt, sand, and gravel is present.

Sample area 3 is near the center of the map area just south of Clay Point, the downstream tip of Clay Island (fig. 1). The Tertiary section, 12 m thick, is horizontal to very gently dipping and stands as bold, dissected, white-colored cliffs. The Palisades Conglomerate of Spurr (1898) is a semiconsolidated granule conglomerate and sandstone. Exposed at river level, it extends about one-fourth of the way up the river bluff (fig. 3). The unit is in fault contact with the overlying silt, sand, and gravel, which are 64 m thick.

The thickest section of Tertiary rocks is exposed at sample areas 4 and 5 on the east side of the map area (fig. 1). More than 30 m of lignite-rich sedimentary rocks is exposed in the river bluff, beginning at river level. This section (fig. 2) is a composite in that the lower 9 m is exposed a few hundred meters upstream from the bulk of the exposed section. At least five distinct lignite beds ranging in thickness from 1 to 5 m, are present. The rocks dip 25° SW and are probably overlain by Pleistocene and Holocene sediments; however, the upper contact is obscured by soil.

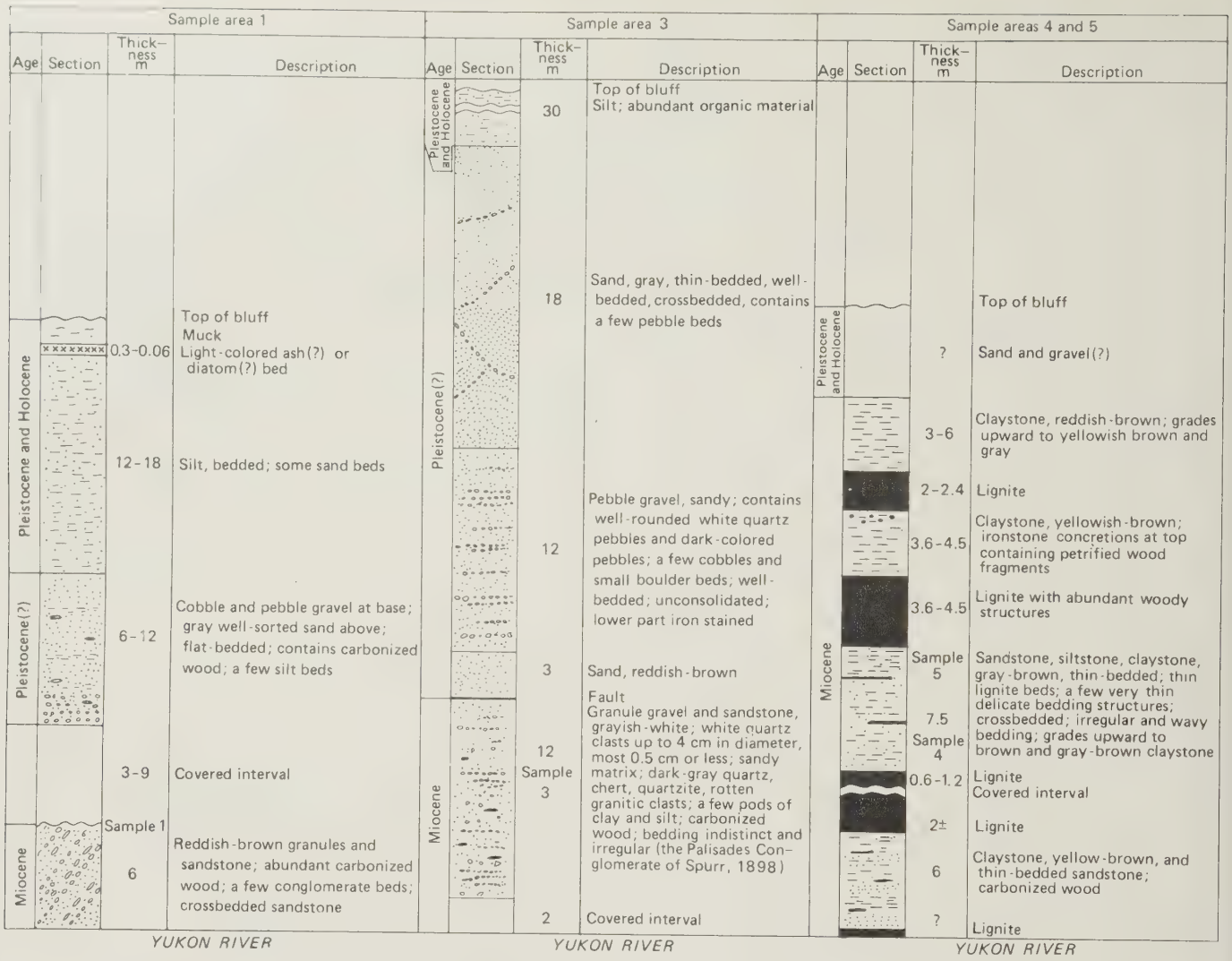

FIGURE 2.—Measured river bank sections at three locations along The Palisades. See figure 1 for sample locations.

FIGURE 3.—Aerial view south across the west tip of Clay Island toward the middle part of The Palisades. The Palisades Conglomerate of Spurr (1898) forms the bold, dissected cliffs extending about one-fourth of the way up the river bluff (sample area 3).

Sample analysis and age of Tertiary rocks

The geographic location of the samples is shown on the geologic map (fig. 1), and their positions in the measured sections are given in figure 2. Samples 1, 3, 4, and 5, collected for pollen analysis, consist of carbonized wood fragments, lignite, carbonaceous material, siltstone, and claystone within the Tertiary rocks. The pollen analysis was done in the U.S. Geological Survey laboratory in Denver, Colo. Samples 1, 3, 4, and 5 are similar in pollen content (table 1), and the pollen of sample 3 was particularly well preserved. The pollen assemblages indicated a pine-spruce-hemlock forest with occasional fir and perhaps juniper. Hardwoods were present, including *Pterocarya*, *Carya*, *Ilex*, and, perhaps, *Populus*(?) and *Ulmus*(?), although these are minor elements amounting to only about 1–4 percent of the pollen spore count. *Betula* and *Alnus* were particularly important in the local

TABLE 1.—*Counts of pollen and spores from four samples collected from The Palisades of the Yukon River*

[From an unpublished report prepared by Estella Leopold and Ellen Daniels. x, present but not in tally]

	Sample numbers			
	1	3	4	5
Pinaceae undetermined	14.7	17.3	16.3	17.1
Pinus	9.9	9.0	24.6	20.2
Picea	5.8	6.5	2.4	8.9?
Abies cf. *lasiocarpa*		.5		
Abies?		.5		
Pseudotsuga type		.3?	.3	.7
Tsuga	1.6		1.0	1.8
T. canadensis type	.5	3.8	.3	.4
T. mertensiana type	.5	x		.4
T. diversifolia type			.7	
cf. *Juniperus*	.2	.3		
cf. *Ephedra*	.2			
Betula	29.3	9.5	20.1	9.2
Betula trilete scar	.5			6.7
Alnus 6 pores, polar scar		.3		.4
6 pores		.3		
5 pores	3.5	5.8	2.1	2.5
4 pores	16.1	14.0	9.0	6.4
3 pores	.2		.3	.4
Ostrya-Carpinus type				
Myrica type		x		
Pterocarya	3.9	1.8	1.0	.7
Carya	.2	.5		1.8
Ilex		x		
Ulmus?	.5?	.3?		
Salix	.9	2.3	11.4	1.8
Populus?				.4
Chenopodiaceae	.2			
Artemisia		.5		
Lonicera		.3		
Ericales	.7	.5	.7	.4
Geranium		.3	.3	
Myrtaceae		.3		
cf. *Acer*		.3		
Myriophyllum			.3	
Larix?			.3	
Onagraceae				
NAP dicots undetermined	.9	2.0		8.5
Cyperaceae	.9	.8	3.5	2.5
Liliales				
Monocots undetermined		.5	.7	.7
Gramineae?		.3		
Sphagnum	3.7	8.0	2.1	3.9
Selaginella selaginelloides				.4
Monolete spores undetermined	3.9	10.0	1.4	2.8
Trilete spores undetermined	.4		.3	
Lycopodium undetermined	.5	.8		1.4
L. clavatum type	.2			
L. annotinum type		2.8		
Total percent	99.9	100.9	99.7	100.4
Total count	(434)	(400)	(289)	(282)
No. exotic taxa	5	6	5	4
Total percent exotic taxa	15.0	15.4	26.9	23.1

vegetation. Various shrubs of Ericales (heath), *Artemisia* (sage), *Lonicera*, and *Salix* were present, as well as herbs such as *Geranium*, sedges, and other monocots. The forest was probably scattered, because tree pollen is only about 25–35 percent of the total count. Birch and alder most likely made up a large part of the intervening cover. Alder suggests wet areas, as do Sphagnum moss and *Myriophyllum;* however, no algae were found. The trees and shrubs that do not currently grow in Alaska include *Pinus*, *Pterocarya*, *Carya*, *Ilex*, *Ostrya-Carpinus* type, *Tsuga* cf. *canadensis*, and *T.* cf. *diversifolia*, *Ulmus* type. Their percentages in the counts range from 15 to 26 percent. These presently exotic elements suggest that the rocks are certainly Neogene in age and are Miocene and probably early or middle Miocene on the basis of pollen analyses from southern Alaska. The presence of *Artemisia* in sample 3 is particularly important, as it is rare to find members of the Compositae in the Neogene of Alaska. The *Alnus* with six pores and a polar scar in samples 3 and 5 suggests *Alnus maximowiczii*, now of Asia. The *Betula* with the polar trilete scar in samples 1 and 5 is a common form in Miocene materials from the Alaska Range. Though it is conceivable that the beds are of Pliocene age, the diversity of hardwoods does not support that interpretation. Also, the counts of exotic (Tertiary-relict) elements are higher than spectra previously considered as Clamgulchian (late Miocene and Pliocene). Therefore, the beds are probably of early or middle Miocene age or equivalent to the Seldovian Stage.

Sample 2 is one-half of a bison skull which I found on the beach (fig. 2). It probably came from the silt exposed upstream between sample localities 3 and 4. It is tentatively identified as a skull of *Bison crassicornis* (Charles Repenning, U.S. Geol. Survey, oral commun., 1976) and may be from the same area as a scapula of *Bison crassicornis*(?) that was collected by Gilmore (1908) at The Palisades on the Yukon River in 1907.

GEOLOGIC HISTORY

Pollen studies suggest a Miocene age for the Tertiary rocks. This is younger than the Tertiary coal-rich rocks exposed upriver near Hess Creek (Drew coal mine area), which are probably Eocene or Oligocene on the basis of pollen analysis (Estella Leopold, unpub. data). However, other small isolated outcrops of Tertiary rocks have been mapped upriver that are believed to be of Miocene and younger(?) age (Chapman and others, 1975; MacNeil and others, 1961).

During Miocene time, the climate was warmer and wetter than at present ,and there were many more types of trees. Certainly the presence of lignite implies a much warmer and wetter climate.

The character of the Pleistocene sediments implies an abundance of running water, probably glacial runoff, as well as windy, dusty conditions leading to the building of thick loess deposits. Small isolated lakes and ponds trapped and preserved various forms of animal and vegetable life, which were subsequently carbonized and partially petrified and frozen.

The Palisades has long been an attraction to scientific parties journeying along the Yukon River. Yet

there has not been, in the 89 years since the area was officially named, a systematic field survey of the vertebrate fossil at the locality. This seems to be a relatively untouched, fertile area of study for a vertebrate paleontologist.

REFERENCES CITED

Brooks, A. H., 1902, The coal resources of Alaska: U.S. Geol. Survey Ann. Rept. 22, pt. 3, p. 557.

Capps, S. R., 1919, The Kantishna region, Alaska: U.S. Geol. Survey Bull. 687, 116 p.

Cass, J. T., 1959, Reconaissance geologic map of the Melozitna quadrangle, Alaska: U.S. Geol. Survey Misc. Geol. Inv. Map I–290.

Chapman, R. M., Yeend, W. E., Brosgé, W. P., and Reiser, H. N., 1975, Preliminary geologic map of the Tanana and northeast part of the Kantishna River quadrangles, Alaska: U.S. Geol. Survey open-file map 75–337.

Collier, A. J., 1903, Coal resources of the Yukon, Alaska: U.S. Geol. Survey Bull. 218, 71 p.

Eardley, A. J., 1938a, Unconsolidated sediments and topographic features of the lower Yukon Valley: Geol. Soc. America Bull., v. 49, no. 2, p. 303–341.

——— 1938b, Yukon channel shifting: Geol. Soc. America Bull., v. 49, no. 3, p. 343–357.

Gilmore, C. W., 1908, Smithsonian exploration in Alaska in 1907 in search of Pleistocene fossil vertebrates: Smithsonan Misc. Colln., v. 51, no. 3, 38 p.

Hrdlička, Aleš, 1943, Alaska diary, 1926–1931: Lancaster, Pa., The Jacques Cattell Press, 414 p.

MacNeil, F. S., Wolfe, J. A., Miller, D. J., and Hopkins, D. M., 1961, Correlation of Tertiary formations of Alaska: Am. Assoc. Petroleum Geologists Bull., v. 45, no. 11, p. 1801–1809.

Maddren, A. G., 1905, Smithsonian exploration in Alaska in 1904 in search of mammoth and other fossil remains: Smithsonian Misc. Colln., v. 49, 117 p.

Orth, D. J., 1967, Dictionary of Alaska place names: U.S. Geol. Survey Prof. Paper 567, p. 736.

Patton, W. W., Jr., 1973, Reconnaissance geology of the northern Yukon-Koyukuk province, Alaska: U.S. Geol. Survey Prof. Paper 774–A, 17 p.

Russell, I. C., 1890, Notes on the surface geology of Alaska: Geol. Soc. America Bull., v. 1, p. 99–162.

Spurr, J. E., 1898, Geology of the Yukon gold district, Alaska: U.S. Geol. Survey Ann. Rept. 18, pt. 3, p. 87–392.

Jour. Research U.S. Geol. Survey
Vol. 5, No. 6, Nov.–Dec. 1977, p. 753–759

PETROLOGY OF BASALT FROM THE EAST PACIFIC RISE NEAR 21° NORTH LATITUDE

By JAMES G. MOORE, WILLIAM R. NORMARK, GORDON R. HESS, and CHARLES E. MEYER, Menlo Park, Calif.

Abstract.—Four dredge hauls of fresh tholeiitic basalt lava were recovered from a 3.3-kilometer-wide zone at the axis of the East Pacific Rise. Petrologic and major-element chemical studies indicate that the basalt ranges from moderately fractionated varieties to one sample enriched in iron and titanium. The four samples show no symmetrical compositional zonation across the ridge axis, but the two least fractionated and youngest samples occur on the east side of the ridge axis.

A rock dredging program at the crest of the East Pacific Rise near lat 21° N. (fig. 1) was carried out in January 1976 aboard the U.S. Geological Survey research vessel *S.P. Lee*. The samples represent young basalt flows formed within 2 kilometers of the rise axis and were collected in water depths of 2630–2680 meters (fig. 2). The bathymetry and structure of the area were mapped in detail in September 1974, using the deep-tow instrument package of the Marine Physical Laboratory of Scripps Institution of Oceanography (Spiess and Tyce, 1973). A relatively high crestal block, about 5 km wide, consists of an inner extrusion zone, about 2.5 km wide, marked locally by rough volcanic relief of about 40 m flanked by lower relief zones of extensive cracking and faulting. Seismic reflection profiles and bottom photographs taken with the deep tow indicate that the main extrusion zone is nearly free of sediment and is characterized by fresh pillowed and sheetlike lava flows (Normark, 1975).

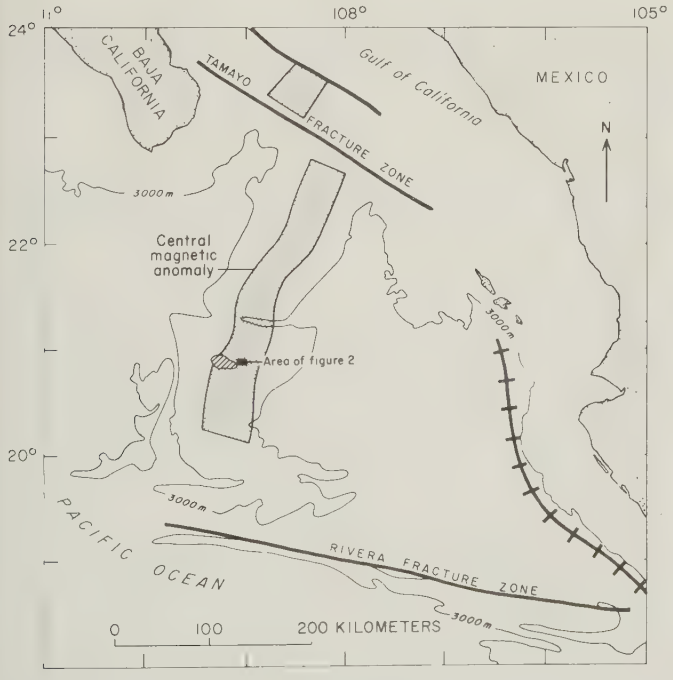

FIGURE 1.—Crest of East Pacific Rise (shown by 3000-m bathymetric contours) and central magnetic anomaly (shaded) near the mouth of the Gulf of California. Small diagonally ruled area is deep-tow study area of Larson (1970); bold railroad line is axis of northern extension of Middle America trench. From Larson and Spiess (1969).

Four dredges of fresh basalt samples were taken within and immediately adjacent to the main extrusion zone (fig. 2) such that the two outermost dredges are about 3.3 km apart and the two inner dredges are evenly spaced between the outer ones and about 1.1 km apart. More than 50 percent of the total dredge attempts failed because of locally rough topography. The dredge locations are based on a combination of satellite positions for the ship and dead reckoning using the echo-sounder depths along the track fitted to the detailed bathymetric map of the crestal area prepared from the deep-tow survey (Normark, 1976). The deep-tow survey used bottom-anchored acoustic transponders that provided relative positioning to ±25 m or less. The positions of the dredge samples with respect to the detailed bathymetry are probably good to within several hundred meters (fig. 2).

The purpose of this sampling program was two-fold: to determine the general petrologic characteristics of the basalt at the axis of this spreading ridge where it is well defined just south of the complexities of the Gulf of California and to compare the basalts with those collected from the Mid-Atlantic Ridge at lat 37° N. (FAMOUS project area) to see

FIGURE 2.—Bathymetric map of crest of East Pacific Rise south of lat 21° N. showing location and direction of four dredge hauls; assumed navigational uncertainly shown by shaded area. Deep-tow bathymetric profile of figure 3 shown where it crosses detailed map area (*A*–*A*)′. Modified from Normark (1976).

if they showed the type of geographic compositional zonation discovered in the inner rift valley at that site (Ballard and others, 1975; Bryan and Moore, 1977).

Acknowledgments.—We thank the captain, F. V. Medeiros, and crew of the *S.P. Lee* for their help on HOTRX, Leg 1 of cruise *Lee* 1–76–MX, and especially Doug Dolan, who assisted on all dredging operations.

TOPOGRAPHY

A deep-tow profile across the entire crestal area of the East Pacific Rise (fig. 3) displays topographic symmetry about the uplifted axial block, which lies near 2600-m water depth. Opposing, inward-facing sets of fault scarps can be matched out to 12 km from the axis. Relief across faults of 100–200 m is typical for the lineated topography on the flanks of the rise (Larson, 1971). The axial block stands on the average only about 100 m above the relatively smooth sea floor to either side and lies on an axis of symmetry that corresponds to the center of the central magnetic anomaly and to the center of an area that is devoid of resolvable sediment cover in profiles taken with the deep-tow seismic reflection system (Normark, 1976; Larson and Spiess, 1969).

The irregular, steep-sided local relief within the central 25 km of the axial block is produced primarily by constructional volcanic accumulations of pillow lava (fig. 3, upper right) and associated rubble piles. Sheetlike lava flows are much less common within this central zone. Bottom photographs indicate little or no sediment dusting the lava surfaces in this main extrusion zone. Lineated topographic forms are uncommon (fig. 2), and few features can be traced between profiles several hundred meters apart.

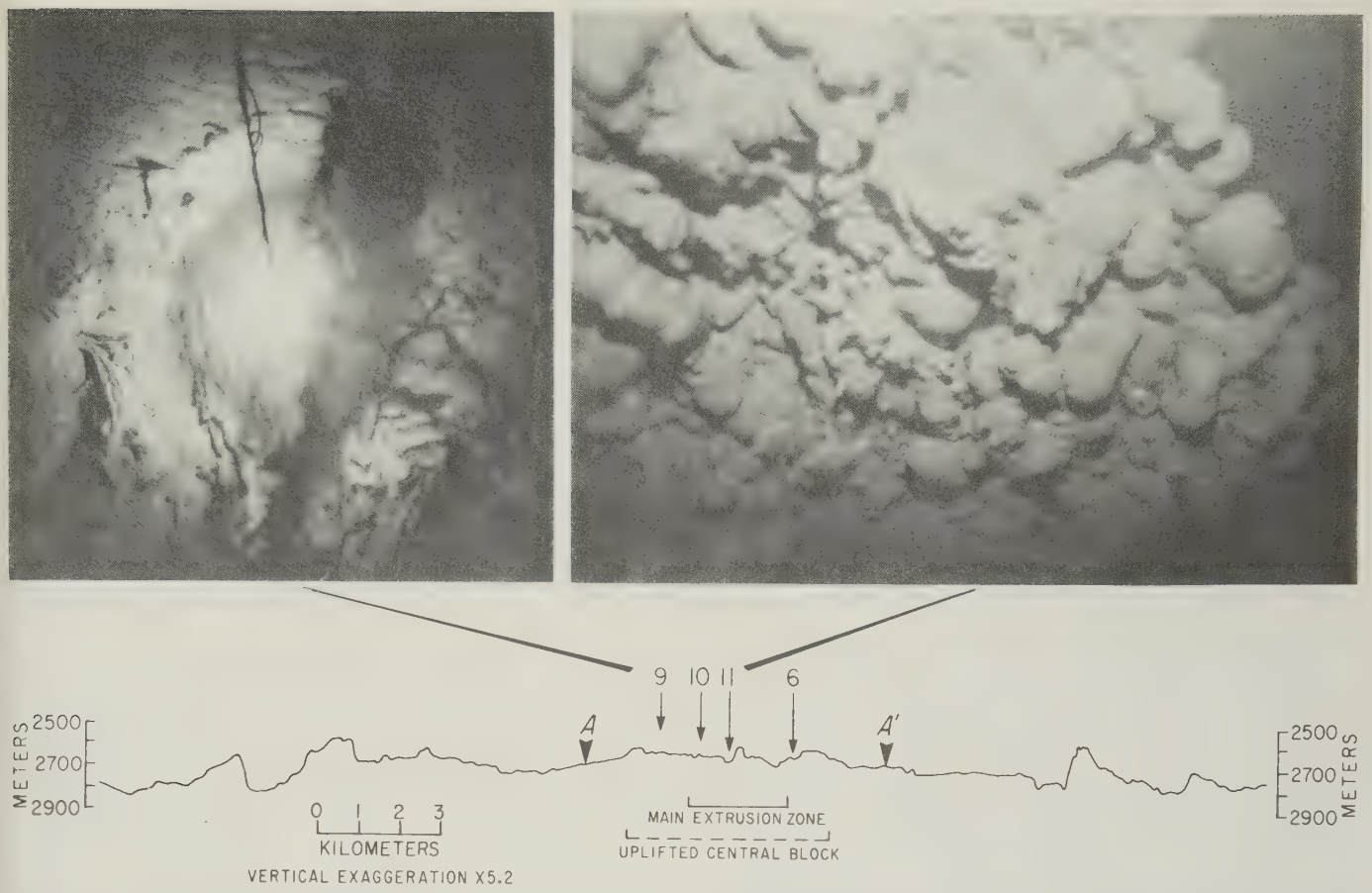

FIGURE 3.—Deep-tow-generated bathymetric profile along line *A–A'* of figure 2. General location of four dredge hauls shown by arrows. Photographs show sheet lava flow cut by fissure near station 9 (upper left) and steep-fronted pillowed flow lobe near station 11 (upper right).

This axial zone of rough volcanic terrain is flanked by zones of more linear topography oriented parallel with the general trend of the East Pacific Rise at lat 21° N. The linear topographic forms appear to be produced by normal faults (Normark, 1976), although scarps rarely reach 50 m in height. This faulting suggests that crustal extension dominates outside the main extrusion zone. Even clearer evidence for extension is found west of the main extrusion zone, where numerous open fissures 1–2 m wide (fig. 3) trend parallel to the axis of the rise. Individual branching and subparallel fissures have been traced for a distance of more than 80 m in bottom photographs. The general relief in the area of the fissures is markedly subdued. The thin sediment cover, seen in bottom photographs but not thick enough to be resolved in the deep-tow reflection profiles, partly covers some lava surfaces but is not thick enough to account for the smooth sea floor (relative to the main extrusion zone). It seems likely that extensive flooding by low-viscosity magmas accounts for the subdued relief outside the main extrusion zone.

The dredged lava samples were collected from these contrasting topographic zones. Dredge 11 is closest to the center of the main extrusion zone; dredges 6 and 10 are from near the edges of this zone of irregular volcanic relief (figs. 2, 3). Dredge 9 is from within the low-relief terrain of numerous open fissures. The amount of freshly broken lava fragments recovered ranges from 8 kilograms (dredge 9) to 110 kg (dredge 11).

PETROLOGY

The dredged rocks consist of fragments of fresh basalt pillows and slabs broken from hollow pillows or sheet flows. Dredge 6 is composed primarily of slabs about 60 mm thick; 9 includes pillow joint blocks as well as thin 10 mm-thick glassy sheets; 10 is a large pillow fragment; and 11 includes pillow and thick slab fragments. All the fragments still retain some of the original glassy crust formed by quenching against sea water at the time of eruption of the flows. The outer glassy crust is weathered, producing a thin

TABLE 1.—*Petrology of East Pacific Rise basalt near lat 21° N.*

Sample No.	Volume percent[1]					Depth (meters)	MnFeO[4]	Palagonite	Specific gravity	Other[5]
	Olivine[2]	Plagioclase[2]	Pyroxene	Glass[3]	Vesicles					
6B	1.4	2.7	--	95.9	0.9	2650-75	10	3	2.81-.82	S
6B2	1.3	3.2	--	95.5	.8		14	4		S
9A	1.7	3.6	--	94.7	.4	2630-40	225	30	2.89	S
9A2	2.4	3.6	.1	93.9	.4		275	20		
10A2	1.7	7.7	.6	90.0	1.5	2670-80	400	36	2.89	
11A	.9	2.3	.4	96.4	.4	2640-60	--	--	2.90-.91	
11A2	.4	1.8	--	97.8	.5		4	4		

[1]Constituents other than vesicles are calculated vesicle-free. More than 1000 points counted.

[2]Phenocrysts, microphenocrysts, and some rounded plagioclase and clinopyroxene crystals.

[3]Includes crystallites.

[4]Average thickness of manganese-iron oxide and palagonite layers in micrometers.

[5]S, small rare spinel crystals.

palagonite rind, which in turn is coated with a thin crust of hydrous manganese-iron oxide.

Thin sections of the glassy crust, which include approximately the outermost 10 mm of the flows, were prepared after impregnation in epoxy. Modal analyses showing the volume percent phenocrysts, glass, and vesicles were made, and the average thickness of the palagonite and MnFeO layers were measured (table 1). These data show that the lavas are relatively poor in early crystals (phenocrysts and microphenocrysts), containing 2–10 volume percent. Plagioclase, the dominant crystal in all samples, is accompanied by and is intergrown with olivine. Plagioclase and olivine occur as euhedral phenocrysts and microphenocrysts that are commonly skeletal when small and more euhedral when larger. The olivine is in the composition range Fo_{79-86}.

Clinopyroxene is present in minor amounts as early formed crystals in samples from three of the four dredge hauls and is commonly intergrown with plagioclase. In sample 10, clinopyroxene occurs in larger resorbed and rounded crystals. The only other crystalline phase enclosed in glass is chrome spinel, which occurs as rare, tiny octahedra in two of the sample sites (table 1).

Small vesicles are present in the outer 10 mm of all the submarine lava samples in amounts of 0.4–1.5 volume percent (average, 0.7). The lavas have about the same vesicularity as lavas dredged from the Juan de

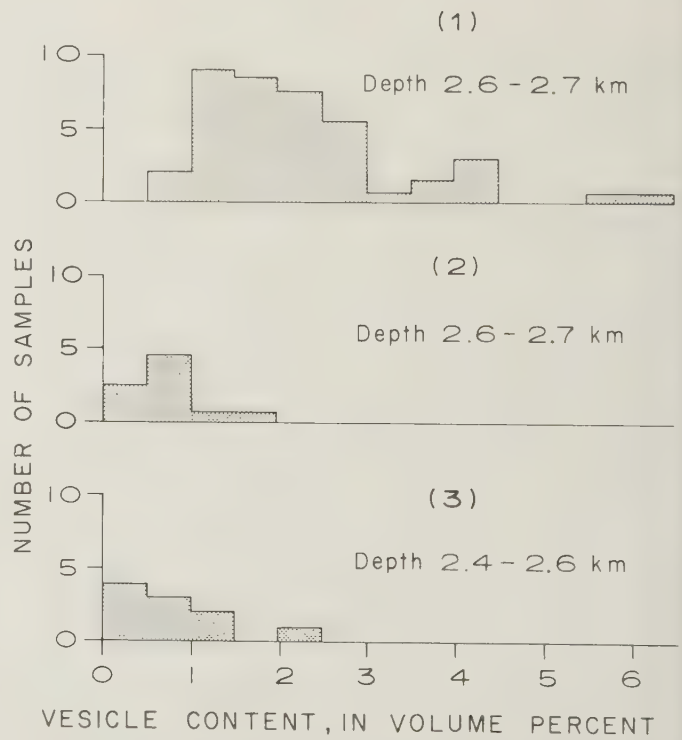

FIGURE 4.—Measurements of percentage of vesicles in outer 10 mm of submarine lava from three spreading-ridge axes: (1) Mid-Atlantic Ridge at lat 37° N. (FAMOUS project area), (2) East Pacific Rise at lat 21° N., and (3) Juan de Fuca Ridge at lat 46° N.

Fuca Ridge near lat 46° N. (fig. 4). Both of these Pacific suites are distinctly less vesicular than samples collected from the Mid-Atlantic Ridge near lat 37° N. at comparable depths. The vesicles are invariably lined with minute (1–2 micrometers) sulfide spherules that systematically increase in size in vesicles inward from the outer pillow surface. Larger sulfide globules (5–20 μm) unassociated with vesicles are common in the glass margins, where they occur as nearly perfect spheres in glass commonly caught in reentrants in skeletal plagioclase and olivine crystals.

The average thickness of palagonite ranges from 3 to 36 μm, and that of MnFeO, from 4 to 400 μm. If the rate of growth of MnFeO is taken as 3 μm/1000 yr, then the rocks range in age from about 1300 to 130 000 yr. The layer thickness permits division into two age groups: samples 6 and 11 belong to a young group, 9 and 10 to an older group.

CHEMISTRY

The basaltic glass and olivine compositions were determined with an ARL–EMX microprobe utilizing a 15-kilovolt excitation potential, 0.025-μA specimen current, and a swept beam raster of 10×10 μm (tables 2, 3). Wet-chemically analyzed natural basaltic glasses and forsteritic olivines were used as standards. Corrections for background, atomic number effects, absorbtion, and characteristic fluorescence were made using a modified online data reduction program (Yakowitz and others, 1973).

Microprobe analyses of basalt glass from outer quenched pillow rims provide a measure of the composition of the basalt liquid at the time of quenching on the ocean floor (table 2). Two chips of glass, which were taken from separate rock fragments in three of the four dredged samples, were each analyzed. The similarity of these duplicate analyses (table 2) demonstrates only a small variation in the basalt glass within the individual dredge hauls. The glasses are undersaturated tholeiites ranging from 4.8 to 13.1 percent normative olivine. The samples show a linear trend in the plot of the FeO/MgO ratio and TiO_2 content (fig. 5) consistent with the general trend of other basalt glasses (Bryan and Moore, 1977). The general range of compositions is similar to rocks analyzed from the Galapagos spreading center (Anderson and others, 1975). One sample (10) is an iron-rich variety similar to those from the Galapagos area that have particularly high magnetic intensities. The presence of iron-rich basalt on this spreading ridge is unexpected because such basalt is associated with large-amplitude magnetic anomalies on the Galapagos spreading ridge (Anderson and others, 1975), whereas the East Pacific Rise at lat 21° N. shows little evidence of a magnetization high within the central anomaly (Klitgord, 1976). Further sampling will be required to determine how extensive the iron-rich basalts are at lat 21° N.

TABLE 2.—*Microprobe analyses of basalt glass from dredge hauls from the East Pacific Rise near lat 21° N.*

	6B	6B2	9A	9A2	10A2	11A	11A2
SiO_2	50.30	50.07	50.63	50.12	50.34	50.73	50.50
Al_2O_3	16.23	16.27	14.82	14.81	14.16	15.15	14.97
FeO*	9.15	9.00	10.65	10.61	12.08	10.11	10.16
MgO	8.05	8.03	7.45	7.46	6.55	7.73	7.68
CaO	11.91	12.01	11.73	11.80	10.68	11.83	11.87
TiO_2	1.40	1.36	1.70	1.70	2.38	1.47	1.50
Na_2O	2.75	2.79	2.70	2.72	2.89	2.68	2.70
K_2O	.22	.21	.10	.09	.14	.12	.12
P_2O_5	.16	.15	.13	.15	.22	.11	.13
Total	100.17	99.89	99.91	99.46	99.44	99.93	99.63

*All Fe reported as FeO

TABLE 3.—*Microprobe analyses of olivine*

	6	9	10	11
SiO_2	40.00	39.46	39.04	39.65
FeO*	13.03	15.61	19.65	15.45
MgO	45.85	43.85	41.63	44.04
Total	98.88	98.92	100.32	99.14
Mol.% Fo	86.1	83.4	79.1	83.6

*All Fe reported as FeO.

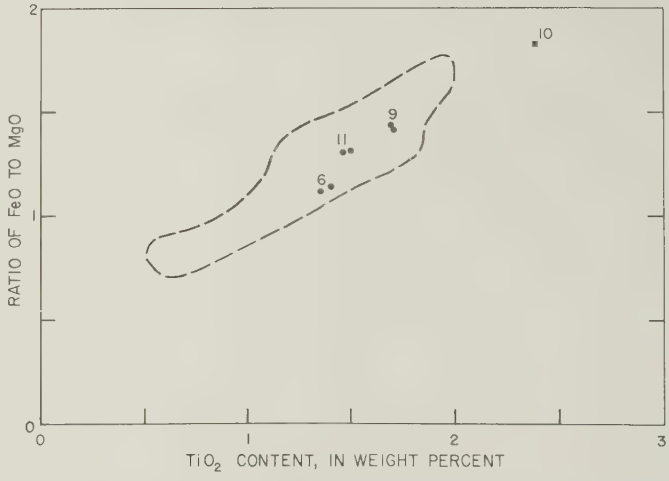

FIGURE 5.—Weight percent of FeO/MgO in relation to TiO_2 content for basalt glass from dredge hauls from East Pacific Rise at lat 21° N. Dashed envelope encloses similarly analyzed glasses from Mid-Atlantic Ridge at lat 37° N. (FAMOUS project area).

The FeO/MgO relative to TiO_2 trend of the samples overlaps the trend of basalt glasses from the Mid-Atlantic Ridge at lat 37° N. (FAMOUS project area) such that more TiO_2-rich samples are represented, but none of the samples contains low TiO_2 contents characteristic of the primitive axially located lavas of the FAMOUS project area.

Samples 6, 9, and 11 are similar in FeO/MgO and TiO_2 content (fig. 5); of those the younger samples (6, 11) show the lowest values (least fractionated). When K_2O and P_2O_5 are compared, however, samples 9 and 11 appear to be the least fractionated, and these are the samples with the lowest vesicle content (table 1). From phenocryst assemblages, samples 6 and 9 appear to be the least fractionated, as they contain more olivine relative to plagioclase, and rare spinel. A larger and more precisely located sample collection is necessary to define the locus and characteristics of the least fractionated lavas.

The temperature of quenching of the lavas can be estimated by comparing the iron and magnesium contents of the basalt liquid (glass) with those of the olivine microphenocrysts, which are in apparent equilibrium with the liquid, using the method of Roeder and Emslie (1970). A plot of the molecular ratio FeO/MgO in olivine and glass (fig. 6) falls on a straight line with a slope of 0.26, suggesting that the liquid and olivine are indeed in equilibrium. This plot, however, is not directly comparable with the data of Roeder and Emslie (1970) because all iron in the glass is calculated as FeO. If about 10 percent of the iron is present as Fe_2O_3, which seems reasonable, then the slope would be more nearly 0.30, the value they determined experimentally.

The temperature of liquid-olivine equilibrium can be estimated by comparing the molecular percent MgO of the liquid with the forsterite content of the olivine (see fig. 7 of Roeder and Emslie, 1970). This method obviates the analysis of both FeO and Fe_2O_3 in the liquid, impractical with the electron microprobe. Using this method, we find a steady decrease of temperature from 1205°C for the least differentiated sample (6) to 1175°C for the most differentiated sample (10) (fig. 6).

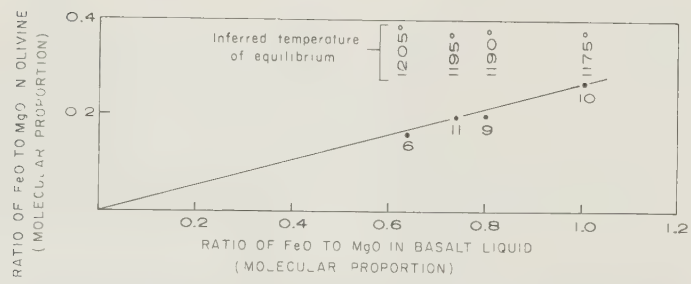

FIGURE 6.—Molecular proportion FeO/MgO in basalt liquid and olivine phenocrysts for samples from the East Pacific Rise at lat 21° N. Inferred temperatures of equilibrium from Roeder and Emslie (1970).

DISCUSSION AND CONCLUSIONS

The four dredged lava samples from the East Pacific Rise at lat 21° N. are undersaturated tholeiites defining a compositional trend ranging from moderately fractionated varieties to a highly fractionated iron-titanium-rich sample. The major-element (whole-rock) composition reported by Larson (1970) for a basalt sample dredged away from the up-lifted central block, approximately 3 km west of the source of sample 9, is consistent with the compositional range of our samples. The thickness of palagonite rind (20–100 μm) on Larson's sample indicates an older age than our samples, as might be expected from its position off the ridge axis. The four samples described here define a smooth trend on variation diagrams, suggesting that they are related to a common parent. The calculated temperature of equilibrium of glass and coexisting olivine indicates a temperature of 1205°C for the least differentiated sample, progressing to 1175°C for the most differentiated sample. Despite these generally smooth trends, the least differentiated sample is notably high in K_2O and P_2O_5.

No geographic zonal arrangement of compositional types relative to the inferred ridge axis can be deduced from the limited collection. However, the two younger dredge samples (6, 11) are the least differentiated and occur in the center and along the east side of the main extrusion zone. The two older, more differentiated samples are from the western margin or west of the main extrusion zone. This suggests that the locus of extrusion shifts through time across the central zone and recently was more active on the east side.

REFERENCES CITED

Anderson, R. N., Clague, D. A., Klitgord, K. D., Marshall, Monte, and Nishimori, R. K., 1975, Magnetic and petrologic variations along the Galapagos spreading center and their relation to the Galapagos melting anomaly: Geol. Soc. America Bull. 86, p. 683.

Ballard, R. D., Bryan, W. B., Heirtzler, J. R., Keller, George, Moore, J. G., and van Andel, Tj. H., 1975, Manned submersible observations in the FAMOUS area, Mid-Atlantic Ridge: Science, v. 190, p. 103.

Bryan, W. B., and Moore, J. G., 1977, Compositional variations of young basalts in the Mid-Atlantic Ridge rift valley near 36°49′N: Geol. Soc. America Bull., v. 88, p. 556–570.

Klitgord, K. D., 1976, Sea-floor spreading—the central anomaly magnetization high: Earth and Planetary Sci. Letters, v. 29, p. 201.

Larson, R. L., 1970, Near-bottom studies of the East Pacific Rise crest and tectonics of the mouth of the Gulf of California: San Diego, California Univ., Ph. D. thesis, 164 p.

——— 1971, Near-bottom geologic studies of the East Pacific Rise crest: Geol. Soc. America Bull. v. 82, p. 823.

Larson, R. L., and Spiess, F. N., 1969, East Pacific Rise crest: a near-bottom geophysical profile: Science, v. 163, p. 68.

Normark, W. R., 1975, A photographic study of the zone of crustal accretion of the East Pacific Rise crest at the mouth of the Gulf of California: Geol. Soc. America Abs. with Programs, v. 7, p. 538.

——— 1976, Delineation of the main extrusion zone of the East Pacific Rise at lat. 21° N.: Geology, v. 4, p. 681–685.

Roeder, P. L., and Emslie, R. F., 1970, Olivine-liquid equilibrium: Contr. Mineralogy and Petrology, v. 29, p. 275.

Spiess, F. N., and Tyce, R. C., 1973, Marine Physical Laboratory deep tow instrumentation system: Scripps Inst. Oceanography, v. 73, no. 4, 37 p.

Yokowitz, Harvey, Myklebrust, R. L., and Heinrich, K. F. J., 1973, FRAME—an on-line correction procedure for quantitative electron microprobe micronanalysis: Natl. Bur. Standards Tech. Note 796, 46 p.

Jour. Research U.S. Geol. Survey
Vol. 5, No. 6, Nov.–Dec. 1977, p. 761–781

GEOLOGY OF THE GABBROIC COMPLEX ALONG THE NORTHERN BORDER OF THE JOSEPHINE PERIDOTITE, VULCAN PEAK AREA, SOUTHWESTERN OREGON

By ROBERT A. LONEY and GLEN R. HIMMELBERG,[1]
Menlo Park, Calif., Columbia, Mo.

Abstract.—The terrane bordering the alpine-type Josephine Peridotite on the north in the Vulcan Peak area, southwestern Oregon, is composed of intrusive hornblende gabbro (Middle Jurassic) and scattered remnants of clinopyroxene-bearing ultramafic rocks and amphibolite. The amphibolite, which preliminary analyses suggest is of andesitic composition, has undergone regional metamorphism to the amphibolite facies and three episodes of plastic folding. The ultramafic rocks overlie the amphibolite with a possible magmatic sedimentary contact, although the contact is not entirely clear and a fault cannot be ruled out. The ultramafic rocks are partially recrystallized owing to the gabbro intrusion and later partially serpentinized; they have undergone two episodes of plastic folding, the second of which correlates with the third in the amphibolite. The intrusion of the gabbro began as early as the second folding episode in the amphibolite and probably continued at least intermittently throughout the third episode of folding and possibly later. After the high-temperature deformation, the Josephine Peridotite was thrust northward over the gabbroic complex along an east-striking south-dipping thrust fault, after which both of these terranes were thrust westward over the Upper Jurassic Dothan Formation along a major north-striking east-dippng thrust fault. The nature of the ultramafic rocks, their association with an extensive gabbro terrane, and the proximity of a large alpine-type periodotite suggest that the gabbroic and ultramafic complexes are part of an ophiolite sequence. However, if the ultramafic rocks are cumulates and were deposited on the amphibolite terrane, then the gabbroic complex is somewhat different from the ideal ophiolite model.

The alpine-type Josephine Peridotite, in southwestern Oregon and northwestern California (fig. 1), is bordered on the northwest by a heterogeneous plutonic terrane that is composed dominantly of gabbroic rocks (Wells and others, 1949; Hotz, 1971; Ramp, 1975). At the southwest end of this terrane in the vicinity of Dry Butte, the westward extension of the Josephine Peridotite, called the Vulcan Peak peridotite by Himmelberg and Loney (1973) and Loney and Himmelberg (1976), is thrust northward over the gabbroic terrane (fig. 2). Hotz (1971) called this terrane the Chetco River complex, but his descriptions mentioned only intrusive gabbro mainly of Jurassic age and did not mention ultramafic rocks and amphibolite, both of which have been intruded by the gabbro in the southern part of the complex. The ultramafic rocks of this complex occur mainly as highly deformed clinopyroxene-bearing remnants scattered in the gabbro and are probably older cumulate rocks. The ultramafic bodies are commonly in contact with the amphibolite, which occurs as an irregular, discontinuous belt that generally separates the gabbro from the Josephine Peridotite and is probably the western continuation of the metamorphic rocks to the east mapped by Wells, Hotz, and Cater (1949) as the Applegate Group of Triassic age. However, recent work in the Rogue River area (Coleman and others, 1976) suggests that these metamorphic rocks more likely correlate with the amphibolite of Briggs Creek of possible Jurassic age. Ramp (1975) correlates scattered parts of the metamorphic rocks with the Rogue Formation of Jurassic age. Recent work by N. J Page (written commun., 1976) suggests that correlation of the amphibolite with the Applegate Group is unlikely; therefore, the amphibolite is considered in this paper to be of Jurassic(?) age. It seems best to exclude both the ultramafic rocks and the amphibolite from the Chetco River complex and not to apply the name to the terrane as a whole. For convenience, the part of this terrane in the present area and its continuation to the east along the north boundary of the Josephine Peridotite will be called informally the Dry Butte terrane. Both this terrane and the Josephine Peridotite have been thrust westward over the Upper Jurassic Dothan Formation along a major north-striking fault, called by Ramp (1975) the Valen Lake thrust fault (fig. 2; see also Loney and Himmelberg, 1976).

[1] Department of Geology, University of Missouri.

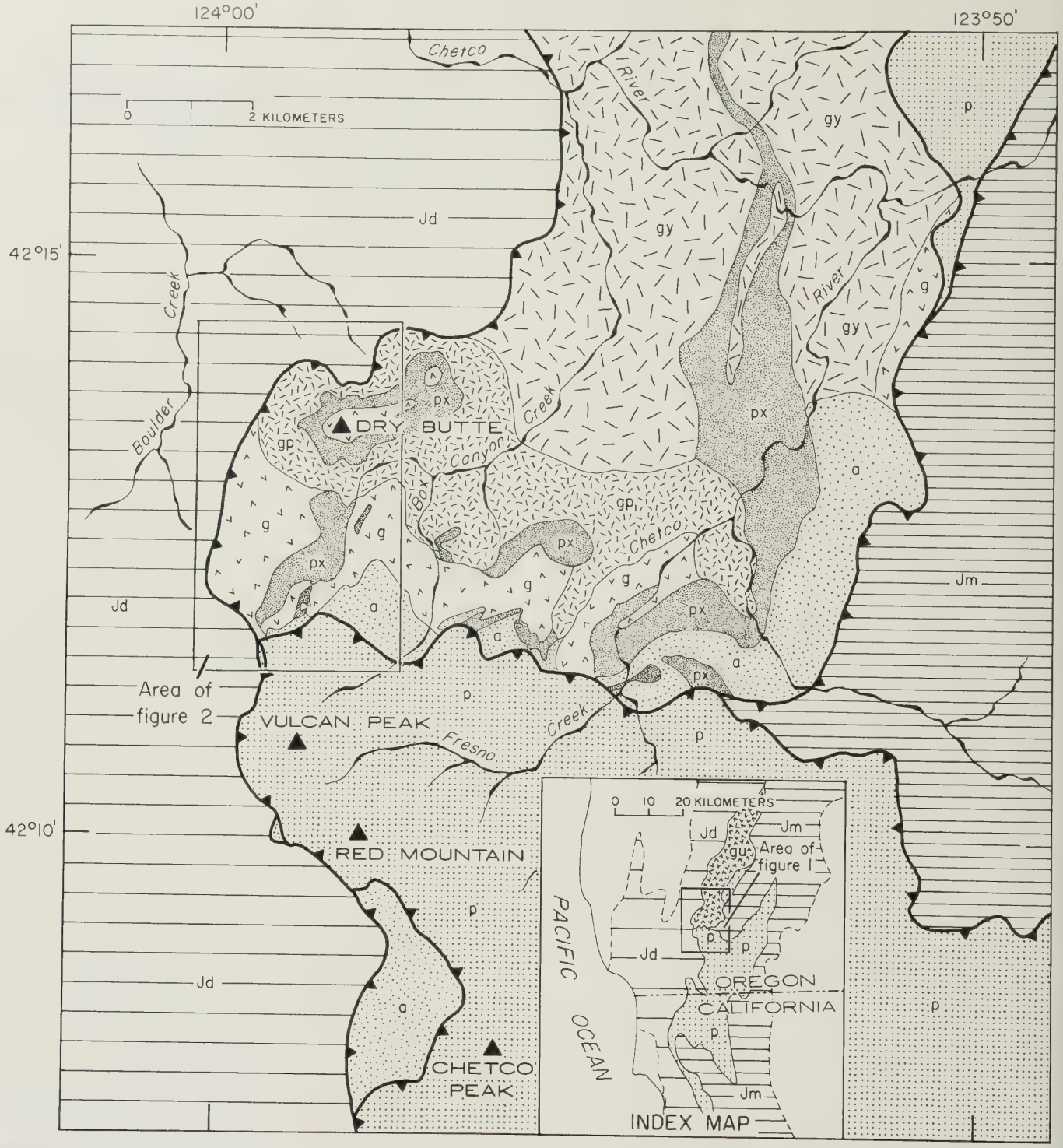

FIGURE 1.—Location and geology of the Vulcan Peak area. Geology modified from Wells, Holtz, and Cater (1949), Hotz (1971), and Ramp (1975). See figure 2 for explanation.

The occurrence of a mafic-ultramafic terrane adjacent to a major harzburgite tectonite mass suggests an ophiolite association (Penrose field conference participants, 1972), and in detail the clinopyroxene-bearing ultramafic rocks are suggestive of cumulate rocks similar to the lower part of an ophiolite gabbro complex. However, the Dry Butte terrane departs from the ideal ophiolite sequence in that the probable ultramafic cumulate rocks occur as scattered metamorphosed remnants in intrusive gabbro and that the remnants are

commonly in contact with and overlie highly deformed amphibolite instead of harzburgite tectonite. Although the nature of the contact between the probable cumulate rocks and the amphibolite is not entirely clear, in the best exposure it seems not to be a fault, and the probable cumulate is structurally higher, suggesting a depositional contact. However, apart from the amphibolite occurrence, the Dry Butte terrane generally resembles part of the gabbroic complex of the classic Troodos ophiolite of Cyprus (Vine and Moores, 1972).

In the Vulcan Peak area, the Dry Butte terrane is separated from the Josephine Peridotite by an east-striking south-dipping fault called the Madstone Cabin thrust fault by Ramp (1975). The thrust fault forms the northern contact of the Josephine Peridotite for a distance of at least 16 km (fig. 1). Along the western 10 km of the fault the Josephine Peridotite is in contact with the Dry Butte terrane, and along the eastern 6 km the peridotite is in contact with metasedimentary and metavolcanic rocks of the Late Jurassic Galice and Rogue Formations and with lenticular masses of sheared serpentinite. It is possible that the thrust then swings northeastward and forms the northwestern contact of the peridotite with the same rocks.

The three units of the Dry Butte terrane, amphibolite, ultramafic rocks, and gabbro, have been deformed in markedly different ways. It is difficult to correlate an event from one unit to another, and for this reason we will describe each unit, both petrographically and structurally, before discussing possible correlations. No correlation of events has been possible between the Dry Butte terrane and the Josephine Peridotite.

DESCRIPTION OF ROCKS

Amphibolite

The amphibolite is composed mainly of dark-gray to black medium-grained regionally metamorphosed hornblende-rich rocks that range from well foliated to massive. The foliation (S_0) is partly defined by compositional layering that ranges from a few millimeters to a few centimeters in thickness (fig. 3) and is most commonly the result of variations in the ratios of hornblende to plagioclase. The presence or absence of a particular mineral such as epidote, diopside, or garnet also contributes to the layering, but such changes are not conspicuous in the field. There are commonly also abrupt changes in grain size from layer to layer and in places grain-size variations within layers. These features, together with the generally uniform thickness of the layering within an outcrop, suggest original sedimentary or volcanic bedding. The foliation is also defined by the planar preferred orientation of flattened hornblende grains and quartz lenses, both of which generally have a nearly equant shape in the foliation plane. Only in a few places does the hornblende display an elongate habit and linear-preferred orientation.

Also interlayered with the amphibolites are thin units (8–10 m) of a medium-grained (approx. 0.5 mm) plagioclase-quartz-white mica-biotite gneiss and of a garnetiferous feldspar-quartz-biotite gneiss with or without hornblende and epidote. The latter rocks commonly contain strongly zoned relict plagioclase grains 0.5 to 1 mm in size in a recrystallized matrix. The mineralogy and texture of the rock suggest that it is a metamorpohsed granodiorite or quartz diorite.

Chemical analyses of two amphibolite specimens are given in table 1. The two analyzed samples are similar in chemistry and modal mineralogy and are comparable in chemical composition to Nockolds' (1954) average andesite, except that the amphibolites have a lower TiO_2 content. Because of the observed range of modal mineralogy of the amphibolites, the analyzed samples cannot necessarily be considered representative of most of the amphibolites of the area.

Nearly all of the amphibolites studied contain hornblende, plagioclase, and quartz with minor amounts of opaqe oxides, apatite, zircon, and commonly sphene. Some amphibolites are garnetiferous, and primary epidote, biotite, and diopside occur locally. Major modal variation of primary minerals is in the amounts of hornblende and quartz. Quartz contents range from less than 5 percent to approximately 45 percent. Hornblende ranges from as low as 10 percent to approximately 60 percent. Retrograde minerals include epidote-group minerals, chlorite, prehnite, sericite, calcite, hematite, and fine powdery clay minerals. The hornblende in all the specimens studied is pleochroic with X = pale yellow, Y = green, and Z = green with a bluish tint. Some hornblende grains are twinned. The plagioclase is commonly twinned and altered.

The granularity of the amphibolites in general ranges from 0.5 to 1 mm, but finer grained varieties (approx. 0.3 mm) are present. In general, the grain size increases toward the gabbro contact. Although most specimens studied are equigranular, several specimens contain plagioclase grains as much as 2 mm in size in an equigranular matrix of grains less than 1 mm. The large plagioclase grains have irregular boundaries, are generally more altered than the matrix plagioclase, and are interpreted as relict nonrecrystallized clasts.

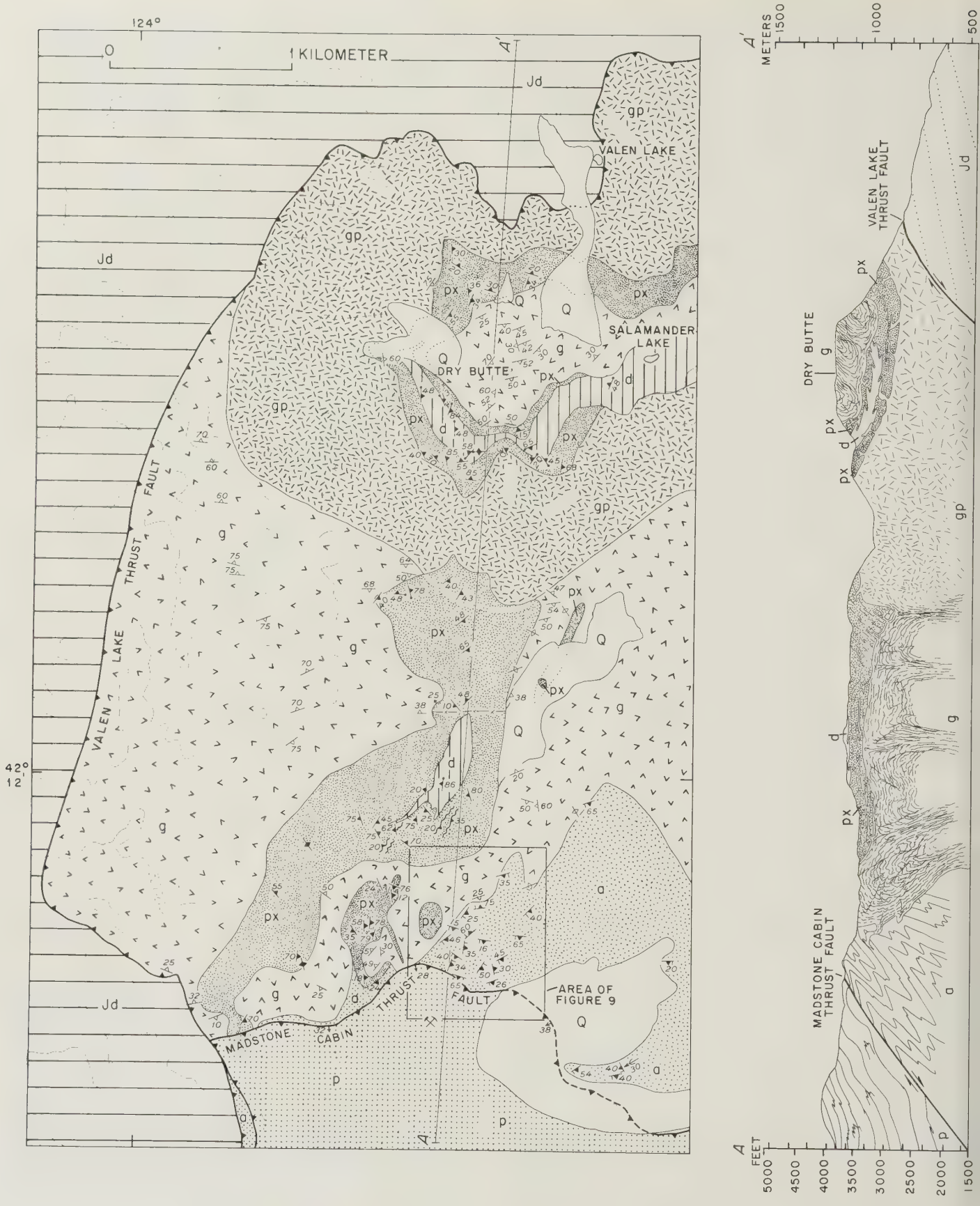
124°
0
1 KILOMETER
A
A'
Jd
gp
VALEN LAKE
SALAMANDER LAKE
DRY BUTTE
px
d
g
Q
a
p
VALEN LAKE THRUST FAULT
MADSTONE CABIN THRUST FAULT
AREA OF FIGURE 9
42° 12'
METERS
1500
1000
500
FEET
5000
4500
4000
3500
3000
2500
2000
1500

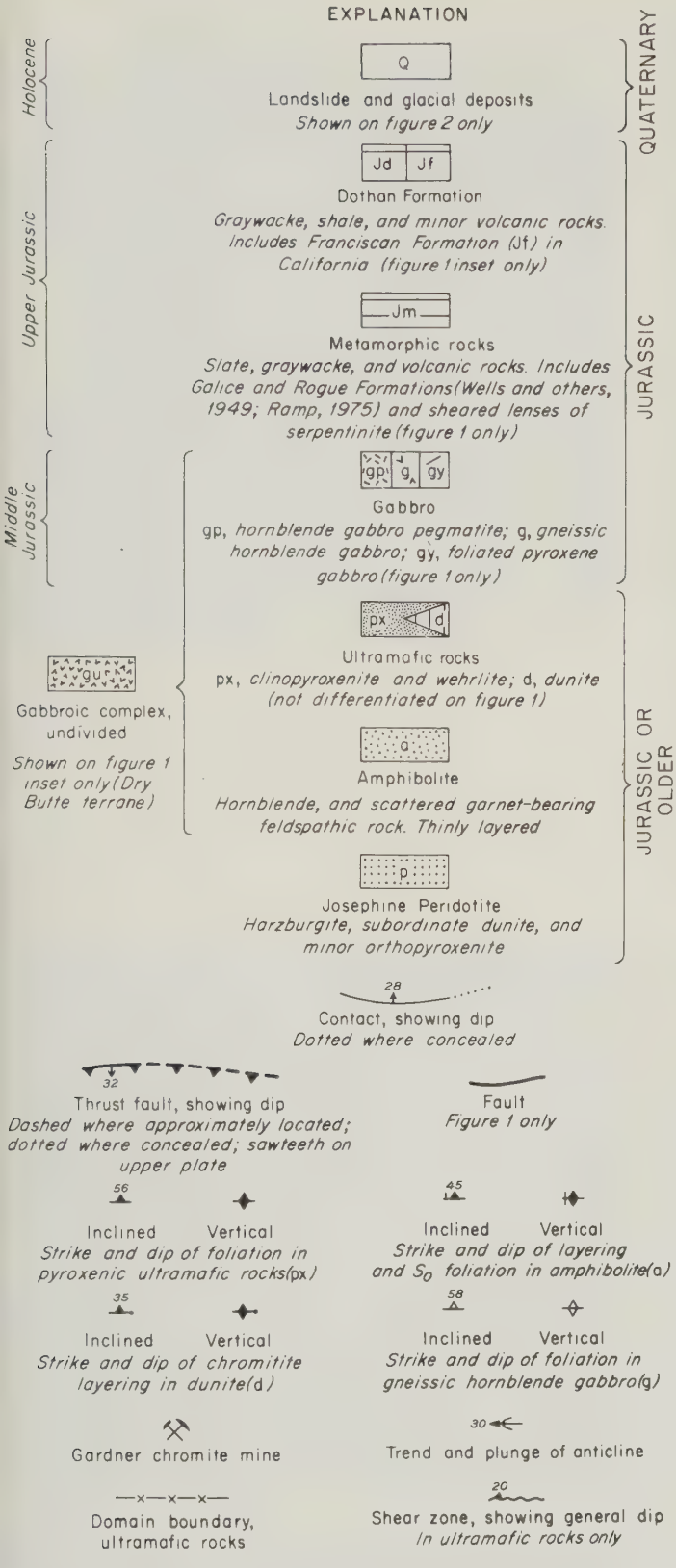

FIGURE 2.—Geologic map and cross section of Dry Butte area. Base from U.S. Geological Survey, scale 1:62 500, Chetco Peak and Mt. Emily, 1954.

TABLE 1.—*Chemical composition, in percent, of amphibolite*

[Bulk analyses by Sam Botts, U.S. Geological Survey, Reston, Va. Methods used are those described by Shapiro (1967). Spectrographic analyses by R. E. Mays, U.S. Geological Survey, Menlo Park, Calif. Looked for but not found: B, Y, Yb]

Sample No.	33-VP-68	17-VP-69
SiO_2	54.5	55.6
Al_2O_3	16.5	16.5
Fe_2O_3	2.5	2.3
FeO	5.9	5.7
MgO	6.3	5.7
CaO	8.9	8.2
Na_2O	2.8	2.9
K_2O	.30	.90
H_2O+	1.7	1.1
H_2O-	.09	.07
TiO_2	.52	.44
P_2O_5	.08	.11
MnO	.10	.13
CO_2	.01	.01
Total	97.20	99.66
Quantitative Spectrographic Analysis		
Ba	0.012	0.035
Co	.0027	.0030
Cr	.0065	.010
Cu	.0042	.0048
Mn	.11	.14
Ni	.0040	.0034
Sc	.0042	.0032
Sr	.014	.028
Ti	.15	.28
V	.020	.017
Zr	.0020	.0040
Ga	.0010	.0012

33-VP-68 quartz (4.3%), plagioclase (35.1%), hornblende (57.7%), others (2.9%).

17-VP-69 quartz (8.4%), plagioclase (32.5%), hornblende (46.3%), epidote (2.1%), others (10.7%).

Ultramafic Rocks

The ultramafic rocks are composed of clinopyroxenite, olivine clinopyroxenite, wehrlite, and dunite with minor amounts of plagioclase-bearing pyroxenites and gabbro (International Union of Geological Sciences classification, Streckeisen, 1973). The various rock types are complexly interlayered with individual

A

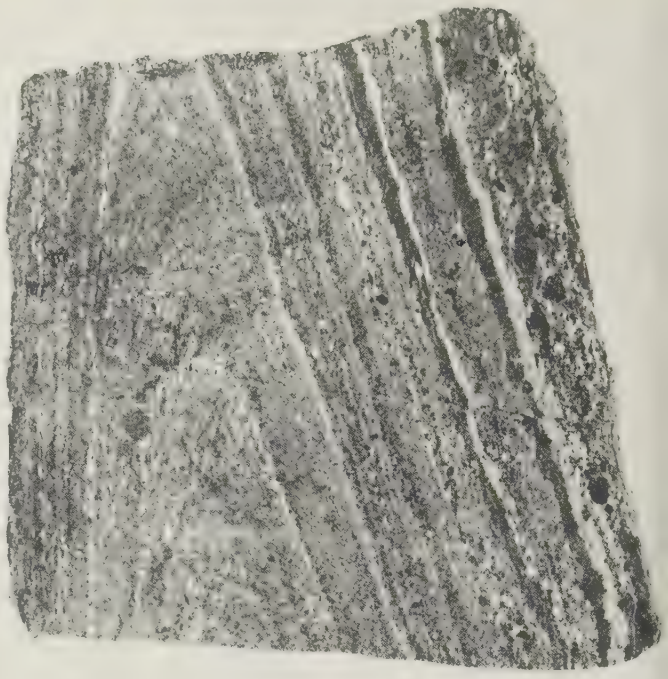

B

C

D

FIGURE 3.—Examples of fold types in S_0 layering, amphibolite unit. *A*, F_1 fold, northwest of Vulcan Peak near contact with peridotite, shows typical isoclinal form; outcrop 50 cm wide. *B*, F_1 fold, from same locality as 3*A*. *C*, Block of coarse-grained amphibolite, about 1.5 m wide near gabbro contact in Box Canyon, shows both F_1 (on right) and F_2 (on left) folds. Note gabbro vein (g). *D*, F_2 folds, north of Gardner chromite mine, show typical open form; field about 2 m wide.

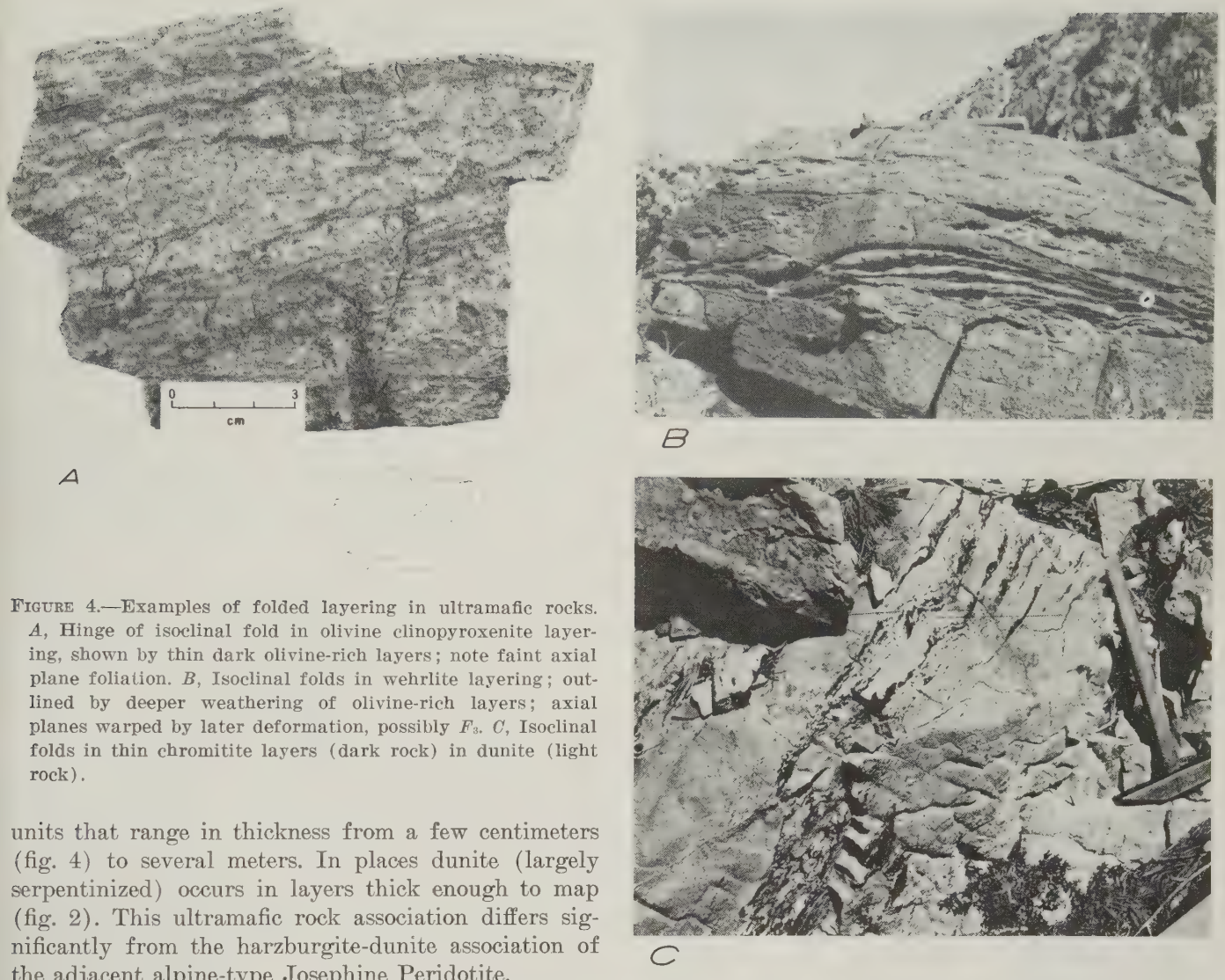

FIGURE 4.—Examples of folded layering in ultramafic rocks. *A*, Hinge of isoclinal fold in olivine clinopyroxenite layering, shown by thin dark olivine-rich layers; note faint axial plane foliation. *B*, Isoclinal folds in wehrlite layering; outlined by deeper weathering of olivine-rich layers; axial planes warped by later deformation, possibly F_3. *C*, Isoclinal folds in thin chromitite layers (dark rock) in dunite (light rock).

units that range in thickness from a few centimeters (fig. 4) to several meters. In places dunite (largely serpentinized) occurs in layers thick enough to map (fig. 2). This ultramafic rock association differs significantly from the harzburgite-dunite association of the adjacent alpine-type Josephine Peridotite.

The ultramafic rocks were partially to completely recrystallized by thermal metamorphism associated with the intrusion of the hornblende gabbro. Thus the characteristic texture of pyroxene-rich rocks consists of a relatively fine grained matrix of pyroxene, minor olivine, and tremolite through which are scattered much larger relict clinopyroxene grains. A prominent foliation generally parallel to the layering (see section entitled "Mesoscopic structure" under "Ultramafic Rocks") is evident in some areas and is a result of late-stage postmetamorphic shearing. The more olivine-rich rocks are serpentinized along the shear planes.

The clinopyroxene-rich rocks tend to be greenish gray on both fresh and weathered surfaces; in contrast, the olivine-rich layers tend to be black on fresh surface and reddish brown on weathered surface because of serpentinization. Commonly, where thin olivine layers or lenses are distributed throughout pyroxene-rich rock, the entire surface may be stained brown. In general, clinopyroxene is more resistant to weathering than olivine, and where both occur together, the clinopyroxene grains project above the smooth olivine surface in rough ridges and knobs. The average grain size varies widely, although it is fairly uniform within individual layers.

Olivine clinopyroxenite specimen 8–VP–68 (fig. 5), which shows the least amount of metamorphic recrystallization, contains the association clinopyroxene, olivine, and tremolite. The clinopyroxene and olivine are interpreted to be primary minerals, but the tremolite is metamorphic. Wehrlite specimen 41–VP–68, although largely serpentinized, shows no evidence of recrystallization and contains the primary mineral association olivine, clinopyroxene, and chromian spinel. Most other specimens are more than 95 percent recrystallized, but a study of relict primary minerals reveals that in addition to primary clinopyroxene and olivine, chromian spinel is a common accessory mineral in

FIGURE 5.—Photomicrograph of least crystallized olivine clinopyroxenite, sample 8–VP–68; crossed nicols, long dimension 3.4 mm. Larger grains are clinopyroxene.

dunite and wehrlite, plagioclase is common to the gabbros and some pyroxenites, and orthopyroxene is rare in the pyroxenites but is present in the gabbros.

The primary clinopyroxene is diopsidic. Relict grains generally have irregular recrystallized borders, but some subhedral crystal boundaries are preserved. Twinning of the clinopyroxene is common, and exsolved orthopyroxene and opaque material occur as small needles or rods oriented in two pyroxene crystallographic directions, as small irregular blebs, and as a fine dust. Primary clinopyroxene grain size is generally on the order of 1 mm, but relict grains as large as 100 to 150 mm were observed. The primary olivine is forsteritic, commonly subhedral, and approximately 0.5 to 1 mm in size. Texture of the least recrystallized olivine clinopyroxenite is granular with subhedral grain boundaries common. The texture suggests a cumulate origin (fig. 5).

The recrystallized mineral association and modal amounts of minerals vary with the original rock composition. By far the most common mineral association is diopside plus tremolite with or without olivine. Plagioclase, orthopyroxene, and chlorite are present in some recrystallized associations, and hornblende is present in place of tremolite in those rocks that originally contained plagioclase. Minor amounts of very fine grained (0.02 mm) opaque oxide are present in most associations. In contrast to the primary diopside the recrystallized clinopyroxene is of a smaller grain size (0.3 to 0.5 mm), is largely free of exsolved phases, and lacks twinning. Excluding obvious metasomatic contact zones and veins, the recrystallized mineralogy suggests that the metamorphism was largely isochemical except for possible addition of H_2O. Texture of the recrystallized association is granular polygonal to decussate with many grains exhibiting good 120° equilibrium boundaries (fig. 6).

Contact zones between pyroxenite and hornblende gabbro consist of monomineralic green hornblende. These zones range from thin selvages to zones several centimeters thick and grade into the pyroxenites. The hornblende gabbros show little mineralogic change except for alteration of plagioclase. Metasomatic contact zones and veins in the wehrlite and dunite are generally zoned and consist of phases such as tremolite, chlorite, anthopyhyllite, and enstatite.

Postmetamorphic alteration includes serpentinization of olivine, alteration of orthopyroxene to a yellowish-brown serpentine-like mineral, and conversion of plagioclase to zoisite (or clinozoisite), prehnite, and an unidentified fine mixture of dark-brown material. Other secondary minerals include amphibole, chlorite, calcite, and magnetite. Locally the late-stage alteration is extensive.

Whole-rock analyses of ultramafic rocks and related gabbro are given in table 2. The wehrlites have undergone considerable serpentinization, and the amounts of H_2O and Fe_2O_3 can be largely attributed to the serpentinization process (Page, 1967; Loney and others, 1971; Coleman and Keith, 1971). In the pyroxenite the H_2O content most probably reflects the amphibole present. Plagioclase in the feldspathic pyroxenite and gabbro is completely altered, and the degree to which this alteration affects the chemistry of these rocks is indeterminate.

The ultramafic rocks contain slightly more iron than alpine-type peridotites and are comparable in composi-

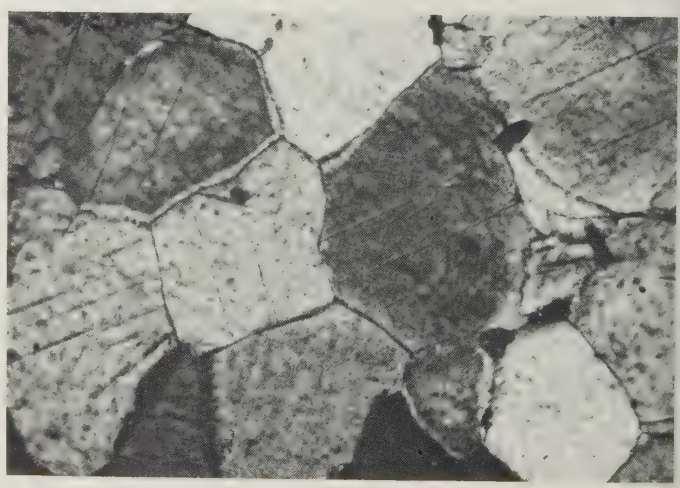

FIGURE 6.—Photomicrograph of recrystallized clinopyroxenite, sample 43–VP–68; crossed nicols, long dimension 0.45 mm. Note equilibrium grain boundaries that commonly subtend angles of 120°. Larger grains in field are clinopyroxene.

tion to those of the critical zone of the Bay of Islands Igneous Complex, Newfoundland (Irvine and Findlay, 1972), and the pyroxenite-gabbro zone of the Canyon Mountain Complex, Oregon (Thayer and Himmelberg, 1968), both of which are believed to be ophiolites.

Hornblende Gabbro

The hornblende gabbro (hornblende diorite of Wells and others, 1949) intrudes the amphibolite and ultramafic rocks and occurs in several textural varieties, of which gneissic and pegmatitic varieties are the most common. The gneissic type is a gray medium-grained (approx. 0.5 mm) equigranular gabbro with a conspicuous alinement of hornblende imparting a gneissose structure to the rock (fig. 7). Structural analysis suggests that the gneissose structure is not a result of a penetrative deformation in the solid but probably of flow and deformation of viscous magma. In the pegmatitic hornblende gabbro, the hornblende crystals range in size from approximately 5 to 200 mm and show no obvious flow alinement. The pegmatitic gabbro may grade into the medium-grained gabbro or the two may be mutually intrusive, although pegmatite intruding gneissic gabbro is more common. Where the gabbro occurs as small dikes (100 to 150 mm thick), either intrusive into ultramafic rocks or the pegmatitic gabbro, in general, the grain size is smaller (0.3 mm) and the flow structure is finer.

Essential minerals of the gabbro are hornblende and plagioclase, and minor amounts of quartz commonly occur in the medium-grained gabbro. Common accessory minerals are opaque oxides and a trace of sphene. The hornblende is green, commonly subhedral, and twinned. The plagioclase is polysynthetically twinned, and some grains show a moderate optical zoning. Relict pale-green clinopyroxene is present in some samples, but since it is most common in thin gabbro dikes intrusive into pyroxenites, the clinopyroxene grains are probably xenocrysts.

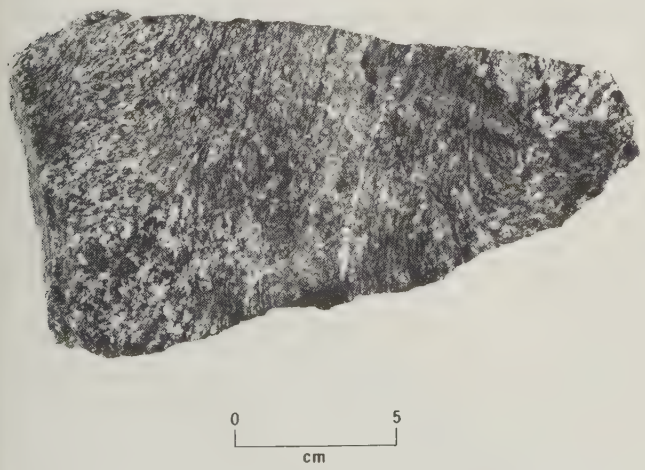

FIGURE 7.—Photograph of typical gneissic hornblende gabbro, showing plastic shear zone.

Alteration of hornblende is generally negligible. Plagioclase is commonly extensively altered, particularly near contacts with ultramafic rocks. The secondary minerals include zoisite (or clinozoisite), sericite, chlorite, prehnite, hematite, sphene, and an unidentified fine mixture of dark-brown material.

Chemically the hornblende gabbro is similar to tholeiitic basalt (Engel and others, 1965; Miyashiro and others, 1969; Kay and others, 1970) except for significantly lower SiO_2 and alkali contents and higher Al_2O_3 values (table 3). The low alkali contents may be a result of modification of the original rock chemistry related to the plagioclase alteration.

STRUCTURE

Amphibolite Unit

Mesoscopic structure

The S_0 foliation in the amphibolite is tightly folded on a small scale by at least three generations of folds. Although S_0 is generally subparallel to the axial planes of the isoclinal first folds (F_1), it clearly bends around the F_1 hinges and is older (fig. 3*A* and *B*). the F_1 folds, the most commonly seen mesoscopic folds in the amphibolite, are sharp-hinged, similar folds that range in width from 0.1 to 2.0 m and have a height-to-width ratio of 3.0 to 4.0. In a few places, a faint axial plane foliation (S_1) crosscuts S_0 in the fold hinges. Although S_1 is faint, it is probable that its development produced the initial pervasive schistose character of the amphibolite. S_1 would be generally parallel to S_0 because of the isoclinal form of the F_1 folds.

Mesoscopic folds tentatively designated as second folds (F_2) are less abundant than F_1 folds, and the mutual relations of the two fold generations are not entirely clear. The mesoscopic F_2 folds are similar in size to F_1 folds (0.5–3.0 m wide) but tend to be more open and disharmonic (fig. 3*C* and *D*). The folds were mostly seen in domelike bosses 10 to 20 m in diameter that are best developed in the terrane north of the Gardner chromite mine. The F_1 folds in these bosses have been bent broadly, apparently around northeast-striking southeast-dipping axial planes that are approximately parallel to the general attitude of S_1, the axial planes of the F_1 folds. It appears, therefore, that F_1 and F_2 have similar axial plane orientations. This parallelism is supported by the folds in a block of amphibolite that came from a nearby outcrop in Box

TABLE 2.—*Chemical composition, in percent, of ultramafic rocks and related gabbro*

[Bulk analyses by Sam Botts, U.S. Geological Survey, Reston, Va. Methods used are those described by Shapiro (1967). Spectrographic analyses by R. E. Mays, U.S. Geological Survey, Menlo Park, Calif. Looked for but not found: Y, Zr, Yb]

Sample No.	41-VP-68	59-VP-68	36-VP-68	8-VP-68	58-VP-68	64-VP-68	65-VP-68
	Wehrlite			Clinopyroxenite		Feldspathic Clinopyroxenite & Gabbro	
SiO_2	36.0	41.8	44.1	49.4	51.5	47.2	47.5
Al_2O_3	.20	.60	.80	2.7	2.2	8.7	14.9
Fe_2O_3	7.2	6.2	5.3	2.0	1.3	1.6	1.4
FeO	2.4	2.8	2.5	5.3	3.5	4.2	5.6
MgO	38.0	33.2	32.6	19.6	20.0	16.8	11.0
CaO	3.0	5.3	7.0	19.2	19.6	18.4	15.1
Na_2O	0	0	0	.20	.30	.30	1.0
K_2O	0	0	0	0	0	.05	.60
H_2O+	11.9	9.2	8.1	1.1	1.2	1.9	2.2
H_2O-	.72	.48	.41	.06	.06	.55	.22
TiO_2	.02	.02	.03	.20	.10	.10	.15
P_2O_5	.02	.02	.02	.02	.02	.02	.06
MnO	.13	.09	.09	.12	.09	.09	.12
CO_2	.21	.01	.08	.06	.08	.01	.06
Total	99.80	99.72	101.03	99.96	99.95	99.92	99.91
	Quantitative Spectrographic Analysis						
B	-	0.0110	0.0090	-	-	-	-
Ba	-	-	-	-	-	0.0007	0.0280
Co	0.0120	.0120	.0090	.0060	.0060	.0065	.0036
Cr	.50	.21	.14	.090	.18	.15	.036
Cu	-	.0008	-	.0009	.0010	.0050	.0020
Mn	.065	.048	.050	.10	.075	.090	.095
Ni	.065	.060	.040	.016	.021	.020	.0070
Sc	.0016	.0026	.0034	.014	.010	.0075	.0065
Sr	-	-	-	.0020	.0014	.0036	.020
Ti	.018	.020	.026	.16	.090	.12	.16
V	.0030	.0048	.0044	.016	.010	.012	.020
Ga	-	-	-	-	-	-	.0008
MgO/(MgO+FeO+MnO)*	.88	.87	.89	.83	.88	.84	.74

*Total Fe calculated as FeO.

TABLE 2.—*Chemical composition, in percent, of ultramafic rocks and related gabbro*—Continued

	Description of analyzed samples
41-VP-68	Nonrecrystallized wehrlite. Olivine (2.1%), clinopyroxene (24.4%), chromian spinel (2.8%), serpentine (70.7%).
59-VP-68	Recrystallized wehrlite. Olivine (0.4%), diopside (19.5%), tremolite (0.8%). Relict nonrecrystallized clinopyroxene (0.9%), serpentine (72.5%), magnetite (5.9%).
36-VP-68	Recrystallized wehrlite. Olivine (3.6%), diopside (21.2%), tremolite (8.5%). Relict nonrecrystallized clinopyroxene (2.7%), serpentine (55.8%), magnetite (7.3%).
8-VP-68	Least recrystallized olivine clinopyroxenite. Clinopyroxene (84.2%), olivine (13.8%), tremolite (2.0%).
58-VP-68	Recrystallized clinopyroxenite. Diopside (70.6%), tremolite (25.0%), enstatite (0.3%), relict nonrecrystallized clinopyroxene (1.2%), serpentine (1.5%), magnetite (0.6%).
64-VP-68	Recrystallized feldspathic clinopyroxenite. Diopside (47.7%), amphibole (25.0%), plagioclase (trace), secondary after plagioclase (17.3%), secondary after enstatite (7.5%), relict nonrecrystallized clinopyroxene (2.5%).
65-VP-68	Recrystallized gabbro. Diopside (22.3%), hornblende (33.5%), enstatite (trace), secondary after enstatite (2.0%), plagioclase (trace), secondary after plagioclase (42.1%).

Canyon, in which the two fold types occur together (fig. 3*C*). This figure suggests that the two types may be variations of one somewhat inhomogeneous folding. The gabbro veins that have cut F_2-type folds have also been folded (fig. 3*C*), indicating that the gabbro intrusion began at least as early as the F_2 folding.

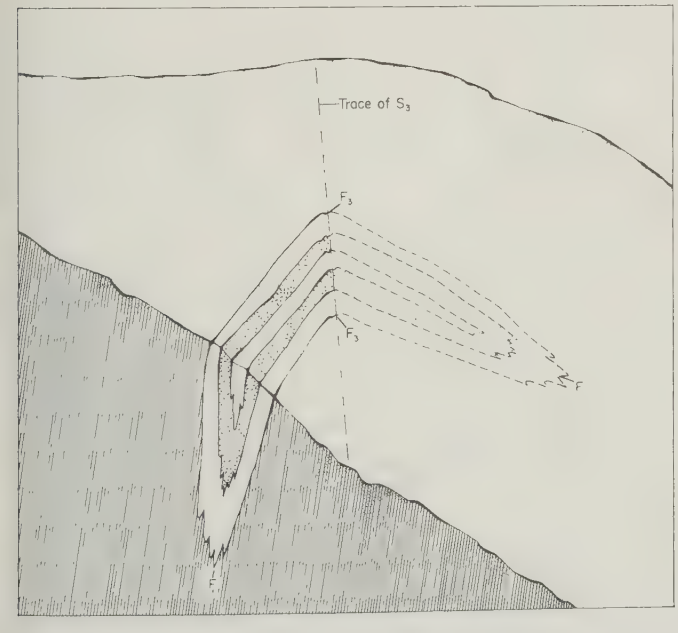

FIGURE 8.—F_1 fold in amphibolite deformed by F_3 fold; fold 0.5 m across.

TABLE 3.—*Chemical composition, in percent, of hornblende gabbro*

[Bulk analyses by Sam Botts, U.S. Geological Survey, Reston, Va. Methods used are those described by Shapiro (1967). Spectrographic analyses by R. E. Mays, U.S. Geological Survey, Menlo Park, Calif. Looked for but not found: B, Y, Zr]

Sample No.	38-VP-68	4-VP-69	3-VP-69	37-VP-68
SiO_2	42.1	43.3	45.3	48.0
Al_2O_3	19.6	19.2	18.1	18.1
Fe_2O_3	3.8	3.6	2.7	3.7
FeO	8.6	6.6	8.4	7.0
MgO	4.5	7.5	7.7	6.3
CaO	14.8	13.1	12.9	11.0
Na_2O	1.9	1.3	1.4	1.7
K_2O	.30	.20	.10	.55
H_2O+	2.7	2.8	1.9	2.1
H_2O-	.07	.34	.19	.15
TiO_2	.88	.42	.60	.59
P_2O_5	.25	.03	.11	.06
MnO	.14	.19	.20	.17
CO_2	.02	.01	.01	.01
Total	99.66	98.59	99.61	99.43
Quantitative Spectrographic Analysis				
Ba	0.019	0.0050	0.0020	0.016
Co	.0016	.0028	.0040	.0037
Cr	-	.0065	.0042	.0032
Cu	.0038	.0080	.0065	.012
Mn	.13	.16	.16	.14
Ni	-	.0022	.0022	.0010
Sc	.0018	.0032	.0044	.0036
Sr	.040	.020	.020	.022
Ti	.46	.24	.34	.34
V	.0040	.019	.032	.020
Ga	.0014	.0012	.0014	.0012
Yb	.0002	-	.0002	-

38-VP-68	8-cm-thick dike in ultramafic rocks. Hornblende (46.6%), plagioclase (trace), secondary after plagioclase (52.5%), opaque oxide (0.9%).
4-VP-69	15-cm dike intrusive into ultramafic rocks. Hornblende (56.6%), plagioclase (1.3%), secondary after plagioclase (41.4%), hematite (0.7%).
3-VP-69	Medium-grained hornblende gabbro. Hornblende (54.5%), plagioclase (11.9%), secondary after plagioclase (31.7%), others (1.9%).
37-VP-68	Medium-grained hornblende gabbro. Hornblende (61.2%), plagioclase (0.8%), quartz (8.6%), secondary after plagioclase (26.2%), sphene (0.2%), others (3.2%).

Identifiable mesoscopic F_3 folds are rare, but one of them (fig. 8) shows clearly its relation to the F_1 folds. As shown diagrammatically in figure 8, a small, nearly isoclinal F_1 fold has been deformed by a moderately open F_3 fold of comparable size, having a subvertical axial plane. The angle between F_1 and F_3 axes is nearly 90°. The geometry of this folding is in harmony with the macroscopic geometry of the amphibolite terrane as a whole, as described below.

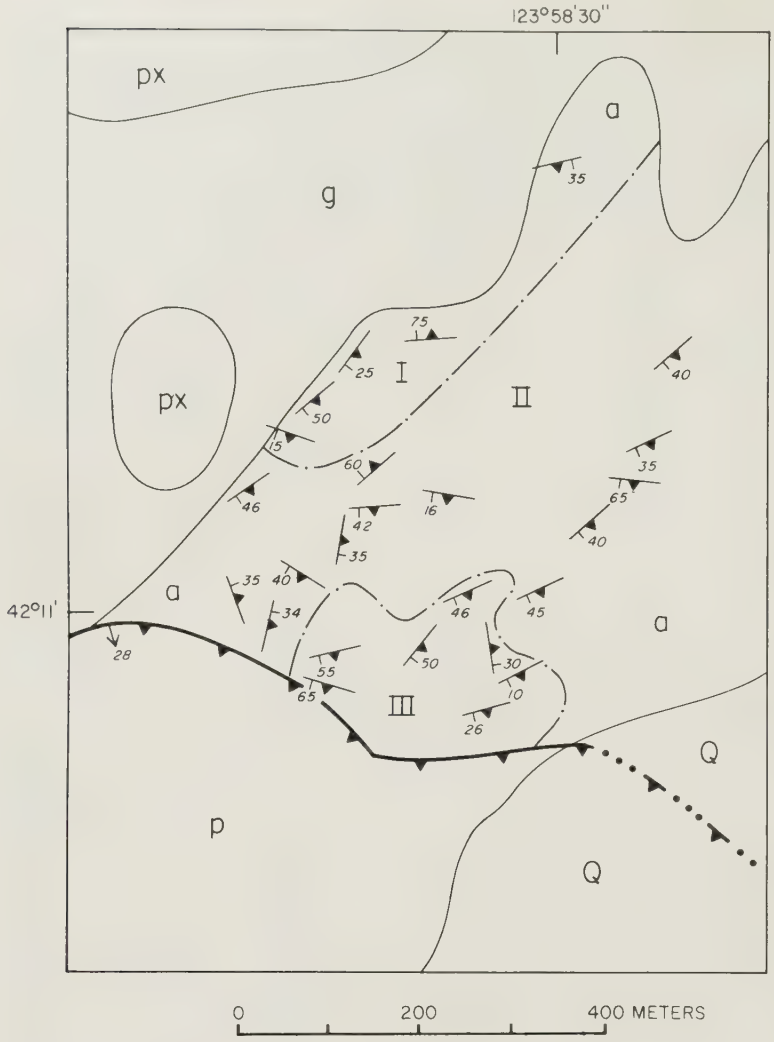

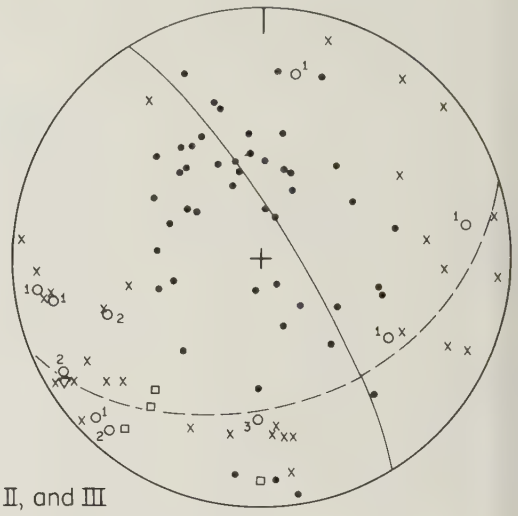

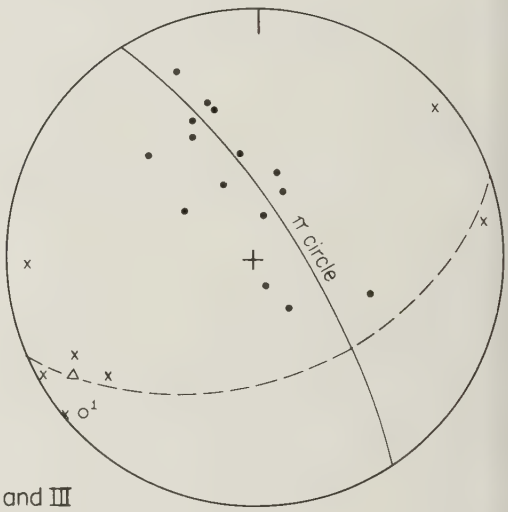

EXPLANATION

Pole to S_0

O^2

Fold axis

Number indicates generation

Hornblende lineation

Local π axis

Domain π axis

π circle

Approximate axial plane

Domain boundary

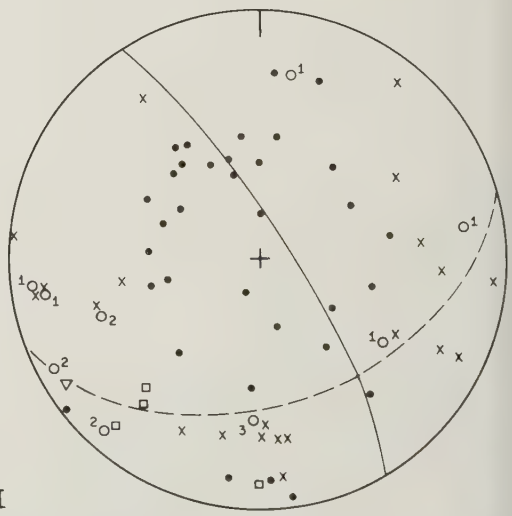

FIGURE 9.—Equal-area lower hemisphere plots of the principal amphibolite terrane. *A*, Collective plot of domains I, II, and III. *B*, Plot of domains I and III. *C*, Plot of domain II. See figure 2 for location of simplified geologic map and explanation of map symbols.

Macroscopic structure

In general the S_0 foliation strikes northeast and dips moderately to the southeast (fig. 2), but in places there are exceptions to this orientation that suggest folding on a larger scale similar to the mesoscopic folding described in the previous section. However, the lack of marker beds and the relatively small scale of the structural inhomogeneity makes it impossible to present a clear picture of the macroscopic fold geometry at the present map scale.

The poles to S_0 (fig. 9*A*) from a broad, northwest-striking, subvertical partial girdle whose π axis plunges gently to the southwest. Most of the local π axes, mesoscopic fold axes, and lineations tend to cluster near the orientation of the π axis. These mesoscopic folds include most of the F_1 and all of the F_2 folds. The remaining F_1 folds plunge from southeast to northeast, lying mostly near a northeast-striking plane that dips moderately southeast (fig. 9*A*, dashed great circle). The pole of this plane lies near the center of the principal concentration of S_0 poles and represents the average orientation of the axial planes of F_1 and possibly F_2 folds, S_1 and S_2 respectively. The single F_3 fold axis measured lies near the intersection of this plane and a north-striking vertical plane that represents the orientation of the axial plane (S_3) as determined in the field.

The greater scattering of F_1 axes as compared to that of the F_2 axes (fig. 9*A*) suggests the rotation of F_1 axes by F_2 folding. But the data are insufficient, especially on F_2 folds, to be certain of rotation paths. The study of the F_1 and F_2 folds is hampered by the similarity of the orientation of their axes and axial planes and also by the effects of the F_3 folding. One effect that might be attributed to F_2 folding is the doubly plunging (southwest-northeast) character of the F_1 axes (see Ramsay, 1967, p. 463–466), but doubly plunging folds have been also attributed to a single folding (Hills, 1963, p. 255).

Within the amphibolite terrane there are two relatively small domains, I and III, whose combined S_0 pole diagram (fig. 9*B*) shows a simple girdle, the π axis of which plunges gently southwest. The single mesoscopic F_1 fold found in the domains lies near the π axis, indicating that π probably equals F_1. The style of folding represented in figure 9*B* supports this correlation, being more like the mesoscopic F_1 folds (fig. 3*A* and *B*) than the mesoscopic F_2 folds (fig. 3*C* and *D*). The average limb orientations of the dominant folds are probably represented by the two submaxima in figure 9*B*. (See also cross section, fig. 2.) These submaxima represent average dips of 15° and 48° to the southeast and indicate an average angle between fold limbs of 33°. The observed F_1 folds have angles that range from about this value to less than 20°, whereas the few F_2 folds seen are much more open, with angles that range from 50° to 80°.

The remaining amphibolite terrane (fig. 9*C*) cannot be subdivided into homogeneous domains at the present scale of mapping, and it is the source of the broad, diffuse pattern that characterizes the collective diagram of the amphibolite terrane as a whole (fig. 9*A*). However, much of this pattern and also that of the linear elements can be explained by the deformation of a more homogeneous F_1 domain, similar to that represented by figure 9*B*, by the F_3 folding. This proposed deformation is supported by the fact that the single south-plunging F_3 axis lies near a cluster of local π axes that probably represent larger scale F_3 folds.

Figure 9*C* differs principally from figure 9*B* in two ways: (1) the partial girdle has been broadened in a northeasterly direction, and (2) the F_1 axes and local π axes have, in addition to southwesterly plunges, gentle southeasterly and northeasterly plunges. The possible effect of F_3 folding on the F_1 geometry is illustrated by figure 10, in which F_3 and S_3 orientations, as well as the amount of rotation of S_0 around F_3, are taken from field measurements of a mesoscopic F_3 fold. It can be seen from figure 10 that the amount of rotation involved in the rather open F_3 folding is enough to spread the S_0 poles east-west by an amount comparable to the width of their field of distribution in figure 9*C*. Although generally southward-plunging, the F_3 axes probably have a complex geometry because of their superposition on a previously folded S_0. The spreading of S_0 poles, therefore, probably took place around a variety of F_3 axial orientations and resulted in the original F_1 girdle being spread laterally along most of its length.

The effect of F_3 folding on the F_1 and F_2 axes is more uncertain and complex. The type of rotation path followed by older fold axes depends on the mechanism of folding (Weiss, 1959), but the data are insufficient to establish such paths. However, either of the two main fold mechanisms, flexural slip and slip, seems adequate to account for the general distribution of axes. In flexural slip folding the possible rotation paths of earlier axes are small circles around the active fold axis (fig. 10*A*); which path is followed depends on the angle between the earlier axes and the fold axis (for 90°, a great circle path). These paths would be dependent on the orientation of F_3, which, as mentioned previously, could have a complex geometry. In slip folding (fig. 10*B*), possible rotation paths of earlier axes are not related to the individual slip fold axes but to the slip direction, which is here

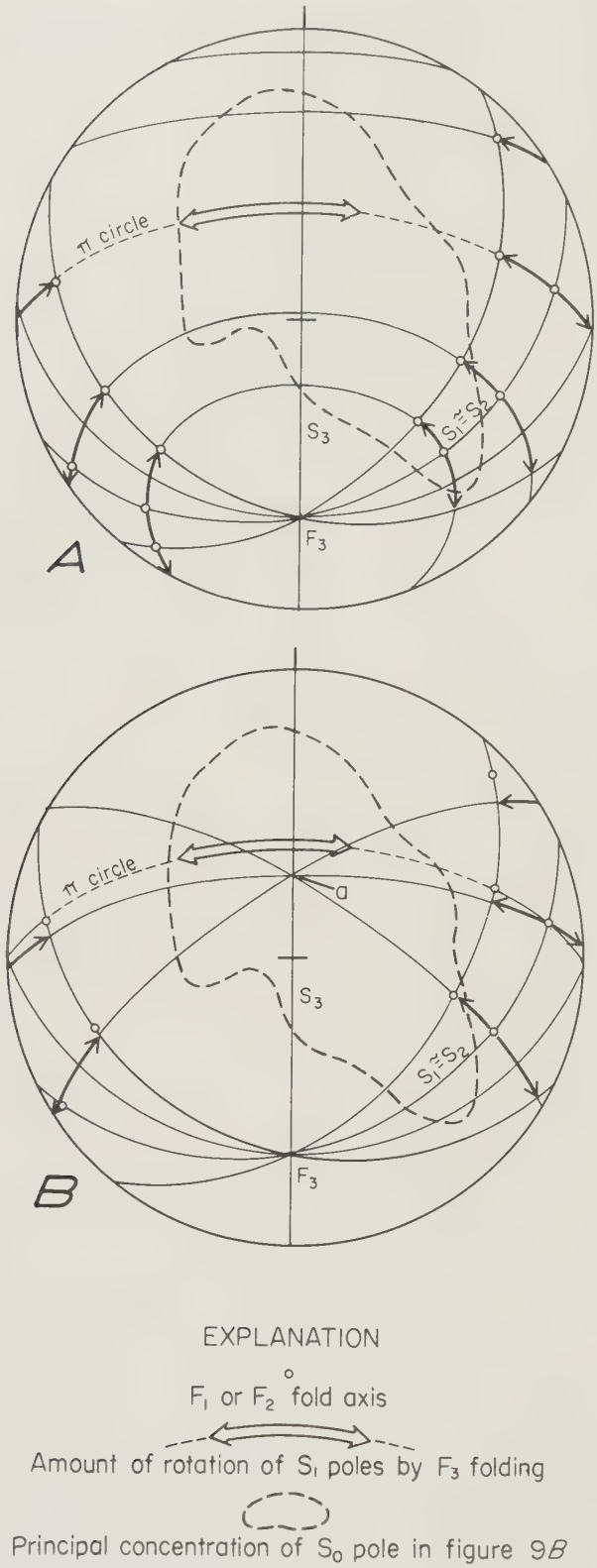

FIGURE 10.—Characteristic rotation paths of earlier fold axes around F_3. *A*, Flexural slip folding. *B*, Slip folding with shear direction at *a*. $S_1 \approx S_2$ average orientation of axial planes of F_1 and F_2 folds at onset of F_3 folding.

unknown but which may be the same throughout a large terrane. The paths are great circles containing an older axis and the slip direction (*a*); thus if the older axes (F_1 or F_2) have more than one orientation at the onset of F_3 folding, separate nonparallel paths exist for each orientation.

Of the two types of rotation paths (fig. 10*A* and *B*), those related to flexural slip seem best to account for the present pattern. For flexural slip to have occured, however, a suitable set of parallel unfolded surfaces must have been present at the onset of folding. The only possible unfolded surface, if F_2 folding was not extensive, is S_1, the axial plane foliation of F_1 folds. If flexural slip occurred on S_1, S_0 in the hinges of F_1 folds would be sheared and disrupted, but there is no indication of this and therefore slip folding must be considered the more probable.

In summary, the F_3 folds seem to have been superposed on the S_0 foliation that had been previously tightly folded, mainly by F_1 folding and possibly locally by F_2 folding. The moderate southward plunge of the F_3 axes reflects the attitude of the limbs of F_1 folds at the onset of F_3 folding. A simplified block diagram of this structure is shown in figure 11. It suggests that the complex hinges (bosses) in the heterogeneous terrane occur where F_3 antiforms have been superposed on F_1 anticlines and that the domains with consistently plunging π axes, either southwest or northeast, represent limbs of large-scale F_3 folds.

Utramafic Rocks

Mesoscopic structure

The metamorphic foliation of the pyroxenitic ultramafic rocks is generally parallel to the primary, probably cumulus, layering, but in detail there is evidence that the foliation is parallel to the axial planes of very sparse, small, isoclinal folds in the layering (fig. 4*A* and *B*). Locally the layering is absent but the foliation is present, whereas in other places both are absent. The foliation is also not megascopically evident in dunite, but it probably is present there as a planar fabric element parallel to the axial planes of the isoclinal folds in chromitite layers (fig. 4*C*). The investigation of the olivine microfabric has been prevented by the intense serpentinization. The isoclinal folds are probably the earliest folds.

Later, more open folds, having steeply dipping axial planes that were formed in both the layering and foliation, are more common. These folds are larger, probably averaging more than 5 m in width, and are generally larger than existing outcrops. They are thus

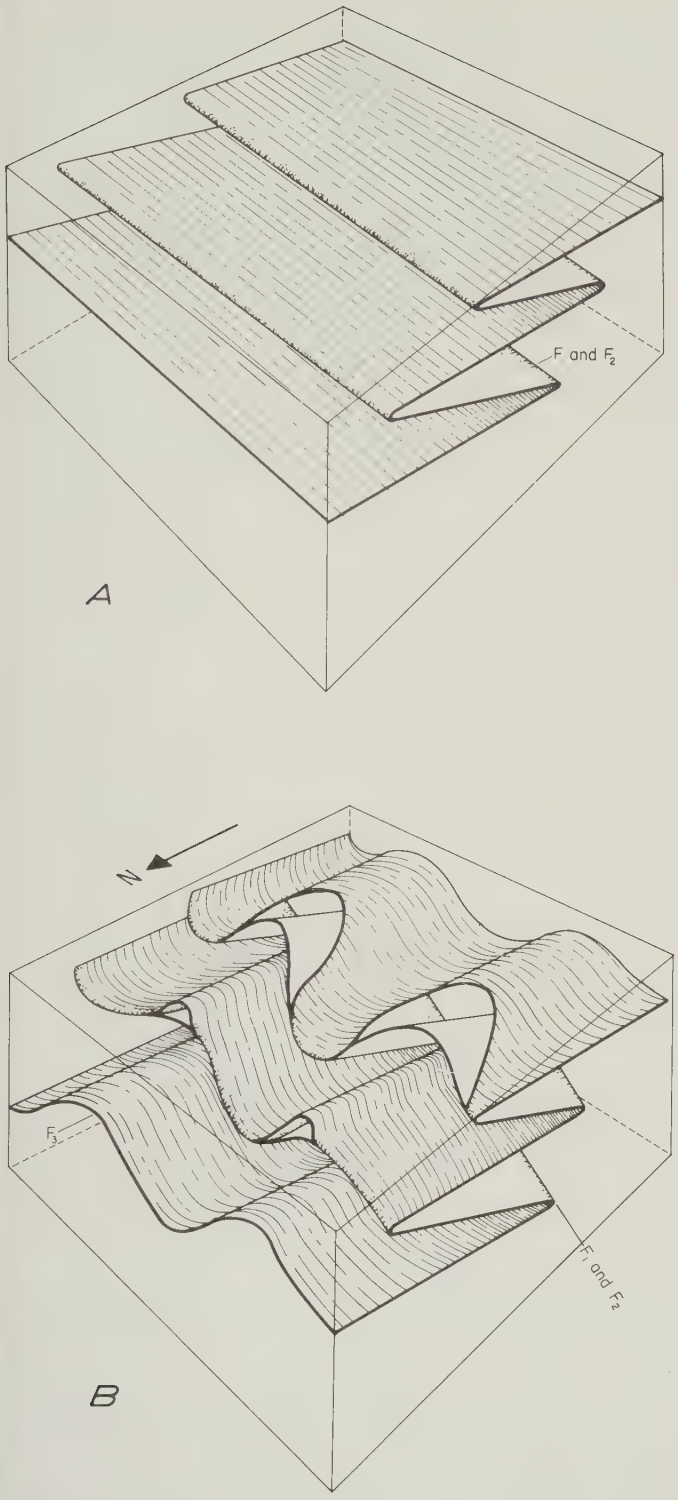

FIGURE 11.—Probable relations between F_1 and F_3 folding in amphibolite terrane. *A*, General attitude of F_1 and possibly F_2 folds before F_3 folding. *B*, After F_3 folding.

transitional between mesoscopic and macroscopic scales, and the details of their style and orientation can seldom be obtained by direct observation in a single outcrop. (See following section entitled "Macroscopic structure.")

Lineations are sparse throughout the ultramafic terrane. They consist of alined elongate minerals (mostly hornblende), ribbing, and streaking, all generally on the foliation or layering surfaces. The correlation of most of the lineations with the fold generations above is uncertain. Some seem to be deformed by the later folding and may be related to the early folds, but most are hornblende lineations that occur in mafic layers and veins and are part of the gabbro intrusion. These lineations probably reflect syntectonic intrusion after the early folding, but before the later folds. (See following section entitled "Macroscopic stucture.")

Later than the folding are gently dipping, undulatory shear zones that are best exposed on the ridge south of Dry Butte (fig. 2). Individual zones range from 0.2 to 1.0 m in thickness and consist of sheared-out lenses of both olivine-rich and clinopyroxene-rich ultramafic rocks that are highly variable in size but commonly range from 10 to 200 mm in length. In addition, the shear zones have generally been injected with gneissic hornblende gabbro of variable thickness that swirls around the sheared ultramafic lenses and is bordered by hornblende reaction zones. (See "Hornblende Gabbro" in "Structure" section.) The shear zones strike northward and dip eastward about 10° to 20°, being markedly discordant with the foliation in the ultramafic rocks. Where best exposed, the zones occur at 1- to 3-m intervals and extend from the east side of the ridge through to the west side.

Macroscopic structure

The dunite bodies shown in figure 2 provide the principal marker units by which the internal structure shown by the plots may be related to the map pattern. Unlike the contacts between the ultramafic rocks and the amphibolite and gabbro, the contacts between the pyroxenite and the dunite are primary ones that are equivalent to the internal layering in the pyroxenite and dunite, in which most of the mesoscopic structures were formed. This layering is probably cumulate in origin.

The poles to foliation (fig. 12*A*) tend to form a broad eastward-striking subvertical girdle that has a subhorizontal north-trending π axis. The scatter in figure 12*A* is reduced by dividing the area into two domains, a southern one (fig. 12*B*) with a north-trending π axis and a northern one (fig. 12*C*) with generally northeast-trending π axes.

In the southern domain (fig. 12*B*), most of the mesoscopic fold axes cluster around the north-trending subhorizontal π axis, whereas most of the lineations

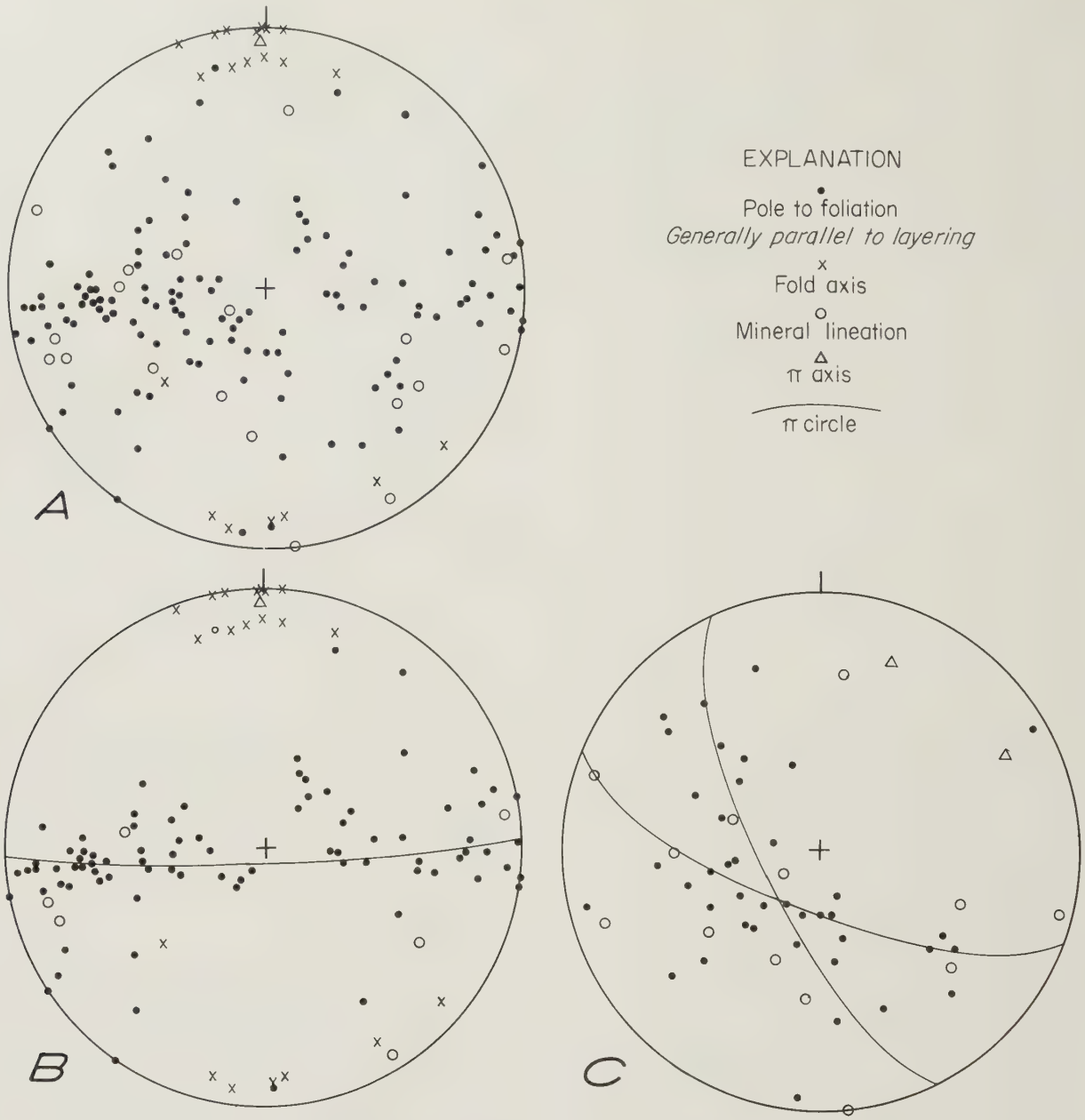

FIGURE 12.—Equal-area lower hemisphere plots for the ultramafic terrane. *A*, Entire terrane. *B*, Southern domain. *C*, Northern domain. (See fig. 2 for location.)

and a single fold axis are scattered near the girdle. This geometry indicates that the macroscopic structure is dominated by the folding that produced the common north-trending mesoscopic folds. The greatest density of poles is in the western half of the girdle and represents a mean eastward dip of approximately 60°. This distribution corresponds well to the form and attitudes of the north-trending mesoscopic folds, most of which have one steep (70°to 80°) overturned east-dipping limb and a gentler (30° to 65°) normal limb, also east dipping. Although the steep limbs are dominantly overturned, the substantial number of poles in the girdle, representing westward dips, indicate that the steep limbs range from east-dipping overturned through vertical to west-dipping normal. The axial planes of the folds consistently strike north and dip steeply to the east.

The lineations in figure 12*C* are elongate hornblende grains along foliation planes in mafic layers. These layers are part of the gabbroic intrusion and are thus later than the primary layering of the ultramafic rocks. The lineations appear to represent an episode of syn-

tectonic intrusion after the early isoclinal folding of the primary layering and before the late north-trending folding. Their scattering along the girdle strongly suggests folding by the late folds.

The dunite in the southern domain (fig. 2) occurs in a single outcrop that caps a northeast- to north-trending ridge where dunite and pyroxenite intertongue. This intertonguing along the southwestern dunite contact is probably the expression of the later folding. The tongues as mapped trend more northeastward than mesoscopic data indicate, but the scattered outcrops prevent a more accurate location of the contacts in that area. The outcrop pattern in general is compatible with subhorizontal north-trending folding. The dunite outcrop may possibly represent the hinge of a very large synform, but there are no repetitions of the dunite elsewhere that suggest north-trending folds of that scale. In any event, most of the terrane where such repetition might occur is now composed of the younger intrusive gabbro.

The plot of the northern domain (fig. 12*C*) shows little indication of north-trending elements and is dominated by a girdle, the π axis of which plunges gently northeast. The domain is not quite homogeneous, and π axes ranging from north-northeast to northeast can be constructed. Mesoscopic fold axes are apparently sparse in the domain; the only such folds seen were small isoclinal ones, the orientation of which could not be determined. The two lineations shown in the northeast and southwest quadrants are of a streak variety, the significance of which is unknown. The distribution of poles in the girdle shows a much higher concentration in the central, more gently dipping part than in the diagram for the southern domain (fig. 12*B*) and reflects a change in style of folding from the upright steep-limbed folds to folds with gently to moderately dipping axial planes and limbs.

Although the attitudes in the northern domain (fig. 2) give ample evidence of folding related to the northeast-trending π axis, the folds are somewhat larger than the existing outcrops ond their exact style cannot be observed directly. The geometry in figure 12*C* is compatible with nearly recumbent isoclinal folds. Such folds on a small scale have been observed in primary layering (fig. 4*B*) and may have larger scale counterparts. On the map (fig. 2) a large-scale, nearly recumbent isoclinal fold is suggested by the pinching out to the north of the dunite layer at Dry Butte and the occurrence of pyroxenite above and below the dunite. Although the hinge area is obscured by landslides and gabbro intrusion, the axis of the possible fold, on the basis of the overall relations, could well plunge gently northeast. Such a synform and subsidiary folds are shown in the cross section (fig. 2) and would explain most of the attitudes on the map and would also be compatible with the geometry in figure 12*C*.

Hornblende Gabbro

Structurally the hornblende gabbro can be divided into (1) gneissic gabbro, (2) relatively thin tabular intrusions in the ultramafic rocks and amphibolite, and (3) pegmatitic gabbro. The structural features of the first two parts seem to reflect intrusion and deformation as a viscous magma, not deformation as a solid. The pegmatitic phase shows generally igneous textures and little indication of plastic deformation.

The gneissic gabbro shows everywhere a swirling gneissose foliation that in detail is the result of mesoscopic plastic shear zones that average about 200 mm in width (fig. 7). The gneissic foliation bends into the shear zone through an outer zone about 50 to 100 mm wide on each side of the shear zone itself. In the shear zones, the foliation becomes thinner and more intensely developed, accompanied by a decrease in the granularity. The abruptness of this bend is variable and in part depends on the initial orientation of the foliation. That the initial orientation was probably variable is indicated by the fact that the axes of bending on opposite sides of some shear zones are grossly divergent. It could not be determined whether or not there are larger scale macroscopic shear zones, but this seems likely. (See cross section, fig. 2.) Plots of the poles to the gneissic foliations and to the few shear zones that could be measured show little preferred orientaion and no recognizable pattern.

The tabular gabbro bodies that cut the ultramafic and amphibolitic terranes range from less than 1 mm to several meters thick and probably average about 150 mm in thickness. These tabular bodies form networks consisting of both dikes and sills that are locally abundant, especially near contacts with the main gabbro mass. They are best exposed in the ultramafic rocks, where they form random networks in dunite but more ordered complexes in layered pyroxenitic rocks. In the latter, the tabular gabbro is commonly parallel to both the layering (sills) and a joint set perpendicular to the layering (dikes). Commonly, the sills and dikes interconnect as continuous intrusions and do not cut one another.

Generally characteristic of the tabular hornblende gabbro bodies is the pronounced flow foliation, which is much thinner and more continuous in aspect than the gneissic foliation of the main gabbro mass. Figure 13*B* shows diagrammatically the details of dike and sill relations in pyroxenitic layered ultramafic rocks. The

A

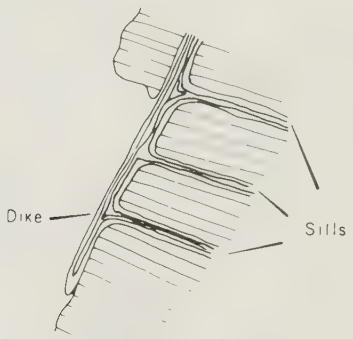

B

FIGURE 13.—Gabbroic dikes and sills in pyroxenitic layered ultramafic rocks. *A*, Gabbroic dike parallel to joint-controlled cliff face formed in layered ultramafic rock, showing flow layering in tonguelike lobe. *B*, Relations of gabbroic dikes and sills and their flow layering to layering and jointing in ultramafic rocks.

face of cliff exposure is a joint face approximately perpendicular to the layering. The magma probably intruded the layering and the joints simultaneously, producing continuous flow banding generally parallel to the contacts with the country rocks. In places, dikes end in sharp, tonguelike lobes, in which the flow banding parallels the lobe surface, producing a foldlike structure (fig. 13*A*). The lobes are coated with hornblende selvages that are continuous with sides of the dikes. The selvages are reaction zones that have been found wherever gabbroic rocks are in contact with ultramafic rocks. The evidence, therefore, indicates that the lobes are original terminations of magma intrusions, or the termination of layers in the magma, and not a product of later deformaion in the solid. Where such flow folds occur in sills, they resemble the early isoclinal folds in the primary layers, except that they occur in hornblende-bearing mafic rock. It is possible that the hornblende lineation seen in the ultramafic terrane is related to the flow folds. (See "Ultramafic Rocks" in "Structure" section.)

Much less commonly, gabbro has been injected into active shear zones in the ultramafic rocks. In a few places the foliation in the ultramafic rocks has been the site of injection by gabbroic material—chiefly plagioclase, quartz, and hornblende. The gabbro has been selectively injected along the foliation surfaces, where it swirls around larger crystals of clinopyroxene and olivine, and thus a strong foliation in which small flow folds occur is produced. Crosscutting dikes and veins of gabbro seem to be absent from the vicinity of the injected zones. The injected zones tend to thin rapidly and die out within a few meters. These features suggest that, during gabbro intrusion, shear movement along foliation surfaces occurred only locally.

In other places, chiefly on the ridge south of Dry Butte, gabbro has been injected into gently dipping shear zones that crosscut the foliation and layering in the ultramafic rock. The gabbro is irregularly foliated in these zones, swirling around sheared-out masses of ultramafic rock. Its thickness is variable but commonly ranges from 50 to 100 mm. The contact between gabbro and ultramafic rock is marked by hornblende reaction zones similar to those described previously, which generally range from 5 to 30 mm in thickness but locally are much thicker. In view of the selective injection of the gabbro in the shear zones and its strongly foliated aspect, the intrusion was at least in part contemporaneous with the shear movement. (For further data on shear zones, see "Ultramafic Rocks" in "Structure" section.)

DISCUSSION AND CONCLUSIONS

The amphibolite unit, of Jurassic(?) age, probably contains the oldest rocks in the Dry Butte terrane. It has undergone regional metamorphism to the amphibolite facies and three episodes of folding. Omitting accessory minerals, maximum phase associations of the amphibolite and associated metamorphosed rocks are as follows:

1. hornblende-plagioclase-epidote-quartz
2. hornblende-plagioclase-diopside-quartz

3. hornblende-plagioclase-garnet-quartz
4. biotite-white mica-plagioclase-quartz
5. biotite-plagioclase-garnet-epidote-quartz

Turner (1968, p. 308) defines the amphibolite facies on the basis of the diagnostic association hornblende + plagioclase ±epidote ±garnet. Thus, on the basis of association 1 and 3, the amphibolites are interpreted to have undergone regional metamorphism to the amphibolite facies. Superposed on this metamorphism is a general increase in granularity and possibly in the amount of feldspar toward contacts with the intrusive gabbro. However, no distinctive mineral associations were found that would differentiate this "contact" metamorphism from the "regional" one described above.

The ultramafic rocks are partially recrystallized, but widespread relict textures suggest that they originated by cumulus processes. Further, they structurally overlie the amphibolite, show a less complex fold geometry, and do not seem to be in fault contact with the amphibolite, although contact relations are not entirely clear. These data suggest that the ultramafic rocks, if truly of cumulus origin, were deposited on a previously deformed and metamorphosed amphibolite terrane.

Recrystallization of the ultramafic rocks is attributed to thermal metamorphism caused by intrusion of the hornblende gabbro. Omitting accessory phases, recrystallized mineral associations are as follows:

1. diopside-tremolite
2. diopside-tremolite-forsterite
3. diopside-tremolite-forsterite-chlorite
4. diopside-tremolite-enstatite
5. diopside-hornblende-plagioclase-(enstatite)

These associations are consistent with those in the CaO-MgO-SiO_2-H_2O system listed by Evans and Trommsdorff (1970) fig. 14).

The common association diopside-tremolite-forsterite is obtained from the univariant reaction 3 (fig. 14):

$$5 \text{ antigorite} + 2 \text{ diopside} = \text{tremolite} + 6 \text{ forsterite} + 9H_2O$$

(Evans and Trommsdorff, 1970) and remains stable over a large range in temperature up to the univariant reaction 9 (fig. 14):

$$\text{tremolite} + \text{forsterite} = 5 \text{ enstatite} + 2 \text{ diopside} + H_2O$$

(Evans and Trommsdorff, 1970). Enstatite is not common in the recrystallized associations, but the presence of diopside-tremolite-enstatite does suggest that locally the physiochemical conditions of recrystallization did exceed those appropriate for reaction 9. Whether reaction 9 was caused by a local increase in temperature or by local fluctuations in P_{H_2O} is indeterminate.

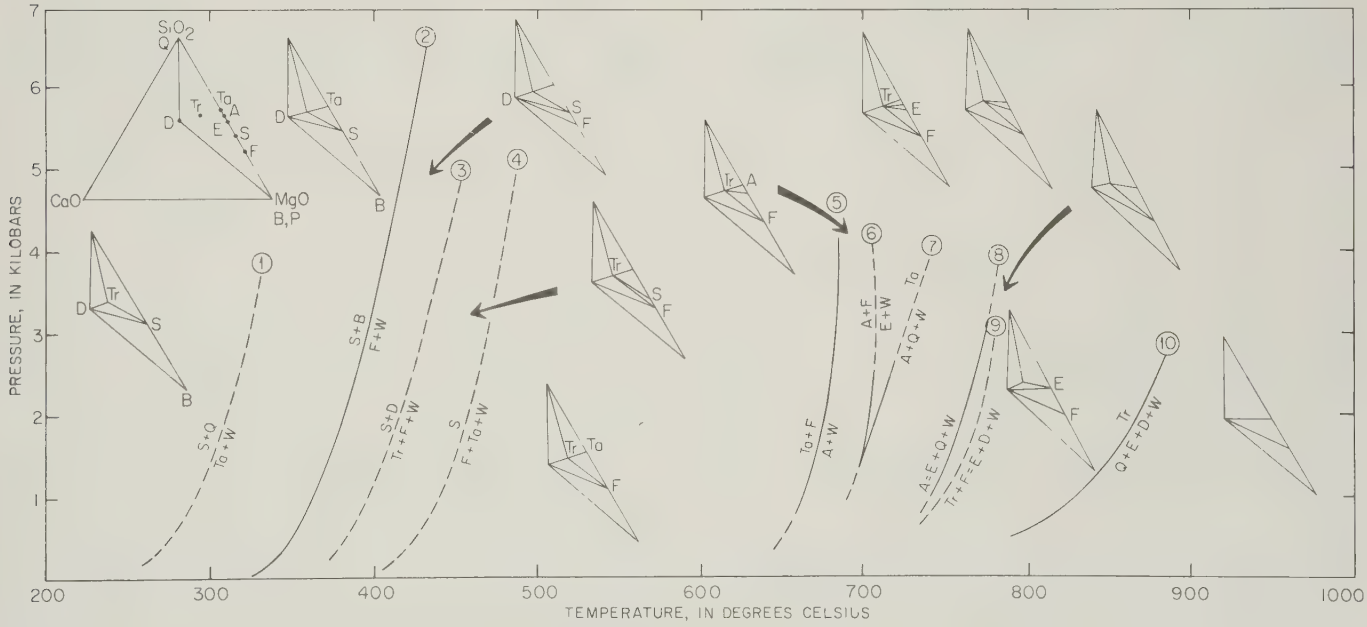

FIGURE 14.—Phase relations in subsystem MgO—$CaMgSi_2O_6$—SiO_2 in which $P_{H_2O}=P_{total}$ (from Evans and Trommsdorff, 1970). Chemographic diagram is a segment of the triangle SiO_2—CaO—MgO shown at left. Solid curves represent experimentally determined equilibria; broken curves represent calculated equilibria. Circled numbers refer to equilibrium reactions discussed in text. A, anthophyllite; B, brucite; D, diopside; E, enstatite; F, forsterite; P, periclase; Q, quartz; S, serpentine; Ta, talc; Tr, tremolite; W, H_2O.

Contact zones of hornblende gabbro with dunite also indicate that the conditions of recrystallization, at least locally, approached that of reaction 9. The contacts are zoned, and proceeding from the hornblende gabbro to the dunite, the interfingering zones are hornblende gabbro, tremolite+chlorite, anthophyllite+chlorite, enstatite, and olivine. These zones range in thickness from 5 to 20 mm. The mineralogical zonation indicates Si, H_2O, and Ca activity gradients decreasing away from the hornblende gabbro. Moreover, the interfingering of enstatite with anthophyllite as well as enstatite-anthophyllite veins limits the physicochemical conditions in the immediate contact zone to those between reactions 6 and 8 in figure 14. Thus, based on the comparison of the recrystallized mineral associations with experientally determined and calculated equilibria, the minimum temperature of recrystallization, assuming $P_{H_2O}=P_{load}$, was approximately 400° C, and the maximum temperature was locally approximately 750° C.

Although the amphibolite terrane was folded prior to the crystallization of the primary ultramafic rocks and the intrusion of the hornblende gabbro, later folding affected all three of these units. The isoclinal F_1 folds are the earliest in the amphibolite and were undoubtedly formed prior to the primary ultramafic rocks. The sparse isoclinal folds in the primary, probably cumulate, layering of the ultramafic rocks are thus not equivalent to F_1 folds in the volcanic-sedimentary layering (S_0) of the amphibolite. The two layerings are thus of an entirely different origin and are probably of different ages. The F_2 amphibolite folds also seem to be absent in the ultramafic rocks, and it is the superposition of F_2 upon F_1 folds that gives much of the amphibolite terrane its structurally complex and inhomogeneous aspect (fig. 9), which is not the case in the ultramafic terrane (fig. 12). Although the F_3 folds have contributed to that complexity, they can be clearly identified only in the ultramafic terrane, where they are important but produce a much simpler, more homogeneous geometry. The evidence indicates that the F_3 folds were superposed on a much more complex structure in the amphibolite terrane (F_1 and F_2) than in the ultramafic terrane (scattered isoclinal folds).

The intrusion of the hornblende gabbro was coeval with much of the foregoing deformation. Probably the earliest evidence of the intrusion is the gabbro veins that are involved in the F_2-type folds in the amphibolite (fig. 3*C*). Other evidence of contemporaneous intrusion and deformation occurs where gabbroic material has been injected along the foliation and in shear zones in the ultramafic rocks. Although injection along the foliation suggests contemporaneous intrusion and plastic deformation, the shear zones represent a more brittle deformation, as do most of the other sites of gabbro intrusion, such as along joints. The gabbro intrusion seems, therefore, to have started during the plastic deformation (F_2 folding) and continued, perhaps intermittently, to the last stages of brittle deformation in the ultramafic rocks and perhaps even afterward. Hornblende lineation in tabular mafic bodies in ultramafic rocks appears to be deformed by the latest folding episode (probably F_3). The pegmatite phase lacks deformation features and may be posttectonic. In any case, the gabbro behaved as a highly viscous liquid throughout the deformation.

The thrusting of the Josephine Peridotite over the Dry Butte terrane along the Madstone Cabin thrust fault was later than the foregoing events but was earlier than the thrusting of both of these terranes over the Dothan Formation of Late Jurassic age along the Valen Lake thrust fault (fig. 2).

In conclusion, the proximity of the alpine-type Josephine Peridotite to the gabbro and probable cumulate ultramafic rocks of the Dry Butte terrane suggests the basal ultramafic tectonite complex and at least part of the gabbroic complex, respectively, of an ophiolite sequence, similar to the Troodos ophiolite of Cyprus (Vine and Moores, 1972). However, the Dry Butte terrane lacks the well-developed cumulate gabbro zone, and instead the only probable cumulates are ultramafic rocks that have been much disrupted and engulfed by intrusive gabbro. It is possible that the Madstone Cabin thrust fault cut out part of the lower cumulate section, but it is unlikely that the fault is responsible for removing the higher gabbro cumulates. These differences, however, may be only variations to be expected in an ophiolite sequence, originating in a tectonically active environment.

The amphibolite, however, unless faulted against the ultramafic cumulate sequence, does not seem to fit the classic ophiolite model. Our preliminary data suggest that the amphibolite was derived from andesitic volcanic material, possibly from an island arc, rather than from a spreading center. There is insufficient data to explore further this aspect of the problem at this time, and, furthermore, a fault contact cannot be ruled out. The tendency for the amphibolite to occur along the Madstone Cabin thrust fault suggests that the amphibolite was brought up as one or more blocks in the fault zone. However, the complex contact relations between the amphibolite and prefaulting rocks (ultramafic cumulates and gabbro) make it unlikely that the amphibolite was brought in by this thrust fault.

REFERENCES CITED

Coleman, R. G., Garcia, Michael, and Anglin, Camille, 1976, The amphibolite of Briggs Creek: A tectonic slice of metamorphosed oceanic crust in southwestern Oregon?: Geol. Soc. America Abs. with Programs, v. 8, p. 363.

Coleman, R. G., and Keith, T. A., 1971, A chemical study of serpentinization—Burro Mountain, California: Jour. Petrology, v. 12, p. 311–328.

Engel, A. E. J., Engel, C. J. G., and Havens, R. G., 1965, Chemical characteristics of oceanic basalts and the upper mantle: Geol. Soc. America Bull., v. 76, p. 719–734.

Evans, B. W., and Trommsdorff, Volkmar, 1970, Regional metamorphism of ultramafic rocks in the central Alps: Paragenesis in the system CaO—MgO—SiO_2—H_2O: Schweizer. Mineralog. u. Petrog. Mitt., v. 50, p. 481–492.

Hills, E. S., 1963, Elements of structural geology: New York, John Wiley & Sons, 483 p.

Himmelberg, G. R., and Loney, R. A., 1973, Petrology of the Vulcan Peak alpine-type peridotite, southwestern Oregon: Geol. Soc. America Bull., v. 84, p. 1585–1600.

Hotz, P. E., 1971, Plutonic rocks of the Klamath Mountains, California and Oregon: U.S. Geol. Survey Prof. Paper 684–B, p. B1–B20.

Irvine, T. N., and Findlay, T. C., 1972, Alpine-type peridotite with particular reference to the Bay of Islands Igneous Complex: Symposium volume on the oceanic crust and recognition of the oceanic crust on the continents: Canada Earth Physics Branch Pub., v. 42, p. 97–128.

Kay, Robert, Hubbard, N. J., and Gast, P. W., 1970, Chemical characteristics and origin of oceanic ridge volcanic rocks: Jour. Geophys. Research, v. 75, p. 1585–1614.

Loney, R. A., Himmelberg, G. R., and Coleman, R. G., 1971, Structure and petrology of the alpine-type peridotite at Burro Mountain, California, U.S.A.: Jour. Petrology, v. 12, p. 245–309.

Loney, R. A., and Himmelberg, G. R., 1976, Structure of the Vulcan Peak alpine-type peridotite, southwestern Oregon: Geol. Soc. America Bull., v. 87, p. 259–274.

Miyashiro, Akiho, Shido, Fumiko, and Ewing, Maurice, 1969, Diversity and origin of abyssal tholeiite from the Mid-Atlantic Ridge near 24° and 30° north latitude: Contr. Mineralogy and Petrology, v. 23, p. 38–52.

Nockolds, S. R., 1954, Average chemical compositions of some igneous rocks: Geol. Soc. America Bull., v. 65, p. 1007–1032.

Page, N. J, 1967, Serpentinization at Burro Mountain, California: Contr. Mineralogy and Petrology, v. 14, p. 321–342.

Penrose field conference participants, 1972, Ophiolites: Geotimes, v. 17, no. 12, p. 24–25.

Ramp, Len, 1975, Geology and mineral resources of the upper Chetco drainage area, Oregon, including the Kalmiopsis Wilderness and Big Craggies Botanical areas: Oregon Dept. Geology and Mineral Industries Bull. 88, 47 p.

Ramsay, J. G., 1967, Folding and fracturing of rocks: New York, McGraw-Hill, 569 p.

Shapiro, Leonard, 1967, Rapid analysis of rocks and minerals by a single-solution method: U.S. Geol. Survey Prof. Paper 575–B, p. B187–B191.

Streckeisen, A. L., 1973, Classification and nomenclature of plutonic rocks: Neues Jahrb. Mineralogie Monatsh., v. 4, p. 149–164.

Thayer, T. P., and Himmelberg, G. R., 1968. Rock succession in the Canyon Mountain alpine-type mafic complex, Oregon: Internat. Geol. Cong., 23d, Prague, Czechoslovakia 1968, Rept. Proc. Sec. 1, p. 175–186.

Turner, F. J., 1968, Metamorphic petrology: Mineralogical and field aspects: New York, McGraw-Hill, 403 p.

Vine, F. J., and Moores, E. M., 1972, A model for the gross structure, petrology, and magnetic properties of oceanic crust: Geol. Soc. America Mem. 132, p. 195–205.

Weiss, L. E., 1959, Geometry of superposed folding: Geol. Soc. America Bull., v. 70, p. 91–106.

Wells, F. G., Hotz, P. E., and Cater, R. W., 1949, Preliminary description of the geology of the Kerby quadrangle, Oregon: Oregon Dept. Geology and Mineral Industries Bull., v. 40, 23 p.

Jour. Research U.S. Geol. Survey
Vol. 5, No. 6, Nov.–Dec. 1977, p. 783–795

HIGH-RESOLUTION GAMMA-RAY SPECTROMETRY IN URANIUM EXPLORATION

By ROBERT M. MOXHAM and ALLAN B. TANNER,
Reston, Va.

Abstract.—Sedimentary-type uranium deposits accumulate at favorable sites along a migration path which may be kilometers in length. Their source is a large volume of rock from which the uranium has been leached. The geochemical mobilities and half lives of uranium and its daughter products vary widely so that they are transported from the source rocks, at different rates, along the migration path to their ultimate site. The radioactive disequilibrium resulting from this process has been well documented in the immediate vicinity of ore deposits, and disequilibrium is commonly recorded on gamma-ray logs up the hydraulic gradient from uranium ore. Little is known about the state of secular equilibrium in the leached host rocks, which often represent the only part of the migration path that is at or near the surface and is thus most accessible to the exploration geophysicist. High-resolution gamma-ray spectrometry provides a means of investigating the disequilibrium associated with uranium leaching and migration. Direct measurement of uranium can be made by this method, and the equivalent weight percents can be determined for six of the seven daughter-product decay groups that characterize the state of radioactive equilibrium. The technique has been used quantitatively in laboratory studies, where the results compare favorably with radiochemical analyses; field experiments suggest that semiquantitative data may be obtained at the outcrop.

Gamma-ray spectrometry has been a valuable field technique in uranium exploration for more than two decades. It permits one to determine, at least qualitatively, whether an observed gamma-ray anomaly is associated with uranium, thorium, potassium, or a fission product. The most common instrument for both ground and airborne surveys is the NaI(Tl) detector with a three- or four-channel pulse-height analyzer. Such systems cannot measure uranium directly. Rather, it is customary to measure one of the ^{214}Bi lines and to assume that radioactive equilibrium exists with ^{238}U. It is well known that equilibrium often does not exist, as ^{214}Bi is far removed from ^{238}U in the decay chain (table 1) and the precursors of ^{214}Bi are of widely varying mobility. For preliminary exploration, however, the state of equilibrium has been regarded as secondary in importance to the location and identification of uranium-associated anomalies. Many explorationists have found a four-channel NaI(Tl) spectrometer adequate for this purpose. Nonetheless, the future discovery of uranium deposits will become increasingly difficult as the more obvious ones, at or near the surface, are exploited. In this respect, uranium will follow the same historical course as other mineral commodities; increasingly sophisticated geophysical approaches will be required to locate the more subtle targets.

The need to identify the state of equilibrium has long been recognized by those responsible for development of mining operations, where one hopes to avoid stripping overburden from ore that has been overestimated in grade because of an excess of uranium daughter products. The same principle applies to solution mining. Disequilibrium also has very important implications for the exploration geophysicist. Rosholt (1961, p. 424) pointed out more than a decade ago that when uranium is leached from its source rocks and is carried by ground water through a sedimentary host to its ultimate destination (hopefully, a uranium deposit), it leaves a trail of radioactive daughter products along its path. Such a migratory pattern greatly enlarges the exploration target and should be used to our advantage.

In order for the radioactive migration pattern to persist, at least some of the long-lived daughters of ^{238}U and ^{235}U must drop out along the pathway. This is fortunately the case. Isotopic fractionation of ^{234}U and ^{238}U was first documented by Syromyatnikov (1960) and has been confirmed since by many others. In addition, protactinium and thorium form insoluble hydroxides so that ^{230}Th and ^{231}Pa are removed from the ground water almost as soon as they are generated. These phenomena of the migratory process have been recognized on gamma-ray logs in drill holes as much as several kilometers, upgradient from roll-type uranium deposits, where gamma-ray anomalies are

TABLE 1.—*The uranium decay chains, showing the principal groups (separated by dashed lines) that determine the state of equilibrium*

[Nuclear constants are from Nuclear Data Sheets, Academic Press, N.Y.]

^{238}U Chain					^{235}U Chain				
Group	Isotope	Half life	Principal γ-lines 20-400 keV	Absolute intensity	Group	Isotope	Half life	Principal γ-lines 20-400 keV	Absolute intensity
							7.13×10^{8} yr	185.7	54.0
Uranium	^{238}U	4.5×10^{9} yr			Uranium	^{235}U		143.8	9.7
	^{234}Th	24.1 d	63.3	5.7				205.3	5.0
			92.6	6.8				163.4	4.6
	[^{234}Pa d/	6.66 h							
	[^{234m}Pa	1.14 min			Protactinium	^{231}Th	25.6h	25.6	12.0
	^{234}U	2.47×10^{5} yr	53.1 b/	0.68		^{231}Pa	3.43×10^{4} yr	27.3	7.8
								302.5	2.0
Thorium	^{230}Th	8×10^{4} yr	67.8	0.4				283.6	1.3
						^{227}Ac	22.0 yr		
Radium	^{226}Ra	1622 yr	186.1 c/	4.0		a/			
						^{223}Fr (1.2%)	21 min		
Radon	^{222}Rn	3.83 d				^{227}Th (98.8%)	18.6d	236.0	10.4
	^{218}Po	3.05 min						256.2	6.0
	^{214}Pb	26.8 min	352.0	36.0		^{223}Ra	11.2d	269.6	13.6
			295.2	18.9		^{219}Rn	3.92s		
			241.9	7.6		^{215}Po	1.83×10^{-3} s		
			53.2	2.2		^{211}Pb	36.1 min		
	^{214}Bi	19.7 min				^{211}Bi	2.16 min		
	a/					a/			
	^{214}Po (99.98%)	1.64×10^{-4} s				^{207}Tl (99.7%)	4.79 min		
	^{210}Tl (.02%)	1.32 min				^{211}Po (0.3%)	0.52s		
Lead	^{210}Pb	22 yr	46.5	4.0		^{207}Pb	Stable		
	^{210}Bi	5.02 d							
	^{210}Po	138 d							
	^{206}Pb	Stable							

a/ The chain branches at this point. (branching ratio is in parentheses.) Angle brackets indicate the two daughters.

b/ Interference with ^{214}Pb at 53.2 keV.

c/ Interference with ^{235}U at 185.7 keV.

d/ Straight brackets indicate isomeric states.

commonly in excess of the equilibrium quantity of uranium. This condition is ordinarily expressed simply as eU>U, and the excess radiation is assigned to ^{214}Bi. Although such may be the fact, some of the ^{214}Bi must be generated by a long-lived ancestor at that site; otherwise the anomaly would not persist for a geologically significant time.

The systematics of uranium daughter distribution in the vicinity of sedimentary uranium-ore deposits have been previously elucidated (Rosholt, Butler, and others, 1965; Rosholt, Tatsumoto, and others, 1965; Dooley and others, 1964). Much less is known about the more distant parts of the migration path and (perhaps most important from the exploration geophysicist's standpoint) about the disequilibrium patterns at the Earth's surface in areas that may have provided the uranium, which may be the only part of the migration trail detectable in surface and airborne prospecting.

Let us first examine the gamma-ray spectrum of uranium. Figure 1 compares the spectra of uranyl nitrate with a typical sandstone-type uranium ore.

The uranyl nitrate contains only the uranium-group isotopes, that is, ^{238}U, ^{234}U, ^{235}U, and their short-lived daughters, ^{234}Th, ^{234m}Pa, and ^{231}Th, whereas the ore sample contains all the uranium-series isotopes. A most important fact is evident, namely that the strong lines from the uranium group and the short-lived daughters all are found in the low-energy part of the spectrum, below 200 keV, with the exception of a ^{234m}Pa line whose importance will be mentioned later. Nearly all field measurements (surface, airborne, and boreholes) made with NaI(Tl) detectors have very poor energy resolution and peak-to-Compton ratios in the low-energy region. Consequently, the lower level discriminator is customarily set to reject all photons of energy less than about 400 keV, and either the total count or the spectral measurements are confined to the high-energy region. In the high-energy part of the spectrum, however, the only lines that can be resolved by th NaI detector are from Pb and Bi daughter products, so that nothing of the uranium content of the target or sample can be established without making (usually) unwarranted assumptions about the state of equilibrium. In contrast with the NaI(Tl) detector, the planar germanium detector achieves both good detection sensitivity and the greatest resolution of any available system in the 45- to 250-keV region. Figure 1 demonstrates that this region contains not only lines from uranium and its immediate decay products but

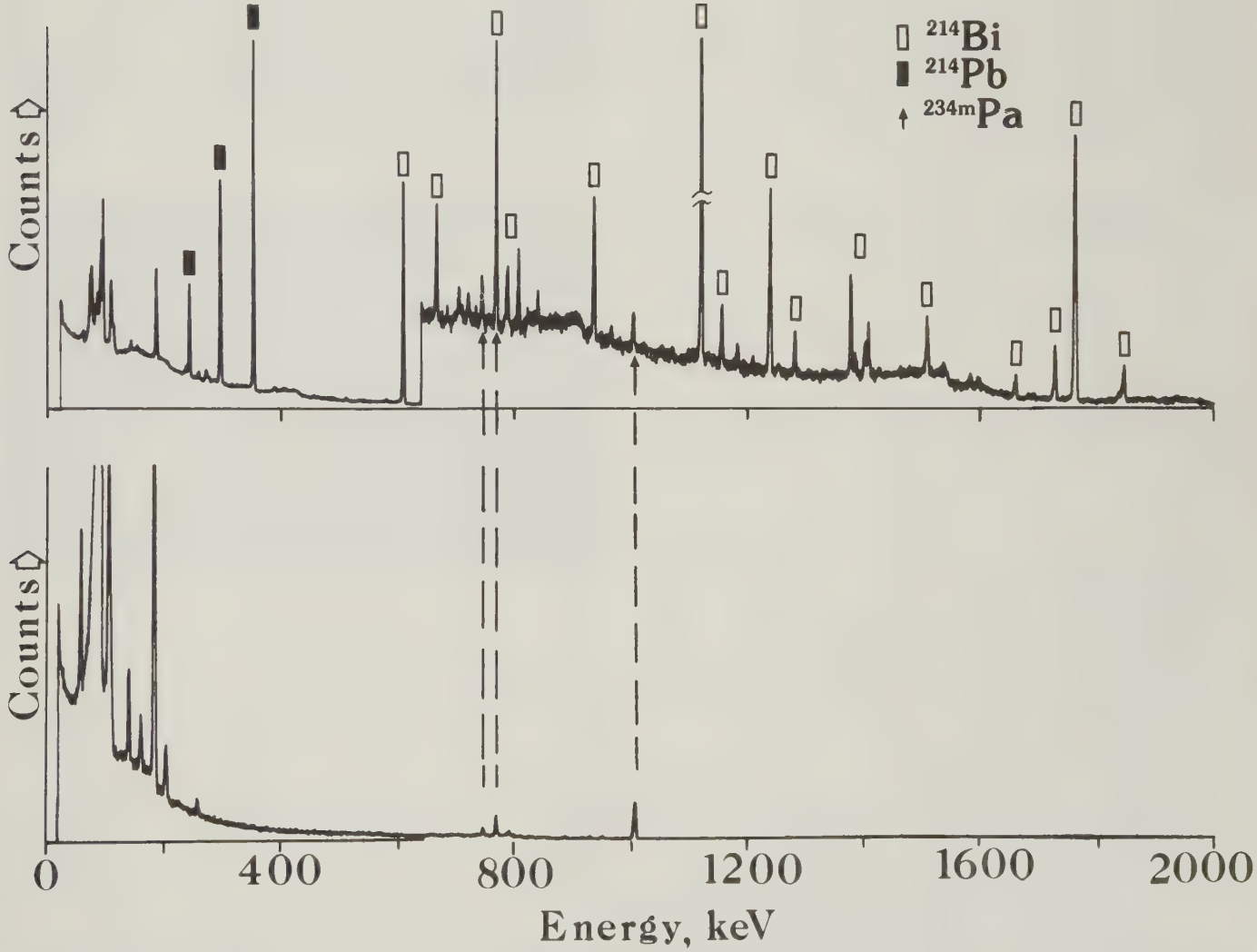

FIGURE 1.—Laboratory gamma-ray spectrum of uranium ore (upper) and uranyl nitrate (lower) made by means of a coaxial Ge(Li) detector. The ore contains all the daughter products in the uranium chain, but the principal peaks in the 200 to 2000-keV region are from ^{214}Bi and ^{214}Pb isotopes that are often out of equilibrium with uranium. One line from ^{234m}Pa occurs at 1001.4 KeV and bears a direct quantitative relationship with ^{238}U. Two other lines from ^{234m}Pa, at 766.5 and 742.8 KeV, have interferences from ^{214}Bi. The uranyl nitrate spectrum shows that the major lines of uranium and its short-lived daughter products occur in the 25- to 200-keV part of the gamma-ray spectrum.

also some strong lines from the remote decay products; thus, characterization of the state of secular equilibrium from a single spectrum is permitted.

The conventional laboratory radioisotope analytical system, devised by Rosholt, requires chemical separations and counting techniques that yield a complete account of disequilibrium in geologic samples. The high-resolution gamma-ray spectrometer systems permit similar studies to be made without prior chemical separations, but some disadvantages are (1) attenuation of low-energy photons within the sample, (2) weak gamma-ray intensities of the ^{231}Pa group isotopes, and (3) interferences which prevent resolution of the ^{234}U and ^{226}Ra peaks. The major advantage of the spectrometric technique is that it can be utilized in surface and borehole exploration as well as in the laboratory. Multiple planar and coaxial intrinsic germanium detector arrays are now available from commercial sources and are being tested for airborne and surface measurements. A borehole sonde with a planar detector has also been constructed and is undergoing field tests.

This paper will describe the general concepts of direct determination of uranium and some of its more important daughter products by high-resolution gamma-ray spectrometry, based upon laboratory experiments, and will demonstrate the practicability of field operations.

INSTRUMENTATION AND DATA PROCESSING

Two types of germanium detectors were used in this work:

1. A 100-mm^2 by 5-mm-thick, high-purity planar germanium detector with a resolution of 540 eV at 122.1 keV and 205 eV at 5.9 keV. Optical reset circuitry is contained within the preamplifier. In the field, the analog signals, blanking pulse, bias, and preamplifier power were transmitted through 30-m-long cables connecting the detector at the outcrop with a truck containing conventional linear electronics, a 4096-channel pulse-height analyzer, a tape recorder, and a minicomputer (fig. 2). The planar detector system was operated at 10 channels/keV, so that a spectrum covered the energy range of 0–410 keV.
2. A 40-cm^3 coaxial Ge(Li) detector having a resolution of 2.5 keV at 1332 keV; the rest of the circuitry as in (1) above, less the blanking signal line.

Two photopeak evaluation techniques were used: (1) a 5-point smoothing routine with the peak area computed using a straight-line fit through the continuum, and (2) a computer program similar in principle to that of Robertson and others (1972). Additional information on the photopeak evaluation methods is given in an earlier report (Moxham, 1976).

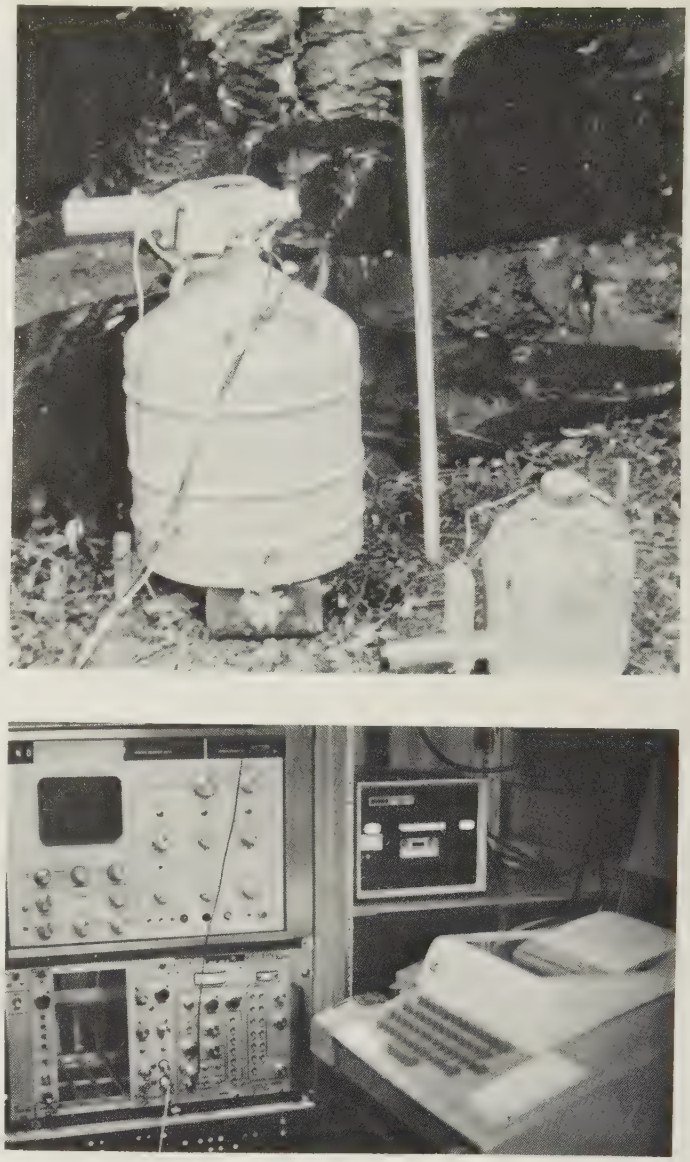

FIGURE 2.—Field instrumentation. Upper: Coaxial Ge(Li) detector (left) and planar intrinsic germanium detector, as they were used in the field; meter stick (center) is shown for scale. Lower: Truck-mounted spectrometer system; rack on left contains 4096-channel analyzer, linear electronics, and Nova minicomputer; a cassette tape recorder and teletype terminal are on the right.

LABORATORY STUDIES

Laboratory tests were made on 90-g samples placed in polystyrene jars, 45 mm in diameter by 60 mm in height, and sealed for at least 30 days. Two suites of samples were used: (1) A set of calibration standards which were obtained from the NBL (New Brunswick

Laboratory) of the U.S. Energy Research and Development Administration, and which contained equilibrated pitchblende-dunite mixtures, and (2) three ore samples that had previously been analyzed by fluorimetric (for uranium) and radiochemical (for the uranium daughter products) methods. Calibration curves were prepared relating the weight percent, or equivalent weight percent of a selected isotope, to the area of the photopeak emitted by that isotope. Equivalent weight percent is defined (Rosholt, 1961) as the amount, in percent, of primary parent, under the assumption of radioactive equilibrium, required to support the amount of daughter product actually present in the sample. For example, if a sample that contained 0.6 percent uranium were in equilibrium, the percent equivalent of each of the daughter products would be 0.6. The deviation of the percent equivalent of the daughter products from the percentage of uranium in the sample is a measure of the radioactive disequilibrium.

Table 2 shows the photopeaks emitted by the several isotopes of interest, their relative intensities with the particular system being used, and the time required to accumulate each peak to an amplitude sufficient to pass a 2σ statistical test. The stated accumulation times were used for peak identification only and would hardly be adequate for meaningful quantitative analysis. The accumulation times used to prepare the calibration curves ranged from 4 h (1.07 percent U) to 57.6 h (0.001 percent U) and are more realistic times.

To completely characterize the state of secular equilibrium in a sample, it would be necessary to measure ^{238}U, ^{234}U, and at least one of the isotopes in each of the remaining decay groups shown in table 1. Table 2 shows that the spectrum from 46 to 242 keV contains lines that are specific for five of the seven desired groups. Radium forms an unresolved doublet with ^{235}U at 186 keV, but the relative contributions of ^{226}Ra and ^{235}U to this photopeak can be determined as detailed below. ^{234}U also yields an unresolved doublet with ^{214}Pb at 53.2 keV. The relative contributions have not yet been determined.

The gamma rays available for analytical purposes are shown in figure 3 and are listed in table 1. Those selected for analysis (table 2) were based upon intensity and freedom from interference. Most of the rejected lines are of lower intensity or have nearby interfering lines, rendering them less useful for analytical purposes. Photopeaks in the 0- to 30-keV region have been avoided because of self absorption, which may be a significant problem at these energies. The X-rays are rejected altogether, as their intensities depend in part on several factors unrelated to the concentrations of their parent atoms in the sample. Uranium X-ray fluorescence, for example, can be induced by the gamma radiation from its daughter products, thereby enhancing the characteristic 98.4-keV peak.

Self absorption

Absorption within the sample of the several gamma-ray lines was determined by the method of Reilly and Parker (1975). The transmission through the samples of gamma rays from ^{241}Am (59.6 keV), ^{133}Ba (356 keV), and ^{57}Co (122.1 keV) is shown in figure 4. The

TABLE 2.—*Photopeaks from isotopes in the uranium decay chain*

Isotope	Isotope group	Photopeak (keV)	Relative intensity [a]	Accumulation time for a 2σ peak (sec) [b]	
				1.07% U	0.01% U
^{234}Th	Uranium	63.3	92	4	512
^{234}Th	Uranium	92.6	100	4	2048
^{230}Th	Thorium	67.8	11	64	4608
$^{226}Ra + {}^{235}U$	Radium + uranium	186.1 + 185.7 [c]	36	32	4096
^{214}Pb	Radon	241.9	20	32	4096
^{210}Pb	Lead	46.5	74	4	256
^{227}Th	Protactinium	236.0	2	1024	

[a] Relative to 100 for ^{234}Th at 92.6 keV, for this particular counting system.

[b] To perform this test, the accumulation time was increased in steps of $2^n + 2^n$ sec (as dictated by the timing controls on the analyzer) until the peak was detected by the computer peak search routine, at a 2σ level.

[c] Unresolved doublet.

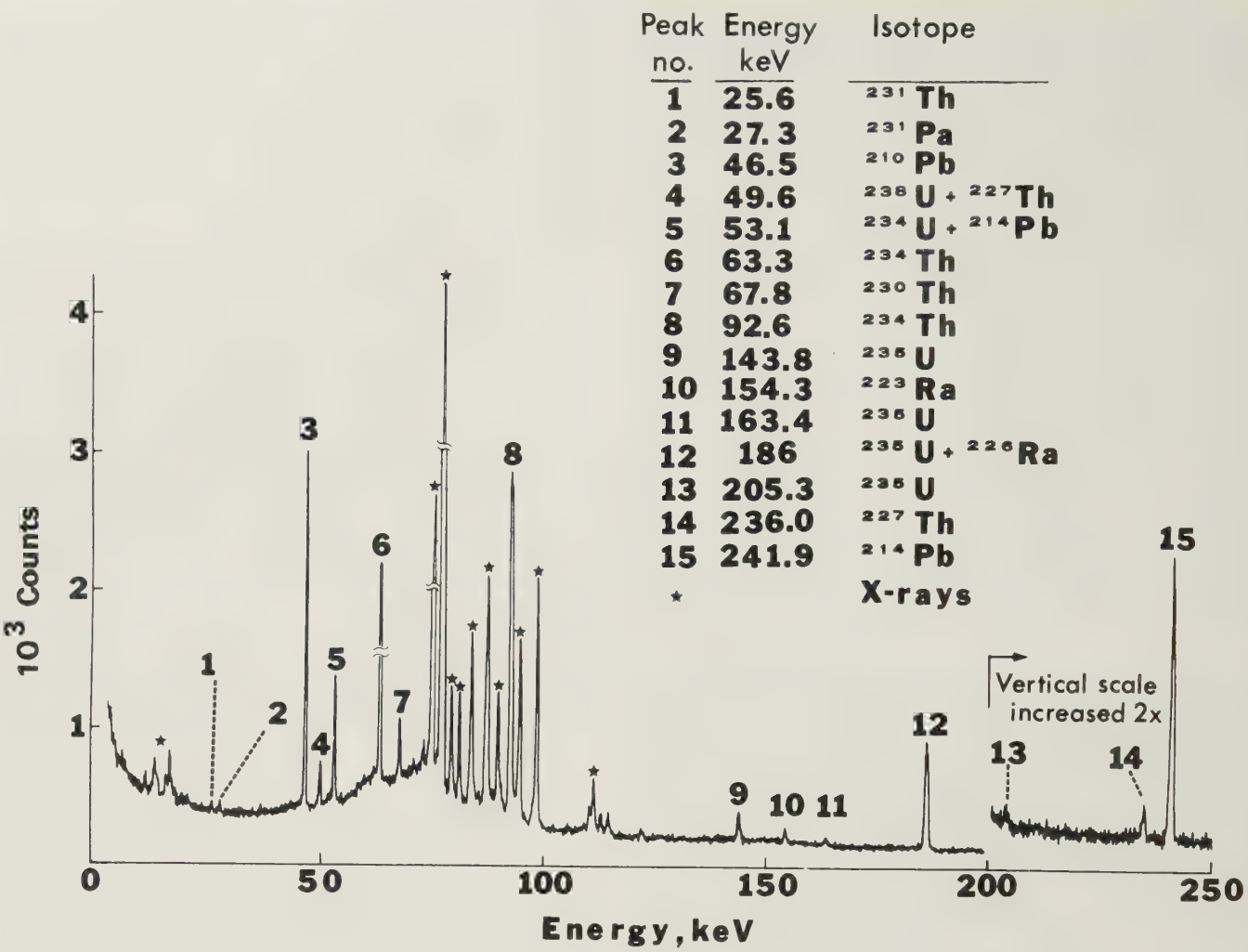

FIGURE 3.—Laboratory spectrum of a 90-g sample of uranium ore; spectrum made by means of an intrinsic planar germanium detector.

data for a given energy indicate that the gamma attenuation is mainly a function of the uranium content of the samples. Absorption of the 356-keV line is nearly constant as uranium increases. At 60 keV, the attenuation becomes appreciable as the uranium content exceeds about 0.2 percent. This effect is reflected in the calibration curves (fig. 5).

Among the gamma rays of interest, those at 46.5 keV should show the greatest attenuation. The photopeak areas for this line were computed with and without an attenuation correction factor. The correction factor afforded no appreciable improvement in the data analysis in the range of 0.001–0.61 percent uranium; consequently, the calibration curves are plots of the uncorrected data.

Direct determination of uranium

The short half-life of ^{234}Th implies that this isotope in geologic samples will be in equilibrium with its parent ^{238}U, and consequently, direct determination of uranium in a sample results from measurement of ^{234}Th. ^{234}Th has two relatively strong peaks at 92.6 keV and at 63.3 keV. Either can be used. The 92.6-keV peak has somewhat greater relative intensity in our system, but two factors should be kept in mind: (1) The 92.6 peak is a doublet (92.5 and 92.8 keV), which distorts the peak shape and may thereby complicate quantitative evaluation of the peak area, and (2) there is a thorium X-ray at 93.3 keV that might create an interference in samples containing elemental thorium, that is, ^{232}Th and its daughter products. The presence of such thorium is easily recognizable by its 238.6 keV line from ^{212}Pb. If that line is present, the 92.6 peak should not be used for uranium measurements. For thorium-free samples, the thorium X-rays created by transitions in the uranium chain are nearly proportional to the uranium content and thus are of little concern. Moreover, the population of thorium

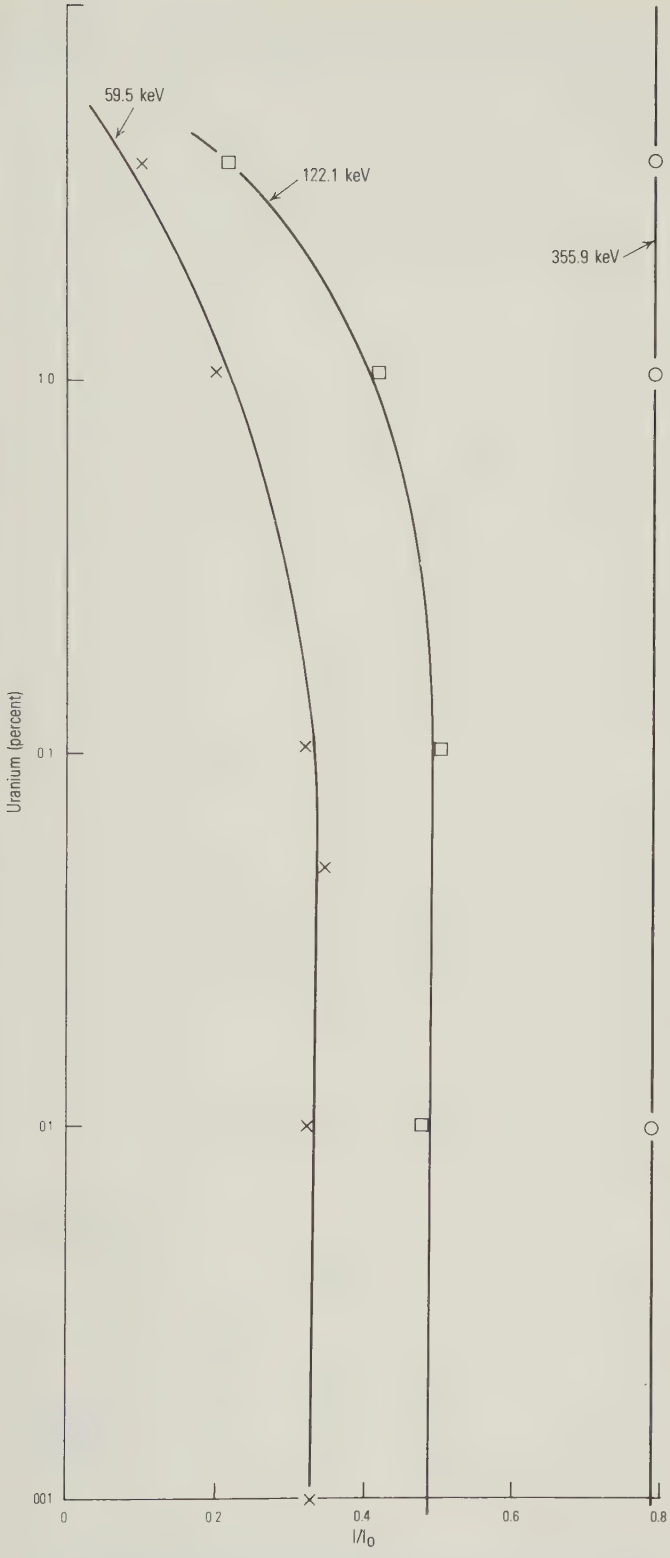

FIGURE 4.—Transmission, I/I_0, of collimated gamma rays from ^{133}Ba (355.9 keV), ^{57}Co (122.1 keV), and ^{241}Am (59.5 keV) through 90-g samples. Self absorption is indicated by the curvature for the 59.5- and 122.1-keV lines.

atoms among the isotopes of the uranium chain is small, so that the creation of thorium fluorescence X-rays is likewise small. The 63.3-keV peak, on the other hand, is well isolated and has none of the deficiencies enumerated above, so that it should give the best results.

Straight-line fits to the observed data for the 63.3-keV and 92.6-keV photopeaks versus uranium content in the range of 0.001 to 0.61 percent both gave standard deviations of 0.002 percent uranium.

It was mentioned above that ^{234m}Pa has a gamma-ray line at 1001.4 keV, which can be used for direct quantitative measurement of uranium, as ^{234m}Pa is a short-lived daughter of ^{234}Th (see table 1; also, Gorbatyuk, Kadisov, Miller, and Troitskii, 1973). Because of the relatively low intensity of the 1001.4-keV line, several investigators have expressed a preference for the ^{234}Th lines in direct uranium determinations (for example, Coles and Meadows, 1974), but some recent borehole experiments by the U.S. Geological Survey have shown that the 1001.4-keV line may be the most useful in drill-hole logging where, in contrast to laboratory measurements, the 4π geometry and large sample volume tend to benefit high-energy lines at the expense of the low-energy lines (Tanner and others, 1977).

Secular equilibrium among the uranium daughters

Disequilibrium in the uranium chain can be evaluated by measuring the uranium content, as described above, the e^{234}U, and by determining also the percent equivalents of at least one isotope each of the thorium, radium, radon, lead, and protactinium groups, which are discussed in turn below.

^{230}Th has a line of moderate intensity at 67.8 keV, which can be evaluated in a straightforward manner.

^{226}Ra unfortunately is denoted only by a line at 186.1 keV that, with the present state-of-the-art instruments, cannot be completely resolved from the ^{235}U line at 185.7 keV. However, the relative contributions of these two isotopes to the 186-keV doublet can be determined experimentally. Gorbatyuk, Kadisov, Miller, and Shaskin (1973) did this by independently measuring the 186-keV peak from a sample of equilibrated pitchblende and a sample of radium. They found the radium contribution to the composite 186-keV peak to be 59.2 percent. We used a similar technique, comparing uranium acetate with a pitchblende standard, which indicated the ^{226}Ra contribution to 186-keV composite peak to be 58.0 percent. This value was used to calculate by equation 1 the equivalent ^{226}Ra shown in table 3.

$$e^{226}Ra = \frac{qU_s(P_u/P_s) - qU_u(1-a)}{a} \qquad (1)$$

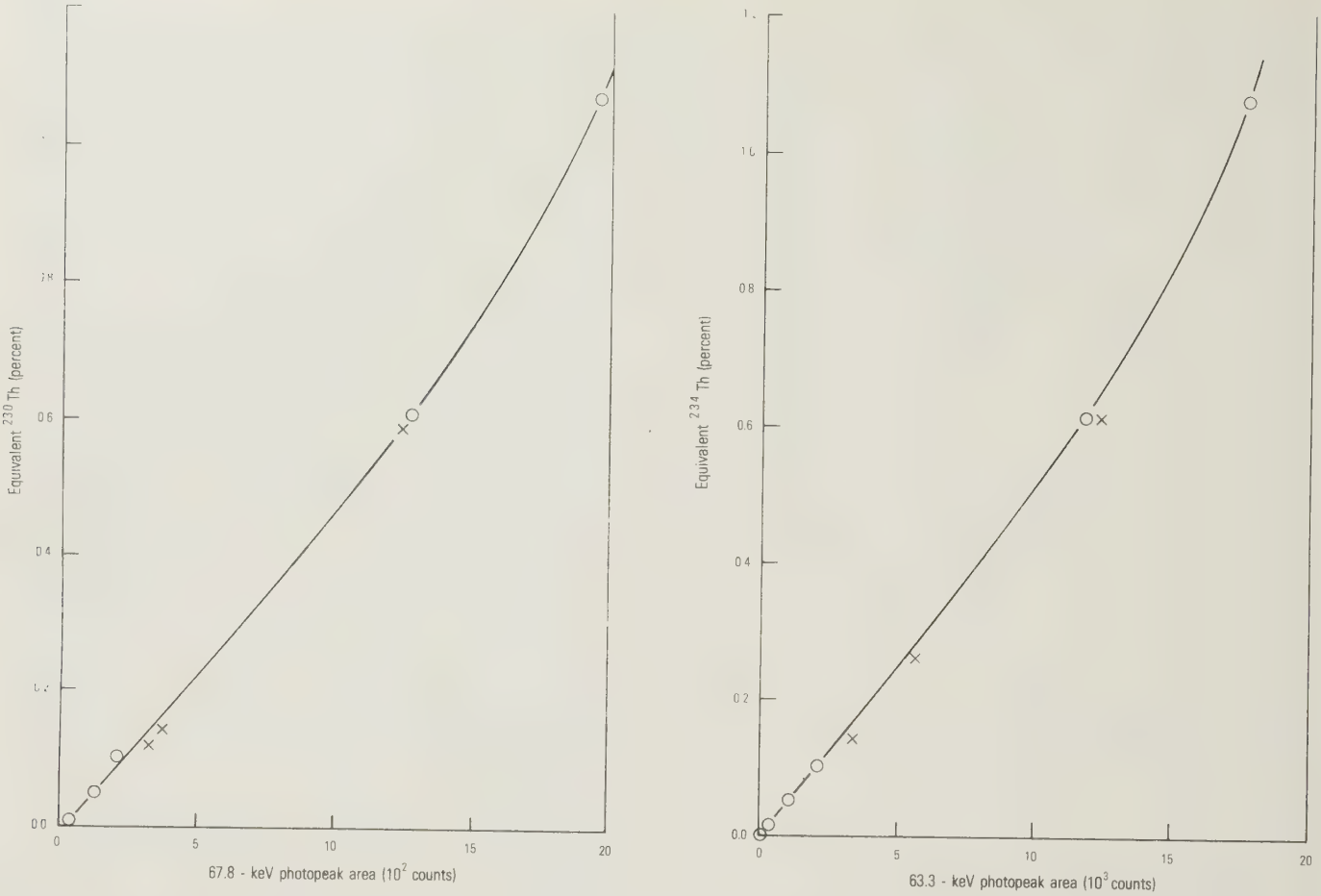

FIGURE 5.—Calibration curves for equivalent ^{230}Th (left) and ^{234}Th (right). Both curves have been drawn through experimental points for equilibrated NBL standards (circles). Samples analyzed by chemical methods are shown by ×'s.

TABLE 3.—*Comparison of chemical and radiochemical analyses with gamma-ray spectrometer analysis*

[P, photopeak evaluated; C, chemical or radiochemical analysis; γ = gamma-ray analysis, using calibration curves, and, for e^{226}Ra, equation (1). Values are equivalent to percent uranium in equilibrium.]

Group	Uranium			Thorium			Radium			Radon			Lead			Protactinium		
Isotope	^{234}Th			^{230}Th			^{226}Ra			^{214}Pb			^{210}Pb			^{227}Th		
Sample No.	P	C	γ	P	C	γ	P	C	γ	P	C[a/]	γ	P	C	γ	P	C[b/]	γ
234601	63.3	0.61	0.64	67.8	0.59	0.59	186	0.24	0.24	241.9	0.24	0.22	46.5	0.24	0.27	236.0	0.60	0.56
	92.6	.61	.61							352.0	.24	.22						
256467	63.3	.14	.16	67.8	.12	.14	186	.20	.22	241.9	.20	.17	46.5	.20	.23	236.0	.15	.17
	92.6	.14	.15							352.0	.20	.16						
256463	63.3	.26	.28	67.8	.15	.16	186	.19	.13	241.9	.19	.14	46.5	.19	.19	236.0	.21	.15
	92.6	.26	.24							352.0	.19	.14						

a/ The radiochemical analyses are for ^{226}Ra. As the samples were sealed for 30 days, it is assumed ^{226}Ra and ^{214}Pb are in equilibrium.

b/ The radiochemical analyses are for ^{231}Pa. It is assumed to be in equilibrium with ^{227}Th.

where subscripts s and u refer to an equilibrated standard and the unknown sample, respectively, qU equals the uranium content (for the unknown sample, this value is obtained from the calibration curves for the 63.3- or 92.6-keV photopeaks), P equals the 186-keV photopeak area, and a equals 0.580 (the fraction of the radium contribution to the 186-keV photopeak).

The radon group can be evaluated by the amount of ^{214}Pb present, for which several prominent lines are available.

The lead group is represented by ^{210}Pb, which has a strong line at 46.5 keV.

The protactinium group is probably the most difficult to analyze. Only a few of the isotopes are gamma emitters, and the lines are very weak. The most favorable seems to be the ^{227}Th photopeak at 236.0 keV.

The results of the measurements of uranium and the percent equivalents of the daughter products in the uranium decay groups are summarized in table 3.

Some of the most obvious manifestations of disequilibrium in the uranium series are shown in figure 6, which compares the computer-processed spectrum from an equilibrated counting standard with that from an ore that is deficient in all the uranium daughter products (sample 234601, table 3). Both samples contain 0.61 percent uranium, by chemical analyses. The 63.3- and 92.6-keV peaks from ^{234}Th are nearly identical in each sample and reflect the correspondence in uranium content. The marked ^{226}Ra deficiency in the ore is depicted by the small 241.9-(^{214}Pb) and 186-keV peaks (in part derived from ^{226}Ra). As the radium daughters, ^{214}Bi and ^{214}Pb, are major producers of high-energy photons, the radium deficiency also decreases X-ray fluorescence, leading to the notably smaller X-ray lines from lead and bismuth, at 74.8 and 77.1 keV, in the ore sample.

Thorium

The ^{232}Th series is generally near equilibrium in most natural materials; consequently, the thorium content of a sample can be determined by comparing the amplitude of the ^{212}Pb line at 238.6 keV with that from well-analyzed thorium standards. None of the samples reported in table 3 contained a detectable quantity of thorium.

Sample volume at low energies

The sample volume "seen" by a 100-mm^2 planar detector was determined experimentally, using crushed ore containing 0.23 percent uranium, having a bulk density of 1.57 g/cm^3. A cylindrical sample container constructed of 0.32-cm-thick acrylic walls and bottom was placed on the detector housing (fig. 7). A spectrum was collected for each of several thicknesses of ore, ranging from 2 to 8 cm. The sample diameter was "infinite" (15 cm) in each instance. Another series of samples of "infinite" thickness (8 cm) was run for samples ranging in diameter from 1 to 15 cm. The results show that, for ore-grade material (0.23 percent uranium), the detector "sees" the 63.3-keV line to a maximum depth of about 6 cm; the maximum penetration of the 46.5-keV line is about 4 cm. The detector "sees" laterally about the same distance that it "sees" in depth, in each instance.

FIELD STUDIES

Fieldwork was undertaken at a roll-type uranium deposit near Penn Haven Junction, Carbon County, Pa., on the west side of the Lehigh River (Klemic and others, 1963). Here, the long axis of the roll front, trending about east, is cut by the Lehigh River gorge, exposing cross sections of the deposit. Very fine grained uraninite is found in a dark-gray graywacke sandstone of Late Devonian age, in crescent-shaped zones convex to the north and having wings or limbs extending southward from the roll fronts. One of the most prominent fronts is discernible by a curved surface, but, in general, the uraniferous zones show no distinctive colors and can be delineated only by means of a radiation detector. The uranium is mostly in primary uraninite; few secondary minerals are present. Klemic and others, (1963, p. 79) reported that some samples from this deposit contain 0.56 percent uranium, but the average grade is probably lower.

The planar and coaxial germanium detectors were placed 30 cm from the uranium outcrop, where the gamma-ray exposure rate was greater than 5 mR/h. The coaxial detector spectrum (fig. 8) records the large number of ^{214}Bi and ^{214}Pb lines in the 242- to 1764-keV region, as well as the small ^{234m}Pa peak at 1001.4 keV. The constraints on using this part of the spectrum for evaluating either the uranium or the state of equilibrium have been discussed above.

The low-energy region recorded by the planar detector is shown in figure 9. The greater efficiency of the coaxial detector is evident from the greater number of counts shown on the ordinate, but in the low energy region, the greater resolution afforded by the planar detector yields more information. In the latter, all the uranium decay groups have lines that were detected in an 8-minute accumulation time.

Any attempts at quantitative evaluation of spectra collected at an outcrop would have several defects: the variation in counting geometry, in self absorption,

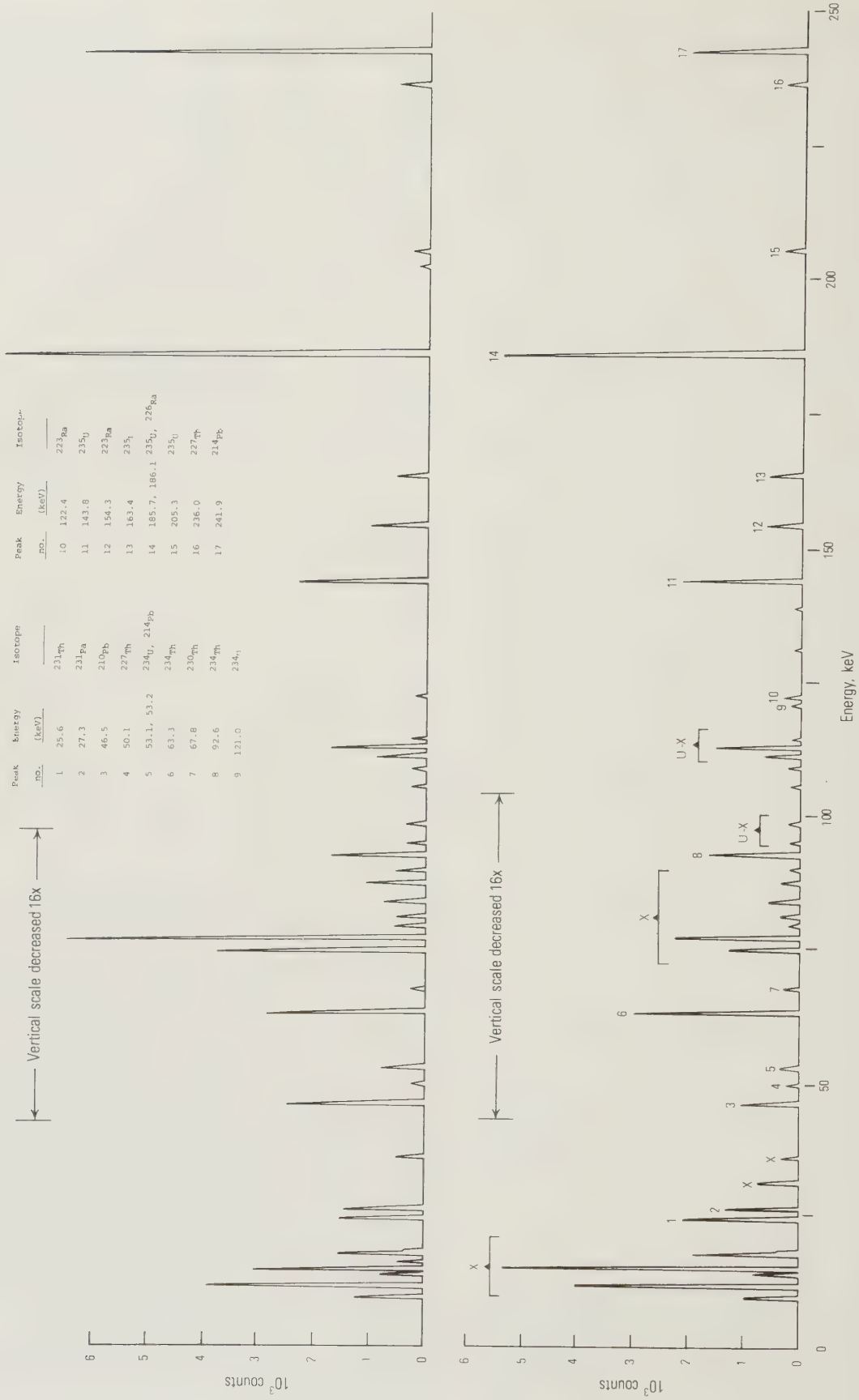

FIGURE 6.—Computer-processed spectra of samples containing 0.61 percent uranium. The top spectrum is from an equilibrated counting standard; the bottom spectrum is from an ore deficient in all daughter products. X, X-ray; U-X, uranium X-ray.

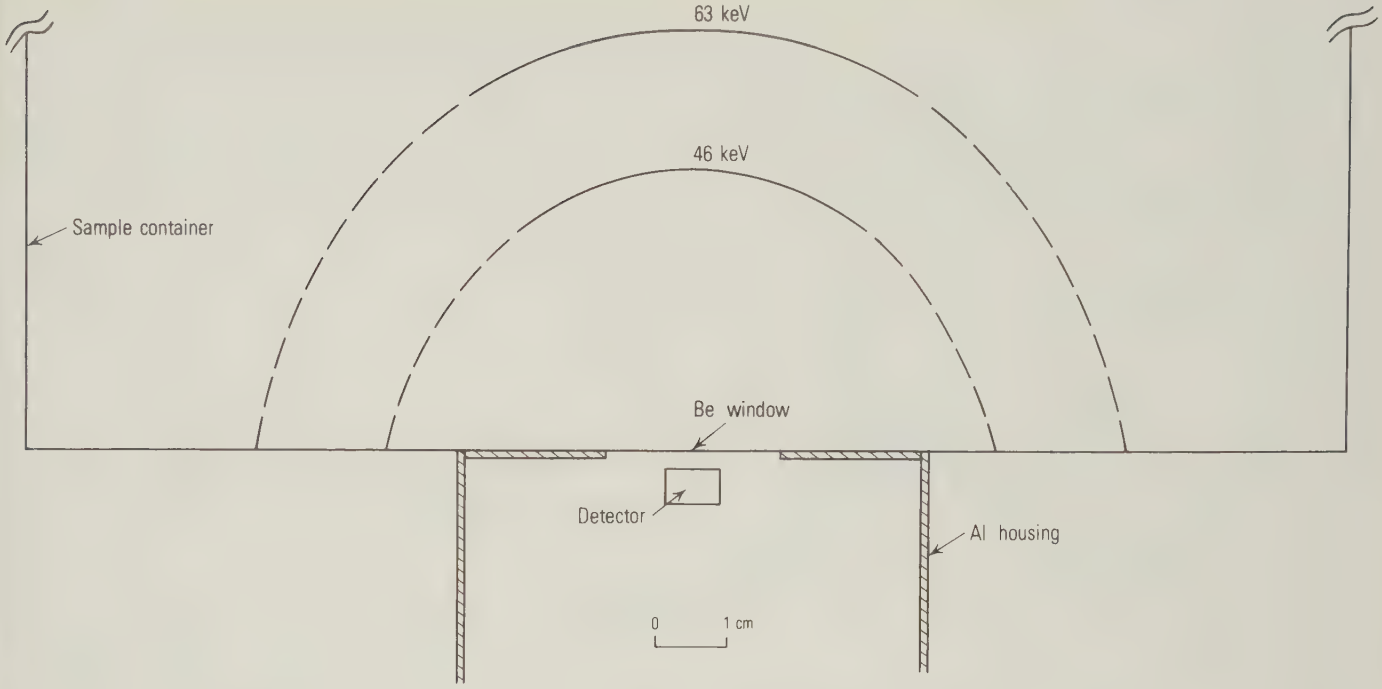

FIGURE 7.—Cross section showing boundaries of an "infinite" sample for the 63.3-keV and 46.5-keV lines from ^{234}Th and ^{210}Pb, respectively.

Peak No.	Energy (keV)	Isotope	Peak No.	Energy (keV)	Isotope
1	63.3	^{234}Th	12	934.8	^{214}Bi
2	74.8 + 77.1	X-rays	13	1001.4	^{234m}Pa
3	87.3 - 98.4	^{234}Th + X-rays	14	1120.4	^{214}Bi
4	111.3	U X-rays	15	1155.4	^{214}Bi
5	185.7 + 186.1	^{235}U + ^{226}Ra	16	1238.3	^{214}Bi
6	241.9	^{214}Pb	17	1378.0	^{214}Bi
7	295.2	^{214}Pb	18	1408.0	^{214}Bi
8	352.0	^{214}Pb	19	1509.0	^{214}Bi
9	609.4	^{214}Bi	20	1728.0	^{214}Bi
10	666.0	^{214}Bi	21	1764.0	^{214}Bi
11	768.7	^{214}Bi			

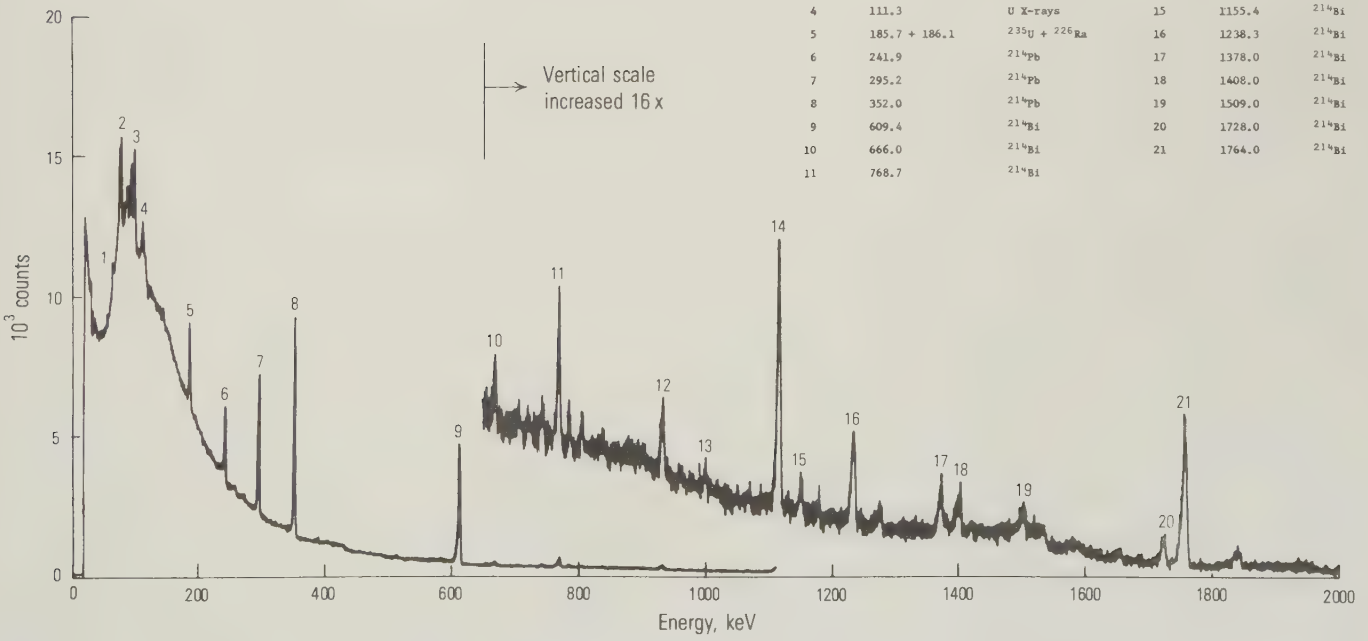

FIGURE 8.—Gamma-ray spectrum of a uranium outcrop near Penn Haven Junction, Pa., made by means of a coaxial Ge(Li) detector. Accumulation time was 8 min.

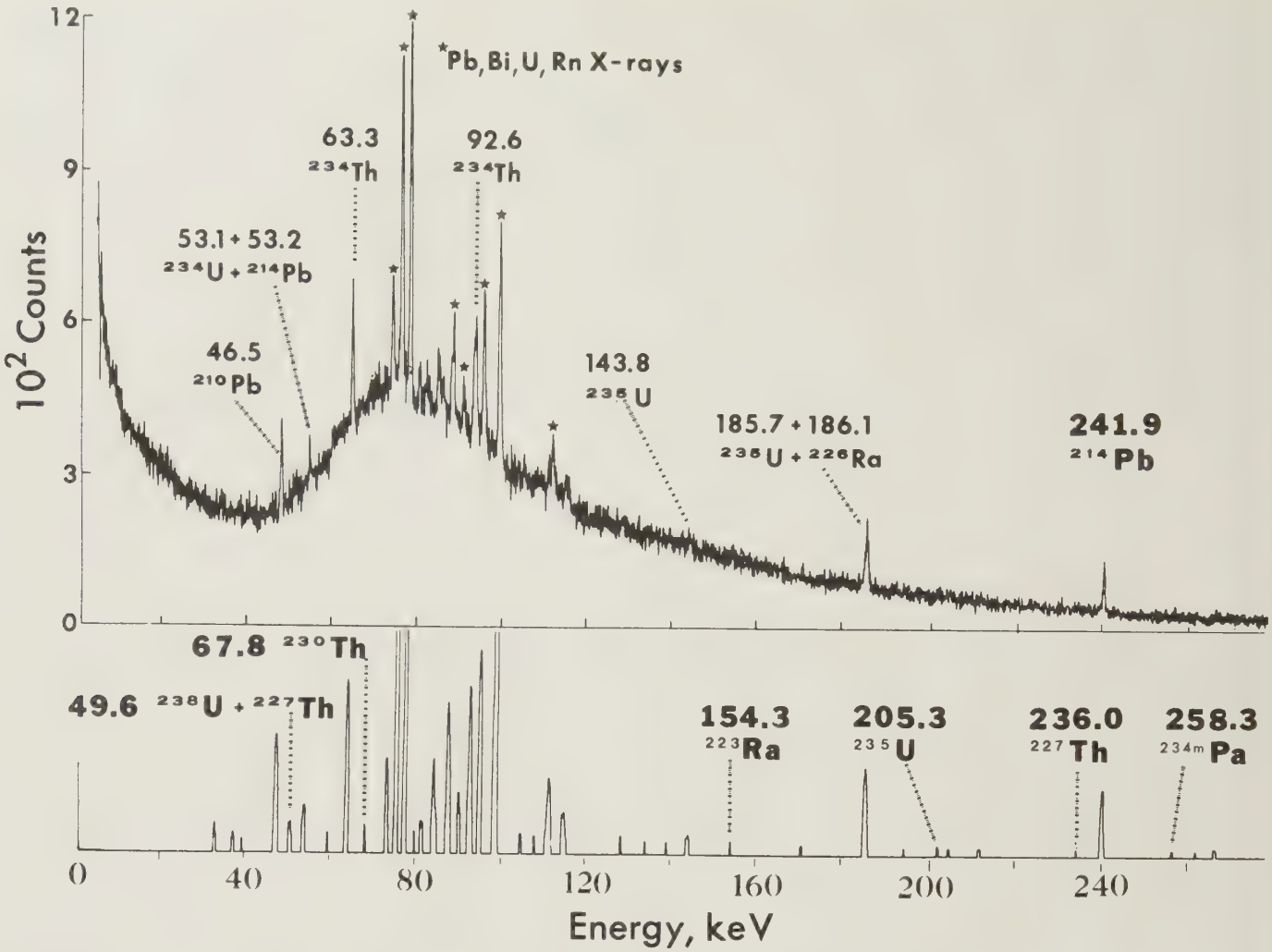

FIGURE 9.—Gamma-ray spectrum of a uranium outcrop at same location as given in figure 8. Accumulation time was 8 min. Upper: Spectrum made by means of a planar intrinsic germanium detector; at least one isotope of each of the uranium series decay groups is represented; the more obvious peaks are labeled. Lower: A computer reduction of the upper spectrum that (1) retains all peaks passing a 2σ statistical test, and (2) zeros the continuum; peaks that are not readily seen on the raw (upper) spectrum are labeled on the computer-reduced (lower) spectrum.

and in sample "size" at different stations. To estimate the magnitude of this effect, 8-min spectra were collected by means of the planar detector at six stations where the gamma-ray exposure rate was $\leqslant$5 mR/h. The detector was placed about 2 cm from the rock surface at each station. An effort was made to select a flat surface, but at all stations there were neighboring irregularities. ^{234}Th and ^{214}Pb each emit two lines. We reason that the deleterious effects would be manifested in a change in the ratio between the two photopeaks for a given isotope because of the differences in their energy. The standard deviation of the 63.3/92.6 keV lines of ^{234}Th was 6.5 percent; that of the 241.9/352.0 keV lines of ^{214}Pb was 6.4 percent. These values are relatively small, so that at least semiquantitative evaluation of uranium and its daughter products at the outcrop seems achievable.

CONCLUSIONS

The results of these experiments show that direct measurement of uranium can be made by means of the ^{234}Th daughter of ^{238}U and that the state of secular equilibrium in the uranium series can be evaluated for samples run in the laboratory. At the outcrop surface, where sample geometry and other parameters cannot be controlled, the data are only semiquantitative. Data of a more quantitative nature could probably be obtained by drilling a hole of sufficient size to insert the detector, thus standardizing the geometry.

Alternatively, a truck-mounted laboratory-type system could utilize prepared samples for quantitative analysis.

The primary advantage of the spectrometric system is the rapidity with which disequilibrium analyses can be made. One obvious application is in determining whether, in areas of potential uranium source rocks, uranium is in equilibrium with its long-lived daughters (and thus uninteresting) or whether there is a deficiency of uranium and a daughter-product excess, suggesting that uranium may have been leached and that a migration path may exist which leads to a deposit somewhere down the hydraulic gradient. Spectrometric analyses of borehole samples can similarly assist in defining the migration path.

REFERENCES CITED

Coles, D. G. and Meadows, J. W., 1974, A convenient method for the direct measurement of uranium in soil samples using high-resolution Ge(Li) gamma-ray spectroscopy: California Univ., Lawrence Livermore Lab. Rept. UCRL 75619, 26 July 1974, 13 p.

Dooley, J. R., Jr., Tatsumoto, M., and Rosholt, J. N., 1964, Radioactive disequilibrium studies of roll features, Shirley Basin, Wyoming: Econ. Geology, v. 59, no. 4, p. 586–595.

Gorbatyuk, O. V., Kadisov, E. M., Miller, V. V., and Troitskii, S. G., 1973, Possible determination of uranium and radium content by measuring γ-radiation in a borehole by a spectrometer with a lithium-doped germanium detector: Atomic Energy, v. 35, p. 355–357 (English translation).

Gorbatyuk, O. V., Kadisov, E. M., Miller, V. V., and Shaskin, V. L., 1973, Use of a γ-spectrometer with lithium-drifted germanium detector for analyzing uranium and thorium ores: Atomic Energy, v. 35, p. 352–355 (English translation).

Klemic, Harry, Warman, J. C., and Taylor, A. R., 1963, Geology and uranium occurrences of the northern half of the Lehighton, Pennsylvania, quadrangle and adjoining areas: U.S. Geol. Survey Bull. 1138, 97 p.

Moxham, R. M., 1976, Gamma-ray spectrometer measurements of $^{238}U/^{235}U$ in uranium ore from a natural reactor at Oklo, Gabon: U.S. Geol. Survey Jour. Research, v. 4, no. 5, p. 589–592.

Reilly, T. D., and Parker, J. L., 1975, A guide to gamma-ray assay for nuclear material accountability: Los Alamos Sci. Lab. Rept. LA–5794–M, 39 p.

Robertson, A., Prestwich, W. V., and Kennett, T. J., 1972, An automatic peak-extraction technique: Nuclear Instruments and Methods, v. 100, p. 317–324.

Rosholt, J. N., 1961, Late Pleistocene and recent accumulation of uranium in ground water saturated sandstone deposits: Econ. Geology, v. 56, no. 2, p. 423–430.

Rosholt, J. N., Butler, A. P., Garner, E. L., and Shields, W. R., 1965, Isotope fractionation of uranium in sandstone, Powder River Basin, Wyoming, and Slick Rock district, Colorado: Econ. Geology, v. 60, no. 3, p. 199–213.

Rosholt, J. N., Tatsumoto, M., Dooley, J. R., Jr., 1965, Radioactive disequilibrium studies in sandstone, Powder River Basin, Wyoming, and Slick Rock district, Colorado: Econ. Geology, v. 60, no. 3, p. 477–484.

Syromyatnikov, N. G., 1960, Interphase isotopic exchange of U^{234} and U^{238}: Geochemistry (English translation of Geokhimiya), no. 3, p. 320–327.

Tanner, A. B., Moxham, R. M., and Senftle, F. E., 1977, Assay for uranium and measurement of disequilibrium by means of high-resolution gamma-ray borehole sondes, *in* Campbell, J. A., ed., Short papers of the U.S. Geological Survey uranium-thorium symposium, 1977: U.S. Geol. Survey Circ. 753, p. 56–57.

Jour. Research U.S. Geol. Survey
Vol. 5, No. 6, Nov.–Dec. 1977, p. 797–806

HEAT CAPACITIES OF GIBBSITE, $Al(OH)_3$, BETWEEN 13 AND 480 K AND MAGNESITE, $MgCO_3$, BETWEEN 13 AND 380 K AND THEIR STANDARD ENTROPIES AT 289.15 K, AND THE HEAT CAPACITIES OF CALORIMETRY CONFERENCE BENZOIC ACID BETWEEN 12 AND 316 K

By BRUCE S. HEMINGWAY, RICHARD A. ROBIE, JAMES R. FISHER, and WILLIAM H. WILSON, Reston, Va.

Abstract.—The heat capacities of gibbsite and magnesite were measured between 13 and 380 K by means of an adiabatic calorimeter. The heat capacity of gibbsite was measured continuously between 340 and 480 K by means of a differential scanning calorimeter. Tables of the thermodynamic functions C_p°, $(H_T^\circ - H_0^\circ)/T$, $-(G_T^\circ - H_0^\circ)/T$, and $S_T^\circ - S_0^\circ$ are presented for these phases at integral temperatures. $S_T^\circ - S_0^\circ$ are 68.44±0.14 J/(K·mol) and 65.09±0.13 J/(K·mol) at 298.15 K for gibbsite and magnesite, respectively. The heat capacities of Calorimetry Conference benzoic acid have been remeasured between 12 and 316 K.

A large body of thermodynamic data must be gathered to provide a data base which can be used in modeling problems associated with the exploitation and development of geothermal power and in proposing and testing solutions to these problems (Brewer and others, 1974). In hot water systems, the disposal of spent brines through reinjection (currently considered the only environmentally feasible disposal method) could result in hydrothermal alteration of the receiving aquifer, which could lead to the precipitation of minerals and subsequent filling of pores and factures, resulting in an early end to the reinjection process. Permeability may also decrease in the producing aquifers as pressure and temperature conditions change.

Fournier (1974) noted that data were lacking for many hydrothermal minerals and that many inconsistencies existed in the thermodynamic data that were available for some minerals.

Hemingway and Robie (1977) recently reevaluated the thermodynamic properties of many of the aluminosilicates on the basis of a new determination of the enthalpy of formation of gibbsite and of the entropy of gibbsite reported in this study. Revised values for gibbsite and magnesite entropies are reported in this work.

Shomate and Cook (1946) measured the heat capacities between 52 and 297 K and the high-temperature heat contents to 425 K of gibbsite. Anderson (1934) measured the low-temperature heat capacities of magnesite between 56 and 292 K. Shomate (unpub. data reported in Kelley, 1960, p. 114) determined the high-temperature heat content of magnesite to 750 K. Because the lower limit of each investigation was approximately 50 K, the standard entropy at 298.15 K for each phase carries a large uncertainty resulting from the rather long extrapolation of the heat capacity to 0 K. We believed that new measurements extending to lower temperatures would be desirable in order to reduce the uncertainties in the standard entropies at 298.15 K for these phases.

The heat capacities of Calorimetry Conference benzoic acid have been redetermined to compare the results of our tests on standard reference materials with those from other laboratories (Robie and others, 1976; Robie and Hemingway, 1972). The data in this paper are the second set of heat capacities reported by this laboratory for the same benzoic acid sample. Previous measurements of this sample have been summarized in Robie and Hemingway (1972).

Acknowledgments.—We gratefully acknowledge the help of several of our colleagues at the U.S. Geological Survey: J. S. Huebner obtained the cell parameters for gibbsite, J. J. Fahey performed the chemical analysis and determined the indices of refraction of the magnesite sample, and J. L. Haas, Jr., and J. J. Hemley offered constructive criticisms. The work reported in this study was supported by the Office of Saline Waters, U.S. Department of the Interior, under agreement number 14–30–3040 with the Geological Survey.

MATERIALS

Gibbsite, $Al(OH)_3$

Gibbsite was prepared from Baker's chemically pure reagent-grade aluminum hydroxide (lot 82545). Stock gibbsite was boiled (50 g in 1 L) in distilled demineralized water under reflux conditions for 1 h. The aqueous phase was analyzed for sodium, which chemical analysis of the gibbsite had shown to be the major impurity. The procedure was repeated until the aqueous sodium concentration had been reduced to the level of the blank solution run as a control. The purified gibbsite was washed with 1 L of distilled demineralized water, dried under vacuum at 298 K, and stored in a desiccator.

The particle size was determined optically to range from 126 to 5 μm; the average particle size was 30 μm. The X-ray diffraction showed only gibbsite lines. The lattice parameters were $a=8.664\pm0.002$ Angström (A), $b=5.0694\pm0.0007$ A, $c=9.719\pm0.001$ A, and $\beta=94°30.0'\pm0.07'$, using BaF_2 ($a=6.2001$ A at 26°C) as the internal standard. A chemical analysis of the sample is given in table 1.

TABLE 1.—*Chemical analyses, in weight percent, of gibbsite and magnesite used for low-temperature heat-capacity measurements*

	Gibbsite[1]	Gibbsite[2 3]	Magnesite[4]	Magnesite[5]
Al_2O_3	65.36	65.4	-----	-----
Fe_2O_3	-----	.06	-----	-----
FeO	-----	.07	-----	-----
MgO	-----	-----	47.81	48.01
Na_2O	-----	.35	-----	-----
H_2O+	34.64	34.5	-----	.02
H_2O-	-----	.1	-----	-----
CO_2	-----	.01	52.19	51.97
Total	100.00	100.49	100.00	100.00

[1] $Al(OH)_3$ (ideal gibbsite).
[2] Synthetic gibbsite. Analyst, Hezekiah Smith, U.S. Geol. Survey.
[3] Sample contained 3 ppm Ba and 20 ppm Ga.
[4] $MgCO_3$ (ideal magnesite).
[5] Synthetic magnesite. Analyst, J. J. Fahey, U.S. Geol. Survey.

The sample was identically the same as the material used by Hemingway and Robie (1977, Baker aluminum hydroxide) for the heats of solution of gibbsite (in 20.1 weight percent hydrofluoric acid reported for the temperatures of 323.4 and 343.1 K). They used a second gibbsite sample (Fisher Scientific Company reagent $Al_2O_3\cdot3H_2O$) for the heats of solution of gibbsite reported for 303.4 K. The heat of formation of gibbsite reported by Hemingway and Robie is based upon the heat of solution of the latter gibbsite sample extrapolated to 303.5 K, by using the temperature coefficient for the solution reaction derived from the data for both gibbsite samples.

Magnesite, $MgCO_3$

Magnesite was prepared from reagent grade MgO, distilled demineralized water, and tank CO_2, which were reacted in a gold-lined, rocking autoclave at 548 K and P_{CO_2} at about 1.1×10^7 Pa for 3 weeks. The sample was stored in a desiccator. A chemical analysis for this sample is given in table 1.

The X-ray analysis showed all lines in good accord with the pattern for $MgCO_3$, except for one faint line near $2\theta=75°$, which showed a deviation of 0.12° in 2Θ. The cell parameters were $a=4.6413\pm0.0004$ A and $c=15.056\pm0.005$ A. Optical examination showed the particle size to be 10–70 μm. The indices of refraction were $\omega=1{,}700$ and $\epsilon=1.508$ (J. J. Fahey, written commun., 1976).

The magnesite was heated at 388 K for half an hour before the sample was sealed in the calorimeter.

Benzoic acid, C_6H_5COOH

The Calorimetry Conference benzoic acid sample has been described elsewhere (Furukawa and others, 1951). The sample was used as furnished by the U.S. National Bureau of Standards.

APPARATUS AND TECHNIQUES

The apparatus and the experimental procedures used in this study have been described elsewhere (Robie and others, 1976; Robie and Hemingway, 1972; O'Neill, 1966).

The thermometer used in the low-temperature heat-capacity calorimeter was calibrated by the U.S. National Bureau of Standards on the International Practical Temperature Scale of 1968 (IPTS–68, see, for example, Bedford and Preston-Thomas, 1969; Bedford and others 1969; Comité International des Poids et Mesures, 1969; Furukawa and others, 1973).

The gram formula weights 78.003, 84,314, and 122.133 for gibbsite, magnesite, and benozoic acid, respectively, were based upon the 1971 atomic weights (Commission on Atomic Weights, 1972).

Each of the samples used in this study was kept in a desiccator filled with anhydrous $CaSO_4$,

EXPERIMENTAL RESULTS

Gibbsite

Seventy-two measurements of the heat capacities of 36.490 g (in vacuo) of gibbsite, $Al(OH)_3$, were made between 13 and 380 K by means of an adiabatic low-

temperature calorimeter. The calculated specific heats are listed in table 2 in chronological order and are shown graphically in figure 1 together with the results reported by Shomate and Cook (1946). The sample represented 33 percent of the observed heat capacity (sample and calorimeter) at 13 K and 63 percent at 380 K.

TABLE 2.—*Specific heats calculated from experimental measurements of heat capacities of 36.490 g of gibbsite,* $Al(OH)_3$

[Heat-capacity measurements for series 1-7 were made using an adiabatic low-temperature calorimeter]

Temperature in K	Specific heat in J/(K·g)	Temperature in K	Specific heat in J/(K·g)	Temperature in K	Specific heat in J/(K·g)
SERIES 1		SERIES 4		SERIES 6	
13.41	.002190	74.97	.1635	227.96	.9051
15.46	.004031	80.83	.1891	234.92	.9347
17.39	.006151	86.69	.2156	241.73	.9635
19.15	.007996	92.29	.2418	248.41	.9907
20.76	.009785	97.48	.2667	254.97	1.017
22.35	.01154	102.65	.2918	261.58	1.043
24.04	.01383	108.24	.3196		
25.92	.01655	114.34	.3504	SERIES 7	
28.11	.01992	120.91	.3842	267.63	1.065
30.64	.02438	127.86	.4200	274.31	1.091
33.70	.03069	134.75	.4556	281.18	1.116
37.24	.03829	141.31	.4895	288.40	1.142
40.97	.04715	147.59	.5216	295.97	1.169
44.83	.05766	153.63	.5524	303.60	1.194
49.10	.06854	159.46	.5822		
		165.10	.6106	DIFFERENTIAL SCANNING CALORIMETER	
SERIES 2					
298.60	1.177	SERIES 5		339.6	1.305
306.48	1.204	159.30	.5815	379.6	1.418
314.42	1.230	164.88	.6093	419.7	1.526
322.34	1.255	170.36	.6369	459.7	1.627
330.34	1.281	175.70	.6634	479.7	1.691
338.42	1.305	181.23	.6905		
346.66	1.331	187.03	.7186		
355.07	1.354	192.93	.7466		
363.36	1.378	200.50	.7821		
371.55	1.402	206.99	.8118		
379.63	1.426	213.74	.8423		
		220.50	.8723		
SERIES 3		227.12	.9011		
52.69	.08010	233.83	.9298		
57.38	.09583				
62.65	.1146				
68.46	.1368				
74.49	.1615				

The heat capacities of gibbsite were measured between 340 and 480 K by using a differential scanning calorimeter (O'Neill, 1966). The heat capacity at each temperature was determined by a comparison of the power consumed in heating 21.1 mg of gibbsite 1 K with that required to heat 30.5 mg of synthetic sapphire through the same temperature interval (see O'Neill, 1966). The heat capacities were calculated at 40-K intervals from data collected continuously from 320 to 480 K. The results are listed in table 2 and are shown graphically in figure 1. The gibbsite sample was heated at a rate of 10 K/min from 320 to 500 K. Thermal decomposition of the gibbsite began at approximately 480 K.

Corrections for the chemical impurities and the slight deviation of the gibbsite sample from stoichiometry were calculated assuming the impurities to be present as the species $FeCO_3$, NaOH, Fe_2O_3, and Al_2O_3 and using the heat-capacity data given by Kelley and King (1961). At all temperatures, the corrections to the measured heat capacities were trival (+0.05 percent at 298.15 K, +0.1 percent at 200 K, and −0.3 percent at 25 K) when compared with the precision of the data and the uncertainties in the assumptions required for the corrections.

Magnesite

Eighty-eight measurements of the heat capacity of 28.173 g (in vacuo) of magnesite have been made between 13 and 380 K. The data are listed in chronological order in table 3 and are shown graphically in figure 2. The heat-capacity data for magnesite reported by Anderson (1934) are also shown in figure 2. The sample represented 10 percent of the observed heat capacity at 13 K and 49 percent at 380 K.

Benzoic acid

Fifty-two measurements of the heat capacity of 22.233 g (in vacuo) of Calorimetry Conference benzoic acid were made between 12 and 316 K. The data are listed in chronological order in table 4 and are shown graphically in figure 3. The sample represented

TABLE 3.—*Specific heats calculated from experimental measurements of heat capacities of 28.173 g of magnesite,* $MgCO_3$

Temperature in K	Specific heat in J/(K·g)	Temperature in K	Specific heat in J/(K·g)	Temperature in K	Specific heat in J/(K·g)
SERIES 1		SERIES 5		SERIES 8	
54.52	.06926	148.94	.5114	337.65	.9711
59.31	.08870	154.52	.5325	345.37	.9836
63.80	.1082	160.39	.5538	353.05	.9956
68.25	.1290	166.55	.5755	360.77	1.007
73.25	.1537	173.00	.5974	368.43	1.019
78.75	.1818	179.87	.6199	376.04	1.030
84.71	.2130	187.26	.6428	383.59	1.042
		195.11	.6660		
SERIES 2				SERIES 9	
46.07	.04708	SERIES 6		12.73	.000270
49.22	.04981	190.95	.6538	14.15	.000448
52.87	.06271	198.92	.6768	15.73	.000707
57.07	.07904	206.73	.6986	17.41	.001079
61.00	.09537	214.26	.7188	19.08	.001629
65.12	.1138	221.56	.7375	20.97	.002442
		228.73	.7551	23.01	.003555
SERIES 3		235.80	.7728	25.19	.005019
55.68	.08373	242.78	.7890	27.72	.007124
60.74	.09471	249.66	.8048	30.54	.009986
66.44	.1205	256.57	.8202	33.51	.01384
72.35	.1492	263.50	.8364	36.59	.01871
77.96	.1778	270.33	.8561	39.80	.02481
83.13	.2047			43.20	.03254
88.09	.2307	SERIES 7		46.77	.04208
		267.93	.8432	50.56	.05444
SERIES 4		274.73	.8577	54.65	.06944
86.11	.2202	281.57	.8710	59.32	.08830
91.15	.2466	288.54	.8851		
96.12	.2722	295.62	.8981		
101.20	.2980	302.90	.9112		
106.53	.3247	310.29	.9246		
112.21	.3525	317.82	.9375		
118.20	.3809	325.40	.9508		
124.37	.4094	332.91	.9636		
130.48	.4363	340.46	.9759		
136.41	.4613	348.05	.9877		
142.18	.4848				
147.87	.5072				
153.59	.5289				

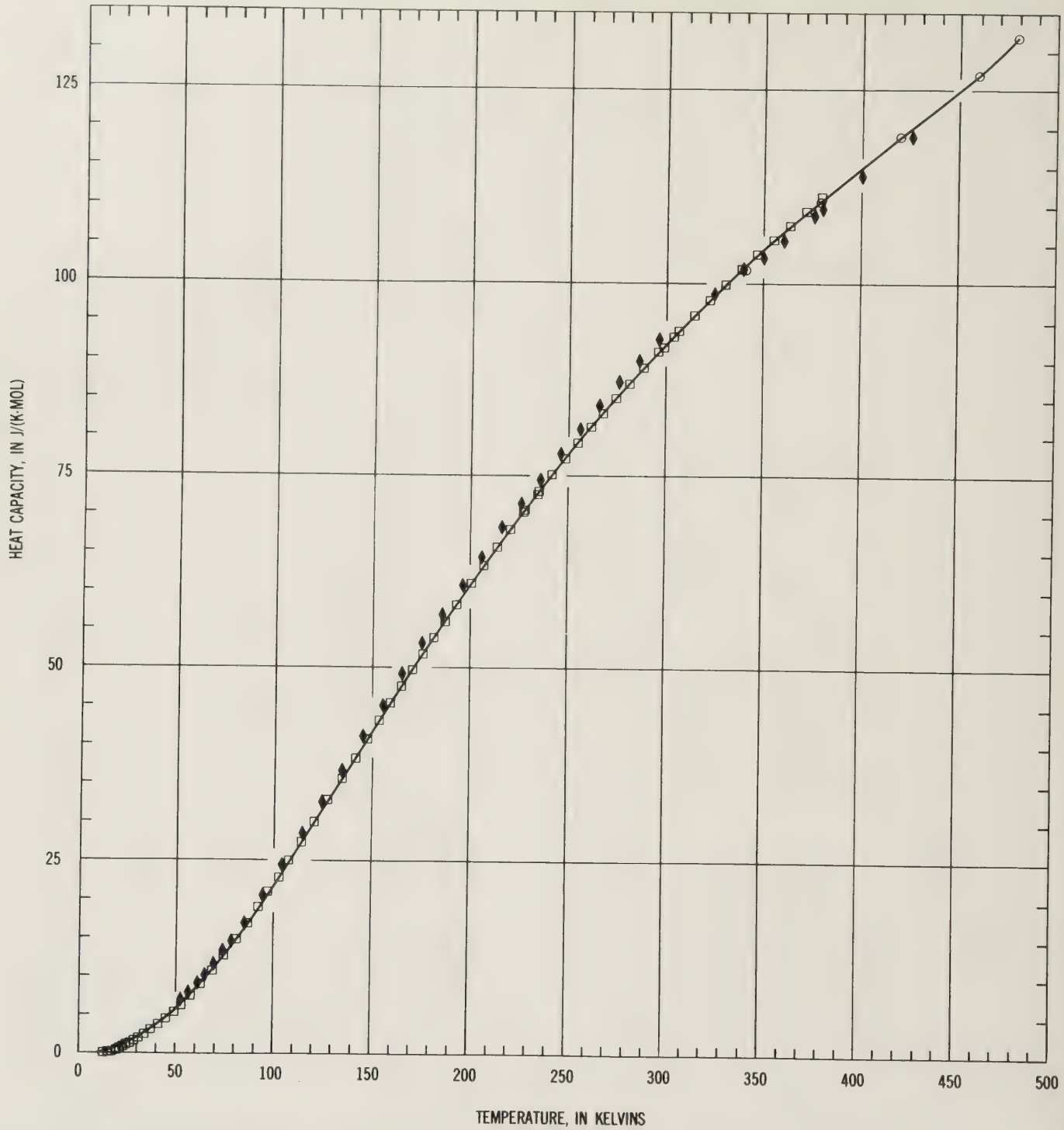

FIGURE 1.—Experimental molar heat capacities between 13 and 480 K for gibbsite. Open squares (adiabatic low-temperature calorimeter) and circles (differential scanning calorimeter), this study; solid diamonds, the measurements by Shomate and Cook (1946); solid line, the least-squares fit to the data.

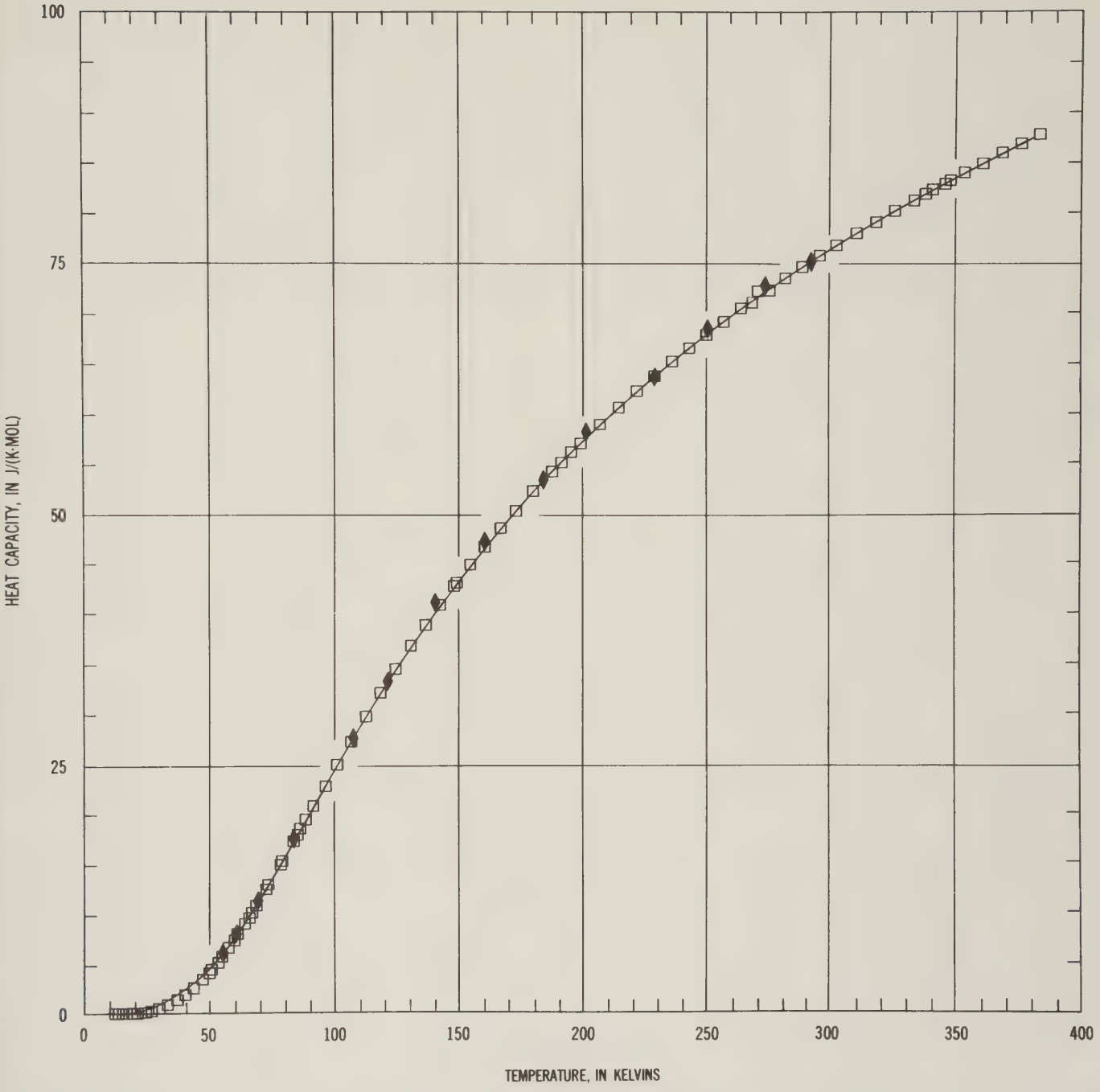

FIGURE 2.—Experimental molar heat capacities between 13 and 380 K for magnesite. Open squares, this investigation; solid diamonds, the measurements by Anderson (1934); solid line, the least-squares fit to the data.

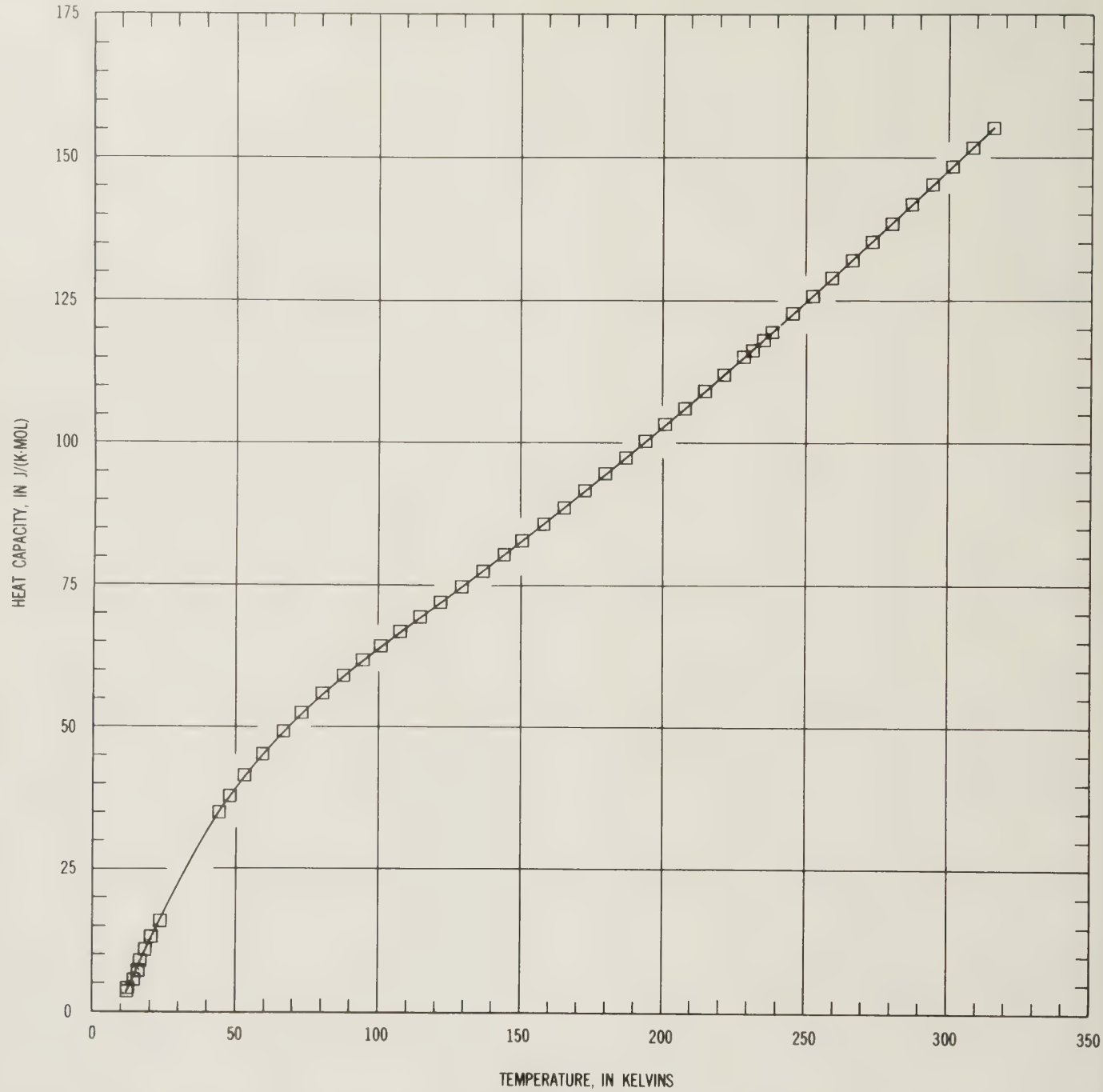

FIGURE 3.—Molar heat capacities between 12 and 316 K for Calorimetry Conference benzoic acid. The solid line is the least-squares fit to the data.

81.3 percent of the observed heat capacity at 12 K and 48.2 percent at 310 K.

The same benzoic acid sample is remeasured whenever a significant change is made in the calorimetric system. The results reported in this study show no significant deviation from earlier measurements from this laboratory or from the compilation of heat-capacity data for benzoic acid given by Robie and Hemingway (1972). They have given smoothed values of the heat capacities of benzoic acid from 10 to 305 K based upon data reported by five laboratories for portions of the same Calorimetry Conference benzoic acid sample. All data points were given equal weight, and no attempt was made to standardize the temperature scales used in the various laboratories.

Robie and Hemingway (1972, p. 16, fig. 7) have shown the result of reducing the same heat-capacity measurements on two different temperature scales. Figure 4, which is similar to figure 7 of Robie and Hemingway, is a graphical display of the deviations of the heat capacities of Calorimetry Conference benzoic acid reported in this study (C_p°, OBS) as calculated on the IPTS–68 and IPTS–48/NBS–55 (International Practical Temperature Scale of 1948 with the extension from 90.188 to 13.81 K according to the National Bureau of Standards 1955 temperature scale)

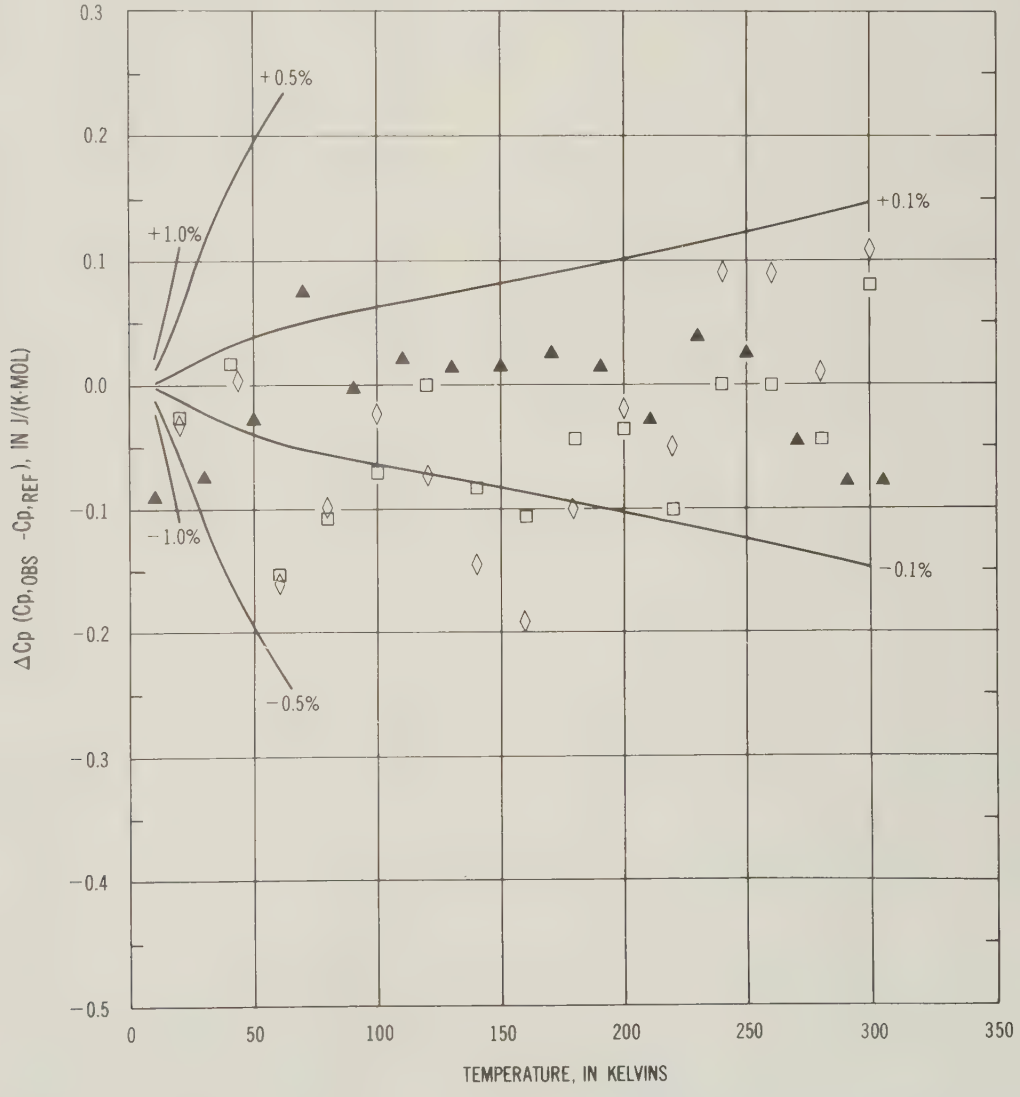

FIGURE 4.—Deviation of experimental (OBS) molar heat capacities (C_p°) of benzoic acid from the reference (REF) values for the heat capacities of benzoic acid given by Robie and Hemingway (1972). Open diamonds, this investigation, the heat capacities, referenced to IPTS–68; open squares, this investigation, the data referenced to IPTS–48/NBS–55; solid triangles, the data of Furukawa and others (1951); solid lines, percentage deviations of ΔC_p° from reference heat capacity.

TABLE 4.—*Specific heats calculated from experimental measurements of heat capacities of 22.233 g of Calorimetry Conference benzoic acid,* C_6H_5COOH

Temperature in K	Specific heat in J/(K·g)	Temperature in K	Specific heat in J/(K·g)	Temperature in K	Specific heat in J/(K·g)
SERIES 1		SERIES 4		SERIES 5	
12.29	.02845	136.09	.6335	231.60	.9532
13.06	.03380	143.46	.6562	238.47	.9786
14.70	.04571	150.72	.6788	245.46	1.004
16.54	.05990	158.11	.7023	252.44	1.030
18.17	.07381	165.52	.7261	259.41	1.056
20.00	.08984	172.86	.7501	266.37	1.082
22.08	.1086	180.02	.7740	273.32	1.108
24.37	.1297	187.09	.7977	280.28	1.134
		194.11	.8215	287.29	1.162
SERIES 2		201.06	.8452	294.34	1.189
44.31	.2873	207.96	.8689	301.43	1.215
48.13	.3104	214.90	.8935	308.57	1.242
53.08	.3393	221.80	.9180	315.76	1.271
59.34	.3712	228.69	.9418		
		235.56	.9671		
SERIES 3					
66.63	.4038				
73.10	.4302				
80.41	.4576				
87.77	.4832				
94.60	.5056				
101.05	.5259				
107.75	.5467				
114.72	.5681				
121.73	.5896				
129.15	.6124				
136.64	.6352				
144.11	.6582				

from the smoothed values reported by Robie and Hemingway (C_p°, REF). The entropy change ($S^\circ_{298.15} - S^\circ_{20}$) of benzoic acid, for the temperature range common to 1) the smoothed data of Robie and Hemingway, 2) the experimental data of Robie and Hemingway (referenced to IPTS68), and 3) the data of the present study are 163.1±0.2, 163.0±0.2, and 162.9±0.2 J/(K·mol), respectively.

THERMODYNAMIC PROPERTIES OF GIBBSITE AND MAGNESITE

Smooth values of the thermodynamic functions C_p° (heat capacity), $S_T^\circ - S_0^\circ$ (entropy), $(H_T^\circ - H_0^\circ)/T$ (enthalpy function), and $-(G_T^\circ - H_0^\circ)/T$ (Gibbs energy function) for gibbsite and magnesite are listed in tables 5 and 6, respectively. $S^\circ_{298} - S^\circ_0$ for gibbsite and magnesite are 68.44±0.14 J/(K·mol) and 65.09±0.13 J/(K·mol), respectively.

Pauling (1930) suggested a structure for gibbsite. Megaw (1934) showed that Pauling's idea was basically correct. Kroon and Stolpe (1959) and Glemser (1959) have confirmed the structure through proton magnetic-resonance experiments, and, more recently, Saalfeld and Wedde (1974) have refined the structure of gibbsite. Oh and others (1973) have determined the crystal structure of magnesite. Both structures are ordered. Consequently, S_0° is zero for both phases.

Shomate and Cook (1946) gave 70.09±0.21 J/(K·mol) for the entropy of gibbsite at 298.15 K on the basis of their heat-capacity measurements between 52 and 296.5 K and an empirical extrapolation of C_p° to 0 K. Their value for S°_{298} contained a contribution of 2.93 J/(K·mol) for the extrapolation of C_p° between 52 and 0 K. Our value, 68.44±0.14 J/(K·mol), includes a contribution of 0.40 J/(K·mol) resulting from the extrapolation of the heat capacity from 13.5 to 0 K.

The gibbsite sample used by Shomate and Cook (1946) was prepared by dissolving aluminum wire in 0.2 *N* potassium hydroxide. The precipitate was washed with 4 *N* hydrochloric acid in order to remove iron hydroxide that precipitated with the gibbsite. The sample was washed with distilled water and dried at 413 K. A complete chemical analysis of the sample was not given by the authors. An X-ray analysis

TABLE 5.—*Molar thermodynamic properties of gibbsite,* $Al(OH)_3$

[Formula weight = 78.003 $g \cdot mol^{-1}$]

Temperature, T, in kelvins	Heat capacity, C_p°, in J/(K·mol)	Entropy, $(S_T^\circ - S_0^\circ)$, in J/(K·mol)	Enthalpy function, $(H_T^\circ - H_0^\circ)/T$, in J/(K·mol)	Gibbs energy function, $-(G_T^\circ - H_0^\circ)/T$, in J/(K·mol)
5	0.017	0.004	0.003	0.001
10	0.093	0.030	0.023	0.008
15	0.307	0.103	0.077	0.026
20	0.680	0.238	0.178	0.061
25	1.183	0.442	0.326	0.115
30	1.822	0.712	0.520	0.191
35	2.603	1.049	0.760	0.289
40	3.496	1.454	1.045	0.409
45	4.522	1.924	1.373	0.550
50	5.609	2.456	1.742	0.714
60	8.185	3.701	2.596	1.105
70	11.15	5.180	3.602	1.579
80	14.45	6.881	4.749	2.133
90	18.01	8.787	6.022	2.765
100	21.76	10.88	7.407	3.470
110	25.64	13.13	8.887	4.245
120	29.60	15.53	10.45	5.084
130	33.61	18.06	12.08	5.984
140	37.64	20.70	13.76	6.941
150	41.65	23.43	15.48	7.948
160	45.63	26.25	17.24	9.004
170	49.55	29.13	19.03	10.10
180	53.39	32.07	20.83	11.24
190	57.15	35.06	22.64	12.42
200	60.82	38.09	24.46	13.62
210	64.40	41.14	26.28	14.86
220	67.88	44.22	28.09	16.13
230	71.27	47.31	29.89	17.41
240	74.56	50.41	31.69	18.72
250	77.76	53.52	33.47	20.05
260	80.86	56.63	35.23	21.40
270	83.85	59.74	36.98	22.76
280	86.73	62.84	38.70	24.14
290	89.51	65.93	40.41	25.53
300	92.19	69.01	42.09	26.93
310	94.79	72.08	43.75	28.33
320	97.31	75.13	45.38	29.75
330	99.77	78.16	46.99	31.17
340	102.2	81.17	48.58	32.59
350	104.5	84.17	50.14	34.03
360	106.7	87.14	51.68	35.46
370	108.9	90.10	53.20	36.90
380	111.0	93.03	54.70	38.34
390	113.1	95.94	56.17	39.77
400	115.1	98.83	57.61	41.22
410	117.1	101.7	59.04	42.66
420	119.1	104.5	60.44	44.10
430	121.0	107.4	61.83	45.53
440	123.0	110.2	63.20	46.97
450	125.0	113.0	64.55	48.41
460	127.0	115.7	65.89	49.84
470	129.2	118.5	67.21	51.27
480	132.0	121.2	68.53	52.70
273.15	84.77	60.72	37.52	23.20
298.15	91.70	68.44	41.78	26.67

TABLE 6.—*Molar thermodynamic properties of magnesite,* $MgCO_3$

[Formula weight = 84.314 g·mol^{-1}]

Temperature, T, in kelvins	Heat capacity, C°_p, in J/(K·mol)	Entropy, $(S^\circ_T - S^\circ_0)$, in J/(K·mol)	Enthalpy function, $(H^\circ_T - H^\circ_0)/T$, in J/(K·mol)	Gibbs energy function, $-(G^\circ_T - H^\circ_0)/T$, in J/(K·mol)
5	0.001	0.0004	0.0003	0.0001
10	0.011	0.003	0.002	0.0008
15	0.049	0.013	0.010	0.003
20	0.169	0.040	0.032	0.008
25	0.413	0.102	0.082	0.020
30	0.795	0.208	0.166	0.042
35	1.359	0.370	0.294	0.077
40	2.126	0.599	0.472	0.127
45	3.176	0.908	0.712	0.196
50	4.436	1.306	1.019	0.286
60	7.695	2.391	1.849	0.541
70	11.61	3.864	2.958	0.906
80	15.88	5.690	4.304	1.387
90	20.28	7.814	5.834	1.981
100	24.63	10.18	7.496	2.680
110	28.83	12.72	9.246	3.476
120	32.82	15.40	11.05	4.358
130	36.59	18.18	12.87	5.314
140	40.14	21.02	14.69	6.334
150	43.47	23.91	16.50	7.410
160	46.59	26.82	18.28	8.531
170	49.52	29.73	20.04	9.693
180	52.28	32.64	21.75	10.89
190	54.89	35.53	23.43	12.11
200	57.35	38.41	25.06	13.35
210	59.66	41.27	26.66	14.61
220	61.84	44.09	28.21	15.89
230	63.93	46.89	29.71	17.18
240	65.97	49.65	31.18	18.47
250	67.97	52.39	32.61	19.77
260	69.88	55.09	34.01	21.08
270	71.66	57.76	35.37	22.39
280	73.30	60.40	36.70	23.70
290	74.85	63.00	37.99	25.01
300	76.37	65.56	39.24	26.32
310	77.90	68.09	40.46	27.63
320	79.40	70.59	41.66	28.93
330	80.84	73.05	42.82	30.23
340	82.21	75.49	43.96	31.52
350	83.55	77.89	45.07	32.82
360	84.84	80.26	46.16	34.10
370	86.12	82.60	47.22	35.38
380	87.37	84.92	48.26	36.65
273.15	72.19	58.60	35.79	22.80
298.15	76.09	65.09	39.01	26.08

showed the sample to have the structure of gibbsite (Shomate and Cook, 1946).

The entropy of gibbsite at 298.15 K reported in this study (68.44±0.14 J/(K·mol)) is 2.4 percent lower than the value given by Shomate and Cook (1946). At 52.8 K, the heat capacity given by Shomate and Cook is 7 percent greater than the value obtained in this study. The difference decreases at higher temperatures (that is, Shomate and Cook's values are 2.5 percent higher than ours at 175.7 K and 1.5 percent higher at 296.5 K). At temperatures above 350 K, the heat capacities calculated from the heat-content data of Shomate and Cook are lower than the results obtained by using the differential scanning calorimeter.

Anderson (1934) used a natural sample of magnesite from Snarum, Norway. The measured heat capacities were corrected for impurities by considering the calcium and iron to be present as 9.0 percent calcite and 1.3 percent siderite. He obtained a value of 65.7±0.8 J/(K·mol) for the entropy of magnesite at 298.15 K based upon a graphical extrapolation of the heat capacity between 56.2 and 0 K. He obtained a second value (66.1±0.8 J/(K·mol) by using a combination of Debye and Einstein functions to extrapolate the measured heat-capacity data to 0 K. Our value, 65.09±0.13 J/(K·mol), is 0.9 percent lower than the graphically extrapolated value and 1.5 percent lower than the value based upon the analytical expressions. Anderson gave 63.44 J/(K·mol) as the entropy obtained graphically from the heat-capacity measurements over the temperature range from 56.2 to 298.1 K. Our value for the same temperature range is 0.5 percent smaller.

REFERENCES CITED

Anderson, C. T., 1934, The heat capacities of magnesium, zinc, lead, manganese and iron carbonates at low temperatures: Am. Chem. Soc. Jour., v. 56, no. 4. p. 849–851.

Bedford, R. E., Durieux, M., Muijlwiji, R., and Barber, C. R., 1969, Relationships between the International Practical Temperature Scale of 1968 and NBS–55, NPL–61, PMRI–54 and PSU–54 temperature scales in the range 13.81 to 90.188 K: Metrologia, v. 5, no. 2, p. 47–49.

Bedford, R. E., and Preston-Thomas, H., 1969, Derivation of the CCT–68 reference function of the International Practical Temperature Scale of 1968: Metrologia, v. 5, no. 2, p. 45–47.

Brewer, Leo, Rossini, F. D., and Westrum, E. F., Jr., 1974, Summary of conclusions and recommendations, *in* National Academy of Sciences, Report of the Conference on Thermodynamics and National Energy Problems, Airlie House, Warrenton, Va, June 10–12, 1974: Washington, D.C., p. iv–xiv.

Comité International des Poids et Mesures, 1969, The International Practical Temperature Scale of 1968: Metrologia, v. 5, no. 2, p. 35–44.

Commission on Atomic Weights, 1972, Atomic weights of the elements 1971: Pure and Appl. Chemistry, v. 30, p. 637–649.

Fournier, R. O., chm., 1974, Panel on geothermal energy, *in* National Academy of Sciences, Report of the Conference on Thermodynamics and National Energy Problems, Airlie House, Warrenton, Va., June 10–12, 1974: Washington, D.C., p. 255–278.

Furukawa, G. T., McCoskey, R. E., and King, G. J., 1951, Calorimetric properties of benzoic acid from 0° to 410° K: U.S. Natl. Bur. Standards Jour. Research, v. 47, p. 256–261.

Furukawa, G. T., Riddle, J. L., and Bigge, W. R., 1973, The International Practical Temperature Scale of 1968 in the region 13.81 to 90.188 K as maintained at the National Bureau of Standards: U.S. Natl. Bur. Standards Jour. Research, v. 77A, p. 309–332.

Glemser, O., 1959, Binding of water in some hydroxides and hydrous oxides: Nature, v. 183, no. 4666, p. 943–944.

Hemingway, B. S., and Robie, R. A., 1977, Enthalpies of formation of low albite ($NaAlSi_3O_8$), gibbsite ($Al(OH)_3$), and $NaAlO_2$; revised values for $\Delta H^\circ_{f,298}$ and $\Delta G^\circ_{f,298}$ of some aluminosilicate minerals: U.S. Geol. Survey Jour. Research, v. 5, no. 4, p. 413–429.

Kelley, K. K., 1960, Contributions to the data on theoretical metallurgy XIII. High-temperature heat-content, heat-capacity, and entropy data for the elements and inorganic compounds: U.S. Bur. Mines Bull. 584, 232 p.

Kelley, K. K., and King, E. G., 1961, Contributions to the data on theoretical metallurgy XIV. Entropies of the elements and inorganic compounds: U.S. Bur. Mines Bull. 592, 149 p.

Kroon, D. J., and Stolpe, C., 1959, Positions of protons in aluminum hydroxides derived from proton magnetic resonance: Nature, v. 183, no. 4666, p. 944–945.

Megaw, H. D., 1934, The crystal structure of hydrargillite, $Al(OH)_3$: Zeitschr. Kristallographie, v. 87, no. 3/4, p. 185–204.

Oh, K. D., Morikawa, H., Iwai, S., and Aoki, H., 1973, The crystal structure of magnesite: Am. Mineralogist, v. 58., no 11–12, p. 1029–1033.

O'Neill, G. J., 1966, Measurement of specific heat functions by differential scanning calorimetry: Anal. Chemistry, v. 38, no. 10, p. 1331–1336.

Pauling, L., 1930, The structure of micas and related minerals: Natl. Acad. Sci. Proc., v. 16, p. 123–129.

Robie, R. A., and Hemingway, B. S., 1972, Calorimeters for heat of solution and low-temperature heat capacity measurements: U.S. Geol. Survey Prof. Paper 755, 32 p.

Robie, R. A., Hemingway, B. S., and Wilson, W. H., 1976, The heat capacities of Calorimetry Conference copper and of muscovite $KAl_2(AlSi_3)O_{10}(OH)_2$, pyrophyllite $Al_2Si_4O_{10}(OH)_2$, and illite $K_3(Al_7Mg)(Si_{14}Al_2)O_{40}(OH)_8$ between 15 and 375 K and their standard entropies at 298.15 K: U.S. Geol. Survey Jour. Research, v. 4, no. 6, p. 631–644.

Saalfeld, H., and Wedde, M., 1974, Refinement of the crystal structure of gibbsite, $Al(OH)_3$: Zeitschr. Kristallographie, v. 139, no. 1/2, p. 129–135.

Shomate, C. H., and Cook, O. A., 1946, Low-temperature heat capacities and high-temperature heat contents of $Al_2O_3 \cdot 3H_2O$ and $Al_2O_3 \cdot H_2O$: Am. Chem. Soc. Jour., v. 68, no. 11, p. 2140–2142.

Jour. Research U.S. Geol. Survey
Vol. 5, No. 6, Nov.–Dec. 1977, p. 807–809

MEASURING TOTAL ANTIMONY IN GEOTHERMAL WATERS BY FLAME ATOMIC ABSORPTION SPECTROMETRY

By ROBERT ELIHU STAUFFER,[1] Menlo Park, Calif.

Abstract.—A flame atomic absorption procedure utilizing an electrodeless discharge lamp is described for determining total solute antimony in silica-rich geothermal waters. Following $NaNO_2$ oxidation of Sb^{+3}, $SbCl_5$ is extracted from 6 *N* HCl solution by using MIBK (methyl isobutyl ketone); silica in the organic layer is removed by centrifugation. The analytical detection limit for antimony is about 6 micrograms per liter in the original sample; the coefficient of variation is 4 percent at the 250 μg/L Sb level. Comparable total antimony levels were found in sample splits which had been either filtered and acidified (to pH less than 1.5) with HNO_3 or left untreated at the time of sample collection.

Antimony has been of geochemical interest in geothermal waters since the early investigations at Steamboat Springs, Nev. (Brannock and others, 1948; White, 1967), revealed total solute antimony as much as 400 micrograms per liter. Ritchie (1961) reported antimony concentrations ranging from 8 to 900 μg/L on 25 samples representing a diverse set of New Zealand hot-spring waters. Primary stibnite (Sb_2S_3) was identified at Steamboat Springs in veinlets and cavities associated with convecting water at temperatures of 100° to 146°C, and amorphous metastibnite was abundantly deposited along with sinter. Similar precipitates have been identified in New Zealand. The deposition of the antimony sulfides has been linked with epithermal deposits of silver, thallium, and gold (Weissberg, 1969).

Ritchie (1961) used the rhodamine B–benzene extraction procedure for determining antimony at concentrations under 200 μg/L and the iodoantimonite method for higher antimony concentrations. The two procedures followed those of Wyatt (1955), who noted that the early rhodamine B procedures for antimony analysis were not entirely satisfactory. Willey, O'Neil, and Rapp (1974) used flame atomic absorption (A.A.) without a preliminary solvent extraction step in their analyses of geothermal waters from Long Valley, California. The reported detection limit of 100 μg/L is too high for the procedure to be useful in studying the chemistry of antimony in geothermal waters.

Anodic stripping voltammetry is a sensitive technique for determining antimony in natural waters (Gilbert and Hume, 1973). In this method, antimony is determined as the difference between the sum of bismuth plus antimony and bismuth alone. The detection limit is about 0.2 μg/L Sb in the absence of bismuth.

Yanagisawa, Takeuchi, and Suzuki (1973) reported a flameless A.A. procedure for antimony which overcomes the poor sensitivity of the flame A.A. analysis. They used a prior solvent extraction separation of antimony which eliminates interfering cations in aqueous solution. In the extraction step, $SbCl_5$ is extracted from 6 *N* HCl solution by using the organic solvent MIBK (methyl isobutyl ketone) following oxidation of Sb^{+3} to Sb^{+5} by using $NaNO_2$. The MIBK extract is injected into the carbon rod analyzer. I report a modification of the procedure of Yanagisawa, Takeuchi, and Suzuki (1973) in which the MIBK extract is centrifuged to remove silica prior to a flame A.A. analytical step.

Acknowledgment.—The author is indebted to E. A. Jenne, J. M. Thompson, and particularly J. W. Ball (all of the U.S. Geological Survey) for access to hot-spring samples and for constructive suggestions in developing the procedure.

EXPERIMENTAL METHOD

A Perkin-Elmer model 306 atomic absorption spectrophotometer was equipped with an antimony electrodeless discharge lamp, which is considered to be an improvement over the hollow cathode lamp for antimony analyses. Analytical measurements were made in an air-acetylene flame at 218 nanometers.

An antimony primary standard was prepared in distilled-deionized water by using potassium antimonyl tartrate. All reagents used were of analytical grade. The concentrated HCl and MIBK used in the solvent extraction step were used without further purification.

[1] Present address: Water Chemistry Laboratory, University of Wisconsin, Madison, WI 53706.

The experimental procedure is as follows:
Add 100 mL of concentrated HCl to 100 mL of sample or standard in a 250 mL separatory funnel. Add 2.0 mL of 7.5 percent $NaNO_2$ and shake. Allow 3 min for the oxidation of Sb^{+3} and then extract the $SbCl_5$ complex by using 20.0 mL of MIBK and by shaking for 3 min. Discard aqueous phase and drain the MIBK layer into a centrifuge tube. Cap and centrifuge for 10 min at 3015 × gravity to remove the silica. Aspirate the MIBK layer during A.A. analysis.

RESULTS AND DISCUSSION

The very high SiO_2 concentrations in geothermal waters (often greater than 300 mg/L SiO_2) result in the formation of silica-MIBK "slush" above the aqueous HCl layer. The centrifugation removes both the solid SiO_2 and the small acid droplets in the MIBK layer.

The concentration factor for antimony in the MIBK phase depends sensitively on the volume ratio of MIBK to sample because a part of the MIBK dissolves in the aqueous phase and $SbCl_5$ partitions strongly into the residual MIBK layer. The sample size extracted and the volume ratio insure both adequate analytical sensitivity for geothermal waters and a sufficiently large volume of centrifuged MIBK phase for multiple A.A. determinations. The optimal tradeoff between improved sensitivity and poorer precision depends on the antimony levels in the samples.

Analytical errors

A low consistent blank of 0.001 absorbance indicated no significant antimony contamination of either the HCl or the MIBK. The mean absorbance of a 250 μg/L Sb standard was 0.0595. (Antimony concentrations always refer to initial aqueous sample or standard.) As expected, absorbance response was a linear function of antimony concentration up to 500 μg/L Sb (the highest concentration tested). The coefficient of variation [2] for standards was 4 and 2 percent, at the 250 and 500 μg/L Sb levels, respectively. The detection limit is approximately 6 μg/L. The coefficient of variation for two high-SiO_2 hot-spring samples was 10 percent at the 100 μg/L Sb level. Considering the increase in the analytical coefficient of variation with decreasing antimony concentration, the precision for samples and standards appears to be similar.

The accuracy of the method was tested by spiking geothermal samples with known amounts of antimony prior to the extraction step. The low (mean, 91 percent) and variable antimony recoveries (table 1) have resulted from the high SiO_2 levels in the samples; the large quantities of SiO_2 in the MIBK layer may reduce the "activity" of the solvent and adversely affect the partitioning efficiency for $SbCl_5$. The effects of high, variable, and chemically unstable SiO_2 concentrations in the samples may possibly be mitigated by a preliminary freeze separation of excess SiO_2 from the field-acidified sample, followed by thawing, then filtering. Alternatively, antimony levels in the samples can be estimated by using the method of standard additions.

[2] Defined as 100 $\hat{\sigma}_x/\bar{x}$ where $\hat{\sigma}_x$ is the sample standard deviation and $\bar{x}$ is the observed sample mean.

TABLE 1.—*Analytical recoveries of antimony added to Yellowstone National Park geothermal water samples*

[A 300 μg/L Sb spike (final concentration) was added to all samples]

Sample	Hot spring	Basin	Recovery (percent)
YS–74–123	Tortoise Shell	Upper	83
YT–73–62	Sapphire Spring	Biscuit	95
YS–74–132	Azure Pool	Lower	99
YT–73–68	Gentian Pool	Lower	88

Sampling effects

A preliminary experiment was conducted to test the effect of filtering and acidifying hot-spring samples in the field in contrast to antimony determinations on unfiltered-unacidified samples. The two alkaline spring samples used in the contrast (table 2) contained 341 and 291 mg/L SiO_2, respectively, and in addition each contained 301 mg/L Cl. The estimated antimony concentrations in the acidified samples were slightly higher. However, because the analytical coefficient of variation is about 10 percent at the 100 μg/L Sb level, the mean difference in antimony concentrations between sample treatments is not statistically significant. Previously, Gilbert and Hume (1973) noted only a very weak tendency for low levels of antimony to sorb on the walls of polyethylene sampling bottles during prolonged storage of ocean samples.

TABLE 2.—*Effects of sample treatment on antimony levels*

Sample	Hot spring [1]	Antimony concentration (μg/L)		
		Unfiltered, unacidified	Filtered, acidified	Difference
YJ–74–68	Lake Side Spring	102	114	—12
YJ–74–70	Ephedra	102	107	—5

[1] Yellowstone National Park, West Thumb Basin.

REFERENCES CITED

Brannock, W. W., Fix P. F., Gianella, V. P., and White, D. E., 1948, Preliminary geochemical results at Steamboat Springs, Nevada: Am. Geophys. Union Trans., v. 29, p. 211–226.

Gilbert, T. R., and Hume, D. N., 1973, Direct determination of bismuth and antimony in sea water by anodic stripping voltammetry: Anal. Chim. Acta, v. 65, p. 451–459.

Ritchie, J. A., 1961, Arsenic and antimony in some New Zealand thermal waters: New Zealand Jour. Sci., v. 4, p. 218–229.

Weissberg, B. G., 1969, Gold-silver ore-grade precipitates from New Zealand thermal waters: Econ. Geology, v. 64, p. 95–108.

White, D. E., 1967, Mercury and base-metal deposits with associated thermal and mineral waters, *in* Barnes, H. L., ed., Geochemistry of hydrothermal ore deposits: New York, Holt, Rinehart, and Winston, p. 575–631.

Willey, L. M., O'Neil, J. R., and Rapp, J. B., 1974, Chemistry of thermal waters in Long Valley, Mono County, Calif.: U.S. Geol. Survey open-file rept. 19 p.

Wyatt, P. F., 1955, Diethylammonium diethyldithiocarbamate for the separation and determination of small amounts of metals. Part 2—the isolation and determination of arsenic, antimony, and tin in organic compounds: Analyst, v. 80, 368–379.

Yanagisawa, M., Takeuchi, T., and Suzuki, M., 1973, Flameless atomic absorption spectrometry of antimony: Anal. Chim. Acta, v. 64, p. 381–386.

Jour. Research U.S. Geol. Survey
Vol. 5, No. 6, Nov.–Dec. 1977, p. 811–814

ACCURACY OF CHANNEL MEASUREMENTS AND THE IMPLICATIONS IN ESTIMATING STREAMFLOW CHARACTERISTICS

By KENNETH L. WAHL, Menlo Park, Calif.

Abstract.—Regional relations between flow characteristics and stream-channel size offer a promising alternative to available methods of estimating flow characteristics for ungauged sites, particularly in semiarid regions. The reliability of such relations and of flow estimates made from them is partly dependent on the user's ability to recognize a suitable reach and the reference levels in that reach. A test was made in northern Wyoming to determine how consistently trained individuals could measure channel size for three different reference levels. Seven participants independently visited 22 sites and measured channel dimensions in sections of their choosing. Assuming that the functional relation between a discharge characteristic (Q) and channel width (W) is log $Q=f(1.5 \log W)$ and that the average log W from seven measurements is the best estimate of log W at a site, an average standard error for discharge of about 30 percent was attributed to differences in width measurements alone.

Hydrologists are frequently faced with the problem of estimating stream-flow characteristics at ungauged sites. These estimates are usually made by transferring information from gauged sites through regional relations between flow characteristics and physical and climatic characteristics of the basins. Unfortunately, flows in arid or semiarid regions are often only poorly related to the size of the drainage basin and to other basin characteristics. Regional relations between flow characteristics and stream-channel size offer a promising alternative under these conditions. Moore (1968) and Hedman (1970) describe such relations between mean annual discharge and the width and mean depth of a channel section defined by the tops of within-channel bars. Hedman, Moore, and Livingston (1972) also used width and average depth of the section defined by within-channel bars but included relations for estimating floods of selected recurrence interval. Hedman, Kastner, and Hejl (1974) used the width and the average depth of a section defined by a feature of higher elevation termed the active-channel section. Riggs (1974) gave relations between floods of selected recurrence interval and the width of the main channel.

The reliability of flow estimates from such relations depends not only on the applicability of the regional relations but also on the ability of different individuals to recognize and measure the channel parameters used as independent variables. This paper reports the results of a test conducted to assess the magnitude of this personal error. The test was not concerned with defining a regional relation between flow characteristics and channel size; that such relations can be developed is demonstrated in the literature cited.

DESCRIPTION OF THE TEST

The purpose of the test was to determine the accuracy with which trained individuals could independently measure the width and the average depth of the channel as defined by three separate reference levels and to determine the effect of variability in channel measurements on estimates of discharge characteristics. The three sections are the section defined by the lowest channel bars, the active-channel section, and the main-channel section. The seven participants were experienced in identifying at least one of the three reference levels and were generally familiar with all three sections.

Section defined by lowest channel bars

The section defined by within-channel bars was described by Moore (1968), Hedman (1970), and Hedman, Moore, and Livingston (1972). The reference level is defined by the tops of the lowest prominent channel bars. In perennial streams, the particles of the bars are moved annually and the bars may be below the water surface for much of the year. In ephemeral streams, particles will be moved by significant flows but may not be moved annually.

Active-channel section

The active channel section was described by Hedman, Kastner, and Heil (1974) and Riggs (1974) as the lower part of the channel entrenchment that is actively involved in transporting water and sediment during the normal regime of flow. Beyond the boundaries of the active channel, the channel features are relatively

permanent and usually are vegetated. The reference point for measuring the active-channel section is the point at which the channel banks or the tops of stabilized channel bars abruptly change to a flatter slope. In a straight reach devoid of channel bars, the width of the section will be the width of the low-water channel.

Main-channel section

The main-channel section was described by Riggs (1974) as that part of the stream channel bounded by the streamward edges of the flood plain or by the lower edge of permanent vegetation. On perennial streams, it is the same as the bankfull stage described by Leopold, Wolman, and Miller (1964) but is measured in a narrow section.

The study area

The test area is located in the Powder River and Bighorn River basins in northern Wyoming. This area was selected because a wide variety of hydrologic conditions and channel types exist in a relatively small area. The elevation ranges from about 1400 m in the plains on the east and west to about 3900 m in the Bighorn Mountains that bisect the study area. Mean annual precipitation ranges from roughly 170 mm at the lower elevation to about 1250 mm in the mountains. Streams flowing from the mountains derive most of their flow from snowmelt and are perennial; streams originating in the plains are ephemeral, with most flows resulting from thunderstorm activity. Streambed composition is quite variable, ranging from cobbles and boulders in the higher elevation, to gravel in the lower mountains, and to mixed silt, clay, and sand in the plains. The variation of stream type and channel size is indicated in table 1; the channel widths shown are the geometric means of the values determined by the test participants.

Test procedure

The test was designed to simulate conditions that might exist in using regional relations to estimate flow characteristics at ungauged sites. To insure objectivity, the majority of the test sites were on ungauged streams. Furthermore, at the time of the test there were no regional relations based on channel size for the test area; thus, measurements at the gauged sites used could not be compared with any other estimates. The seven participants were given directions to the 22 sites, which they visited independently. Because only general reaches of each stream were identified, the specific cross sections at which the participants measured channel dimensions were of their own choosing. Thus, the variability of measurements by the participants reflects the combined effects of differences in cross-section locations within the test reach and differences in identification of the reference levels. This should be indicative of the true variability that would result if trained individuals measured channel size in an ungauged reach.

Table 1.—*Average channel widths of test sites*

Site	Stream type[1]	Geometric means of measured width, in meters		
		Low bar	Active channel	Main channel
1	E	1.03	2.21	4.11
2	E	1.56	3.27	4.72
3	P	10.1	13.6	15.6
4	P	5.81	7.15	8.20
5	P	4.61	5.55	7.31
6	P	5.30	5.94	7.48
7	P	6.82	8.40	12.1
8	E	2.59	5.18	9.86
9	E	2.37	5.55	9.20
10	E	2.65	6.37	10.3
11	E	1.56	2.72	6.08
12	P	16.7	60.8	65.2
13	E	.61	.92	2.11
14	E	1.10	2.06	3.58
15	P	6.52	8.40	10.1
16	I	1.39	2.78	4.21
17	P	1.30	2.11	3.50
18	P	17.1	18.4	21.6
19	P	11.6	12.1	13.9
20	P	2.54	2.98	4.02
21	P	2.98	4.31	5.67
22	E	5.68	9.20	12.1

[1] P = perennial, E = ephemeral, I = intermittent

Weather was a factor in the test. Several participants were unable to visit some of the sites because of recent snowfall. Also, higher-than-normal precipitation caused increased flows, which inundated the lowest channel feature at a few sites. This was not felt to be detrimental to the test, however, as it added to the realism.

ANALYSIS OF DATA

The test was intended to define the variability of channel measurements by individuals and to give some insight into potential advantages and disadvantages of the three reference levels. There was no attempt to evaluate hydrologic considerations such as determining the reference level most closely related to a given flow variable.

The number of sites for which a given reference level could be identified is certainly one measure of the usefulness of the reference level. With 22 sites and 7 participants, there were potentially 154 measurements for each reference level. Because of inclement weather, however, three participants did not visit site 10, one did not visit sites 12–15, and one did not visit sites 19–21. Thus, the maximum sample for a

given reference level would have been 144 measurements. A total of 109 measurements was made for the section defined by the within-channel bars, 141 were made for the active-channel section, and 136 were made for the main-channel section; these represent 76, 98, and 94 percent, respectively, of the measurements that could have been made.

The low percentage of measurements for the low-bar section resulted in part from that reference level being submerged in perennial streams. Flows during the test period were higher than base flow, and two-thirds of the sites at which the low-bar section was not located by the participants were on perennial streams. This, however, would also be a factor in applying a regional relation so it must be recognized as a constraint on the utility of the low-bar section.

Agreement between participants

Two tests were conducted to assess the degree of consistency among channel measurements by participants. In one test, the cross-correlation coefficients were defined for all possible pairs of participants. Correlation coefficients for width and depth were considered separately for each reference level, and the mean and standard deviation computed for correlation coefficients from all the possible pairs of participants. Results are shown in table 2 and indicate a high degree of consistency for measurements of width for all three reference levels. In contrast, the degree of consistency for depth measurement is relatively low. It appears from this test that different individuals can measure width more consistently than depth.

Table 2.—*Summary of cross correlations between measurements by participants*

Section	Statistics of correlation coefficients		
	Mean	Standard deviation	Range
Low bar—width	0.95	0.055	0.74–0.99
depth	.74	.128	.51– .93
Active channel—width	.97	.028	.91– .99
depth	.59	.164	.27– .83
Main channel—width	.92	.067	.79– .99
depth	.59	.193	.16– .89

Analysis of variance was used to test the hypothesis that there was no difference among individuals in the average value of a given channel size parameter. Widths and depths of the low-bar section for participants 1, 4, and 6 and the depths of the active-channel and main-channel sections for participant 1 were not included in the analysis because of inadequate sample size. The hypothesis of no difference among means for participants was accepted at the 95-percent level for the widths of all three reference levels and for the average depth of the low-bar section. The hypothesis was rejected for mean depth of both the active-channel and the main-channel sections; however, upon eliminating results for participant 1 and retesting, the hypothesis of no difference among means was accepted. Thus, while participant 1 apparently measured a section somewhat more shallow than that measured by other participants, the difference was not reflected in the measured widths.

Variability in discharge estimates

In analyzing the test data, the average of the logarithms of the seven measurements of channel width (W) at a given site was assumed to give the best estimate of log W, and departures of individual values of log W from the average for a site were examined. The mean and standard deviation of the departures are summarized in table 3 for each participant and for the three reference levels. The mean of the absolute values of the seven average departures represents the average of individual bias in log W for the reference level without regard to the direction of bias. The average standard deviation for a particular section represents the mean standard error in log W resulting from the combined effects of individual differences in reach selection and identification of the reference level. The effect of this variability on computed discharge is defined below.

Relations between a discharge characteristic and channel width usually take the form

$$\log Q = \log a + b \log W,$$

where a and b are constants of regression. Given a relation of this form, the standard error in log Q produced by variation in estimates of W is b times the standard error of log W.

In relations developed to date, the regression coefficient, b, has averaged about 1.5. Using this value and the average standard deviations for log W in table 3, the corresponding standard errors in log Q are as shown in table 4.

The average bias in estimates of log Q is also shown in table 4. This bias results from an individual consistently measuring either larger or smaller widths than the average. It must be emphasized, however, that the bias shown is only correct if the average of log W is the true value of log W.

The summary of errors in estimates of discharge characteristics shown in table 4 are the values that would result only from variability and bias in measuring channel width; they do not reflect the model

Table 3.—*Statistics of differences from the mean logarithm of width at each site. Units are base 10 logarithms*

Individual	Section					
	Low bar[1]		Active channel		Main channel	
	Average departure	Standard deviation	Average departure	Standard deviation	Average departure	Standard deviation
1	−0.0459	0.1310	0.0001	0.0873	−0.0241	0.0956
2	.0322	.0812	−.0009	.0907	.0435	.1150
3	−.0418	.0876	.0418	.0554	−.0196	.0673
4	−.0127	.0737	−.0612	.0484	−.0557	.0904
5	.1241	.1068	.0622	.0859	.0153	.1140
6	−.0270	.1283	.0164	.1018	.0760	.1048
7	−.0805	.0770	−.0548	.0859	−.0239	.0524
Average	[2].0521	.0979	[2].0340	.0793	[2].0369	.0913

[1]Sites 8 and 10 were excluded as the low-bar feature was only measured by 3 individuals.
[2]Mean of the absolute values of average departure.

Table 4.—*Errors in discharge estimates attributable to variability of width measurements.*

Section	Average standard error in Q		Average bias in Q	
	Log units	Percent	Log units	Percent
Low bar	0.147	33	0.078	18
Active channel	.119	27	.051	12
Main channel	.137	32	.055	13

error or the error of the streamflow characteristics used to develop the regional relation. The total error would include all of these components. Although these components cannot be separated at present, some insight can be gained by assuming that a regional relation between a discharge characteristic and width has a standard error of 0.13 log units (30.4 percent) and that the widths used to develop the relation were averages of measurements by a number of individuals. This standard error should approximate the combination of model error and sampling error of the flow characteristics. However, true error of applying the relation by one individual would include components of error resulting from both variability and bias in measuring width; the approximate magnitudes of these components would be 0.13 log units (30.4 percent) and 0.06 log units (13.9 percent), respectively, from table 4. If the three errors are independent, the true standard error would be the square root of the sum of the squares of the components. Thus, the true standard error of discharge would be about 0.193 log units (about 46 percent).

SUMMARY

Results of this test do not indicate a marked superiority of any one of the three reference levels presently being used to develop regional relations for flow characteristics. The variation in independent measurements of the three levels is comparable. However, submergence of the low-bar section at medium and high stages limits its usefulness.

As might be expected, the study indicated that trained individuals measure width more consistently than depth. Cross-correlation coefficients and analysis of variance failed to display any significant inconsistency between measures of width by the participants. Cross-correlation coefficients for depth were lower than for width, and analysis of variance indicated that, at the 95-percent confidence level, one participant measured significantly shallower depths than the average.

Given a regional relation between a flow characteristic and channel width, a standard error of about 30 percent in estimated discharge could be expected from the sampling error in width measurements by trained individuals, assuming a perfect model and no sampling error in streamflow characteristics. Bias in measuring width could produce about a 14-percent standard error in discharge. If the errors are independent, a regional relation with model and streamflow sampling error of 30 percent would have a true standard error of about 46 percent.

REFERENCES CITED

Hedman, E. R., 1970, Mean annual runoff as related to channel geometry of selected streams in California: U.S. Geol. Survey Water-Supply Paper 199–E, 17 p.

Hedman, E. R., Kastner, W. M., and Hejl, H. R., 1974, Selected streamflow characteristics as related to active-channel geometry of streams in Kansas: Kansas Water Resources Board Tech. Rept. No. 10, 21 p.

Hedman, E. R., Moore, D. O., and Livingston, R. K., 1972, Selected streamflow characteristics as related to channel geometry of perennial streams in Colorado: U.S. Geol. Survey open-file report, 14 p.

Leopold, L. B., Wolman, M. G., and Miller, J. P., 1964, Fluvial processes in geomorphology: San Francisco, W. H. Freeman, 522 p.

Moore, D. O., 1968, Estimating mean runoff in ungaged semiarid areas: Internat. Assoc. Sci. Hydrology Bull. vol. 13, no. 1, p. 28–39.

Riggs, H. C., 1974, Flash flood potential from channel measurements, Flash floods symposium: Internat. Assoc. Sci. Hydrology, Pub. 112, p. 52–56.

Jour. Research U.S. Geol. Survey
Vol. 5, No. 6, Nov.–Dec. 1977, p. 815–821

SOLUTION OF WATER-TABLE AND ANISOTROPIC FLOW PROBLEMS BY USING THE STRONGLY IMPLICIT PROCEDURE

By S. P. LARSON and PETER C. TRESCOTT, Reston, Va.

Abstract.—The use of the strongly implicit procedure (SIP) with an additional iteration parameter, β, to scale the residual vector is advantageous to the solution of some ground-water-flow problems. For steady-state water-table problems plagued by excessive elimination of grid blocks during the iteration process, selection of $\beta<1$ can be effective in limiting the deletion of blocks to a reasonable number. Also, a linear problem characterized by large anisotropy and layers of contrasting hydraulic conductivity was solved more efficiently with $\beta=1.5$. Effective values of β are generally in the range $0<\beta<2$ and are easily determined by trial. Use of a β parameter in the SIP algorithm provides an effective solution technique for a class of ground-water-flow problems that previously was burdened by significant computational difficulty.

Model studies of ground-water-flow systems often require the steady-state solution for a water-table-aquifer system. To obtain this solution by using the Dupuit-Forchheimir assumptions, transmissivity must be considered to be a function of water-level in the aquifer, and, thus, the resulting partial-differential equation used to describe ground-water movement is nonlinear. A commonly used form of the equation (Bredehoeft and Pinder, 1970) in two spatial dimensions is

$$\frac{\partial}{\partial x}\left(K_{xx}b\frac{\partial h}{\partial x}\right)+\frac{\partial}{\partial y}\left(K_{yy}b\frac{\partial h}{\partial y}\right)=W(x,y), \quad (1)$$

where K_{xx}, K_{yy} are the principal components of the hydraulic conductivity tensor, h is hydraulic head, b is the saturated thickness of the aquifer, and $W(x,y)$ is the volumetric flux of recharge or discharge per unit surface area of the aquifer. Equation 1 is based on the assumption that the coordinate axes are colinear with the principal components of the hydraulic conductivity tensor. It is nonlinear because saturated thickness, b, is a linear function of the hydraulic head.

Standard five-point finite-difference techniques can be used to approximate equation 1. If the approximating equation is written for each block of a grid that represents the geometry of the aquifer system and is combined with equations describing boundary conditions for the system, a set of simultaneous equations results. The next step is the linearization of these equations in some manner, so that a solution can be obtained.

A two-dimensional ground-water-flow simulator, constructed by Trescott, Pinder, and Larson (1976) and commonly used by the U.S. Geological Survey, includes a choice of three iterative methods for solving the simultaneous equations: (1) line-successive overrelaxation (LSOR), as described by Young (1954); (2) the iterative alternating-direction implicit procedure (ADI), as presented by Peaceman and Rachford (1955), and (3) the strongly implicit procedure (SIP), as introduced by Stone (1968). The extended two-dimensional correction (2DC) for LSOR, as described by Aziz and Settari (1972), is also available.

In this simulator, a Picard-type iteration (Remson and others, 1971) is used to linearize the equations. This is done in water-table problems by updating transmissivity at the end of each iteration of the solution method used (LSOR, ADI, or SIP). If, during the iterative process, the aquifer water level for a grid block is computed to be below the base of the aquifer, the transmissivity is set equal to 0 and that block is eliminated from the remainder of the simulation. Thus, the edges of an eliminated block become a no-flow boundary.

This approach is generally satisfactory for transient water-table simulations. In most cases, water levels move in one direction (rising or declining), and the water levels at the beginning of a time step are close to those at the end of the step. However, if the steady-state equation is being solved, the initial estimates of water levels may not be close to the solution, and oscillations may be introduced that prevent a satisfactory solution. Figure 1 is a fictitious example that illustrates the oscillation problem for one block that would be incorrectly eliminated from the solution on the first iteration. This difficulty is common to all of the solution methods as originally coded in the simulator. The objective of this paper is to describe a simple mod-

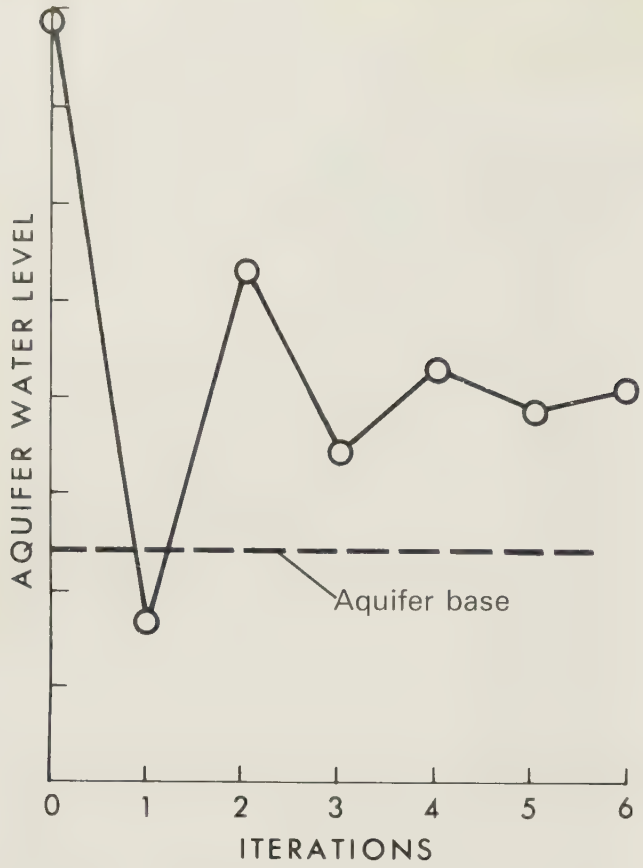

FIGURE 1.—Oscillation of computed head during the iterative process.

ification to the SIP code that resulted in several successful water-table-aquifer simulations.

STRONGLY IMPLICIT PROCEDURE

Stone (1968), in developing the SIP algorithm, mentions that an additional iteration parameter, β, can be used but found that, for his problems, values other than unity were not particularly advantageous. However, in dealing with functional transmissivity coefficients of water-table ground-water-flow problems, this parameter can control the oscillatory effects that may be induced by the Picard scheme and the standard SIP algorithm.

To illustrate the effect of the β parameter, a brief outline of the SIP algorithm is presented. The set of equations consisting of the finite-difference equation (or boundary-condition equation) at each grid block can be expressed in matrix form as

$$[A]\{h\}=\{Q\} \tag{2}$$

where $\{h\}$ is a vector of unknown heads, $[A]$ is a matrix of known coefficients, and $\{Q\}$ is a vector that includes all known terms for each grid block. A matrix $[A+B]$ is constructed so that it is "close" to $[A]$ but can be factored into sparse upper and lower triangular matrices. See Stone (1968), Remson, Hornberger, and Molz (1971), or Trescott, Pinder, and Larson (1976) for details. The matrix equation becomes

$$[A+B]\{h\}=\{Q\}+[B]\{h\} \tag{3}$$

Equation 3 leads to an iteration scheme,

$$[A+B]\{h\}^n=\{Q\}+[B]\{h\}^{n-1} \tag{4}$$

where n is the iteration index. The right side of equation 4 is known and because matrix $[A+B]$ can be factored into sparse upper and lower triangular matrices, vector $\{h\}^n$ can be determined efficiently by Gaussian elimination.

To reduce roundoff errors, the matrix equation is commonly transformed into a residual form in which the solution yields the change in head from one iteration to the next. $[A+B]\{h\}^{n-1}$ is subtracted from each side of equation 4 which, after rearranging, becomes

$$[A+B]\{\xi\}^n=\{R\}^{n-1} \tag{5}$$

in which $\{\xi\}^n=\{h\}^n-\{h\}^{n-1}$ and $\{R\}^{n-1}=\{Q\}-[A]\{h\}^{n-1}$. Note that $\{R\}^{n-1}$ is the vector of residuals obtained by substituting the heads at the old iteration level into the finite-difference equation 2 for each block.

In the standard application of SIP, a set of iteration parameters is computed and used cyclically to define $[B]$ at each iteration. The additional iteration parameter β premultiplies vector $\{R\}^{n-1}$ and has the net effect of scaling the solution vector $\{\xi\}^n$. The matrix equation becomes

$$[A+B]\{\xi\}^n=\beta\{R\}^{n-1}.$$

With use of the SIP algorithm without the β parameter ($\beta=1$), it was observed that the intermediate solution often caused the numerical difficulties illustrated in figure 1. For some problems, many blocks were eliminated in this fashion, thus creating a false geometry to the problem.

APPLICATION

The solution of a field problem (fig. 2), which was designed by Konikow (1974) in his analysis of ground-water pollution at the Rocky Mountain Arsenal northeast of Denver, Colo., illustrates the effect of the β parameter. This test problem was used because it is typical of many field problems with water-table boundaries for which it is difficult to obtain a steady-state solution using any of the iterative methods available in the simulator.

Characteristics of the problem include extensive areas where the surficial deposits are unsaturated. The finite-difference grid was 25×38, with square blocks

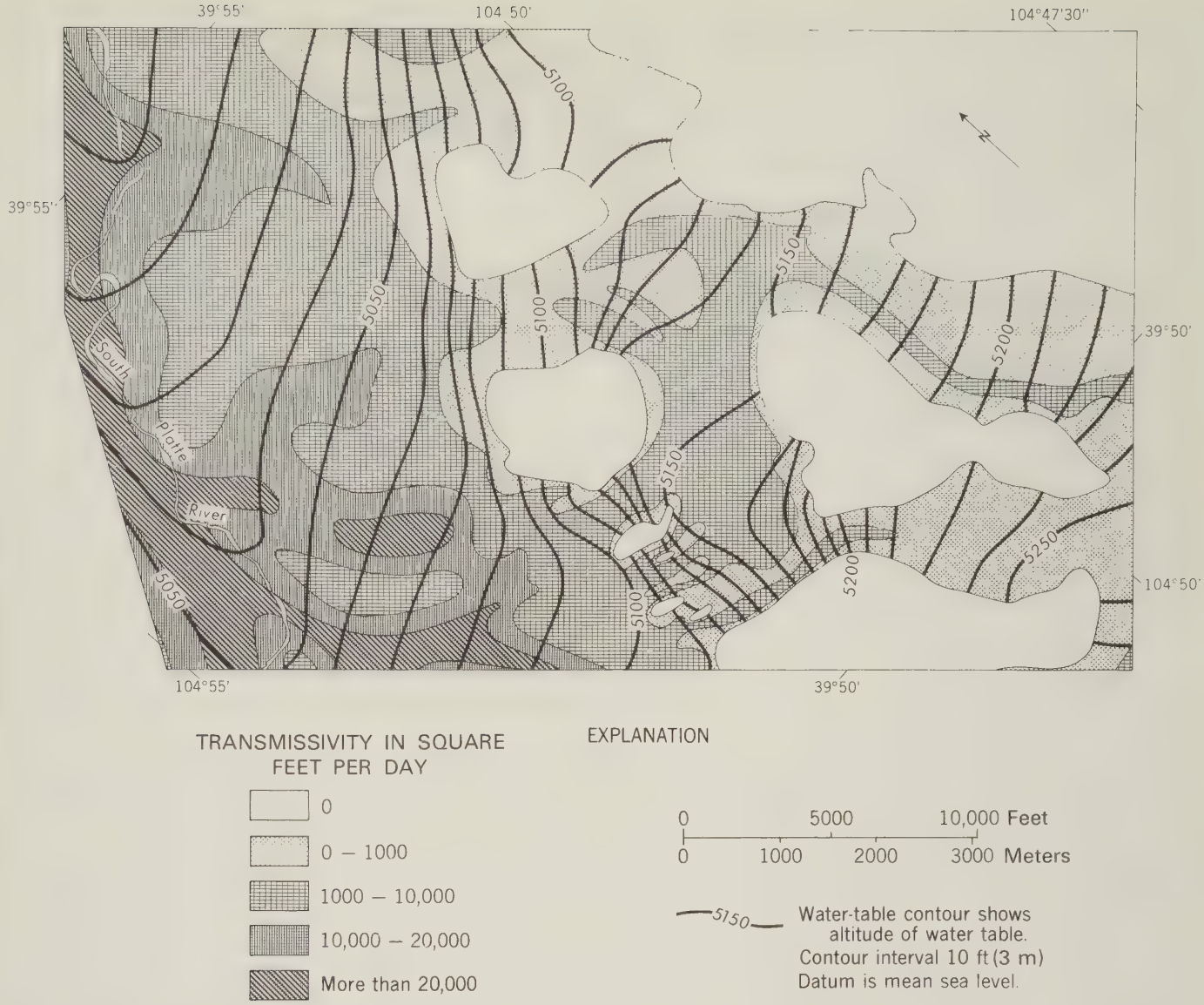

FIGURE 2.—Transmissivity and observed water-table configuration for a nonlinear problem (fieldwork and model design by Konikow, 1975). To convert transmissivity to square meters per day, multiply by 9.29×10^{-2}. To convert water-table contours to meters, multiply by 3.05×10^{-1}.

300 meters on a side. Constant-head conditions were imposed along the South Platte River and along the boundary where the aquifer extended beyond the limits of the modeled area. Forty-nine wells were used to represent discharge from farm wells and constant evaporation from ponds. The aquifer is recharged by infiltration from canals and irrigated areas.

By modifying the iterative methods (SIP, ADI, and LSOR), a solution was obtained with SIP (with $\beta<1$), and a potentially convergent sequence of intermediate values (heads at each iteration) was obtained for ADI and LSOR. For LSOR (or LSOR+2DC), an overrelaxation factor, ω, of 0.5 was used, and, although this is effectively "underrelaxation," it was necessary to obtain a reasonable intermediate solution. For ADI, it was necessary to (1) adjust the minimum iteration parameter, ω_{min}, (2) cycle the parameters from largest to smallest, and (3) weight the computed change in water level over a complete iteration (row and column calculation) to produce an effect similar to that of the β parameter in SIP.

A comparison of convergence rates is shown in figure 3, which depicts the absolute value of the maximum residual for each iteration versus computational work. Following Stone (1968), the SIP and ADI curves connect the smallest maximum residual for each cycle of

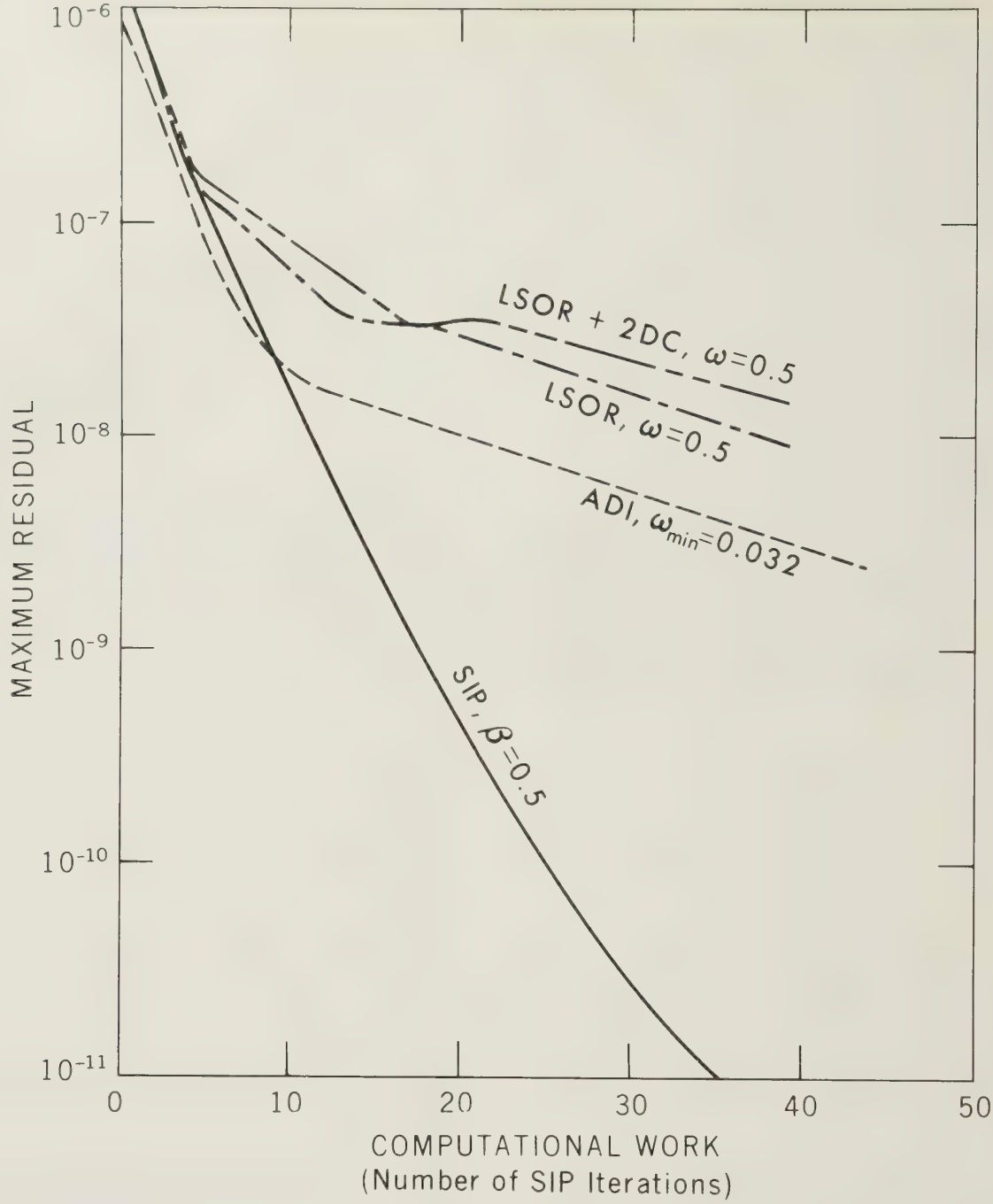

FIGURE 3.—Computational work required by different iterative methods for test problems.

iteration parameters. Each unit of work is equal to the time required to complete one SIP iteration. Relative work per iteration is about 1 for ADI, 0.6 for LSOR, and 0.8 for LSOR+2DC. A solution to this problem seems to be acceptable if the maximum residual is less than about 4×10^{-9}; thus, SIP, with $\beta=0.5$, is clearly the most effective method for this problem. Also, for ADI the difficulty in finding a convergent combination of iteration parameters and weighting factor further diminishes its utility.

Selection of an optimum value of β was made easily by trial, as shown in fig. 4. Solutions that eliminated only three or four grid blocks were reasonable, considering the hydrogeology of the problem; for $\beta>0.6$, either satisfactory convergence was not obtained or an excessive number of grid blocks were eliminated. By using $\beta=1$, more than 20 percent of the original 516 grid blocks were eliminated during the iteration process. Other water-table problems analyzed by the authors in which steady-state solutions were difficult to

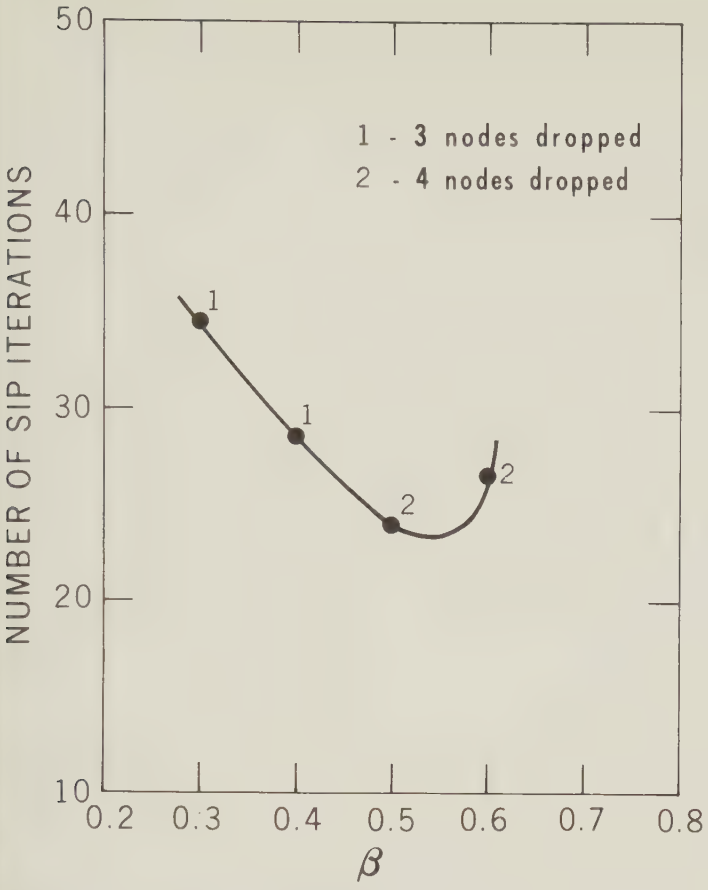

FIGURE 4.—Number of iterations required for solution of a nonlinear test problem by SIP using different values of β.

obtain with the standard iterative methods were easily solved by SIP, using a β parameter of about 0.5.

In addition to water-table aquifer simulations the solution of some linear problems can be expedited using the β parameter. A problem considered by Trescott, Pinder, and Larson (1976) was a hypothetical section with three horizontal layers. Each layer had a ratio of horizontal to vertical hydraulic conductivity of 100 to 1, and the middle layer was 1000 times less permeable than the other layers. However, the grid spacing was 100 times greater in the horizontal direction than in the vertical direction, resulting in a horizontal to vertical co-efficient ratio of 1 to 100. This anisotropy and the boundary conditions created small hydraulic gradients in some parts of the system, and a poor choice of initial head estimates resulted in slow convergence. Convergence was accelerated by selecting $\beta>1$, thus overestimating the residual vector at each iteration. In figure 5, a comparison of convergence rates for the steady-state solution indicates that SIP with $\beta=1.5$ is more efficient than standard SIP ($\beta=1$), and both are more effective than LSOR. Application of the two-dimensional correction to LSOR significantly improves its convergence rate. By experimenting with various minimum iteration parameters. ADI was made to converge as fast as SIP ($\beta=1.5$). Figure 6 illustrates the number of iterations required for a solution using different values of β. Divergence resulted for $\beta\geqq1.7$.

CONCLUSION

Use of an additional iteration parameter β has made SIP a powerful numerical technique for solving flow problems in water-table aquifers that can be described by nonlinear equations. Oscillations in the iteration scheme can be effectively controlled and excessive elimination of grid blocks can be prevented by selecting $\beta<1$. A value greater than 1 can also be used to expedite the convergence rate of SIP for problems involving strongly anisotropic conditions described by linear equations. In general, values of β are in the range, $0<\beta<2$ and are easily determined by trial.

Figures 5 and 6 follow "References Cited."

REFERENCES CITED

Aziz, K., and Settari, A., 1972, A new iterative method for solving reservoir simulation equations: Jour. Canadian Petroleum Technology, v. 11, no. 1, p. 62–68.

Bredehoeft, J. D., and Pinder, G. F., 1970, Digital analysis of areal flow in multiaquifer ground-water systems—A quasi three-dimensional model: Water Resources Research, v. 6, no. 3, p. 883–888.

Konikow, L. F., 1974, Modeling mass transport in a shallow aquifer: Am. Geophys. Union, Trans., v. 55, no. 4, p. 256.

——— 1975, Hydrogeologic maps of the alluvial aquifer in and adjacent to the Rocky Mountain Arsenal, Colorado: U.S. Geol. Survey Open-File Report 74–342, 17 p.

Peaceman, D. W., and Rachford, H. H. Jr., 1955, The numerical solution of parabolic and elliptic differential equations: Soc. Indus. Appl. Math. Jour., v. 3, no. 1, p. 28–41.

Remson, I., Hornberger, G. M., and Molz, F. J., 1971, Numerical methods in subsurface hydrology: New York, Wiley-Interscience, 389 p.

Stone, H. L., 1968, Iterative solution of implicit approximations of multi-dimensional partial differential equations: Soc. Indus. Appl. Math., Jour. Numerical Analysis, v. 5, no. 3, p. 530–558.

Trescott, P. C., Pinder, G. F., and Larson, S. P., 1976, Finite-difference model for aquifer simulation in two dimensions with results of numerical experiments: U.S. Geol. Survey Techniques Water Resources Inv., TWI 7–C1, 116 p.

Young, D. M., 1954, Iterative methods for solving partial differential equations of the elliptic type: Am. Math. Soc. Trans., v. 76, p. 92–111.

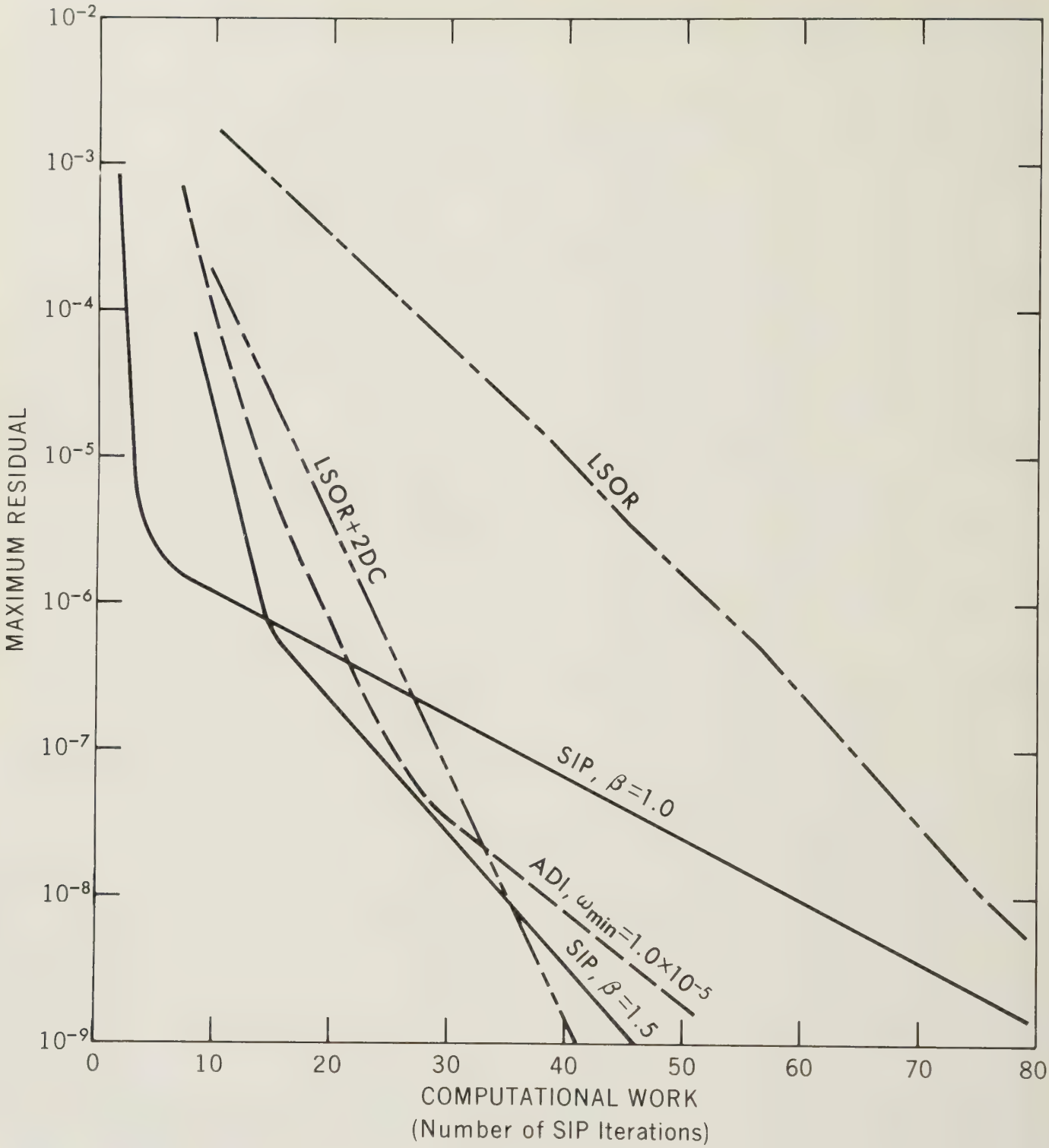

FIGURE 5.—Computational work required by different iterative techniques for a linear test problem.

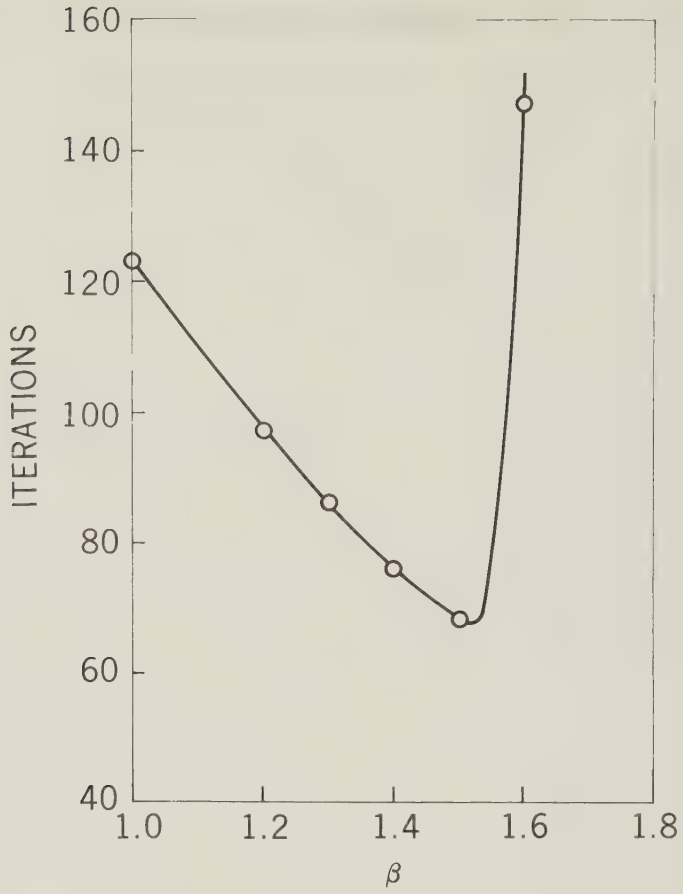

FIGURE 6.—Number of iterations required for solution of a linear test problem by SIP using different values of β.

Jour. Research U.S. Geol. Survey
Vol. 5, No. 6, Nov.–Dec. 1977, p. 823–834

QUALITY OF STORM-WATER RUNOFF FROM A RESIDENTIAL AREA, BROWARD COUNTY, FLORIDA

By H. C. MATTRAW, Jr., and C. B. SHERWOOD, Miami, Fla.

Prepared in cooperation with Broward County Water Management Division, Broward County Environmental Quality Control Board, and the Florida Department of Transportation

Abstract.—Rainfall, runoff, and water-quality information were collected in a 19.2-hectare single-family residential area in Broward County, Fla., between April 1974 and September 1975. During this period, 231 rainfall periods were recorded; 106 were large enough to produce runoff, and 30 were sampled for chemical analyses.

The fraction of rainfall that runs off is low, usually 5 to 10 percent. Several factors which combine to reduce runoff are the large area of pervious lawns (61 percent), the gentle slope of the area, and the use of grassy swales for routing storm water.

Bulk precipitation (rainfall plus dry fallout) quality is good by comparison to that of other metropolitan areas. As a consequence of the low runoff and the low concentrations of the bulk precipitation, loads for this residential area are small. Estimated annual load for chemical oxygen demand was 22.5 kilograms per hectare; total residue, 85.3 kg/ha; total nitrogen, 1.48 kg/ha; and total phosphorus, 0.21 kg/ha.

Numerous investigations of storm-water quality indicate that the particulate and dissolved material in urban runoff is a major cause of quality deterioration in receiving waters. This is noticeable in the densely populated coastal area of southeast Florida where most of the runoff enters flow-controlled canals of the regional water management system. This paper summarizes constituent concentrations and loads in runoff from a small drainage basin in northeast Broward County, Fla., from April 1974 through September 1975. The basin is occupied exclusively by single-family dwellings.

The 19.2-ha single-family residential area (fig. 1) was selected to measure concentrations and loads of major constituents in runoff—typical of a humid, subtropical environment. An automatic data collection system (Smoot and others, 1974) was used to measure rainfall and runoff and to collect samples. All three functions were recorded on a six-channel analog recorder. Chemical analyses were performed on 12 samples per storm period for 30 periods between April 15, 1974, and September 26, 1975. Loads computed for COD (chemical oxygen demand), total residue (dissolved plus suspended solids), total nitrogen, and total phosphorus were used to estimate annual loads of these entities.

The results reported here are part of an investigation of rainfall, runoff, and runoff quality in three "urban-type areas" in northeast Broward County. Similar information is also being collected at a highway site and at a commercial site by the U.S. Geological Survey in cooperation with Broward County and the Florida Department of Transportation. These pilot

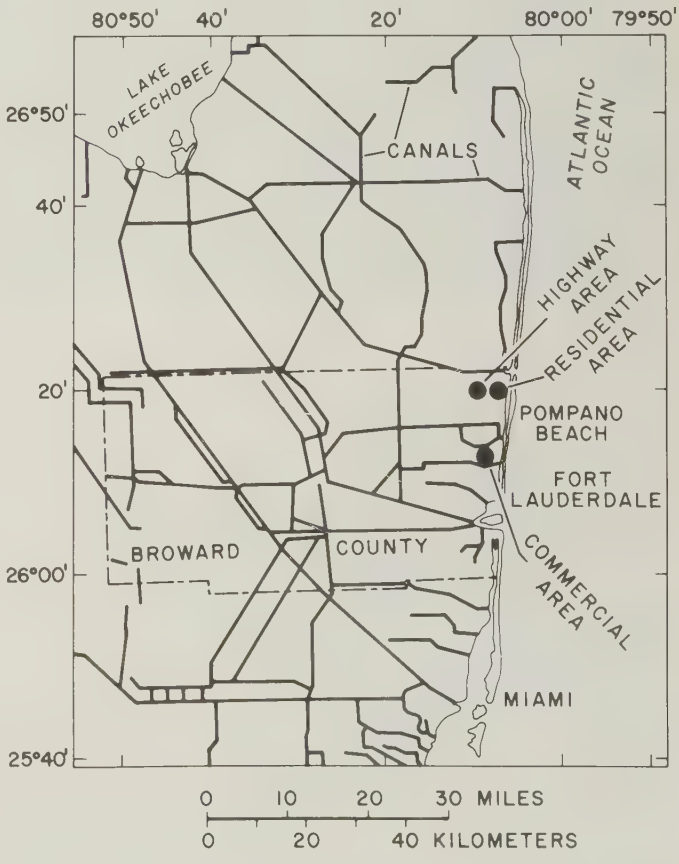

FIGURE 1.—Location of storm-water runoff areas in Broward County.

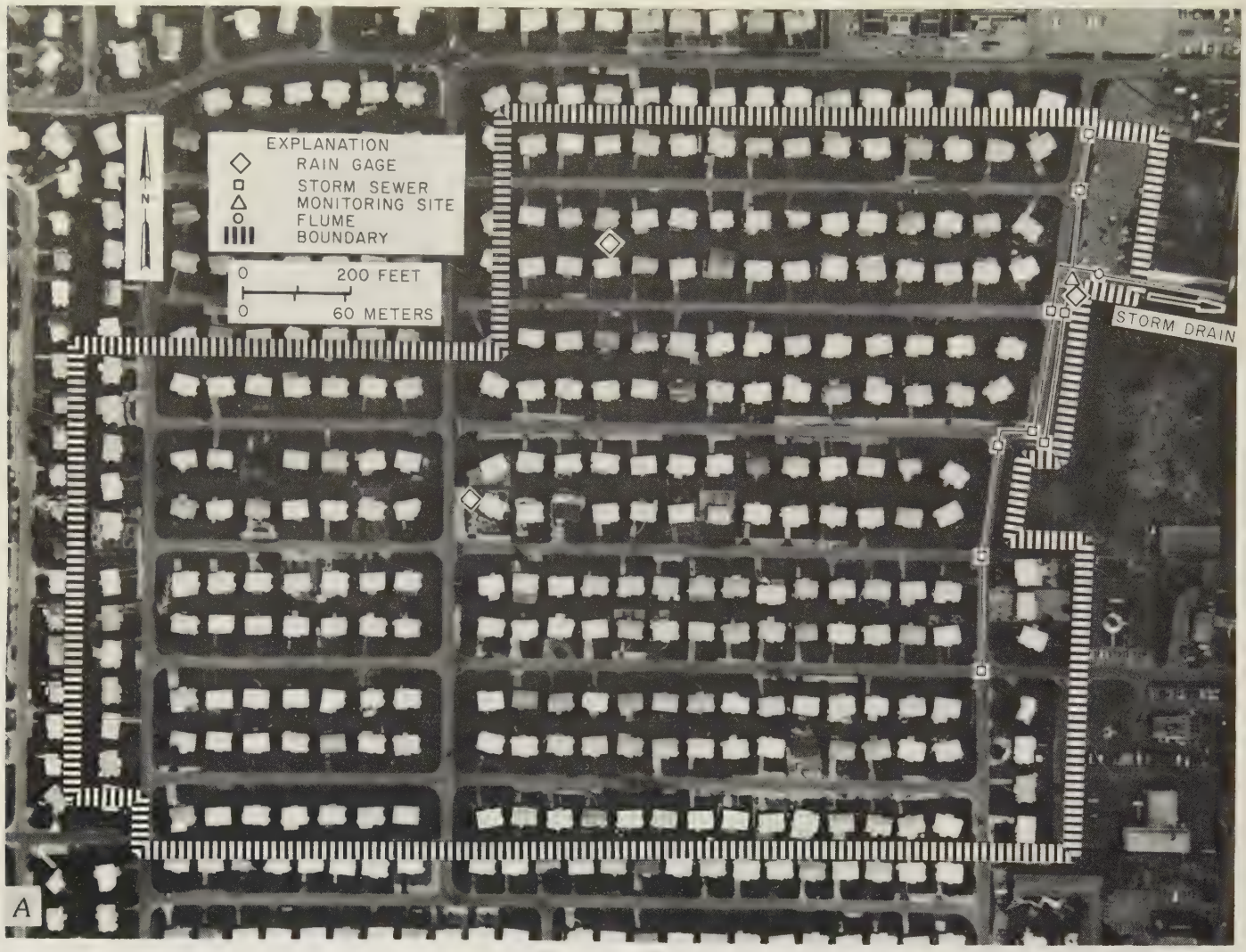

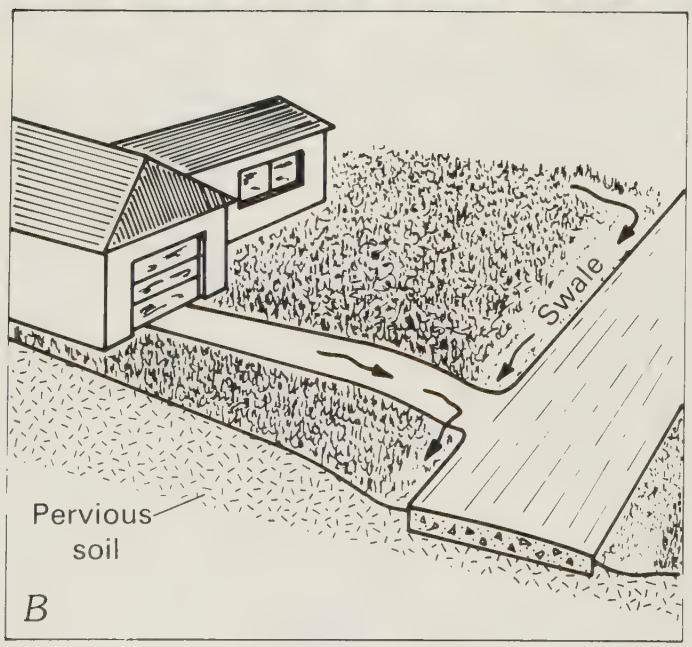

FIGURE 2.—Residential storm-water area. *A*, Plan view of basin. *B*, Typical residence showing swale-type drainage.

installations are a key element of the basic information needs recommended by the American Society of Civil Engineers (1969).

BASIN DESCRIPTION

This small drainage basin has an area of 19.2 ha. Figure 2 shows the basin and the salient drainage features. Land surface is flat and slopes gently eastward toward the coast. Storm water is routed eastward through grassy roadside swales (fig. 2*B*) into a sewer collector system along the east boundary of the area. The collector system feeds a 914-mm-diameter storm drain which flows eastward to a tidal waterway. The flume for monitoring flow is in the storm drain, approximately 18 m downstream from the end of the collection system. The instrument shed is located near

the junction of the collector and storm-drain lines (fig. 2*A*).

There are 239 concrete-block, single-family homes with approximately 600 residents within the drainage area. Most of the homes are 18 yr old. Little or no construction took place during the 17-month sampling period. The soil is a medium to fine quartz sand with good permeability and infiltration capacity. Most of the grass is a bermuda-grass muck sod laid on the native sand. Sixty-one percent of the area is grassed and is pervious, and 39 percent is covered by roofs, driveways, and roads (table 1).

TABLE 1.—*Land use in the residential area*

Land use	Acres [1]	Percent
House roofs	9.13	19
Driveways	4.42	9
Streets	5.15	11
Lawns	28.80	61
Total	47.50	100

[1] 1 acre=0.4047 ha.

INSTRUMENTATION

Instruments at the site recorded rainfall and runoff and activated the water sampler. These instruments were housed in a 2.7- × 3.7-m shed located adjacent to the 914-mm-diameter storm drain (fig. 2*A*). Rainfall and runoff data were recorded at 36-s intervals by a six-channel recorder.

Rainfall was recorded at three rain gages within the basin. Rainfall was measured on a 0.25-mm interval by commercial tipping bucket rain gages. The tips were relayed by commercial telephone lines to the recording system where they were accumulated and recorded. The signal from the first rain gage tip turned on the recording system and documented the time of the first tip.

Flow in the storm drain was computed from the continuous record of water pressure at a piezometer in the storm drain and a piezometer in a U-shaped venturi-type constriction. The piezometer in the storm drain is 1.5 m upstream from the piezometer in the constriction. The pressure measurement was obtained by gently bubbling nitrogen gas from the two piezometers. The gas pressure for a given water level in the storm sewer was converted to an electrical response by transducers. The responses (water depth) were printed on the recording chart. The gentle slope (0.00476) of the 914-mm-diameter storm drain precluded supercritical flow. The equation used to compute open-channel flow from the stage measurement in the storm drain is (J. Davidian, written commun., 1973)

$$\frac{Q}{D^5/2} = 1.034\left(1.2\frac{d_4}{D} + K - 0.191\right)^{1.756} \quad (1)$$

where Q = Discharge, in cubic meters per second,
D = Diameter of the pipe, in meters,
d_4 = Piezometer reading in storm drain, in meters, and
K = A constant for a particular installation, a function of pipe slope.

The stage records were converted to digital form (digitized) and entered into a programable calculator where the discharge computations were made by means of the above equation. The continuous record of discharge was printed, and a hydrograph was prepared by an accessory plotter to the calculator.

The continuous flow water-quality sampler system collects 24 2-L samples on a preset time interval. The duration of the interval between samples is adjustable in multiples of 36 s up to 144 s. Sampling was started by a preselected water-level reading on the upstream piezometer. Upon initiation of the sampling mode, storm water was continuously pumped through a distribution system. The sampler filled a 2-L polypropylene bottle in 10 s. The time of each sample was relayed back to the recorder. Between sample collection periods, the waste water flowed back to the storm drain. When the sample distributor had cycled through the 24 samples, a trip switch shut off the pump and collector system. The bottles were housed in a commercial freezer maintained at 4°C. Samples were retrieved and delivered to the laboratory for chemical analyses.

Bulk precipitation (dry fallout and rainfall) was collected with a 279-mm-diameter polypropylene funnel on the roof of the instrument shed. The height of the funnel is approximately 2.7 m above the road crown. Water ran through tygon tubing into a 2-L collection bottle in the freezer.

STORM-WATER DATA

Rainfall and runoff

Characteristically, southeast Florida is "dry" from November through May and "wet" from June through October. Figure 3 shows the monthly rainfall by months for the residential area for April 1974 through September 1975. From April 15, 1974, to September 26, 1975, a total of 231 rainfalls occurred. A rainfall is defined as any precipitation which is greater than 0.25 mm and which had 45 minutes of prior rain-free conditions. Flow was computed for 106 runoff periods, and runoff from 30 of the 231 rainfall periods was sampled. During the year, from June 1, 1974, to May

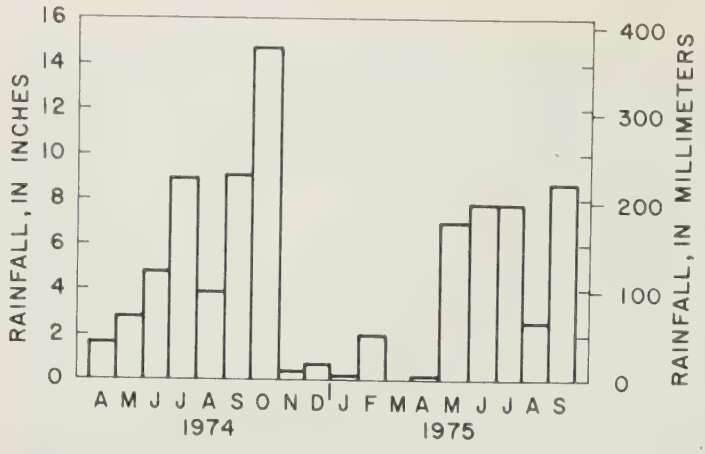

FIGURE 3.—Monthly rainfall for the residential area, April 1974 through September 1975.

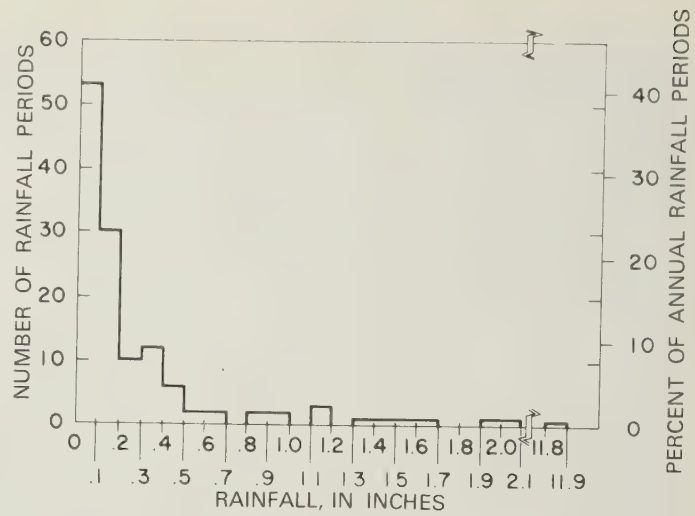

FIGURE 4.—Rainfall size frequency, June 1, 1974, to May 31, 1975.

31, 1975, approximately 41 percent of the rainfall periods were less than 2.5 mm (fig. 4).

The relation between runoff and rainfall for various storms between April 15, 1974, and September 26, 1975, is shown in figure 5. Usually, only 5 to 10 percent of the total rainfall ran off because of the flat terrain and permeable surficial sands.

Several design features in the residential area facilitate rainfall infiltration. There are no curbs and gutters in the area. Drainage is routed along the road edge and through grassy swales and is collected by sewers only along the eastern border of the area (fig. 2*A*). The storm-water flow path to the sewer collector system is long, and the very gentle slopes of the residential area encourage ponding and infiltration. Additionally, the roofs do not have gutters. Thus most of the roof runoff reaches the thick bermuda-grass muck-sod lawns.

Constituent concentrations

Maximum, minimum, and average concentrations of several constituents for samples collected during 30 storms, from April 15, 1974, to September 26, 1975, are listed in table 2. Maximum concentrations or values of

TABLE 2.—*Maximum, minimum, and average concentrations and analytical techniques used for measuring constituents in runoff samples collected during 30 storms, April 15, 1974, to September 26, 1975*

Parameter	Lab.*	Analytical Technique	Number of Samples	Average Value	Maximum	Minimum
Turbidity (JTU)	2	Spectrophotometric	344	12.8	70	3.0
Color (Pt.-Co Units)	2	Platinum-Cobalt Comparison	311	32.8	160	5.0
Specific conductance (mhos/cm)	1	Wheatstone bridge	621	98.9	350	5.5
Biochemical oxygen demand (mg/l)	1	5-day incubation	188	8.3	>18	1.9
Chemical oxygen demand (mg/l)	2	Titrametric	339	43.8	289	4.0
Total residue (mg/l)	2	Drying at 105°C	332	117	625	11.0
Dissolved residue (mg/l)	2	Drying dissolved solids at 105°C	331	89.7	574	9.0
Suspended solids (mg/l)	2	Drying filtrate	331	27.8	249	.0
Total nitrogen as N (mg/l)	2	Summation	290	1.93	11.5	.40
Total organic nitrogen as N(mg/l)	2	Digestion auto analyzer	344	1.23	9.4	.18
Total ammonia as N (mg/l)	2	Auto analyzer	342	.343	2.6	.01
Total nitrite as N (mg/l)	2	Auto analyzer	345	.051	1.5	.00
Total nitrate as N (mg/l)	2	Auto analyzer	344	.484	2.1	.00
Total phosphorus as P (mg/l)	2	Auto analyzer	344	.317	2.4	.06
Orthophosphate as P (mg/l)	2	Auto analyzer	345	.218	1.8	.03
Total carbon as C (mg/l)	2	Infrared analyzer	329	20.7	120	3.0
Total inorganic carbon as C (mg/l)	2	Infrared analyzer	329	5.96	17	1.0
Total iron (mg/l)	3	Atomic absorption	275	.317	5.3	.0

* Lab, laboratory; 1, Miami; 2, Ocala; 3, Atlanta.

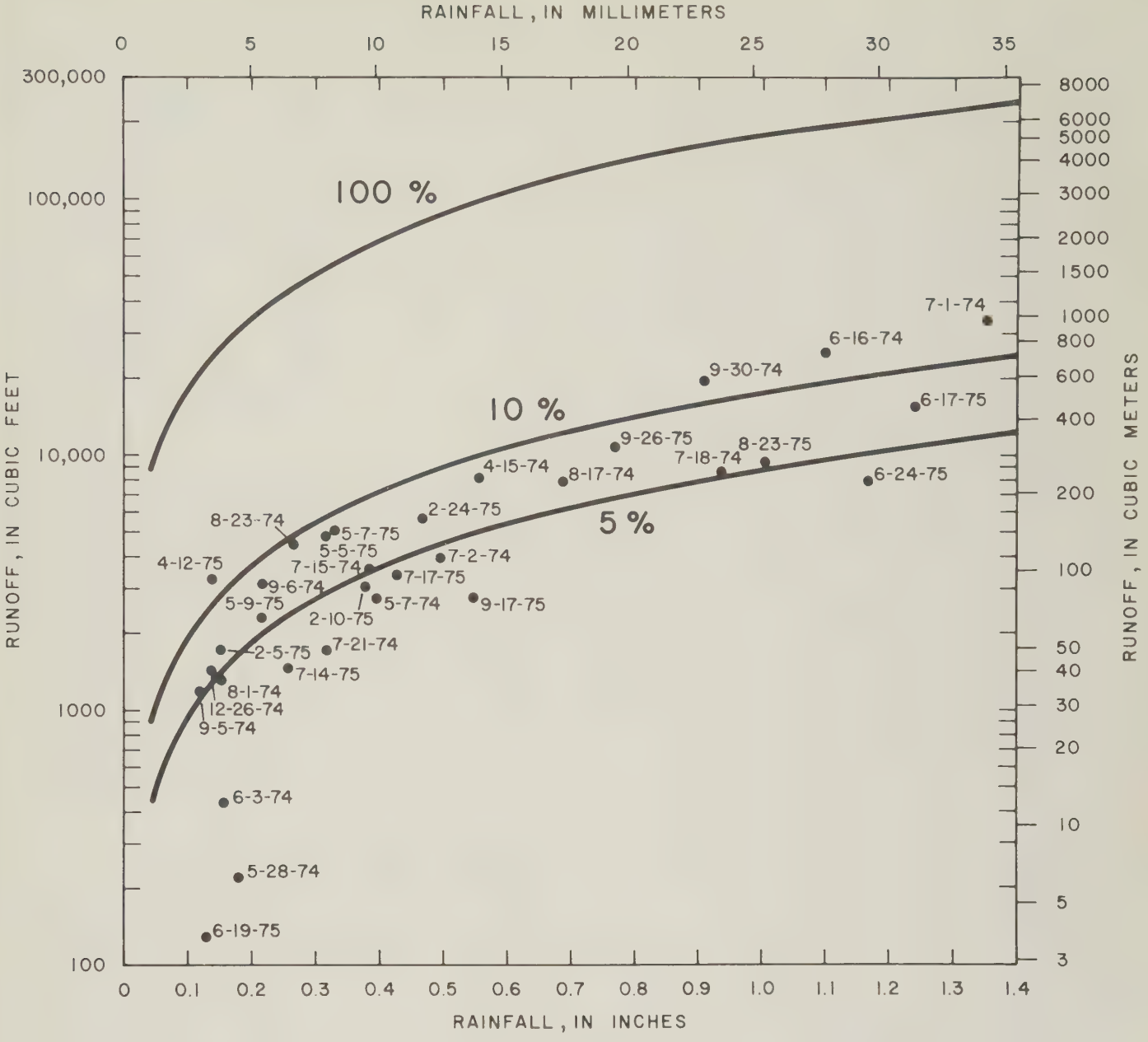

FIGURE 5.—Relation of runoff to rainfall in the residential area, April 15, 1974, to September 26, 1975.

the physical and chemical characteristics generally were five or more times greater than the average concentrations.

Concentrations of the several constituents analyzed in samples collected during individual storm periods were highest in April and May of 1974 and 1975 (table 3) resulting from the long periods of antecedent dry conditions in the spring. Typically, the concentrations of all analyzed constituents in the first samples of a runoff period are 10 to 50 percent higher than in samples collected later in the period.

Three samples of dry fallout and rainfall were collected (table 4). Thirty-five precipitation samples from Cincinnati, Ohio, (Weibel and others, 1966), had higher average concentrations than constituents observed in this investigation. Steps taken in the Cincinnati study minimized the dry fallout component. Concentrations of constituents in bulk precipitation at Pompano Beach, Fla., are low by comparison.

In general, the concentrations of the analyzed constituents were lower than the average concentrations in samples of runoff. However, the constituent levels

TABLE 3.—*Concentrations of selected constituents in runoff, April 1974 to September 1975*

[1 in = 25.4 mm ; 1 ft^3/s = 0.02832 m^3/s]

Date		Total Rain (inch)	Max. Discharge (ft^3/s)	Specific Conductance (micromhos/cm)	Total Nitrogen (N) (mg/l)	Organic Nitrogen (N) (mg/l)	Ammonia Nitrogen (N) (mg/l)	Total Nitrite (N) (mg/l)	Total Nitrate (N) (mg/l)	Total Phosphorus (P) (mg/l)	Biochemical Oxygen Demand (mg/l)	Chemical Oxygen Demand (mg/l)	Turbidity 1/	Total Residue (mg/l)	Total Filterable Residue (mg/l)	Suspended Solids (mg/l)	Total Carbon (C) (mg/l)	Color 2/
	Max.		4.1		3.9	3.1	0.14	0.06	0.80	0.88		290	47				38	80
Apr.	Min.				2.0	1.3	.02	.02	.45	.32		57	10				25	30
15	Avg.	0.56			2.4	1.7	.06	.03	.63	.50		150	20				32	38
	Max.		1.6	180	8.3	5.7	.82	.24	1.2	1.5		59	52	375	126	249	38	60
May	Min.			100	2.8	1.0	.50	.04	.46	.14		23	3	116	102	2	17	40
07	Avg.	.40		136	4.0	2.4	.59	.10	.76	.44		39	23	189	114	74	27	47
	Max.		0.19	186	4.4	2.1	1.4	.07	.93	.41	16	92	13	164	142	26	40	70
May	Min.			130	3.3	1.4	.97	.06	.76	.34	13	68	4	67	58	5	31	50
28	Avg.	.18		158	3.8	1.7	1.2	.07	.85	.37	15	78	7.9	124	114	11	36	61
	Max.		0.32	140	2.4	1.2	.40	.06	.88	.29	10	67	13	118	111	26	28	
June	Min.			76	2.1	.92	.32	.06	.74	.27	6.0	39	6	88	83	5	15	
03	Avg.	.16		100	2.3	1.1	.36	.06	.82	.27	8.2	54	8.4	102	93	14	22	
	Max.		1.8	79	2.0	1.9	.26	.03	.61	.47		54	14	140	78	62	29	30
June	Min.			59	.96	.38	.06	.02	.38	.17		13	8	72	53	19	7	20
15	Avg.	.39		65	1.5	.98	.19	.02	.47	.28		33	10.9	100	63	37	14	25
	Max.		19	47	1.2	1.0	.10	.02	.20	.28		15	16	114	51	63	7.0	15
June	Min.			40	.74	.47	.02	.01	.15	.13		5	4	54	26	21	3.0	5
16	Avg.	1.10		44	.91	.67	.06	.01	.17	.20		8	10	69	34	35	4.9	7.9
	Max.		3.3	105	1.7	1.1	.41	.02	.29	.22		42	12	112	74	45	13	5
July	Min.			60	.53	.27	.01	.01	.18	.11		4	4	40	34	2	4	5
02	Avg.	.50		85	.75	.44	.07	.07	.01	.13		14	8.2	77	54	23	7	5
	Max.		2.3	81	2.3	1.6	.25	.02	.83	.38	15	39	14	142	92	66	18	30
July	Min.			71	1.4	.78	.02	.02	.50	.15	10	22	8	11	52	3	10	20
15	Avg.	.39		76	1.7	1.0	.11	.02	.60	.26	13	30	11	89	69	33	14	25
	Max.		5.7	61	1.7	1.3	.11	.03	.34	.27	7.2	27	17	108	48	60	10	30
July	Min.			43	.48	.44	.01	.01	.19	.18	3.4	5	8	32	10	16	7	10
18	Avg.	.94		48	.88	.62	.03	.02	.23	.21	4.3	12	12	72	38	30	8	19
	Max.		0.83	110	2.2	1.4	.15	.05	.86	.20	12	61	8	115	106	16	21	50
July	Min.			74	.93	.45	.02	.03	.38	.14	6.5	34	3	9	50	2	13	30
21	Avg.	.31		88	1.4	.78	.07	.04	.58	.17	9.4	45	4.8	82	82	6.4	17	38
	Max.		.69	135	1.1	.83	.01	.03	.34	.37	12	58	16	94	52	57	25	20
Aug.	Min.			75	.75	.33	.01	.01	.17	.10	4.6	22	5	32	27	4	9	10
01	Avg.	.15		93	.80	.50	.01	.02	.28	.23	7.4	36	8.1	49	36	14	16	13
	Max.		4.4	86	1.8	1.2	.01	.02	.68	.58		64	20	142	72	70	18	30
Aug.	Min.			5	.97	.56	.01	.01	.38	.24		10		69	44	13	12	20
17	Avg.	.69		67	1.3	.84	.01	.02	.48	.38		28	11	88	59	29	15	25
	Max.		2.33	85	2.4	2.1	.06	.03	.26	.60	8.7	31	17	173	88	10	17	20
Aug.	Min.			7	.90	.56	.01	.01	.10	.14	3.8	10	5	73	58	7	6	10
23	Avg.	.27		66	1.1	.76	.03	.02	.19	.27	6.5	22	9.1	99	72	27	14	18
	Max.		0.53	122	1.9	1.6	.10	.03	.31	.24	9.9	69	11	140	124	35	32	45
Sept.	Min.			68	1.0	.77	.02	.01	.12	.13	3.6	26	4	82	68	5	16	10
05	Avg.	.12		106	1.3	.99	.05	.02	.24	.18	7.6	52	5.8	113	99	14	22	29
	Max.		1.5	62	1.8	1.6	.07	.03	.11	.16	3.3	22	9	103	68	35		10
Sept.	Min.			38	.40	.24	.01	.01	.06	.08	2.1	7	3	42	36	4	8	10
06	Avg.	.22		58	.63	.49	.03	.02	.09	.11	3.0	16	5.8	59	48	11	11	10
	Max.		14	76	1.5	.70	.18	.04	.59	.13	6.7	19	27	99	84	38	11	10
Sept.	Min.			42	.59	.23	.08	.01	.21	.08	2.2	7	5	25	20	5	5	10
30	Avg.	.91		56	.77	.44	.12	.02	.35	.09	4.8	13	10	50	34	14	7	10
	Max.		.72	220	2.3	1.7	.29	.04	.46	.44		88	15	148	132	42		
Dec.	Min.			130	1.1	.60	.04	.01	.01	.15		28	3	91	76	1		
26	Avg.	.14		162	1.5	1.1	.14	.02	.22	.22		49	7	119	102	17		
1975	Max.		.92	260	5.0	3.7	2.3	.10	.93	1.6	18	180	55	383	222	163	66	70
Feb.	Min.			115	2.9	1.6	.17	.07	.87	.31	13	56	15	159	138	20	21	40
05	Avg.	.15		172	3.8	2.2	.64	.08	.99	.75	15	104	31	240	162	78	33	58
	Max.		2.0	110	3.9	3.3	.17	.06	.41	.67	10	30	25	248	96	152	23	35
Feb.	Min.			70	1.1	.60	.01	.02	.31	.19	6.2	12	8	86	60	19	11	20
10	Avg.	.38		97	1.6	1.1	.10	.02	.37	.29	8.7	20	18	131	71	59	15	28
	Max.		2.1	100	1.6	1.4	.11	.02	.25	.50	9.0	49	70	127	72	71	15	30
Feb.	Min.			50	.69	.51	.01	.01	.12	.16	3.6	14	9	49	34	15	6	20
24	Avg.	.47		53	.92	.67	.04	.01	.16	.30	6.7	27	22	90	52	38	10	26
	Max.		.97	349	11	9.4	2.6	1.5	2.1	2.4		250	40	625	574	80	120	160
Apr.	Min.			135	5.9	2.3	.84	.06	0	.65		94	10	190	152	32	46	50
12	Avg.	.14		285	8.1	4.9	1.5	.46	1.1	1.4		165	25	302	250	52	76	114
	Max.		3.1	350	11	7.7	2.2	.08	1.3	.71	19	130	45	535	294	240	79	120
May	Min.			150	4.3	2.1	1.0	.06	.10	.39	17	32	15	169	110	19	32	40
05	Avg.	.32		204	5.8	3.5	1.5	.07	.84	.58	17	66	22	258	188	70	46	79
	Max.		3.6	116	4.7	2.7	1.3	.06	.68	.49		30	30	322	264	58	36	50
May	Min.			84	2.5	.85	1.1	.05	.42	.18		14	10	92	78	9	17	30
07	Avg.	.33		100	3.0	1.3	1.2	.05	.52	.30		20	19	140	114	25	24	44
	Max.		.35	185	4.5	2.6	1.2	.13	1.0	.45		52	20	188	150	52	39	70
May	Min.			123	3.2	1.5	.83	.08	.58	.27		24	7	108	98	8	19	30
09	Avg.	.22		168	3.8	1.9	1.0	.09	.84	.35		42	12	156	134	18	2.9	58
	Max.		8.2	122	2.7	2.1	.10	.14	.59	.40		53	40	329	250	79	20	40
June	Min.			62	1.5	.97	.01	.02	.32	.21		13	7	114	106	3	9	20
17	Avg.	1.24		79	1.8	1.3	.05	.03	.46	.28		26	18	198	150	33	12	29
	Max.		.27	195	1.0	.68	.03	.04	.32	.25	8.4	36	20	186	174	21	16	40
June	Min.			53	.76	.51	.01	.03	.15	.07	3.6	28	9	133	112	2	12	25
19	Avg.	.13		84	.83	.57	.02	.04	.21	.16	5.7	32	13	155	144	10	14	32
	Max.		3.0	76	2.3	1.2	.07	.03	1.1	.13	6.2	24	15	65	48	23	9.0	20
June	Min.			52	.51	.18	.02	.02	.26	.07	2.6	7	7	11	9	2	5.0	20
24	Avg.	1.17		60	.85	.39	.04	.02	.38	.08	4.3	12	12	37	25	11	6.4	20
	Max.		1.1	88	.64	.49	.02	.01	.14	.09			8	76	64	12	12	5
July	Min.			46	.50	.34	.01	.0	.10	.06			5	32	32	0	6.0	5
14	Avg.	.26		59	.57	.43	.01	.01	.12	.07			7	57	51	5	10	5
	Max.		4.2	57	1.1	.88	.03	.01	.23	.21		38	15		98	19	9.0	10
Aug.	Min.			34	.29	.14	.01	0	.12	.09		10	6		38	5	3.0	5
23	Avg.	1.01		40	.52	.34	.02	0	.16	.12		16	10		58	9	5.1	8
	Max.		1.0		1.0	.74	.07	.02	.20	.27	5.2	30	20	80	66	20	17	30
Sept.	Min.				.60	.37	.02	.01	.18	.15	1.9	16	8	67	54	4	10	20
17	Avg.	.55			.74	.49	.04	.01	.19	.20	3.5	21	12	72	60	12	13	23
	Max.		8.1		2.5	1.8	.27	.02	.40	.53		30	25	94	70	40	12	10
Sept.	Min.				.61	.40	.03	.01	.17	.17		2	5	49	40	3	7	5
26	Avg.	.77			1.5	1.1	.13	.01	.26	.30		17	13	63	50	13	9	9

1/ Jackson Turbidity Units.
2/ Platinum-Cobalt Units.

TABLE 4.—*Rainfall and dry fallout quality*

	8-23-75	9-17-75	9-26-75
Inches[1] of rainfall	1.01	0.55	0.77
Antecedent dry period (h)	50	191	179
Color (Pt-Co Units)	5	5	10
Turbidity (JTU)	7	4	4
COD (mg/l)	22	12	4
Total residue (mg/l)	22	18	24
Suspended solids (mg/l)	4	2	10
Total nitrogen as N (mg/l)	.30	.84	.29
Organic nitrogen as N (mg/l)	.15	.09	.12
Ammonia as N (mg/l)	.01	.01	.04
Nitrite as N (mg/l)	.00	.01	.01
Nitrate as N (mg/l)	.14	.73	.12
Total phosphorous as P (mg/l)	.01	.02	.05
Orthophosphate as P (mg/l)	.01	.01	.03
Total carbon as C (mg/l)	3	3	2
Organic carbon as C (mg/l)	1	3	2
Inorganic carbon as C (mg/l)	2	0	0

[1]1 in = 25.4 mm.

indicate that a significant portion of most parameters in runoff is derived from rainfall and dry fallout. In two of three samples one of the constituents analyzed was higher than the average concentration in runoff. The COD (table 4) for the August 23, 1975, sample of bulk precipitation was 22 mg/L while the average COD concentration of runoff (table 3) was 16 mg/L. On September 17, 1975, the bulk precipitation concentration of nitrate was 0.73 mg/L. The average nitrate concentration in runoff was 0.19 mg/L.

Six metals were chosen for analyses (table 5). Concentrations of cadmium, chromium, and copper never exceeded 41 μg/L in runoff samples from eight selected storm periods. Concentrations of iron and lead were generally above 100 μg/L, and each exceeded 1 mg/L on one occasion. Iron values observed in the storm-water runoff are very similar to concentrations observed in surface water samples throughout southeast Florida (Goolsby and others, 1976). Concentrations of lead in the storm water (30–1100 μg/L) were 10 or more times higher than surface water in southeast Florida. However, the lead concentrations were lower than those reported by other investigators. In a study of storm-water runoff quality in Durham, N.C., Bryan (1974) reported a range of lead concentrations from 12 800 μg/L to less than 100 μg/L.

Samples from seven storms were transferred in ice chests to the Miami laboratory of the Geological Survey and filtered for bacteria less than 6 h after collection. The samples were filtered through 0.45-μm filters and incubated at the appropriate temperatures for determination of total coliform, fecal coliform, and fecal streptococci. Table 6 shows the number of samples and the maximum, minimum, and median colony counts per 100 mL. Total coliforms determined for this investigation (24 000-1 800 000 colonies/100 mL) are higher than those observed by Bryan (1971) in Durham, N.C. These high bacteria counts may be associated with the warm humid climate of southeast Florida. Values of bacteria in the runoff are two orders of magnitude greater than existing Florida

TABLE 5.—*Range and average metal concentrations in runoff, in micrograms per liter*

	Cadmium			Chromium		Copper			Iron			Lead			Zinc		
Date	Max	Min	Avg	Max	Min	Max	Min	Avg	Max	Min	Avg	Max	Min	Avg	Max	Min	Avg
5/ 5/75	6	1	2.4	20	<10	41	13	20	1500	200	625	760	270	424	560	100	184
5/ 9/75	2	1	1.3	10	<10	23	9	13	500	210	288	1100	140	249	260	80	151
6/17/75	1	0	.7	10	<10	10	5	6.7	620	60	207	310	30	122	150	30	68
6/23/75	1	0	.4	<10	<10	8	3	5.7	190	50	102	220	85	119	160	10	63
7/14/75	1	0	.3	<10	<10	11	5	7.6	250	40	93	140	64	89	70	20	42
8/23/75	1	0	.2	10	<10	5	1	2.8	210	60	122	130	35	91	80	30	53
9/17/75	0	0	0	10	10	9	4	5.8	170	0	75	240	83	128	110	40	64
9/26/75	3	0	1.4	<10	<10	11	0	4.8	360	20	98	310	56	114	160	40	69
Southeast Florida Surface Water	12	0	.7	80	<10	90	0	5.0	2800	0	231	56	0	7.0	380	0	28
Durham, N.C. (Bryan 1974)												12600	<100	480			

TABLE 6.—*Summary of bacterial analyses, in colonies per 100 mL*

	Total Coliform				Fecal Coliform				Fecal Streptococci			
Date	n*	Max.	Min.	Med.	n*	Max.	Min.	Med.	n*	Max.	Min.	Med.
5/28/74	16	210,000	35,000	92,000	4	47,000	22,000	30,000	4	79,000	31,000	57,000
6/ 3/74	16	1,780,000	206,000	570,000	19	490,000	72,000	290,000	21	125,000	60,000	100,000
7/21/74	6	320,000	42,000	170,000	6	79,000	10,000	24,000	6	18,000	5,000	9,000
7/31/74	6	950,000	68,000	170,000	6	23,000	4,000	12,000	6	101,000	25,000	40,000
8/23/74	6	1,800,000	340,000	1,000,000	6	62,000	12,500	35,000	5	102,000	49,000	79,000
6/19/75	6	140,000	24,000	35,000	6	45,000	1,000	14,000	6	23,000	7,000	12,500
7/17/74	4	70,000	35,000	37,500	4	9,000	4,000	5,500	4	46,000	17,000	26,500

* n = number of samples.

State standards (2400 colonies/100 mL) for surface waters (Florida Administrative Code, 1972).

Fecal coliform and fecal streptococci bacterial counts are very similar to those from the Plantation Hills development in Knoxville, Tenn. (Betson and Buckingham, 1970). However, unlike the Knoxville results, the fecal coliform (FC) to fecal streptococci (FS) ratio in this study is highly variable. It should be noted that there is approximately one dog to every four people in southeast Florida and that the excrements from the dogs may be a major source of the high bacteria counts. The highly variable FC/FS ratio may be a result of different die-off rates for the two bacteria populations or variations in the contributing

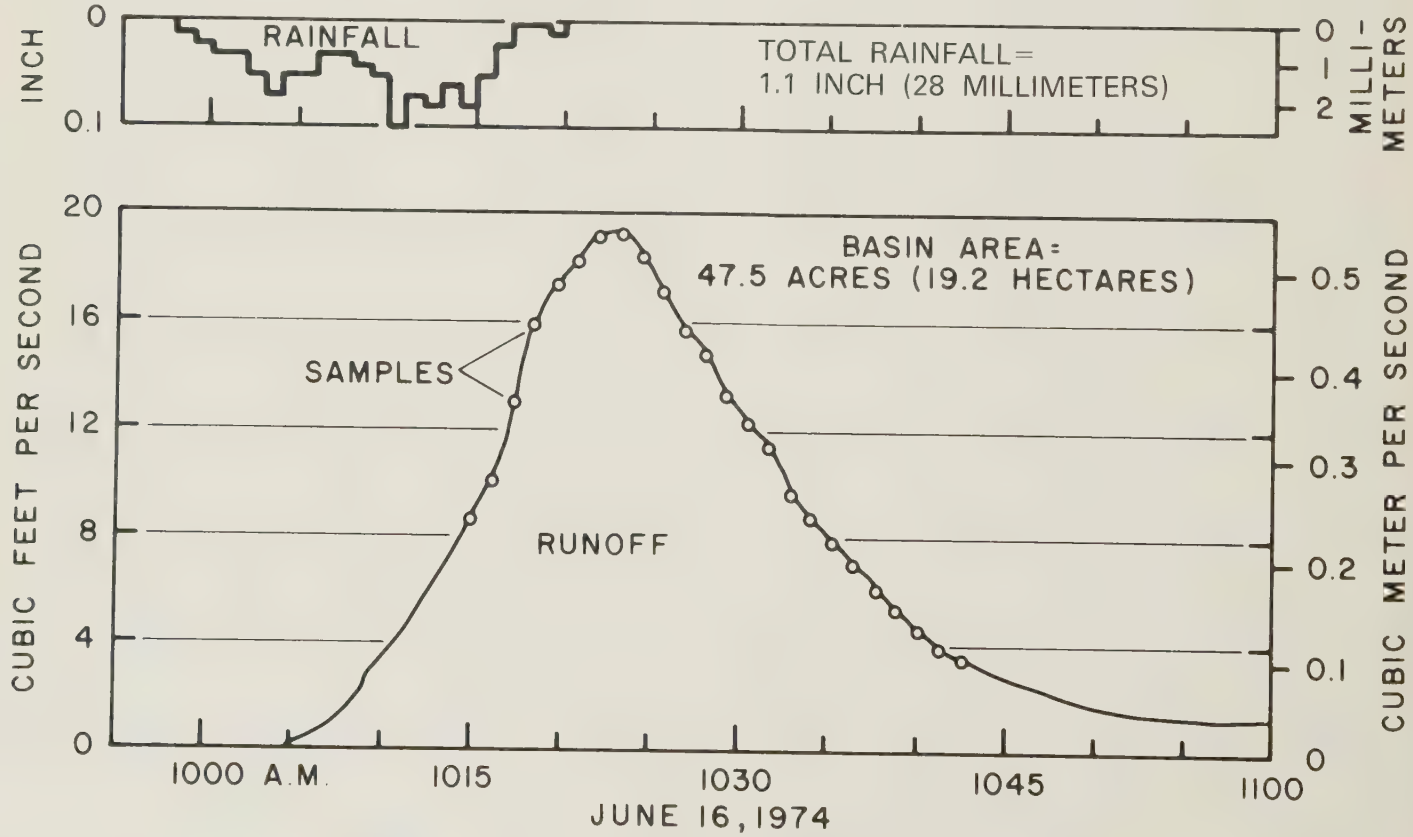

FIGURE 6.—Rainfall, runoff, and sampling sequence, June 16, 1974.

animal populations; other animal sources that may be significant bacteria contributors include cats and pigeons.

ANALYTICAL RESULTS

The quality or chemical purity of storm-water runoff is affected by many hydrologic variables. Those thought to be most important are physical characteristics of the watershed, duration of the antecedent precipitation conditions, amount of rainfall-runoff, and rainfall intensity.

An example of data on rainfall, runoff, and constituent concentration and load for a rainfall on June 16, 1974, is shown in figures 6 and 7. Total rainfall depth was 28 mm, peak discharge was about 0.5 m^3/s, and samples were collected at 72-s intervals. Light rainfall began at 0955 and increased sharply at 0957. Flow in the storm sewer became appreciable at 1005. The 8- to 10-min time lag is due to basin storage caused by the gentle slope and the swale-type drainage in the residential area. The concentrations of total nitrogen in 12 samples collected during runoff are superimposed on the discharge hydrograph in figure 7. Total nitrogen concentrations were highest, 1.2 mg/L, in the first sample collected, and lowest, 0.69 mg/L, in a sample collected at 1036, during the latter part of the runoff. The load of nitrogen in pounds is obtained by multiplying the discharge, the number of seconds in the sampling interval, the concentration of nitrogen for the sample collected in that interval, and 6.24×10^{-5}, a conversion factor. The total nitrogen load for the storm period is the sum of pounds for each interval. Samples were collected during 87 percent of the runoff volume. The concentrations in the initial and later runoff were estimated by using the concentration of the appropriate adjacent sample.

The total nitrogen load in runoff for the rainfall of June 16, 1974, was about 0.7 kg. Although the concentration of nitrogen was greatest in the early samples, the instantaneous load was greater during the

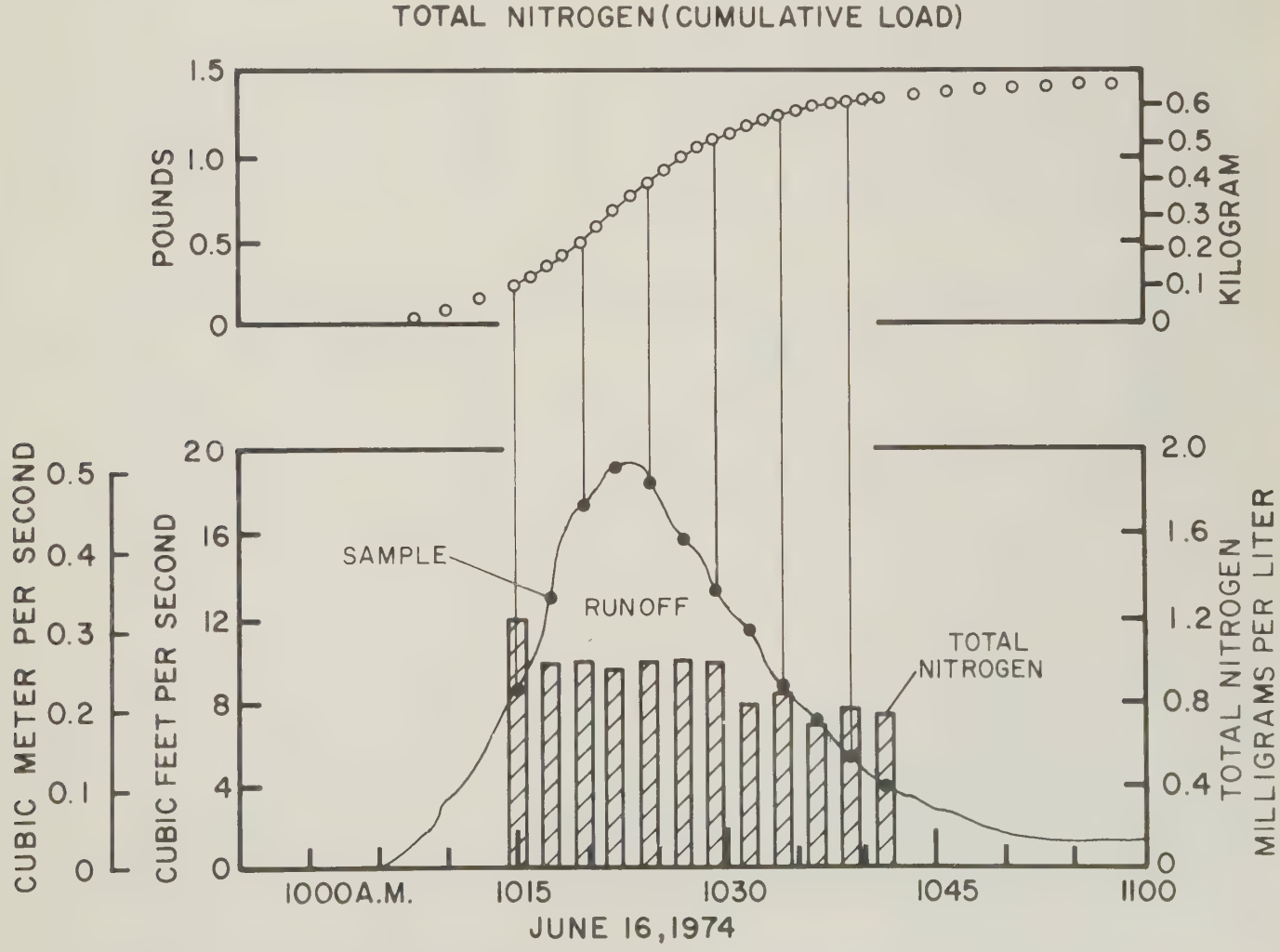

FIGURE 7.—Concentration and cumulative load of total nitrogen in runoff from a rainfall period, June 16, 1974.

peak flow period. The total load was influenced most by the total volume of runoff. Runoff from this storm also contained 0.15 kg of phosphorus, 5.4 kg of COD, and 50 kg of total residue.

The variation in constituent levels from one storm to another was even greater than the variation during individual storms. In general, concentrations of most constituents were greatest in runoff from storms which occurred after long dry periods and least during periods of frequent and heavy rainfall. The normal rainy season in south Florida is June through October; rainfall during the rest of the year is sporadic. The rainfall of June 16, 1974, was one of many frequent, intense rains, and the concentrations of chemical constituents in runoff samples were among the lowest observed (table 3). The relation between rainfall and nitrogen concentrations during April 1974 through September 1975 (fig. 8) shows that nitrogen concentrations were greatest in May after a period of little or no rainfall during February to April and decreased sharply in May to July as rainfall increased.

Runoffs from 30 rainfall periods between April 15, 1974, and September 26, 1975, were sampled and analyzed for chemical constituents. Table 7 shows the sampling date, inches of rainfall, the computed discharge (runoff), the percentage of the total flow that was sampled, and computed loads of COD, total residue, total nitrogen, and total phosphorus. The loads of COD were greatest in April 1974 and April 1975. This is again an indication of the influence of the seasonal dry period; also important is the volume of the runoff period.

Estimated monthly and annual loads for COD, total residue, total nitrogen, and total phosphorus are listed in table 8. Although all rainfall and runoff from the site were measured, not all the runoff was sampled. The method used to obtain monthly loads is based on an extrapolation from the rainfall and computed loads for runoff from the storms sampled during that month. Loads for the month are based on the rainfall periods large enough to produce runoff.

During individual storm periods the heaviest constituent loads per unit of rainfall occurred in runoff during the dry season when constituent levels are highest. However, in a year of normal rainfall distribution, the greatest rainfall and the largest loads would occur during the wet season. During the year shown in table 8, high loads occurred during October 1974 and May 1975 because of above average rainfall.

SUMMARY

A 19.2-ha single-family residential area in Broward County, Fla., was selected to evaluate storm-water quality. Rainfall, runoff, and water-quality information were collected between April 1974 and September 1975.

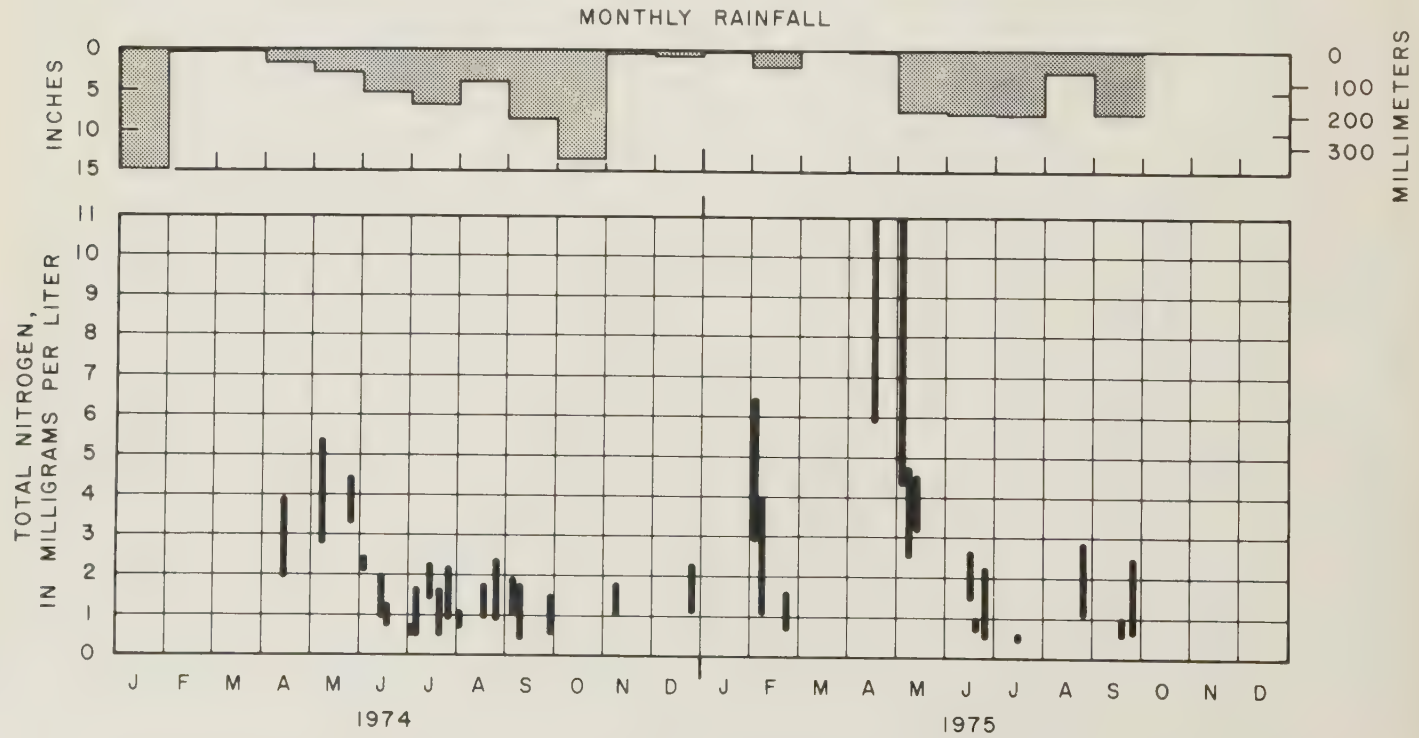

FIGURE 8.—Range of total nitrogen concentrations and monthly rainfall, April 1974 through September 1975.

TABLE 7.—*Computed loads of COD, total residue, total nitrogen, and total phosphorus*
[1 in = 25.4 mm ; 1 ft³ = 0.02832 m³ ; 1 lb = 0.4536 kg]

Date	Rainfall (inches)	Discharge (cubic feet)	Percentage of flow with samples	COD[1]	TR[2]	TN[3]	TP[4]
4-15-74	0.56	8,200	39	64.	-	1.28	0.323
5- 7-74	.40	2,790	21	8.4	21.9	.53	.077
5-28-74	.18	227	61	1.2	1.8	.05	.005
6- 3-74	.16	435	77	1.5	3.0	.07	.007
6-16-74	1.10	25,200	87	12.0	110	1.48	.320
7- 2-74	.50	3,910	99	4.5	19.6	.21	.035
7-15-74	.39	3,560	58	7.8	13.8	.36	.063
7-18-74	.94	8,270	65	4.2	33.1	.41	.101
7-21-74	.31	1,750	90	4.9	9.2	.15	.019
8- 1-74	.15	1,320	73	3.2	4.9	.09	.018
8-17-74	.69	8,110	93	19.7	55.1	.74	.191
8-23-74	.27	4,580	67	6.2	25.3	.25	.063
9- 5-74	.12	1,220	59	4.3	9.1	.10	.016
9- 6-74	.22	3,180	57	2.8	10.0	.10	.021
9-30-74	.91	19,300	85	13.5	49.7	.92	.104
12-26-74	.14	1,410	90	5.1	10.4	.13	.021
2- 5-75	.15	1,730	93	12.5	28.8	.47	.080
2-10-75	.38	3,130	76	3.8	25.9	.32	.065
2-24-75	.47	5,910	36	7.1	29.1	.28	.087
4-12-75	.14	3,320	53	32.3	65.7	1.62	.251
5- 5-75	.32	4,850	90	17.8	74.2	1.73	.179
5- 7-75	.33	5,130	87	7.0	44.0	.96	.111
5- 9-75	.22	2,300	47	4.4	19.0	.52	.049
6-17-75	1.24	15,600	94	23.7	210	1.73	.248
6-19-75	.13	130	100	0.3	1.3	.01	.001
6-24-75	1.17	8,130	78	6.3	20.1	.36	.041
7-14-75	.26	1,510	100	1.6	5.3	.06	.007
8-23-75	1.01	9,880	91	8.4	40.2	.29	.359
9-17-75	.55	2,860	88	4.3	13.2	.15	.034
9-26-75	.77	11,000	97	11.3	47.2	.77	.164

[1]COD = pounds of chemical oxygen demand.
[2]TR = pounds of total residue.
[3]TN = pounds of total nitrogen (as N).
[4]TP = pounds of total phosphorus (as P).

Rainfall was measured to 0.25 mm by commercial tipping bucket rain gages. Telephone lines relayed rainfall data to a nearby recorder. Flow was measured in a 914-mm-diameter storm drain. Twenty-four water-quality samples were collected at intervals of either 72 or 144 s. The master recorder unit recorded rainfall, pressure, and time of water-quality sampling.

Between April 15, 1974, and September 26, 1975, 231 rainfall periods were recorded at the residential study site; 106 were large enough to produce runoff, and 30 were sampled and analyzed for chemical constituents. The fraction of rainfall that ran off was low, usually 5 to 10 percent. Several factors which combined to reduce runoff were the large area (61 percent) of pervious lawns, the gentle slope of the area, and the use of grassy swales for routing storm water.

Bulk precipitation (rainfall plus dry fallout) quality was good in comparison to that of other metropolitan areas. As a consequence of the low runoff and the low concentrations in the bulk precipitation, loads for

TABLE 8.—*Estimated monthly and annual loads of COD, total residue, total nitrogen, and total phosphorus, from June 1, 1974, to May 31, 1975*

[1 in = 25.4 mm; 1 lb = 0.4536 kg; 1 lb/acre = 112.1 mg/m² = 1.121 kg/ha]

	Month	Sampled Rainfall inches	Total* Monthly Rainfall inches	Sampled COD Measured in pounds	Estimated Monthly COD in pounds	Sampled Total Residue Measured in pounds	Estimated Monthly Total Residue in pounds	Sampled Total Nitrogen Measured in pounds	Estimated Monthly Total Nitrogen in pounds	Sampled Total Phosphorus Measured in pounds	Estimated Monthly Total Phosphorus in pounds
Wet	June 1974	1.26	4.35	13.5	47	113	390	1.55	5.4	.327	1.1
	July	2.36	8.46	24.6	88	80.6	290	1.22	4.4	.236	.85
	August	.96	3.47	25.9	94	80.4	290	.99	3.6	.254	.92
	September 1/	1.25	8.96	20.6	150	68.8	490	1.12	8.1	.141	.99
	October 2/	(1.25)	13.93	(20.6)	230	(68.8)	770	(1.12)	13	(.141)	1.60
	November 2/	(.14)	.30	(5.1)	11	(10.4)	22	(.13)	.29	(.021)	.05
	December	.14	.71	5.1	26	10.4	53	.13	.66	.021	.11
	Jan. 1975 3/	(.57)	.13	14.3	3.3	47.1	11	.60	.14	.127	.03
Dry	February	1.00	1.78	23.4	42	83.8	150	1.07	1.9	.232	.41
	March	0.00	.00	.0	.0	.0	.0	.0	.0	.0	.0
	April	.14	.14	32.3	32	65.7	66	1.62	.23	.251	.04
	May	.87	6.95	29.2	230	137	1100	3.21	26	.339	2.7
	Annual total	8.00	49.44		953		3630		63.7		8.8
	Pounds/acre				20.1		76.4		1.34		.185

* Total inches of monthly rainfall for storms larger than 0.09 inch.
1/Used September 1974 rainfall and load.
2/Used December 1974 rainfall and load.
3/Used average December 1974 and February 1975 rainfall and load.

this residential area were small. Estimated annual load for COD was 22.5 kg/ha; total residue, 85.3 kg/ha; total nitrogen, 1.48 kg/ha; and total phosphorus, 0.21 kg/ha. (Note: 1 kg/ha = 10^2 mg/m².)

REFERENCES CITED

American Society of Civil Engineers, 1969, Basic information needs in urban hydrology: 112 p.

Betson, R. P., and Buckingham, R. A., 1970, Fecal coliform concentrations in stormwaters: Am. Geophys. Union, Ann. Mtg. 51st, Washington, D.C., Apr. 20–24, 1970, 20 p.

Bryan, E. H., 1971, Quality of stormwater drainage from urban land: Am. Water Resources Conf., 7th, Washington, D.C., Oct. 28, 1971, 11 p.

——— 1974, Concentrations of lead in urban stormwater: Jour. Water Pollution Control Federation, v. 46, no. 10, p. 2419–2421.

Florida Administrative Code, 1972, Rules of the Department of Pollution Control: Pollution of Waters, Supp. No. 25, Chap. 17–3, p. 7–12A.

Goolsby, D. A., Mattraw, H. C., Lamonds, A. G., Maddy, D. V., and Rollo, J. R., 1976, Analysis of historical water-quality data and description of a plan for a sampling network in central and southern Florida: U.S. Geol. Survey Water-Resources Inv. 76–52, 124 p.

Smoot, G. F., Davidian, J., and Billings, R. H., 1974, Urban storm rainfall runoff-quality instrumentation: Internat. Assoc. Sci. Hydrology, Pub. 112, p. 44–47.

Weibel, S. R., Weidner, R. B., Cohen, J. M., and Christianson, A. G., 1966, Pesticides and other contaminants in rainfall and runoff: Jour. Am. Water Works Assoc., v. 58, no. 8, p. 1075–1084.

ANNUAL INDEX TO VOLUME 5

Journal of Research of the U.S. Geological Survey

[Issue number precedes colon : page number follows colon]

SUBJECT INDEX

Page

A

Activity-product constants of brucite, experimental and calculated, from 10° to 90°C ---------- 2:227

Age determination, alkalic and mafic rocks in south-central Colorado ---------- 6:673

intrusive rocks, Alaska---- 2:155

metamorphic rocks, Alaska- 2:173

plutonic and structural history, Santa Catalina and Tortolita Mountains, Ariz ---------- 6:705

Precambrian W Puritan Quartz Monzonite, Michigan ---------- 2:185

prehistoric mudflows, California ---------- 1:17

uranium ore, Dakota Sandstone -------- 6:669

young minerals, effect of initial radioactive-daughter disequilibrium on U-Pb isotope apparent ages ---------- 6:663

Airborne radiometric survey, San Joaquin nuclear project site, California -------- 4:431

Alabama, miospore diversity and lithology, Coker Formation -------- 4:463

surface water, transverse dispersion in Mobile River ---------- 1:11

Page

Alaska, Brooks Range, Dietrich River, faunal sampling ---------- 4:519

Goat Island, spherulites in rhyolite dike ----- 4:445

Gravina-Nutzotin belt, platinum-group metals- 5:629

intrusive rocks, south-central part ------ 2:155

limnology, large meromictic lake ---------- 3:319

metamorphism, south-central part ---------- 2:173

palynology, Tertiary and Quaternary deposits at The Palisades-- 6:747

plutonic rocks, minor elements in sphene -- 5:623

Alkalic rocks, south-central Colorado, age determination and tectonic setting -- 6:673

Ammonite, new species, Wyoming ---------- 4:457

Amphibolites, Montana-Wyoming, geochemistry 1:53

Analbite, enthalpy of formation ---------- 4:413

Analyses. *See specific types:*

Atomic absorption,

Chromatography,

Neutron activation,

Selenium hydride–atomic absorption.

Analytical techniques, uranium and thorium and potassium in granitic rocks ---------- 1:83

See also Methods and techniques.

Page

Antimony, determination in coal by absorption spectrometry ----- 4:405

determination in geothermal waters by flame atomic absorption spectrometry ----- 6:807

Aquifers, artesian, identification of recharge leakage ---------- 4:491

flow to partially penetrating trench, northeast Mississippi --- 5:535

See also Ground water.

Arizona, Santa Catalina and Tortolita Mountains, middle Tertiary plutonism -------- 6:705

Arsenic, determination in coal by atomic absorption spectrometry - 4:405

Astronaut training, Nevada, test site craters--- 6:719

Atomic absorption–selenium hydride technique, test for homogeneity of USGS standard rocks ---------- 4:403

Atomic absorption spectrometry; arsenic, antimony, and selenium determination in coal -- 4:405

Atomic absorption spectroscopy, determination of thallium content in 16 USGS standard rocks ---------- 5:579

B

Baculites reduncus, Rock River Formation Wyoming -------- 4:457

Page

Bank-storage studies by remote sensing ----- 1:1
Basalt, petrology, East Pacific Rise ---------- 6:753
Basaltic lava. *See* Pele's hair.
Benthonic foraminifer assemblage, California, Santa Lucia Range 6:735
Benzoic acid, Calorimetry Conference, remeasurement of heat capacities ---------- 6:797
Biostratigraphy, California, Santa Lucia Range 6:735
diagnostic ostracodes, Virginia and North Carolina coastal plain ---------- 3:373
Bloedite and related minerals, marine shale, California ---------- 5:637
Brooks Range, Alaska, faunal sampling in Dietrich River ------- 4:519
Brucite, experimental and calculated activity-product constants from 10° to 90°C-- 2:227

C

Calcium fluoride, determination of solubility product ---------- 4:509
California, bloedite and related minerals, Diablo and Temblor Ranges ---------- 5:637
fault studies, San Joaquin nuclear project site ---------- 4:431
granitic intrusions, Pelona and Orocopia Schists ---------- 5:643
lower Tertiary biostratigraphy, Santa Lucia Range ---------- 6:735
olivine in ultramafic rock, northern Sierra Nevada ---------- 2:217
petrology, Lakeview Mountains pluton ------ 1:103
phytoplankton distribution and primary productivity, Donner Lake ---------- 2:265
Pleistocene fish, Alameda County ---------- 2:209
prehistoric mudflows, Monterey County ----- 1:17
quality of water, Sacramento River ------ 5:547

Page

steady-state model of shallow hydrothermal system, Imperial Valley ---------- 4:497
surface deformation, San Jacinto Valley ---- 1:117
surface water, south-central Sierra Nevada --- 1:33
Tertiary nannoplankton, technique for concentrating -------- 2:207
Campanian age, new ammonite zone, Wyoming --- 4:457
Canada, fluorite solubility studies, Madoc, Ontario ---------- 4:509
Carbon, primary productivity, Donner Lake, Calif ---------- 2:265
Carbon determination by combustimetric method 5:583
Carbon-14 dating, prehistoric mudflows, Monterey County, Calif ----- 1:17
Carbonatites, south-central Colorado, age determination and tectonic setting---- 6:673
Cenozoic, intrusive rocks, south-central Alaska --- 2:155
Channel geometry, Missouri River basin, relations to streamflow characteristics --- 3:285
Channel measurements, accuracy, Wyoming ---------- 6:811
Chemical dissolution, sulfide minerals ---------- 4:409
Cheswold aquifer, recharge study ---------- 4:491
Chlorophylls, separation by chromatography -- 2:263
Chromatographic analysis, chlorophylls *a* and *b* from freshwater algae ---------- 2:263
Clays. *See* Hectorite.
Coal; determination of arsenic, antimony, and selenium by atomic absorption spectrometry ---------- 4:405
Colorado, lower Paleozoic alkalic and mafic rocks, age determination and tectonic setting ------ 6:673
mercury in oil shale, Green River Formation -- 2:221

Page

structural, geology, gravitational spreading and fracturing --- 3:359
vertical electrical soundings, Rio Blanco County 2:193
Combustimetric determination of carbon -------- 5:583
Computer technology, comparison of extended *Q*-mode factor analysis and correspondence analysis when applied to compositional data ------- 1:103
Copper-uranium deposits, geochemical studies, Pennsylvania ----- 5:609
Cretaceous, intrusive rocks, south-central Alaska ---------- 2:155
metamorphism, south-central Alaska ---- 2:173

D

Delaware, recharge studies, Dover ---------- 4:491
Depositional environments, guide to uranium mineralization, Utah ---------- 3:365
Dewatering of aquifer, simulation of flow to partially penetrating trench, northeast Mississippi ------- 5:535

E

Earthquakes, relation to injection of radioactive wastes into shale ---------- 2:253
strong motion records, use in seismic risk analysis and earthquake-resistant design of structures- 4:437
East Pacific Rise, basalt, petrology ---------- 6:753
Electrical soundings, Rio Blanco County, Colo ----- 2:193
Engineering seismology, application of a hybrid computer ---------- 5:651
Enthalpy–dissolved silica plots, use in estimating temperature of hot-water component in mixed water ----- 1:49

Page

Enthalpy-of-formation studies. *See* Thermodynamic studies.
Entropies, standard, gibbsite 6:797
standard, magnesite 6:797
Eocene, intrusive rocks, south-central Alaska 2:155
Erosion, relation to geometry of hillslope profiles 4:487
Estuarine studies, effects of dredged channels on trace-metal migration 2:243

F

Fault studies, San Joaquin nuclear project site, California 4:431
Faunal sampling in arctic streams 4:519
Fish, Pleistocene, California 2:209
Fission-track ages, Santa Catalina and Tortolita Mountains, Ariz 6:705
Flame atomic absorption spectrometry, antimony determination in geothermal waters 6:807
Flooded urban areas, method for adjusting values of Manning's *n* 5:541
Florida, biostratigraphically diagnostic ostracodes, coastal plain areas 3:373
storm-water quality, Broward County 6:823
Fluid-inclusion homogenization temperatures, pressure corrections, system NaCl-H_2O 5:603
Fluorine, improved method for rapid determination in rocks and soils 5:589
removal from hectorite by wide-ranging pH solutions 2:235
Fluorite, natural, solubility at 25°C 4:509
Foraminifers, benthonic and planktonic, Santa Lucia Range 6:735
Globigerinoides pseudoruber, lectotype 4:453

Page

G

Galerkin finite-element analysis, steady-state flow and heat transport in shallow hydrothermal system, California 4:497
Geochemistry, amphibolites, Montana-Wyoming 1:53
comparison of analytical techniques for determining uranium, thorium, and potassium in granitic rocks 1:83
copper-uranium deposits, Pennsylvania 5:609
effect of pH on fluorine and lithium removal 2:235
enthalpies of formation of low albite, gibbsite, and some aluminosilicate minerals 4:413
plutonic rocks, Alaska 5:623
Utah and Colorado, mercury in oil shale from Mahogany zone of Green River Formation 2:221
Wyoming, uraniferous granite 1:61
Geochronology, metamorphic and igneous and hydrothermal events, Puerto Rico and the Virgin Islands 6:689
Newberry Crater, Oreg., volcanism 3:337
See also Age determinations.
Geographic studies, framework for monitoring land-use and land-cover changes 2:143
Geomorphology, erosion related to geometry of hillslope profiles 4:487
Geophysics, high-resolution gamma-ray spectrometry 6:783
uranium exploration techniques 3:343
Georgia, biostratigraphically, diagnostic ostracodes, coastal plain areas 3:373
land use change, detected by using Landsat data 5:529
Geothermal studies, warm springs 1:49

Page

Geothermal system, Galerkin finite-element analysis, steady-state flow and heat transport 4:497
Gibbsite, enthalpy of formation 4:413
heat capacities, standard entropies 6:797
Globigerinoides pseudoruber, designation and illustration of lectotype 4:453
Granite, uraniferous, Wyoming 1:61
Granitic intrusions, California, Pelona and Orocopia Schists 5:643
Granitic rocks, comparison of analytical techniques for determining uranium, thorium, and potassium 1:83
Gravina-Nutzotin belt, Alaska, volcanic and plutonic rocks 5:629
Green River Formation, Utah and Colorado, mercury in Mahogany zone oil shale 2:221
Ground water, Powder River Basin, resource analysis 4:473
use of thermal infrared imagery in bank-storage studies 1:1
Ground-water-flow problems, strongly implicit procedure, iteration parameter 6:815
Ground-water study, Rio Blanco County, Colo 2:193

H

Hawaii, Kilauea Volcano, some characteristics of Pele's hair 1:93
Heat capacities, Calorimetry Conference benzoic acid, remeasurement 6:797
gibbsite, standard entropies 6:797
magnesite, standard entropies 6:797
Heat-of-formation studies. *See* Thermodynamic studies.
Hectorite, removal of fluorine and lithium by wide-ranging pH solutions 2:235

Page

Hillslope profiles, differences in erosion rates ____ 4:487
Humic acids, generalized chemical structure_ 5:565
molecular aggregation of some fractions in *N*, *N*-dimethylformamide ____ 5:571
Hydrologic techniques, application of hydrometeorological model to south-central Sierra Nevada, California 1:33
equations describing solute transport by turbulent flow in a natural channel __ 3:277
estimating streamflow characteristics from channel-geometry measurements ____ 3:285
Hydrometeorological model, application to south-central Sierra Nevada, California 1:33

I

Illinois, fluorite solubility studies, Rosiclare__ 4:509
Infrared imagery, use in bank-storage studies ___ 1:1
Intrusive rocks, south-central Alaska ____ 2:155
Ion-selective electrode method, improved, for rapid determination of fluorine in rocks and soils ____ 5:589

J

Jurassic, intrusive rocks, south-central Alaska ____ 2:155

K

Kilauea Volcano, some characteristics of Pele's hair ____ 1:93

L

Lake studies. *See* Limnology.
Landsat data, detection of land use change, Georgia ____ 5:529
monitoring changes in land use and land cover 2:143
Land use change, framework for monitoring ___ 2:143
Georgia, detected by using Landsat data ____ 5:529

Page

Lava. *See* Pele's hair.
Limnology, Alaska, large meromictic lake ____ 3:319
California ____ 2:265
Lithium, removal from hectorite by wide-ranging pH solutions ____ 2:235
Lithology, relationship to miospore diversity, Coker Formation of western Alabama ____ 4:463
Low albite, enthalpy of formation ____ 4:413

M

Madison Limestone; Wyoming, Montana, North Dakota, South Dakota; aquifer studies ____ 4:473
Mafic rocks, south-central Colorado, age determination and tectonic setting ___ 6:673
Magnesite, heat capacities, standard entropies_ 6:797
Manning's *n*, method for adjusting values for flooded urban areas ____ 5:541
Mapping, for monitoring land-use and land-cover changes ____ 2:143
Marine shale, occurrence of bloedite and related minerals, California ____ 5:637
Mercury, migration in estuarine dredged channels__ 2:243
Utah and Colorado, Green River Formation oil shale ____ 2:221
Meromictic lake, southeastern Alaska, reconnaissance study ____ 3:319
Metamorphism, south-central Alaska ____ 2:173
Methods and techniques, atomic absorption analysis, arsenic and antimony and selenium in coal ____ 4:405
chlorophylls *a* and *b* determined from freshwater algae ____ 2:263
combustimetric carbon determination ____ 5:583
epithermal neutron-activation analysis of new USGS standard rocks ____ 3:397

Page

faunal sampling in arctic streams ____ 4:519
flame atomic absorption spectrometry, antimony determination in geothermal waters ____ 6:807
fluorine in rocks and soils, rapid determination ____ 5:589
hybrid computer in engineering seismology_ 5:651
Manning's *n* adjusted for flooded urban areas ____ 5:541
nannoplankton concentrated from Tertiary rocks ____ 2:207
pyrite-coated sand grains prepared for research on roll-type uranium deposits__ 5:595
recharge-leakage areas of artesian aquifers identified ____ 4:491
salt solubility determined in aqueous solutions at elevated temperatures ____ 3:389
selenium hydride–atomic absorption, test for homogeneity of USGS standard rocks ____ 4:403
uranium and thorium and potassium in granitic rocks, analyses compared ____ 1:83
uranium exploration by borehole geophysical measurements__ 3:343
Michigan, age determinations, Precambrian W Puritan Quartz Monzonite ____ 2:185
Micropaleontology, diagnostic ostracodes, Pliocene and lower Pleistocene of Virginia and northern North Carolina____ 3:373
technique for concentrating nannoplankton from Tertiary rocks ___ 2:207
Minerals. *See specific names.*
Minnelusa Formation; Wyoming, Montana, North Dakota, South Dakota; aquifer studies ____ 4:473

Page

Miocene, metamorphism, south-central Alaska ___ 2:173
planktonic foraminifer, *Globigerinoides pseudoruber*, lectotype _____ 4:453
Miospore diversity, relationship to lithology, Coker Formation of western Alabama _____ 4:463
Missouri River basin, streamflow characteristics related to channel geometry _____ 3:285
Model, shallow hydrothermal system, California_ 4:497
Montana, aquifer studies, Powder River Basin _____ 4:473
geochemistry, central Beartooth Mountains __ 1:53

N

Nannoplankton, California Tertiary rocks, technique for concentrating _____ 2:207
Neutron-activation analysis, new USGS standard rocks, minor and trace elements_ 3:397
Nevada, structural geology, near Mount Lewis _____ 3:325, 331
test site craters, astronaut training _____ 6:719
New Mexico, uranium ore, age determination ____ 6:669
New York, storm-water basins, analysis of recharge potential _____ 3:307
North Carolina, diagnostic ostracodes, Pliocene and lower Pleistocene _____ 3:373
North Dakota, aquifer studies, Powder River Basin _____ 4:473

O

Oil shale, Green River Formation, mercury content _____ 2:221
Olivine, ultramafic rock, California _____ 2:217
Ontario, fluorite solubility studies, Madoc ___ 4:509

Page

Ophiolite sequence probability, gabbroic complex along northern border of Josephine Peridotite, Oregon_ 6:761
Oregon, geology of gabbroic complex, northern border of Josephine Peridotite _____ 6:761
hydration dating of volcanism, Newberry Crater _____ 3:337
Ostracodes, diagnostic, Pliocene and lower Pleistocene of Virginia and northern North Carolina _____ 3:373
late Paleozoic, muscle scars _____ 1:135
Paleozoic, epigenetic radial shell structures __ 1:125

P

Paleontology, *Baculites reduncus*, Wyoming__ 4:457
California, Pleistocene fish fauna _____ 2:209
freshwater ostracodes, muscle scars _____ 1:135
Globigerinoides pseudoruber, designation and illustration of lectotype _____ 4:453
Paleozoic, epigenetic radial shell structures _____ 1:125
technique for concentrating nannoplankton from Tertiary rocks ____ 2:207
See also Micropaleontology, Palynology.
Paleozoic, freshwater ostracode muscle scars _____ 1:135
intrusive rocks, south-central Alaska _____ 2:155
ostracodes, epigenetic radial shell structures ___ 1:125
Palynology, Tertiary and Quaternary deposits, central Alaska _____ 6:747
Pele's hair, petrology _____ 1:93
Pelona and Orocopia Schists, California, granitic intrusions _____ 5:643
Pennsylvania, geochemical studies, copper-uranium deposits__ 5:609
Periphyton in the Sacramento River, Calif _____ 5:547

Page

Petrology, basalt, East Pacific Rise _____ 6:753
Lakeview Mountains pluton, southern California batholith _____ 1:103
Pele's hair _____ 1:93
Wyoming, uraniferous granite _____ 1:61
pH, effect on fluorine and lithium release in hectorite _____ 2:235
Phytoplankton, Donner Lake, Calif _____ 2:265
Sacramento River, Calif___ 5:547
Planktonic foraminifer, California, Santa Lucia Range _____ 6:735
Miocene, lectotype for *Globigerinoides pseudoruber* _____ 4:453
Platinum-group metals, volcanic and plutonic rocks, Alaska _____ 5:629
Pleistocene, California, freshwater fish fauna___ 2:209
Virginia and northern North Carolina, diagnostic ostracodes _____ 3:373
Pliocene, Virginia and northern North Carolina, diagnostic ostracodes _____ 3:373
Pollen studies. *See* Palynology.
Potassium, comparison of analytical techniques ___ 1:83
Potassium-argon ages, Santa Catalina and Tortolita Mountains, Ariz _____ 6:705
Powder River Basin, aquifer studies _____ 4:473
Precambrian, Michigan, age determinations of Puritan Quartz Monzonite _____ 2:185
Prehistoric mudflows, dating and recurrence, Monterey County, Calif _____ 1:17
Pressure corrections, fluid-inclusion homogenization temperatures, system $NaCl–H_2O$ _____ 5:603
Puerto Rico, geochronology, metamorphic and igneous and hydrothermal events ___ 6:689
Puritan Quartz Monzonite, Michigan, age determination _____ 2:185

Page

Pyrite coating of sand grains, experiments on genetic chemistry of roll-type uranium deposits ---------- 5:595
Pyroclastic ejecta. *See* Pele's hair.

Q

Q-mode factor analysis, extended method, comparison with correspondence analysis when applied to compositional data --- 1:103
Quality of water, California, periphyton and phytoplankton in the Sacramento River ---------- 5:547
remote measurement of solutes in water -- 5:561
storm-water runoff, Florida ---------- 6:823
Quaternary. *See* Pleistocene.

R

Radioactive wastes, injection into shale, relation to earthquakes --- 2:253
Recharge potential, storm-water basins, New York - 3:307
Recharge studies, Dover, Del-- 4:491
Remote sensing, comparison with ground-based techniques in measurement of transverse dispersion in Mobile River, Ala ------- 1:11
land use change, framework for monitoring --- 2:143
land use change, Georgia -- 5:529
measurement of solutes in water ---------- 5:561
thermal infrared imagery in bank-storage studies 1:1
Rock River Formation, Wyoming, paleontology ---------- 4:457
Roughness coefficient, method for adjusting values for flooded urban areas ---------- 5:541
Rubidium-strontium dating, Puritan Quartz Monzonite, Michigan ---------- 2:185

S

Salt solubility, determination of, new method ------ 3:389
San Joaquin nuclear project site, California, fault studies ---------- 4:431
Sedimentology, estuarine, effects of dredged channels on trace-metal migration ---------- 2:243
Seismology, application of a hybrid computer -- 5:651
Selenium, determination in coal by atomic absorption spectrometry - 4:405
Selenium hydride–atomic absorption technique, test for homogeneity of USGS standard rocks ---------- 4:403
Silica-enthalpy plot, use in estimating temperature of hot-water component in mixed water ---------- 1:49
Solubility studies, natural fluorite at 25°C ---------- 4:509
Solute transport, turbulent flow in a natural channel 3:277
South Dakota, aquifer studies, Powder River Basin ---------- 4:473
Sphene, plutonic rocks, west-central Alaska --- 5:623
Spherulites, in rhyolite dike, Goat Island, Alaska ---- 4:445
Storm drains, routing of storm-water flows ------ 3:301
Storm-water basins, analysis of recharge potential, New York -------- 3:307
Storm-water flows, routing through storm drains ---------- 3:301
Storm-water runoff, Florida, Broward County residential area ------ 6:823
Stratigraphy, Chinle Formation, San Rafael Swell, Utah ---------- 3:365
Rio Blanco County, Colo-- 2:193
Streamflow characteristics, estimation, Wyoming - 6:811
Missouri River basin, relation to channel geometry --------- 3:285
Strong motion records, earthquake studies, use in seismic risk analysis and earthquake-resistant design of structures -------- 4:437
Structural geology, gravitational spreading and fracturing, Colorado -- 3:359
near Mount Lewis, Nev ---------- 3:325, 331
Sulfide minerals, chemical dissolution ------- 4:409
Surface deformation, San Jacinto Valley, Calif ------ 1:117
Surface water, Alabama, transverse dispersion in Mobile River ----- 1:11
Alaska, large meromictic lake ---------- 3:319
California, application of hydrometeorological model to south-central Sierra Nevada ---- 1:33
Missouri River basin, flow characteristics related to channel geometry --------- 3:285
See also Estuarine studies, Limnology.

T

Tectonic setting, alkalic and mafic rocks in south-central Colorado -- 6:673
Temperature studies. *See* Geothermal studies.
Tennessee, earthquakes, relation to injection of radioactive wastes into shale ---------- 2:253
Tertiary, California, technique for concentrating nannoplankton --------- 2:207
intrusive rocks, south-central Alaska ---------- 2:155
See also Pliocene.
Test site craters, Nevada, astronaut training ----- 6:719
Texas, southern part, uranium exploration techniques ---------- 3:343
Thallium content, determination in 16 USGS standard rocks -------- 5:579
Thermodynamic studies, some aluminosilicate minerals --------- 4:413
Thermostatic water bath, experimental studies in aqueous solutions-- 5:597
Thorium, comparison of analytical techniques ---- 1:83
veins in south-central Colorado, age determination and tectonic setting ---------- 6:673

Page
Trace metals, migration in estuarine dredged channels ---- 2:243
Trenching, effects on water table, northeast Mississippi ---- 5:535
Triassic, intrusive rocks, south-central Alaska --- 2:155

U

Ultramafic rock, northern Sierra Nevada, Calif ---- 2:217
Uranium, age determination, Dakota Sandstone- 6:669
comparison of analytical techniques ---- 1:83
depositional environments, Utah ---- 3:365
exploration, high-resolution gamma-ray spectrometry ---- 6:783
geophysical exploration techniques ---- 3:343
pyrite coating of sand grains in experiments on genetic geochemistry of roll-type deposits 5:595
Wyoming, Granite Mountains ---- 1:61

Page
Uranium-lead isotope apparent ages, young minerals, effect of initial radioactive-daughter disequilibrium ---- 6:663
Urban area studies, method for adjusting values of Manning's *n* under flooded conditions -5:541
USGS standard rocks, a determination of 22 minor and trace elements in 8 new rocks by epithermal neutron-activation analysis- 3:397
selenium hydride–atomic absorption technique to test for homogeneity ---- 4:403
Utah, mercury in oil shale, Green River Formation -- 2:221
uranium mineralization, depositional environment ---- 3:365

V

Virgin Gorda batholith, age determination, Virgin Islands ---- 6:689
Virgin Islands, age of the Virgin Gorda batholith -- 6:689

Page
Virginia, diagnostic ostracodes, Pliocene and lower Pleistocene ---- 3:373
Volcanic rocks. *See* Pele's hair.
Volcanism, hydration dating, Newberry Crater, Oregon ---- 3:337

W

Warm springs, estimation of hot-water component temperature ---- 1:49
West Virginia, paleontology, freshwater ostracode muscle scars ---- 1:135
Wyoming, aquifer studies, Powder River Basin ---- 4:473
channel-measurement accuracy, implication in streamflow estimate ---- 6:811
geochemistry, central Beartooth Mountains -- 1:53
Granite Mountains ---- 1:61
paleontology, Rock River Formation ---- 4:457
petrology, Granite Mountains ---- 1:61

AUTHOR INDEX

Page

A

Adam, D. P---- 2:209
Anderson, J. R---- 2:143
Armbrustmacher, T. J---- 1:53
Aronson, D. A---- 3:307
Aruscavage, P. J---- 4:405; 5:579
Ashley, R. P---- 6:705
Averett, R. C---- 2:265

B

Babcock, R. S---- 3:389
Banks, N. G---- 6:705
Barnhard, J. A---- 4:437
Berg, H. C---- 5:629
Blackmon, P. D---- 3:343
Booker, S. E---- 5:565
Brabb, E. E---- 2:207
Britton, L. J---- 5:547
Brown, D. L---- 3:389
Brown, D. W---- 4:509
Brownfield, I. K---- 5:623

Page
Bunker, C. M---- 1:61, 83
Bush, C. A---- 1:61, 83

C

Campbell, D. L---- 2:193
Campbell, E. Y---- 4:403; 5:579
Casteel, R. W---- 2:209
Chao, T. T---- 4:409
Christopher, R. A---- 4:463
Cobban, W. A---- 4:457
Colton, R. B---- 3:359
Conklin, N. M---- 5:623
Cox, D. P---- 6:689
Creasey, S. C---- 6:705

D

Daniels, J. J---- 3:343
Doering, W. P---- 1:61
Dong, A. E---- 2:265
Donnell, J. R---- 2:221
Duffield, W. A---- 1:93

Page
E

Eberlein, G. D---- 4:445
England, A. W---- 4:431

F

Fisher, J. R---- 6:797
Fournier, R. O---- 1:49
Friedman, Irving---- 3:337

G

Gardner, J. M---- 2:235
Gent, C. A---- 5:595
Gibson, E. K., Jr---- 1:93
Gilluly, James---- 3:325
Goldberg, M. C---- 5:561
Granger, H. C---- 6:669
Greenland, L. P---- 4:403

H

Hadley, R. F---- 4:487
Haffty, Joseph---- 5:629

Page

Hays, W. W---- 5:651
Hazel, J. E---- 3:373
Head, W. J---- 4:473
Hedman, E. R---- 3:285
Heiken, G. H---- 1:93
Hejl, H. R---- 5:541
Hemingway, B. S---- 4:413; 6:797
Hess, G. R---- 6:753
Hietanen, Anna---- 2:217
Himmelberg, G. R---- 6:761
Holmes, C. W---- 2:243
Hopkins, D. M---- 5:589
Hostetler, P. B---- 2:227; 5:597
Hudson, Travis---- 2:155, 173
Huffman, Claude, Jr---- 1:83

J

Jackson, L. E., Jr---- 1:17
Jennings, M. E---- 3:301
Johnson, G. R---- 4:431
Johnston, R. H---- 4:491

K

Kastner, W. M---- 3:285
Keefer, T. N---- 3:301
Keil, R. L---- 1:83

L

Lanphere, M. A---- 2:155
Larson, S. P---- 6:815
Leahy, P. P---- 4:491
Leake, S. A---- 5:535
Lesure, F. G---- 5:609
Link, M. H---- 6:735
Lium, B. W---- 2:263
Loney, R. A---- 6:761
Ludwig, K. R---- 6:663, 669
Lupe, Robert---- 3:365

M

McCoy, G. A---- 3:319
McGee, K. A---- 2:227; 5:597
M'Gonigle, J. W---- 6:689
McGuire, R. K---- 4:437
McIntyre, D. H---- 6:689
Marvin, R. F---- 6:673, 689
Mattraw, H. C., Jr---- 6:823
Mehnert, H. H---- 6:673
Merkel, R. H---- 4:473

Page

Meyer, C. E---- 6:753
Meyer, William---- 1:11
Miesch, A. T---- 1:103
Millard, H. T., Jr---- 1:83
Miller, F. K---- 5:643
Miller, R. E---- 4:497
Moore, H. J---- 6:719
Moore, J. G---- 6:753
Moore, S. W---- 2:207
Morton, D. M---- 1:103, 117; 5:643
Motooka, J. M---- 5:609
Mountjoy, Wayne---- 2:235
Moxham, R. M---- 6:783
Murata, K. J---- 5:637

N

Nauman, J. W---- 4:519
Nkomo, I. T---- 1:83
Normark, W. R---- 6:753

O

Olson, J. C---- 6:673

P

Page, N. J---- 5:629
Park, R. B---- 5:651
Parker, R. L---- 6:673
Peterman, Z. E---- 2:185
Pinckney, D. J---- 5:565, 571
Plafker, George---- 2:155, 173
Poore, R. Z---- 4:453; 6:735
Potter, R. W., II---- 3:389; 5:603
Prill, R. C---- 3:307
Prinz, W. C---- 2:185

R

Radbruch-Hall, D. H---- 3:359
Rasmussen, L. A---- 1:33
Roberson, C. E---- 4:509
Robie, R. A---- 4:413; 6:797
Rogers, C. L---- 6:689
Rosholt, J. N---- 1:83
Rowe, J. J---- 3:397

S

Sanzalone, R. F---- 4:409
Scott, J. H---- 1:61; 3:343

Page

Shaw, V. E---- 2:221
Sherwood, C. B---- 6:823
Shoaf, W. T---- 2:263
Siebert, R. M---- 5:597
Silberman, M. L---- 3:331
Simon, F. O---- 5:579
Simons, F. S---- 1:53
Sims, P. K---- 2:185
Slack, K. V---- 4:519
Sliter, W. V---- 6:735
Sohn, I. G---- 1:125, 135
Staatz, M. H---- 5:623
Starkey, H. C---- 2:235; 3:343
Stauffer, R. E---- 6:807
Steinnes, Eiliv---- 3:397
Stuckless, J. S---- 1:61, 83
Sun, R. J---- 2:253
Szabo, B. J---- 6:669

T

Tangborn, W. V---- 1:33
Tanner, A. B---- 6:783
Theodore, T. G---- 6:705
Thompson, T. H---- 1:1
Tilley, L. J---- 4:519
Tillman, J. H---- 5:583
Todd, W. J---- 5:529
Toy, T. J---- 4:487
Trescott, P. C---- 6:815
Truesdell, A. H---- 1:49
Turner, D. L---- 2:173

V

Varnes, D. J---- 3:359
Vennum, W. R---- 4:445

W

Wahl, K. L---- 6:811
Warren, A. D---- 2:207
Weiner, E. R---- 5:561
Weis, P. L---- 5:609
Wershaw, R. L---- 5:565, 571
Wilson, W. H---- 6:797
Wrucke, C. T---- 3:331

Y

Yeend, W. E---- 6:747
Yotsukura, Nobuhiro---- 3:277

CHANGE OF ADDRESS FORM

NAME—FIRST, LAST

COMPANY NAME OR ADDITIONAL ADDRESS LINE

STREET ADDRESS

CITY | STATE | ZIP CODE

PLEASE PRINT OR TYPE

(or) COUNTRY

Mail this form to: NEW ADDRESS

Superintendent of Documents
Government Printing Office SSOM
Washington, D.C. 20402

Attach last subscription label here.

SUBSCRIPTION ORDER FORM

SUBSCRIPTION ORDER FORM

ENTER MY SUBSCRIPTION TO:

@ $ Domestic; @ $ Foreign.

NAME—FIRST, LAST

COMPANY NAME OR ADDITIONAL ADDRESS LINE

STREET ADDRESS

CITY | STATE | ZIP CODE

PLEASE PRINT OR TYPE

(or) COUNTRY

☐ Remittance Enclosed (Make checks payable to Superintendent of Documents)

☐ Charge to my Deposit Account No. .....

MAIL ORDER FORM TO:
Superintendent of Documents
Government Printing Office
Washington, D.C. 20402

RECENT PUBLICATIONS OF THE U.S. GEOLOGICAL SURVEY

The following books may be ordered from the Branch of Distribution, U.S. Geological Survey, 1200 South Eads Street, Arlington, VA 22202 (an authorized agent of the Superintendent of Documents, Government Printing Office). Prepayment is required. Remittances should be sent by check or money order payable to U.S. Geological Survey. Give series designation and number, such as Bulletin 1368–A, and the full title. Prices of Government publications are subject to change. Increases in costs make it necessary for the Superintendent of Documents to increase the selling prices of many publications offered. As it is not feasible for the Superintendent of Documents to correct the prices manually in all the previous announcements and publications stocked, the prices charged on your order may differ from the prices printed in the announcements and publications.

Professional Papers

P 640–G. Eocene corals from Eua, Tonga, by J. W. Wells, *with a statement on* Eocene fish fauna of Eua, Tonga, based on additional otoliths, by J. E. Fitch. 1976(1977). p. G1–G18; 3 pls. 95¢.

P 655–M. Effects of phreatophyte removal on water quality in the Gila River phreatophyte project area, Graham County, Arizona, by R. L. Laney, *with a section on* Statistical analysis, by H. W. Hjalmarson. 1977. p. M1–M23; plates in pocket. $3.

P 655–N. The hydrologic history of the San Carlos Reservoir, 1929–71, with particular reference to evapotranspiration and sedimentation, by F. P. Kipple. 1977. p. N1–N40. $2.

P 942. Flood-prone areas and land-use planning—selected examples from the San Francisco Bay region, California, by A. O. Waananen, J. T. Limerinos, W. J. Kockelman, W. E. Spangle, and M. L. Blair. 1977. 75 p. $2.20.

P 994–A. Depositional environment of Upper Cretaceous Black sandstones of the western interior, by R. S. Houston and J. F. Murphy. 1977. p. A1–A29. $2.

P 1005. Lithium resources and requirements by the year 2000, edited by J. D. Vine. 1976. 162 p. $3.25.

P 1014. Late Quaternary depositional history, Holocene sea-level changes, and vertical crustal movement, southern San Francisco Bay, California, by B. F. Atwater, C. W. Hedel, and E. J. Helley. 1977. 15 p.; plate in pocket. $1.85.

P 1021. Movement of moisture in the unsaturated zone in a loess-mantled area, southwestern Kansas, by R. C. Prill. 1977. 21 p. $1.70.

P 1022–A. Assessment of increased thermal activity at Mount Baker, Washington, March 1975–March 1976, by David Frank, M. F. Meier, D. A. Swanson, *with contributions by* J. W. Babcock, M. O. Fretwell, S. D. Malone, C. L. Rosenfeld, R. L. Shreve, and R. E. Wilcox. p. A1–A49. $2.25.

Bulletins

B 1377. Bibliography and index of U.S. Geological Survey publications relating to coal, 1882–1970, by Paul Averitt and Lorreda Lopez. 1972. 173 p. $2.50.

B 1391–E. Mineral resources of study areas contiguous to the Uncompahgre Primitive Area, San Juan Mountains, southwestern Colorado, by T. A. Steven, P. W. Lipman, F. S. Fisher, C. L. Bieniewski, and H. C. Meeves. 1977. p. E1–E126, plates in separate case. $7.

B 1433. Eocene rocks in northeast Washington—radiometric ages and correlation, by R. C. Pearson and J. D. Obradovich. 1977. 41 p.; plate in pocket. $2.25.

Water-Supply Papers

W 1887. Maximum floodflows in the conterminous United States, by J. R. Crippen and C. D. Bue. 1977. 52 p. $1.70.

W 2162. Ground-water levels in the United States, 1971–74, southwestern States. 1977. 86 p. $2.25.

W 2163. Ground-water levels in the United States, 1972–74, north-central States. 1977. 89 p. $2.25.

Back issues of the "Journal of Research of the U.S. Geological Survey" available at reduced prices—for limited time only. Copies of individual issues of volumes 1, 2, 3, and 4, published in 1973–76, are available at $1.25 per issue until December 31, 1977, or sooner if stocks become depleted. Order from U.S. Geological Survey, Branch of Distribution (Book Sales), 1200 South Eads Street, Arlington, VA 22202. Prepayment is required. Make check or money order payable to U.S. Geological Survey.

U.S. GOVERNMENT
PRINTING OFFICE
PUBLIC DOCUMENTS DEPARTMENT
WASHINGTON, D C 20402

OFFICIAL BUSINESS
PENALTY FOR PRIVATE USE $300

POSTAGE AND FEES PAID
U.S. DEPARTMENT OF THE INTERIOR
INT 413

U.S.MAIL

Special
fourth-class
rate books